

An Efficient Telemetry System for Restoring Sight

by

Nabeel Abdulrazzaq Fattah

A thesis submitted to the Department of Electrical and Electronic Engineering

In conformity with the requirements for

The degree of Doctor of Philosophy at Newcastle University

School of Electrical and Electronic Engineering

Newcastle University

(May 2018)

Copyright ©Nabeel Fattah, 2018

Abstract

The human nervous system can be damaged as a result of disease or trauma, causing conditions such as Parkinson's disease. Most people try pharmaceuticals as a primary method of treatment. However, drugs cannot restore some cases, such as visual disorder. Alternatively, this impairment can be treated with electronic neural prostheses. A retinal prosthesis is an example of that for restoring sight, but it is not efficient and only people with retinal pigmentosa benefit from it.

In such treatments, stimulation of the nervous system can be achieved by electrical or optical means. In the latter case, the nerves need to be rendered light sensitive via genetic means (optogenetics). High radiance photonic devices are then required to deliver light to the target tissue. Such optical approaches hold the potential to be more effective while causing less harm to the brain tissue. As these devices are implanted in tissue, wireless means need to be used to communicate with them. For this, IEEE 802.15.6 or Bluetooth protocols at 2.4GHz are potentially compatible with most advanced electronic devices, and are also safe and secure. Also, wireless power delivery can operate the implanted device.

In this thesis, a fully wireless and efficient visual cortical stimulator was designed to restore the sight of the blind. This system is likely to address 40% of the causes of blindness. In general, the system can be divided into two parts, hardware and software. Hardware parts include a wireless power transfer design, the communication device, power management, a processor and the control unit, and the 3D design for assembly. The software part contains the image simplification, image compression, data encoding, pulse modulation, and the control system. Real-time video streaming is processed and sent over Bluetooth, and data are received by the LPC4330 six layer implanted board. After retrieving the compressed data, the processed data are again sent to the implanted electrode/optrode to stimulate the brain's nerve cells.

Acknowledgements

First of all, I would like to thank my GOD (Allah) for helping and guiding me to the right path in my life.

I would like to express my special and wholehearted thanks to my main supervisor Dr. Patrick Degenaar. He is a matchless person. Many thanks for all your time and effort of the wonderful supervision. Many thanks for your support and help in bringing this work to its final form. His door was always open for his students, and he visited us in the lab asking about our progress and discussing the outcomes. I also give my special thanks to my second supervisor Dr. Graeme Chester. He helped me a lot with his experience, and I learned a lot from him. My sincere respect and thanks to my third supervisor, Dr. Danil Sokolov. I cannot find the right words to compliment his support and continuous help. Many thanks also to my postgraduate panel Andrey Mokhov and Alex Bystrov for their efforts.

Thank you with all of my heart to all my colleagues in the biomedical lab and all my friends in the microsystem group, especially Oras Al-Ani, Sabah Nayyef, Walid Al-Atabany, Mark Cunningham, Ahmed Soltan, Musa Al-Yaman, Graeme Coapes, Lijuan Xia, Jun Luo, Austin Ogwen, Rachael Savidis, Reza Ramezani, Fahimeh Dehkhoda and Dimitrios Firfilionis.

I would also like to thank all the lovely and friendly staff in the school of Electrical and Electronic Engineering, especially those who helped me with making this work become possible.

My gratitude is also great to my family, who encouraged and supported me to finish this work, especially my wife and son, who helped me with the financial issues during the last two years.

I apologize if I have missed mentioning your name, and I thank you very much for your support and help.

Gratitude for their great support

Dedication

To my wife

*Thank you for all of your love, effort and
continuous support. You are the best wife I'll ever know.*

To my son

*Thank you for all of your efforts and support for our
family. You are the only and most lovely son I have.*

List of Achievements

Submitted

International conference papers

- N. Fattah, S. Laha, D. Sokolov, G. Chester, and P. Degenaar, "Wireless data and power transfer of an optogenetic implantable visual cortex stimulator," in *2015 37th Annual International Conference of the IEEE Engineering in Medicine and Biology Society (EMBC)*, 2015, pp. 8006-8009. (Oral Presentation – 12 minutes)
- Lijuan Xia, Nabeel Fattah, Ahmed Soltan, Andrew Jackson, Graeme Chester and Patrick Degenaar, "A Low Power Flash-FPGA based Brain Implant Micro-System of PID", Preprint submitted to 39th Annual International Conference of the IEEE Engineering in Medicine and Biology Society. Received in February 2017.

International and local Symposium

- N. Fattah, W. Al-Atabany, D. Sokolov, G. Chester, P. Degenaar (Newcastle University, Newcastle upon Tyne/UK), "Real-Time Fully Wireless Implantable Optogenetics Visual Cortical Stimulator," the 2nd International Symposium on Artificial Vision in Aachen, Germany, 2015. (Oral Presentation – 13 minutes)
- Dr Patrick Degenaar and Nabeel Fattah, "Lighting up the visual cortex: Optogenetic Cortical prosthesis," Brain Hardcourt Memorial Meeting, Hazelwood Castle, York, UK, 10th May 2016. (Oral Presentation – 30 minutes)

Local conferences and meetings contributions

- N. Fattah, G. Chester, D. Sokolov and P. Degenaar, "Wireless Neuroprosthesis Implant," HCDP conference, Nottingham, 16 Sep 2013, Poster.
- N. Fattah, G. Chester, D. Sokolov and P. Degenaar, "Wireless Neuroprosthesis Implant," North East Epilepsy Research Network meeting, Durham, 27 Sep 2013
- School of Electrical and Electronic Engineering, Newcastle University, Annual Research Conference 23/24 January 2014, poster. Best Poster Award
- School of Electrical and Electronic Engineering, Newcastle University, Annual Research Conference, 21/22 January 2015, (Oral Presentation – 12 minutes).

- N. Fattah, G. Chester, D. Sokolov and P. Degenaar, “Optogenetic visual cortex implant,” NUIAPGR Research Day, North Great Museum, Newcastle, 10 March 2015, poster. Best Poster Award.
- N. Fattah, G. Chester, D. Sokolov and P. Degenaar, “Optogenetic visual cortex implant,” Biomedical Engineering Day, Newcastle, 15 December 2015, poster.
- N. Fattah, G. Chester, D. Sokolov and P. Degenaar, “Wireless power transfer for the Optogenetic implantable visual cortex stimulator,” ARC conference, 20/21 January 2016, paper, (Oral Presentation – 12 minutes), Best Paper Presentation Award.
- N. Fattah, G. Chester, D. Sokolov and P. Degenaar, “Optoelectronic Visual Prosthesis,” Engineering and Physical Sciences Research Council (EPSRC), Newcastle, UK, 19 April 2016.
- S. Nayyef, N. Fattah, W. Al-atabany, G. Chester, D. Sokolov and P. Degenaar, “Image processing and still Image Transferring for Optogenetics Visual Cortical Stimulator”, Biomedical Engineering Day, Newcastle University, UK, 2015

Group presentations

15 presentations to the biomedical lab group.

To be submitted

Journal paper

- Ahmed Soltan, Nabeel Fattah, Pleun Maaskant, Lionel Chaudet, Walid Al-Atabany, Sabah Nayyef, Mark Neil, Brian Corbett, Graeme Chester, Danil Sokolov, Patrick Degenaar "A head mounted optoelectronic stimulator for optogenetic retinal prosthesis" – to be submitted to Journal of Neural Engineering.

International conference papers

- Nabeel Fattah, Sabah Nayyef, Lijuan Xia and Patrick Degenaar "An Efficient Microcontroller for Visual Cortical Prosthesis", - to be submitted to Annual International Conference of the IEEE Engineering in Medicine and Biology Society.

List of Acronyms

Ψ	Magnetic Flux
μ	Permeability
μ LED	Micro Light-Emitting Diode
AC	Alternating Current
AIMD	Active Implantable Medical Devices
AM	Additive Manufacturing
AM	Amplitude Modulated
AMD	Age-Related Macular Degeneration
ASK	Amplitude Shift Keying
B	Magnetic Flux Density
BGA	Ball Grid Array
BLE	Bluetooth Low Energy
BPSK/QPSK	Binary/Quadrature Phase Shift Keying
CANDO	Controlling Abnormal Network Dynamics Using Optogenetics
CCK	Complementary Code Keying
CCS	Current Controlled Stimulation
Chr2	Channel-Rhodopsin 2
COFDM	Coded Orthogonal Frequency Division Multiplexing
CRC	Cyclic Redundancy Check
DBS	Deep Brain Stimulation
DC	Direct Current
DCT	Discrete Cosine Transform
DFT	Discrete Fourier Transform
DSP	Digital Signal Processing
EEG	Electroencephalogram
EPD	Even Power Distributor
FDA	Food and Drug Administration
FFC	Far Field Communication
FM	Frequency Modulation
FSK	Frequency-Shift Keying
GFSK	Gaussian Frequency Shift Keying
H	Magnetic Field Strength
IC	Integrated Circuit
ICVP	Intracortical Visual Prosthesis

IDCT	Inverse Discrete Cosine Transform
ISO	International Organization For Standardization
JPEG	Joint Photographic Experts Group
JTAG	Joint Test Action Group
KDS	Kinetis® Design Studio
LSK	Load Shift Keying
MEMS	Microelectromechanical Systems
M-QAM	M-Ary Quadrature Amplitude Modulation
MSE	Mean-Square Error
N	Number of Turns
NFC	Near Field Communication
NI	National Instrument
NORD	National Organization for Rare Disorders
OCD	Obsessive Compulsive Disorder
Optrode	Optical Probes
O-QPSK	Offset Quadrature Phase Shift Keying
PCB	Printing Circuit Board
PCE	Pearl Chain Effect
PM	Phase Modulation
PSK	Phase Shift Keying
PSNR	Peak Signal to Noise Ratio
RFID	Radio Frequency Identification
RP	Retinal Pigmentosa
SAR	Specific Absorption Rate
SLA	Stereolithography Apparatus ()
STL	Stereo Lithography
SWG	Standard Wire Gauge
UPS	Uninterruptible Power Supply
UWB	Ultra-Wideband
VCP	Visual Cortical Prosthesis
VCS	Voltage-Controlled Stimulation
UEA	Utah Electrode Array
USEA	Utah Slanted Electrode Array
WHO	World Health Organization
WPT	Wireless Power Transfer

Relative contribution

This table shows what I did and what others did for this project. They participated either by providing coding software or by assistance.

Name	Parts	Subject
Nabeel Fattah	Hardware	Wireless Power Transfer system
Nabeel Fattah	Hardware	All the PCBs
Nabeel Fattah and Walid Al-Atabany (jointly)	Software	Image simplification
Nabeel Fattah	Software	Image compression
Nabeel Fattah and Sabah Nayyef	Software	Image decompression
Nabeel Fattah and Sabah Nayyef (jointly)	Software	Pulse Modulation
Ahmed Soltan	Software	μ LED drive
Nabeel Fattah, Patrick Degenaar and Sabah Nayyef (jointly)	Software	Comparison between DCT-Blocks and DCT-Zigzag
Nabeel Fattah and Danil Sokolov (jointly)	Software	Data analysis of five videos
Nabeel Fattah	Software	Communication
Nabeel Fattah	Software	3D modelling
Nabeel Fattah	In vitro test	Wireless Power Transfer and Communication

Contents

CHAPTER 1. VISUAL CORTICAL PROSTHESIS.....	1
1.1 INTRODUCTION	1
1.2 THE HUMAN EYE, VISION AND BLINDNESS	2
1.3 EXAMPLES OF EYE DISEASES CAUSING BLINDNESS.....	5
1.4 REQUIREMENTS FOR MEDICAL IMPLANTS	5
1.5 MAIN COMPONENTS OF VISUAL PROSTHESIS.....	8
1.6 HUMAN HEALTH AND SAFETY CONSIDERATIONS	10
1.7 THESIS.....	10
1.7.1 <i>The motivations</i>	10
1.7.2 <i>The aim</i>	10
1.7.3 <i>The objectives</i>	11
1.7.4 <i>The achievements</i>	11
1.7.5 <i>The outline</i>	11
CHAPTER 2. LITERATURE REVIEW	13
2.1 INTRODUCTION	13
2.2 NEUROPROSTHETICS HISTORY.....	14
2.3 VISUAL PROSTHESIS.....	15
2.4 IMAGE PROCESSING.....	21
2.5 IMAGE COMPRESSION	22
2.6 COMMUNICATION	24
2.6.1 <i>Near Field Communication</i>	24
2.6.2 <i>Far Field Communication</i>	25
2.7 DATA TRANSFER	26
2.8 IMPLANT MATERIAL	27
2.9 HERMETIC ENCAPSULATION	29
2.10 STIMULATION PROBES	29
2.10.1 <i>Electrical stimulation</i>	30
2.10.2 <i>Optical stimulation</i>	31
2.11 POWERING MEDICAL IMPLANTS	33
2.11.1 <i>Battery</i>	34
2.11.2 <i>Wireless power transfer</i>	36
2.12 ELECTROMAGNETIC RADIATION AND HEALTH	37
CHAPTER 3. WIRELESS POWER TRANSFER	38
3.1 INTRODUCTION	38
3.2 PHYSICS OF WIRELESS POWER TRANSFER.....	39

3.2.2 Magnetic field strength	40
3.2.3 Magnetic flux and magnetic flux density	42
3.2.4 Inductance	42
3.2.5 Mutual inductance	46
3.2.6 Coupling coefficient	47
3.2.7 Resonance	48
3.2.8 Power efficiency	49
3.2.9 Impedance matching	49
3.2.10 Skin effect	51
3.2.11 Class E power amplifier	52
3.2.12 Voltage rectification	53
3.2.13 Voltage Regulation	55
3.2.14 Matlab simulation for Wireless Power Transfer	56
3.3 POWER SYSTEM DESIGN	60
3.3.1 Battery	60
3.3.2 Embedded system power management	61
3.3.3 Power transmitter	63
3.3.4 AC to DC converter	68
3.3.5 Voltage regulator	69
3.4 PORTION OF POWER CONSUMPTION	70
CHAPTER 4. REAL TIME DATA TRANSFER	73
4.1 SOFTWARE DESIGN	73
4.1.1 An overview of retinal processing	75
4.1.2 Image simplification and edge highlighting	79
4.1.3 Image compression	81
4.1.4 Image decompression	82
4.1.5 Pulse modulation	83
4.2 VISUAL INFORMATION SYSTEM	84
4.2.1 Camera	84
4.2.2 Embedded processor	85
4.2.3 Microcontroller	86
4.2.4 Data link	88
4.3 SOFTWARE CONFIGURATION	89
4.3.1 Image acquisition	91
4.3.2 Image simplification	91
4.3.3 Data analysis	93
4.3.4 Image compression	95
4.3.5 Data link	96
4.3.6 Image decompression	98

4.3.7 Pulse modulation	100
4.3.8 μ LED display.....	101
4.3.9 Processing requirement	102
4.3.10 Implantable microcontroller unit	103
4.4 COMPARISON BETWEEN DCT-BLOCKS AND DCT-ZIGZAG	109
4.4.1 Embedded system integration	113
4.4.2 Implantable system integration.....	114
CHAPTER 5. SYSTEM INTEGRATION AND PACKAGING	117
5.1 HARDWARE OVERVIEW	117
5.1.1 External power management unit	118
5.1.2 Power Transmitter	120
5.1.3 Coil Inductors	123
5.1.4 Power receiver	124
5.2 CAMERA	127
5.3 PCB LAYOUT CONSIDERATION	127
5.4 SECURITY AND SAFETY.....	127
5.5 SYSTEM LEVEL TESTING	129
5.5.2 Optrodes	133
5.6 ASSEMBLY OF VISUAL CORTICAL PROSTHESIS	133
CHAPTER 6. DISCUSSION AND CONCLUSION	136
6.1 WIRELESS POWER TRANSFER	136
6.2 IMAGE PROCESSING.....	138
6.2.1 Hardware	138
6.2.2 Software.....	138
6.3 SAFETY	139
6.4 CONCLUSION	140
CHAPTER 7. FUTURE WORK.....	142
Headset.....	183
Implantable unit	184

List of Figures

FIGURE 1-1: THE ANATOMY OF THE HUMAN EYE. THE CORNEA IS AT THE FRONT OF THE EYEBALL AND IT ENDS AT THE OPTIC NERVE. LIGHT PASSES THROUGH DIFFERENT LAYERS AND MEDIUMS UNTIL IT REACHES THE RETINA. THERE IS A CORNEA, AQUEOUS HUMOUR, A LENS, VITREOUS HUMOUR, AND A RETINA [16].	3
FIGURE 1-2: THE VISUAL PATHWAY FROM THE EYE TO THE VISUAL CORTEX IN THE BRAIN. REAL TIME IMAGES ARE PROCESSED IN THE EYE AND TRANSFERRED VIA THE OPTIC NERVE TO THE VISUAL CORTEX.	4
FIGURE 1-3: EXAMPLES OF DBS AND THE HISTORY OF THE AIMDS. THE HISTORICAL PERIODS DEPENDS ON THE EARLY INVENTION AND TESTING TIMES. ALL THOSE LISTED ARE STILL IN THE DEVELOPING AND IMPROVEMENT STAGE [34].	8
FIGURE 1-4: THE CONCEPT OF A FULLY WIRELESS OPTOGENETIC VISUAL CORTEX IMPLANT FOR RESTORING SIGHT. THE SYSTEM COMPRISES A WIRELESS POWER DELIVERY TO THE IMPLANT SYSTEM, THE RETINAL IMAGE PROCESSING AND THE WIRELESS DATA LINK. THE BRAIN CELLS ARE INJECTED WITH CHANNEL-RHODOPSIN2 TO RESPOND TO THE LIGHT STIMULATOR.	9
FIGURE 2-1: PRINCIPLE COMPONENTS OF A VISUAL PROSTHESIS. FIRST, A CAMERA CAPTURES REAL TIME IMAGES, AND THEN THE IMAGES ARE PROCESSED IN A SIMILAR TO HOW THE RETINA WOULD DO SO. FINALLY, VISUAL CELLS ARE STIMULATED WITH ELECTRODES/OPTRODES (FROM DEGENAAR LECTURE NOTES 2017).	16
FIGURE 2-2: A TRADITIONAL SCHEMATIC OF THE RETINAL PROSTHESIS. REAL TIME VIDEO IS WIRELESSLY TRANSFERRED TO THE IMPLANT PART, AND THE RECEIVED DATA, AFTER BEING PROCESSED, ARE SENT TO ELECTRODE ATTACHED TO THE RETINA [65].	17
FIGURE 2-3: THE VISUAL CORTICAL IMPLANT DEVICE OF DOBELLE FROM 1978-2000. THE LOW QUALITY CAMERA MOUNTED ON GLASSES IS CONNECTED TO THE IMPLANT DEVICE VIA TRANSCUTANEOUS WIRES [76].	20
FIGURE 2-4: EXAMPLE OF IMAGE PROCESSING FOR THE RETINAL PROSTHESIS, SHOWING THE EFFECT OF SCENE SIMPLIFICATION IN REDUCING IRRELEVANT INFORMATION BUT LEAVING ONLY THE RELEVANT OBJECTS. THE LEFT COLUMN IS FOR AN IMAGE SIZE OF 256x256 PIXELS, AND THE RIGHT COLUMNS ARE FOR AN IMAGE SIZE OF 16x16 PIXELS TOP SET: IS A SPATIAL DERIVATIVE IMAGE WITH THE LOW CONTRAST BACKGROUND. AFTER RETINAL PROCESSING, THE IMAGE IS CLEARER THAN THE LIZARD IN THE LOW CONTRAST BACKGROUND FOR LOW QUALITY IMAGES. BOTTOM SET: IS THE SIMPLIFIED AND EDGE ENHANCED SCENE [82].	22
FIGURE 2-5: (A) DISCRETE SIGNAL. (B) THE DFT SPECTRUM. (C) THE DCT SPECTRUM. (D) COMPARISON OF THE DCT, DFT AND THE ORIGINAL SIGNAL $x(n)$.	24
FIGURE 2-6: OPTOGENETIC ENGINEERING. (A) THREE TYPES OF LIGHT SENSITIVE PROTEINS. TOP: AN EXAMPLE OF A PROTEIN SENSITIVE TO BLUE LIGHT, CALLED CHANNEL-RHODOPSIN-2 (ChR2). MIDDLE: A PROTEIN EXAMPLE SENSITIVE TO YELLOW LIGHT, CALLED NATRONOMONAS PHARAONIS HALORHODOPSIN (NpHR). BOTTOM: OPTOXRS, WHICH RESPONDS TO GREEN LIGHT. (B) SIMPLIFIED STEPS OF OPTOGENETIC ENGINEERING, SHOWS ADDING THE PROMOTOR TO THE OPSIN GENE THEN INJECTING IT TO A VIRUS. (C) EXAMPLE OF LIGHT DELIVERY TO AN ENGINEERED BRAIN CELL IN A MOUSE [146].	32
FIGURE 2-7: MEDICAL IMPLANT DEVICES AND THE CONCEPTUAL RANGE OF POWER CONSUMPTION. THE POWER CONSUMPTION LINE FOR ELECTROMAGNETIC [152], DRUG PUMP [153], NERO-STIMULATOR [154] CENTRAL NERVOUS SYSTEM AND PERIPHERAL NERVE STIMULATION, PACEMAKER [155], CORTICAL PROSTHESIS [156], RETINAL PROSTHESIS [157] AND COCHLEAR IMPLANT [2] ARE PRESENTED.	33

FIGURE 2-8: SIMPLE SCHEMATIC OF WIRELESS RADIO FREQUENCY FOR RECHARGING AN IMPLANTABLE BATTERY [176].	35
FIGURE 3-1: THE GENERAL CONCEPT OF WIRELESS POWER TRANSFER. K REPRESENTS THE COUPLING COEFFICIENT, WHICH DEPENDS ON THE DISTANCE BETWEEN THE TRANSMITTER AND THE RECEIVER COILS.	39
FIGURE 3-2: MAGNETIC FLUX SURROUNDS THE STRAIGHT WIRE. THE DIRECTION OF THE MAGNETIC FLUX CAN BE ASSIGNED USING THE RIGHT GRIP RULE. WHERE I REPRESENTS CURRENT FLOW IN THE WIRE AND H IS THE MAGNETIC FIELD.	40
FIGURE 3-3: CURRENT FLOWS IN A CIRCULAR SHAPED WIRE AND THE MAGNETIC FIELD STRENGTH IS THE DISTANCE x FROM THE COIL.	41
FIGURE 3-4: THE MAGNETIC FLUX AND MAGNETIC FLUX DENSITY MODIFIED FROM [201].	42
FIGURE 3-5: THIN FILM CONDUCTOR.	44
FIGURE 3-6: SQUARE LOOP INDUCTORS. WHERE t TRACE THICKNESS, N IS THE NUMBER OF TURNS, A IS THE LENGTH OF THE FIRST TRACE AND W IS WIDTH.	44
FIGURE 3-7: SOLENOID COIL.	46
FIGURE 3-8: MUTUAL INDUCTANCE BETWEEN TWO COUPLED COILS. THE DISTANCE BETWEEN THE TWO COILS IS EQUAL TO x , AND R REPRESENTS THE COIL'S RADIUS.	47
FIGURE 3-9: RESONANT CIRCUIT AFTER ADDING THE CAPACITOR C_2 IN PARALLEL WITH THE COIL.	48
FIGURE 3-10: 'L' MATCHING NETWORK.	50
FIGURE 3-11: THE CLASS E POWER AMPLIFIER SCHEMATIC EXAMPLE (IMAGE FROM [215]).	52
FIGURE 3-12: CIRCUIT SCHEMATIC AND WAVEFORM OF (A) THE HALF-WAVE RECTIFIER AND (B) THE FULL-WAVE RECTIFIER (IMAGE FROM [218]).	54
FIGURE 3-13: EXAMPLE OF THE ADJUSTABLE OPERATION OF THE VOLTAGE REGULATOR. LT1763 IS A LOW DROPOUT, LOW NOISE REGULATOR FROM THE LINEAR TECHNOLOGY COMPANY. IT IS USED FOR FIXED AND ADJUSTABLE OUTPUT VOLTAGE.	55
FIGURE 3-14: THE MAGNETIC FIELD IS PROPORTIONAL TO THE RADIUS OF THE PRIMARY COIL AND REVERSE-PROPORTIONAL TO THE DISTANCE FROM THE POINT OF THE MEASUREMENT. FOR A DISTANCE OF LESS THAN 50 MM THE SMALLER COIL IS BETTER, BUT FOR MORE THAN 50 MM THE LARGER RADIUS COIL IS BETTER.	56
FIGURE 3-15: DEPENDENCY OF THE MAGNETIC FIELD ON THE PRIMARY COIL RADIUS. A SMALL COIL FOR A SMALL DISTANCE OF LESS THAN 50 MM IS BETTER THAN THE LARGE COIL.	57
FIGURE 3-16: RELATION BETWEEN THE MAGNETIC FIELD STRENGTH (H) AND THE NUMBER OF TURNS IN THE PRIMARY AND SECONDARY COILS. A SMALL COIL IS BETTER THAN A LARGE COIL OVER SMALL DISTANCES, AND BY INCREASING THE NUMBER OF TURNS IT BECOMES MORE EFFICIENT.	57
FIGURE 3-17: THE RELATION BETWEEN THE MAGNETIC FIELD STRENGTH (H) AND CHANGE IN CURRENT FLOW IN THE COPPER WIRES (COILS). INCREASING CURRENT FLOW IN THE SMALL COIL OVER A THE SMALL DISTANCE HAS THE SAME EFFECT AS INCREASING THE NUMBER OF TURNS.	58
FIGURE 3-18: RELATION BETWEEN CHANGE IN THE RADIUS OF THE INNER COIL, THE DISTANCE BETWEEN THE TWO COILS AND CHANGE IN RADIUS FOR THE IMPLANTED COIL WITH THE MUTUAL INDUCTANCE (TOP). THE RELATION BETWEEN THE POWER EFFICIENCY AND THE LOAD RESISTANCE (BOTTOM).	59
FIGURE 3-19: SHOWS BATTERY CHARGE AND DISCHARGE (IMAGE FROM TEXAS INSTRUMENTS [221]).	61
FIGURE 3-20: THE BLOCK DIAGRAM OF CONNECTING THE RASPBERRY PI ZERO WITH THE STEP-UP VOLTAGE CONVERTER (POWER BOOST). IT ALSO SHOWS THE BATTERY CONNECTIONS TO THE SYSTEM. THE POWER BOOST CONVERTS THE VOLTAGE FROM 3.7 V TO 5 V (GREEN BLOCKS). IT CONNECTS THE POWER BOOST 1000C TO THE WIRELESS POWER	

TRANSMITTER. THE STEP-UP VOLTAGE (DESIGNED POWER BOOST) POWER CONVERTER FROM 5 V TO 12 V IS PUT IN BETWEEN (ORANGE BLOCKS).....	62
FIGURE 3-21: THE LTC3122 POWER BOOST, A DC-DC CONVERTER FROM 5 V TO 12 V. THE HEADER J1 IS FOR INPUT 5V, AND THE HEADER J2 IS FOR THE OUTPUT. THE SCHEMATIC WAS PROVIDED BY THE LINEAR TECHNOLOGY COMPANY. ..	63
FIGURE 3-22: CIRCUIT DIAGRAM OF DS1085L FOR PROGRAMING AND GENERATING THE SINE WAVES AT A SPECIFIC FREQUENCY.....	64
FIGURE 3-23: SCHEMATIC OF THE TIMER 555. THE TOTAL OUTPUT TIME IS EQUAL TO T1 PLUS T2, AND OUTPUT VOLTAGE DEPENDS ON VCC. THE TWO RESISTORS R1 AND R2 ARE USED TO CONTROL THE OUTPUT FREQUENCY.	64
FIGURE 3-24: THE SWITCH PERFORMANCE OF THE CLASS E POWER AMPLIFIER. THE SWITCH REPRESENTS A TRANSISTOR. THE VALUE OF RESISTANCE R DEPENDS ON LT AND CT.....	67
FIGURE 3-25: THE CIRCUIT SCHEMATIC OF THE VOLTAGE RECTIFIER AND THE RESULT OF THE OUTPUT VOLTAGE WITH AND WITHOUT THE SMOOTHING CAPACITOR, WHILE THE PEAK OF THE RIPPLE VOLTAGE (V_{DC}) DEPENDS ON THE CURRENT ACROSS THE LOAD RESISTANCE TO THE FREQUENCY AND SMOOTHING CAPACITOR (BOTTOM WAVEFORM).	68
FIGURE 3-26: SIMULATION CIRCUIT SCHEMATIC FOR LT1763CDE-1.8, LT1763CDE-3.3 AND LT1763CDE-5 REGULATORS. IN THIS TEST, THE CIRCUIT DESIGNED FOR OBTAINING THREE OUTPUTS AS THEY ARE 1.8 V, 3.3 V AND 5 V.	70
FIGURE 3-27: PORTION OF THE POWER CONSUMPTION FOR THE TRANSMITTER SIDE (LEFT) AND THE RECEIVER SIDE (RIGHT).	71
FIGURE 4-1: THE FLOW OF IMAGE PROCESSING. THE EXTERNAL DEVICES START WITH THE CAMERA FOR CAPTURING LIVE STREAMING AND END WITH DATA ENCODING, WHILE THE IMPLANT DEVICES START WITH DATA DECODING AND END WITH THE STIMULATORS.	74
FIGURE 4-2: THE EYE AND THREE LAYERS OF THE RETINA, INCLUDING THEIR CELL TYPES. THE LIGHT PASSES THROUGH THE OUTER LAYER INTO THE INNER LAYER AND STARTS TO BE ABSORBED IN THE INNER LAYER BY CONES AND RODS. SIGNALS ARE SENT TO THE GANGLION CELLS VIA THE BIPOLAR CELLS. FROM THE BIPOLAR CELLS, DATA IS FORWARDED TO THE OPTIC NERVE (IMAGE FROM NATURE REVIEWS DRUG DISCOVERY [227]).	76
FIGURE 4-3: THE RECEPTIVE FIELDS IN THE GANGLION LAYER ON-CENTRE AND OFF-SURROUNDED (LEFT), OFF-CENTRE AND ON-SURROUNDED (RIGHT).	76
FIGURE 4-4: THE RESPONSE OF AN ON-CENTRE GANGLION CELL TO A SPOT OF LIGHT (A) THE LIGHT ENTERS THE SURROUNDING REGION OF THIS ON-CENTRE GANGLION CELL AND THE LEVEL OF ACTIVITY IN THE CELL WILL DECREASE. (B) A SPOT OF LIGHT IN THE CENTRE OF THE RECEPTOR FIELD INCREASES THE FIRING RATE. (C) THE MAXIMUM RESPONSE IN THE ON-CENTRE GANGLION CELL IS ACHIEVED WHEN THE ENTIRE CENTRE OF THE FIELD IS ILLUMINATED. (D) IF ONLY THE SURROUNDING OF THE CELL IS ILLUMINATED WITH A RING OF LIGHT, THE GANGLION CELL IS MAXIMUMLY INHIBITED. (E) ILLUMINATING BOTH THE CENTRE AND SURROUNDING REGION MEANS THE RESPONSE IS JUST ABOVE THE BASELINE. THIS OCCURS BECAUSE THE CENTRE EFFECTS ARE SLIGHTLY STRONGER THAN THE SURROUNDINGS. THE RESPONSE OF AN OFF-CENTRE GANGLION CELL: (F) THE LIGHT ENTERS THE SURROUNDING REGION OF THE OFF-CENTRE GANGLION CELL. THE LEVEL OF ACTIVITY RECORDED IN THE CELL INCREASES. (G) A SPOT OF LIGHT IN THE CENTRE OF THE RECEPTOR FIELD DECREASES THE FIRING RATE. (H) IF THE ENTIRE CENTRE OF THE OFF-CENTRE GANGLION CELL IS ILLUMINATED, THE CELL IS MAXIMUMLY INHIBITED. (I) MAXIMUM RESPONSE IS ACHIEVED WHEN THE ENTIRE SURROUND IS ELIMINATED BY THE RECEIVING FIELD. (J) WITH THE CENTRE GANGLION CELL, IF WE ILLUMINATE THE CENTRE AND SURROUNDING REGION, THE RESPONSE WILL CHANGE VERY LITTLE FROM A BASELINE (THE CONCEPT OF THE IMAGE FROM NEUROSCIENCE [228]).	77

FIGURE 4-5: RESPONSES OF THE HYPOTHETICAL POPULATION ON THE CENTRE GANGLION CELL. (i) THERE IS NO RESPONSE FROM THE RECEPTOR CELL. (ii) RESPONSE RATE BELOW THE SPONTANEOUS LEVEL OF ACTIVITY. (iii) NO RESPONSE. (iv) THE HIGHEST RESPONSE RATES. (v) THERE IS A RESPONSE BUT IT IS LOW (IMAGE CONCEPT FROM NEUROSCIENCE [228]).	78
FIGURE 4-6: THE STEPS OF THE IMAGE COMPRESSION USING THE DCT-BLOCK. MATLAB SIMULINK WAS USED TO IMPLEMENT THE CODE TO THE LPC4330 MICROCONTROLLER. THIS EXAMPLE IS FOR 61% COMPRESSION RATIO.	82
FIGURE 4-7: IMAGE DECOMPRESSION STEPS USING THE DCT-BLOCK. MATLAB SIMULINK WAS USED TO IMPLEMENT THE CODE IN THE LPC4330 MICROCONTROLLER. THIS EXAMPLE IS FOR 61% OF THE COMPRESSION RATIO.	83
FIGURE 4-8: THE BLOCK DIAGRAM OF THE HARDWARE OF THE TRANSMITTER PART FOR THE VISUAL INFORMATION SYSTEM. THE SYSTEM CONSISTS OF A CAMERA, RASPBERRY PI ZERO, AND BLUETOOTH.	84
FIGURE 4-9: LOGITECH C270 720P HD WEBCAM IS USED ON THE TRANSMITTER SIDE FOR LIVE VIDEO STREAMING.	85
FIGURE 4-10: BLOCK DIAGRAM OF THE MICROCONTROLLER ARCHITECTURE. IN GENERAL, MICROCONTROLLERS CONSIST OF A CENTRAL PROCESSING UNIT (CPU), RANDOM ACCESS MEMORY (RAM), READ ONLY MEMORY (ROM), INTERNAL CLOCK AND PORT INTERFACING WITH EXTERNAL DEVICES (IMAGE FROM eBook TITLED DIGITAL SYSTEM DESIGN –USE OF MICROCONTROLLERS [233]).	87
FIGURE 4-11: (A) BLUETOOTH 4.0 ADAPTER MODEL PLUGABLE USB 2.0. IT IS USED ON THE TRANSMITTER SIDE, AND IT SUPPORTS ALL RASPBERRY PI MODELS. IT IS COMPATIBLE WITH CLASSIC BLUETOOTH [242]. (B) THE HC05 BLUETOOTH MODULE FOR THE RECEIVER SIDE. THE BOARD IS SOLDERED TO THE IMPLANTED BOARD.	89
FIGURE 4-12: THE IMAGES ARE CONVERTED TO GRAYSCALE INTENSITY AFTER BEING CAPTURED BY THE USB CAMERA. THEN, THE IMAGE IS RESIZED TO 64x64 PIXEL SIZE AND SIMPLIFIED ACCORDING TO THE RETINAL PROCESSING.	90
FIGURE 4-13: BLOCK DIAGRAM SHOWING THE IMAGE PROCESSING ON THE TRANSMITTER SIDE.	90
FIGURE 4-14: BLOCK DIAGRAMS OF THE IMAGE PROCESSING ON THE RECEIVER SIDE. THE COMPRESSED IMAGES RESTORED TO THE SIMPLIFIED IMAGE. THEN, CONVERSION OF AN INDIVIDUAL IMAGE TO PULSE MODE, AND TRANSITION TO THE OPTRODE.	91
FIGURE 4-15: EXAMPLE OF IMAGE PROCESSING STEPS ON THE TRANSMITTER SIDE, CONSISTING OF IMAGE SIMPLIFICATION THAT INCLUDES IMAGE CARTOONIZATION AND EDGE HIGHLIGHTING. THE SIZE OF THE IMAGES IS 4096 BYTES, WHICH MEANS 64x64 PIXELS.	92
FIGURE 4-16: RELATIONSHIP BETWEEN THE NUMBER OF ITERATIONS, THE NUMBER OF IMAGES PER SECOND, AND THE QUALITY OF IMAGES. BETTER QUALITY IS IN THE LOWER NUMBER OF ITERATIONS REGION, AND FOR THE 25 FRAMES PER SECOND, THE NUMBER OF ITERATIONS IS EQUAL TO 7.	93
FIGURE 4-17: FIVE VIDEOS FOR DATA ANALYSIS. THEY WERE TAKEN WITH DIFFERENT BACKGROUNDS AND DIFFERENT LIGHT SOURCES. THE LENGTH OF EACH VIDEO IS 21 SEC. A MOBILE PHONE SAMSUNG GALAXY NOTE II WAS USED TO CAPTURE THESE SCENES.	94
FIGURE 4-18: RELATIONSHIP BETWEEN THE DATA RATE AND THE NUMBER OF PIXELS FOR DIFFERENT BACKGROUNDS. THERE IS A NOTICEABLE SHIFT FOR THE VIDEOS WITH NATURAL LIGHT BACKGROUNDS.	95
FIGURE 4-19: THE NOVEL TWO-WAY COMMUNICATION THROUGH THE AIR USING BLUETOOTH BETWEEN TWO RFDUINO. RFDUINO IS AN EXAMPLE OF BLUETOOTH 4.0 AND BLUETOOTH LOW ENERGY (BLE). THE TEST WAS REPEATED BY SENDING THE DATA THROUGH WATER AND PORK.	96

FIGURE 4-20: EXPERIMENTAL RIG WITH FARADAY CAGE TO MEASURE WIRELESS DATA AND POWER TRANSFER THROUGH PORK.	
THE IMPLANTED DEVICE (INSIDE THE CAGE) IS POWERED WIRELESSLY. THE TRANSMITTER RFDUINO IS FIXED ON A ROD AT 25 CM DISTANCE FROM THE RX, AND IT IS POWERED BY A BATTERY SOURCE.	97
FIGURE 4-21: SCREENSHOT CAPTURED FROM LIVE STREAMING FOR DIFFERENT COMPRESSION RATIOS. THE DCT-BLOCKS WERE IMPLEMENTED FOR IMAGE COMPRESSION. THE 2x2 BLOCKS FOR THE 93% COMPRESSION, 3x3 FOR THE 86% COMPRESSION AND THE 4x4 FOR THE 75% IMAGE COMPRESSION.	99
FIGURE 4-22: THE RESULT OF IMAGE SIMPLIFICATION AND COMPRESSION FOR FIVE RECORDED VIDEOS. V1 WAS IN THE LAB, V2 WAS IN THE CORRIDOR, V3 WAS IN THE ELEVATOR, V4 WAS IN THE GARDEN, AND V5 WAS A MIXED NATURAL BACKGROUND. IN V1, V2 AND V5, THE SCENES CAN BE RECOGNISED, WITH A COMPRESSION RATIO OF UP TO 86%. IN V3 AND V4, IT IS CLEAR FOR UP TO 75%.	100
FIGURE 4-23: EXAMPLE OF SUB-FRAMES FOR PULSE-MODULATION. THE NUMBER OF SUB-FRAMES DEPENDS ON THE INTENSITY LEVEL REQUIREMENT FOR THE DISPLAY ON THE μ LED MATRIX/OPTRODES. IN THIS EXAMPLE, 16 SUB-FRAMES WERE SUBTRACTED FROM 255 FRAMES.	101
FIGURE 4-24: A μ LED MATRIX OF 90x90 PIXELS DISPLAYING THREE EXAMPLES OF IMAGES. FOR TESTING, THE μ LED DISPLAY WAS USED INSTEAD OF 3D OPTRODES. THE TOP ROW IS IMAGED AFTER SIMPLIFICATION AND THE BOTTOM ROW SHOWS THE EXAMPLES TAKEN FROM THE μ LED MATRIX. THE IMAGES ARE (LEFT COLUMN) A BOY IN A FIRE ENGINE. (MIDDLE COLUMN) A TRAIN. (RIGHT COLUMN) A BIRD.	102
FIGURE 4-25: PORTION OF THE ELAPSED TIME FOR IMAGE PROCESSING AT THE TRANSMITTER AND RECEIVER SIDE. IN THE FRONT END PROCESSES, THE IMAGE COMPRESSION TAKES LONGER, AND AT THE RECEIVER, END DECOMPRESSION TAKES LONGER.	103
FIGURE 4-26: THE PCB LAYOUT FOR MK64FN1MOVLL12 USING THE ALTIVM DESIGNER 16.1. IT IS ONLY TWO LAYERS, AND THE DIAMETER OF THE BOARD IS 30 MM, THE WIDTH IS 2.68 MM, AND THE WEIGHT IS LESS THAN 3G. THERE IS NO COMMUNICATION OR POWER LINK.	104
FIGURE 4-27: MICROCONTROLLER POWER CONSUMPTION VARIES ALMOST LINEARLY WITH THE FREQUENCY. THE LIMIT OF POWER CONSUMPTION IS BELOW 76.56 AND 57.59 mW WITH AND WITHOUT DSP, RESPECTIVELY.	105
FIGURE 4-28: PERFORMANCE OF THE MICROCONTROLLER IN CLOCK SEVERAL FREQUENCIES WITH DIFFERENT COMPRESSION RATIOS. WITH A HIGHER COMPRESSION RATE, MORE FRAMES PER SECOND ARE ACHIEVED, WHICH MEANS THAT THE MICROCONTROLLER CAN PERFORM FASTER.	106
FIGURE 4-29: PERFORMANCE OF THE MICROCONTROLLER FOR 86% CR WITH AND WITHOUT DSP. WITH THE DSP, THE MICROCONTROLLER CAN RUN AT A LOWER FREQUENCY WITH HIGH PERFORMANCE. THE MICROCONTROLLER RUNNING AT 120 MHz WITHOUT DSP HAS THE SAME PERFORMANCE AT 20 MHz WITH THE DSP.	106
FIGURE 4-30: ENERGY EFFICIENCY FOR THE MICROCONTROLLER WITH AND WITHOUT DSP FOR DIFFERENT CLOCK FREQUENCIES AT 86% CR. USING THE DSP IS UP TO FOUR TIMES MORE ENERGY EFFICIENT THAN IF IT IS RUN WITHOUT THE DSP.	107
FIGURE 4-31: COMPARISON BETWEEN MK64FN1MOVLL12 AND LPC4330 POWER CONSUMPTION AT DIFFERENT FREQUENCIES. BASICALLY, THE POWER CONSUMPTION OF THE LPC4330 IS LOWER THAN THE MK64FN1MOVLL12 BY APPROXIMATELY 10 mW IN EACH FREQUENCY RANGE.	108
FIGURE 4-32: THE FINAL IMPLANTED BOARD USING LPC4330 ARM CORTEX M4F&M0 DUAL-CORE MICROCONTROLLER. THE BOARD IS SIX LAYERS AND DOUBLE-SIDED. (A) THE BLUETOOTH MODULE. (B) SWITCH FOR BOOT SELECTION. (C) EXTERNAL FLASH MEMORY. (D) SERIAL PERIPHERAL INTERFACE HEADER. (E) JOINT TEST ACTION GROUP (JTAG)	

INTERFACE CONNECTION PORT. (F) THE 3.3 V AND 5 V VOLTAGE REGULATORS. (G) DUAL-CORE LPC43XX SERIES MICROCONTROLLER. (H) RIBBON CABLE HEADER TO CONTROL THE OPTRODES.	109
FIGURE 4-33: PEAK SIGNAL-TO-NOISE RATIO THAT ILLUSTRATES VISUAL VIEWS COMPARING DCT-BLOCKS AND DCT-ZIGZAG.	
THERE IS A SLIGHT DIFFERENCE BETWEEN THE TWO METHODS, WHICH CAN BE IGNORED.....	110
FIGURE 4-34: PEAK SIGNAL-TO-NOISE RATIO BETWEEN THE ORIGINAL AND COMPRESSED IMAGES. DCT-ZIGZAG IS BETTER QUALITY THAN DCT-BLOCKS BUT THERE IS NO SIGNIFICANT DIFFERENCE.....	111
FIGURE 4-35: THE MEAN SQUARE ERROR (MSE) FOR DCT-BLOCKS AND DCT-ZIGZAG. DCT-BLOCK COMPRESSION IS BETTER THAN DCT-ZIGZAG BECAUSE IT HAS A LOWER VALUE OF MSE.	111
FIGURE 4-36: AVERAGE DIFFERENCE IN THE NUMBER OF PIXELS BETWEEN THE ORIGINAL AND COMPRESSED IMAGES. DCT-BLOCKS ARE BETTER THAN DCT-ZIGZAG FOR COMPRESSION RATIOS OF UP TO 75%, WHEREAS AT 75% THEY ARE MORE SIMILAR.	112
FIGURE 4-37: MAXIMUM DIFFERENCES BETWEEN THE NUMBER OF PIXELS IN THE ORIGINAL AND COMPRESSED IMAGES. IN GENERAL, BOTH METHODS HAVE CLOSER SIMILARITY AT 75% COMPRESSION RATIO.....	113
FIGURE 4-38: THE WIRELESS POWER TRANSFER BOARD WAS TUNED AT A FREQUENCY OF 13.56 MHZ. THE 2N7000 USED A SWITCH TRANSISTOR.....	114
FIGURE 5-1: THE SYSTEM IS DIVIDED INTO TWO PARTS, THE TRANSMITTER AND RECEIVER. THE EXTERNAL PARTS ARE PLACED ON THE GLASSES AND THE CASE. THE INTERNAL PARTS ARE COLLECTED ON THE IMPLANTABLE BOARD.....	117
FIGURE 5-2: ADAFRUIT POWER BOOSTS 1000C. WHILE IT IS CONVERTING FROM 3.7 V TO 5 V OUTPUT VOLTAGE, IT CAN BE USED TO RECHARGE A BATTERY. THE WEIGHT OF THE BOARDS IS 6 G. THE POWER CONSUMPTION OF THE BOARD IS APPROXIMATELY 18.5 mW (IMAGE FROM ADAFRUIT WEB PAGE [245]).	118
FIGURE 5-3: LTC3122 POWER BOOST BOARD FOR REGULATING VOLTAGE 5 V TO 12 V.....	119
FIGURE 5-4: SIMULATION RESULTS FOR THE 12 V AND 800 mA OUTPUT FROM THE LTC3122 REGULATOR. THE INPUT VOLTAGE IS 5 V FOR THE REGULATOR. THE OUTPUT CURRENT (LEFT Y-AXIS) AND THE OUTPUT VOLTAGE (RIGHT Y-AXIS).	119
FIGURE 5-5: THE BASIC BLOCK DIAGRAM OF THE WIRELESS POWER TRANSMITTER. THE PULSE GENERATOR OPERATES THE SWITCH BJT/MOSFET TRANSISTOR. THEN, THE TRANSISTOR INCREASES THE POWER TO THE SYSTEM.	120
FIGURE 5-6: OSCILLOSCOPE SCREENSHOT FOR 6.78 MHZ AND 13.56 MHZ FREQUENCIES FOR THE PROGRAMMABLE OSCILLATOR DS1085L AND OSCILLOSCOPE SCREENSHOT OF 555 TIMERS AT 1.63 MHZ FREQUENCY.	121
FIGURE 5-7: CLASS E POWER AMPLIFIER SCHEMATIC CIRCUIT. THE MAIN SIGNIFICANT FACTORS IN THE CIRCUIT ARE C_b AND C_1 . THE TRANSISTOR ACTS AS A SWITCH AND SHOULD SATISFY THE REQUIRED SPEED OF THE SYSTEM AS THE FREQUENCY IS 13.56 MHZ.	122
FIGURE 5-8: PLANER FLAT COIL AT THE FRONT END (A), A PLANAR COIL AT THE FRONT END AND RECEIVER SIDE (B), AND PRINTED COIL ON THE BOARD JUST FOR THE RECEIVER SIDE (C).	124
FIGURE 5-9: EXAMPLE OF THE FULL WAVE VOLTAGE RECTIFICATION ON THE RECEIVER SIDE BEFORE ADDING THE SMOOTHING CAPACITOR.	125
FIGURE 5-10: VOLTAGE RECTIFIER EXAMPLE AFTER CONNECTING THE SMOOTHING CAPACITOR IN PARALLEL.....	125
FIGURE 5-11: THE RELATION BETWEEN POWER, CURRENT AND REGULATED VOLTAGE OUTPUT WITH DIFFERENT LOADS. THE KEY ISSUE IS TO MAINTAIN THE REQUIRED VOLTAGE ACROSS THE LOAD. BELOW 100 OHMS, THE VOLTAGES DROP OFF BECAUSE THE POWER MANAGEMENT CANNOT SUPPLY SUFFICIENT CURRENT TO THE LOAD.	126

FIGURE 5-12: POWER CONSUMPTION ALLOWANCE IS BELOW THE TEMPERATURE CHANGE LIMITATION. FOR A BOARD SIZE OF 30 MM, THE LIMITATION OF POWER CONSUMPTION IS AROUND 480 MW. THE POWER CONSUMPTION OF THE IMPLANTED BOARD IS APPROXIMATELY 300 MW.....	128
FIGURE 5-13: VERTICAL DISTANCE BETWEEN TWO COILS. THE TWO COILS ARE CONTACTED (TOP LEFT), 5 MM DISTANCE BETWEEN TWO COILS (BOTTOM LEFT) AND THE DISTANCE BETWEEN TWO COILS IS 10 MM (RIGHT).	129
FIGURE 5-14: MAXIMUM HORIZONTAL ALIGNMENT BETWEEN THE TWO COILS SHOWS THAT THE VOLTAGE IS STABLE AFTER MOVING THE TX COIL TO THE CENTRE OF THE RX COIL. THE VOLTAGE WAS STABLE, AND THERE WERE NO CHANGES.	130
FIGURE 5-15: WPT CIRCUIT SCHEMATIC USED FOR TRANSFERRING POWER THROUGH AIR, WATER, AND PORK. THE PROGRAMMABLE OSCILLATOR WAS SET TO 13.56 MHZ. THE POWER SOURCE OF THE DEVICE WAS FROM KESIGHT E3648A DUAL OUTPUT DC POWER SUPPLY.	131
FIGURE 5-16: RECEIVED DC POWER THROUGH THE AIR, WATER, AND PORK. AT THE 5 MM DISTANCE BETWEEN TWO COILS AFTER TRANSFER THROUGH THE PHYSICAL MEDIUMS, THE POWER-DEGRADED AROUND 40%.	131
FIGURE 5-17: (A) TOP LEFT, PLASTIC FOR SPACING BETWEEN TWO COILS FOR THE AIR GAP, AND THE REST IS THE EXPERIMENTAL RIG FOR THE WIRELESS POWER TRANSFER THROUGH PORK. (B) THE BOX IS LABELLED ON TOP AND THE BOTTOM IS FILLED WITH WATER. THIS ILLUSTRATES THE POWER TRANSMISSION THROUGH WARM WATER.	132
FIGURE 5-18: THE 90x90 μ LED MATRIX USED TO ILLUSTRATE THE VISUAL CORTICAL STIMULATOR.	133
FIGURE 5-19: THE TRANSMITTER PARTS OF THE WIRELESS VISUAL CORTICAL STIMULATOR ARE DIVIDED INTO TWO PARTS, CASE AND GLASSES. THE WIRELESS POWER TRANSMITTER CIRCUIT, TRANSMITTER COIL AND THE CAMERA ARE MOUNTED ON THE GLASSES. THE RASPBERRY PI ZERO, RECHARGEABLE BATTERY, POWER BOOST 1000C, A POWER BOOST FOR WPT, USN HUB AND BLUETOOTH ADAPTER ARE PLACED IN THE CASE.....	134
FIGURE 5-20: THE RECEIVER PARTS OF THE WIRELESS VISUAL CORTICAL STIMULATOR. THE TARGETED 3D OPTRODE WILL BE USED IN FUTURE WORK. μ LED 90x90 IS USED TO ILLUSTRATE THE RESULT AND SINGLE OPTRODE FOR THE BLINKING TEST.	135
FIGURE 7-1: THE FRAME TO FRAME TECHNIQUE SHOWS THE NUMBER OF SAVED BLOCKS. EACH BLOCK IS 8 X 8 PIXELS, AND THE TOTAL NUMBER OF BLOCKS IN EACH FRAME IS 64 BLOCKS FOR THE FRAME SIZE OF 64 X 64 PIXELS [WORK BY SABAH NAYYEF].	142
FIGURE 7-2: THE THREE DIMENSIONAL OPTRODE EXEMPLAR DESIGNED BY PATRICK DEGENAAR FOR THE CANDO PROJECT. THIS WILL BE USED FOR A VISUAL CORTICAL PROSTHESIS IN FUTURE WORK.....	144

List of Tables

TABLE 2-1: CURRENT VISUAL CORTICAL PROSTHESIS WORKING GROUPS WORLDWIDE.	18
TABLE 2-2: COMPARISON BETWEEN COMMON COMMUNICATION PROTOCOLS [95].	26
TABLE 2-3: LIST OF BIOCOMPATIBLE MATERIAL AND THEIR APPLICATIONS	28
TABLE 2-4: EXAMPLES OF THE PRIMARY BATTERIES USED FOR THE MEDICAL IMPLANT DEVICES.	34
TABLE 2-5: EXAMPLES OF RECHARGEABLE BATTERIES POWER SOURCES.	35
TABLE 2-6: WIRELESS POWER TRANSFER FOR THE IMPLANT DEVICE	36
TABLE 3-1: THE RELATIVE PERMEABILITY OF TISSUE AT 37 °C [202]	43
TABLE 3-2: PARAMETERS OF THE PRINTED CIRCUIT	66
TABLE 3-3: PARAMETERS FOR SINGLE AND MULTICORE COILS.....	66
TABLE 3-4: SPECIFICATION OF THE SCHOTTKY DIODES USED IN THE AC/DC CONVERTER CIRCUIT.....	69
TABLE 4-1: COMPARISON BETWEEN HIGHLIGHTED MICROCONTROLLERS FOR MID PURPOSE	88
TABLE 4-2: EXAMPLES OF AVAILABLE MEDICAL DEVICES COMMUNICATING WITH BLUETOOTH [37]	88
TABLE 4-3: EXAMPLES OF THE IMAGE COMPRESSION.....	96
TABLE 4-4: COMPARISON RESULTS FOR DIFFERENT COMMUNICATION PROTOCOLS.	98
TABLE 5-1: LIST OF PARAMETERS/COMPONENTS USED IN THE CLASS E POWER AMPLIFIER.	123

Chapter 1. Visual cortical prosthesis

1.1 Introduction

As the world population rises, so too does the proportion of elderly and disabled people [1]. Older people suffer from increased morbidity and various age-related conditions. Furthermore, a significant proportion of society is disabled. Medical problems include blindness, loss of limb function, and hearing loss. There are many general treatment methods for illness and disability, including pharmaceutical, physical (e.g. physiotherapy), clinical surgery and biological therapies (e.g. monoclonal antibodies and cancer vaccines).

One method of treatment is the use of Active Implantable Medical Devices (AIMDs). Today, there are more than 600 million people who have an AIMD, such as a pacemaker [2]. In the United States of America every year more than 150,000 pacemakers are manufactured [3], and around the world more than 60,000 deaf people use cochlear implants [4]. Therefore, the need for AIMDs is increasing each year [5]. Implants are usually made of biocompatible materials such as titanium, silicone and ceramics so that the human body does not reject them [6]. An example of an application for current implants is electronic stimulation and recording techniques such as in vision prostheses, and cochlear or cardiac pacemakers [7].

To restore sight to blind people, retinal prostheses achieved regulatory approval in 2013. The first device approved for human use was called Argus I, manufactured by the 2nd Sight Company [8]. However, the retinal prosthesis is bounded by some technical and usage limitations, such as poor quality vision. Maximum quality is around 1,500 pixels by Retina AG devices, in comparison to human vision at about 120 million pixels [9]. Also, a retinal prosthesis is only suitable for retinal disorders such as retinitis pigmentosa (RP). That is to say, a retinal prosthesis can assist in restoring the vision of millions of people worldwide [10]. For those with glaucoma and trauma, the best option for recovering vision is a visual cortical prosthesis, which may help a greater number of the blind worldwide with better quality images [11].

There are two types of visual cortical stimulation: electrical and optical. Electrical stimulation was performed for the first time by Dobelle in the 1970s and Brindley in 1982 [12]. For optical stimulation, Channelrhodopsin-2 is employed as a light sensitive protein. There is a method for engineering the nerve cells called optogenetics; this can be used to make the nerve cells respond to light. Optogenetic retinal prostheses [13] open the door for researchers in this area to use light for brain cell stimulation to restore vision.

1.2 The human eye, vision and blindness

The perception of the world by a human is achieved with sensory neurons [14], which perceive sight, hearing, taste, touch, smell and balance; defects to any of these result in a sensory disorder [15]. Visual disorders are a significant issue to humanity as the visually impaired cannot see the beauty of the world, and managing their daily needs can be arduous. People may not require external support when they lose other sensory systems, but the blind require considerable support.

To understand the journey of the image from the eye to the brain, one needs to understand the anatomy of the eye and its functionality. The eye can be compared to a man-made camera. A diagram of the human eye is shown in Figure 1-1, taken from [16]. As shown in the figure, from left to right, the eye structure is as follows: The cornea is at the front of the eye, and is transparent to the light. The iris and pupil come after the cornea. The iris offers the beauty of the eye by its attractive colour, and its job is to control the size of the pupil by a tension and release mechanism. Then, the lens is behind the pupil and is also transparent to the light. Its physical properties are similar to rubber or jelly. The retina is located at the back of the eyeball and its function is to convert light into electrochemical signals. There are three main structured layers in the retina, and from outside to inside these are: the ganglion cell layer, bipolar cell layer, and photoreceptor layer. In the photoreceptor layer, there are two types of photoreceptor: rods and cones. Their names are identical to their shapes. Cones can be subcategorised into three types based on their response to the light wavelength: red, green and blue. The eye is connected to the brain via the optic nerve. The optic nerve for both eyes is

joined at a point called the optic chiasma. The optic nerve extends from the optic chiasma to the primary visual cortex area at the back of the brain.

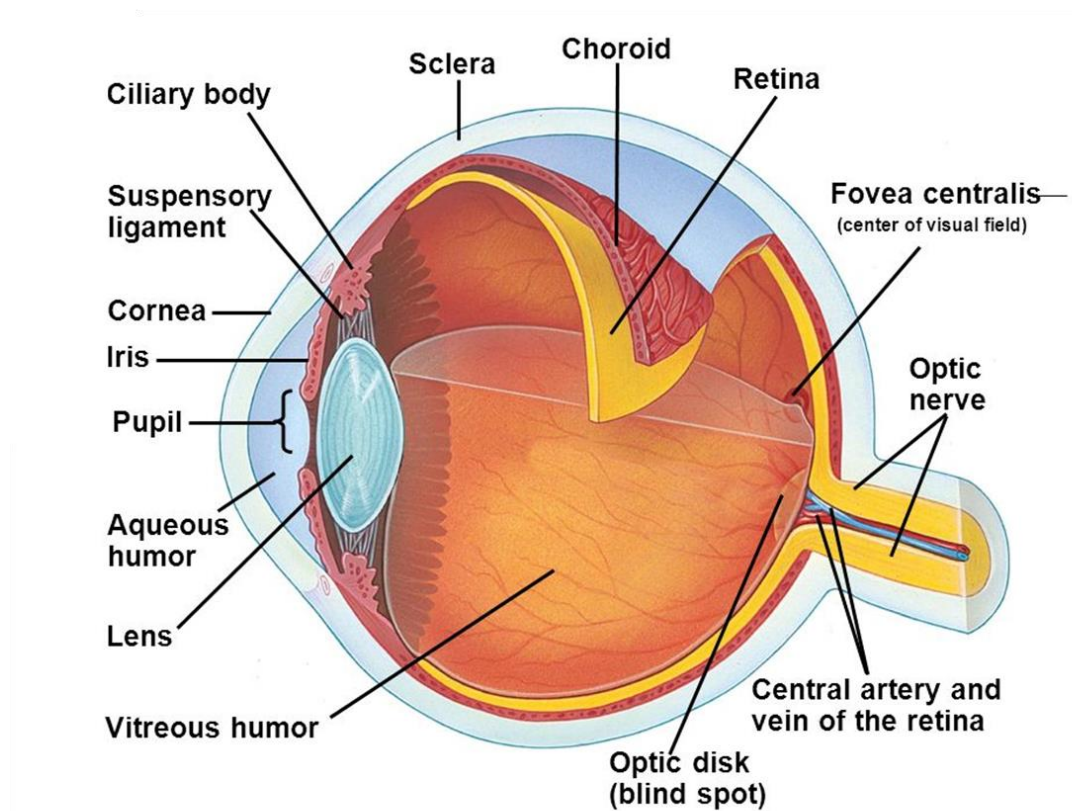


Figure 1-1: The anatomy of the human eye. The cornea is at the front of the eyeball and it ends at the optic nerve. Light passes through different layers and mediums until it reaches the retina. There is a cornea, aqueous humour, a lens, vitreous humour, and a retina [16].

The image starts by passing through the eye from the cornea (which provides 40 diopters of fixed optical power) and focuses a part of the image on the lens (which provides 20 diopters of variable power) via the pupil. The pupil/iris controls the amount of light entering the eye. By the tension and relaxation of the lens, the lens can focus the scene on the retina. The light passes through the ganglion layer to the photoreceptor cells. Rods (night vision) and cones (colour/day vision) in the photoreceptor layer absorb the light and convert it to electrochemical signals. For night vision and dim light, rods take responsibility, while cones are responsible for visible colours. Each cone is sensitive to a range of colours and in combination they can deliver information in all visible

colours. This processing starts with the inner layer, called the first layer. Then the data is forwarded to the third layer via the middle layer. After processing the data in the third layer, it redirects to the optic disc. The most significant image processing occurs in the retina. The signals from the optic disc are sent to the primary visual cortex through the optic nerve.

The higher level processing of the visual pathway starts in the visual cortex area. The visual cortex can be divided into two parts: primary and secondary visual cortex, which are further subcategorised. For example, the parts responsible for motion, colour, recognition, attention, and face detection functions have been adopted. The details of the anatomy of the human eye and its link to the brain network are not illustrated here due to the need for simplicity.

From the cortical nerve cells, the signal is then transformed into useful information which the brain can analyse. A simple diagram in Figure 1-2 tracks the journey of the image from the eye to the brain.

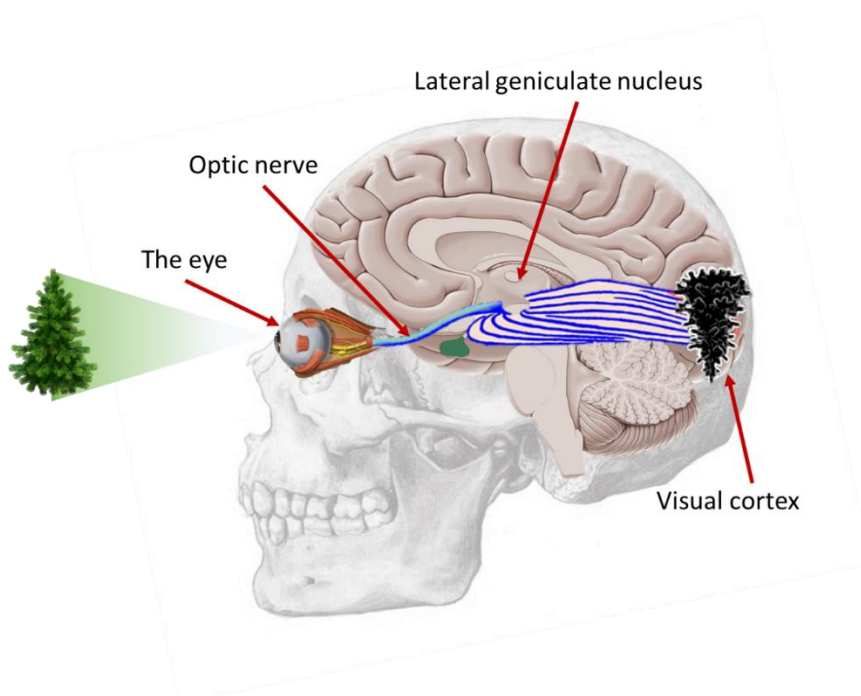


Figure 1-2: The visual pathway from the eye to the visual cortex in the brain. Real time images are processed in the eye and transferred via the optic nerve to the visual cortex.

1.3 Examples of eye diseases causing blindness

There are several eye diseases which may cause visual impairment or blindness [17]:

- **Glaucoma:** is a group of eye diseases which damage the optic nerve, causing loss of vision. In general, it is related to a pressure increase in the eye, which causes damage to the retinal projections in the optic nerve. Usually, there are no symptoms in the early stages of glaucoma. Advanced glaucoma can be decelerated with pharmaceutical eye drops or laser and surgical techniques.
- **Cataract:** when the eye lens is lost, the transparency of vision is blurred. This mostly occurs in the elderly but can also be caused by trauma, diabetes, the use of some medication for other eye diseases, and moreover ultraviolet light may affect the transparency of the lens. It can be treated by lens replacement.
- **Age Related Macular Degeneration:** this affects the macula, and normally starts in the 60s. It can be divided into two types: dry and wet. In the first case, abnormal blood vessels behind the retina grow, and leaked blood causes a loss of central vision in the retina. In the second case, the central vision of the retina slowly reduces over time because of waste products that build up in the retina.
- **Diabetic retinopathy:** this affects the blood vessels in the eye especially those in the inner layer of the retina. As laser treatment may cause damage, the best option for preventing this disease is to control glucose.
- **Trauma:** this is also known as an eye injury, for example by chemical burn, radiation exposure, penetrating foreign bodies, and blows to the eyes. Minor injuries may require medication and painkillers, and sometimes surgery is required for treatment.

1.4 Requirements for medical implants

There are significant requirements for an AIMD to be implanted in a human body cavity [6]. The main specifications for active medical implantable devices, in general, are as follows:

Infection free

Implantable devices should not cause infections. Communication between the implanted device and outside the body is achieved by a percutaneous cable, which is risky.

Lightweight

The placement of the implant device will determine the maximum allowed weight to be implanted in the body. For example, retinal implants should be light compared to breast implants.

Small in size

Similar to the weight requirement, the size of the implanted device depends on the place, purpose and application of the implant. For example, compared to the size of a cardiac pacemaker, the retinal prosthesis is much smaller.

Ergonomic

Implant devices should be comfortable to wear because the patient will carry it for a long period.

Safe operation

Safety is the most significant key requirement with implanted devices. The implant device should not have any side effects on the surrounding tissue, for example injury, infection, burning or damage.

Low power

All the active AIMDs require a power source for its operation. There are several ways to power medical implant devices: piezoelectric [18], thermoelectric [19], kinetic [20], ambient energy harvesting [21], and a certain wavelength of light [22]. It is widely used today in medical implant devices to transfer power and data [23]. A wireless system performs various functions depending on the type of application, which includes wireless power transfer, wireless programming, data control, wireless sensors, and data transfer [24]. Recently, microcontrollers have become popular to enable researchers to collect data, record automatically or stimulate, control remotely, and process data [25].

For relieving neurological disease or sensory shape replacement caused by disease or injury, stimulating therapy has certain achievements when using implantable medical devices [26]. Such diseases as Parkinson's, epilepsy and dystonia can be treated with deep brain stimulation (DBS). For the DBS power source, a battery is used which is placed in the chest cavity as there is more space available. Also, from the chest, it is connected to the brain by passing through the neck [27].

Generally, batteries power implant devices, but these are limited according to the system's power consumption and their lifetime. The battery needs to be replaced every five to ten years by surgery. Otherwise, it is a source of risk due to electronic failure [28]. An alternative solution for powering up the implant devices with low risk is wireless power transfer. For example, the lifetime of a battery in a pacemaker is up to ten years and requires a surgical procedure to change it at the end of the battery lifecycle [29], which may have complications and is costly. For rechargeable batteries or direct power units, a percutaneous cable causes infection and is not an effective solution in reality [30].

Exemplar applications

An example of a medical implant device is neuroprosthesis in deep brain stimulation (DBS) [31]. Surgery is required to implant electrodes in the globus pallidus or subthalamic nucleus. The location of the electrodes in the brain depends on the purpose of the implant device, e.g. for epilepsy it is a brain surface or deep brain stimulation technique [32, 33]. DBS can be used for various purposes, such as:

- Depression
- Obsessive compulsive disorder (OCD)
- A cluster headache
- Chronic and phantom limb pain
- Tourette's syndrome
- Eating disorders
- Post-traumatic coma

Historical periods of the active implanted medical devices are shown in Figure 1-3. The time listed depends on the discovery and early human trials.

1947 – 1963 Pacemaker

1961 – 1967 Functional electrical stimulator

1963 – 1970 Visual prosthesis

1971 – 1980 Cochlear prosthesis

1990 – 2000 DBS, Retinal prosthesis

2000 – 2010 Defibrillation, Closed loop systems

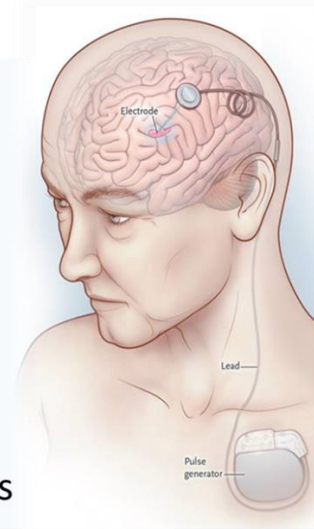


Figure 1-3: Examples of DBS and the history of the AIMDs. The historical periods depends on the early invention and testing times. All those listed are still in the developing and improvement stage [34].

1.5 Main components of visual prosthesis

Active medical devices require wireless power transfer and communications [35]. The hardware components for the wireless power transfer consist of two parts: the transmitter and the receiver parts. In the transmitter side, the battery energy source is essential for operating all the system. In the transmitter side of the wireless power transfer circuit, there is a moderator to generate the required frequency. To ensure sufficient power in the wireless power system on the transmitter side, adding the power amplifier is essential [36]. The coil size (transmitter coil, Tx) and shape need to be calculated for the delivery of efficient power. On the receiver side, the receiver coil has the same consideration as the Tx coil, but also depends on the implanted place. The AC voltage needs to convert to DC voltage, and the output voltage should be adjusted.

The components of the communication system can be divided into two parts: hardware and software. The hardware parts, like the power transfer, have transmitter and receiver parts, and a camera is essential for capturing real time scenes. The data needs

to be processed and sent to the receiver end. After the data reach the receiver side, they are processed to retrieve the original data and then used to drive the stimulator.

For image processing on the transmitter side, after the images were captured by the camera, the data are processed. For low quality images, image simplification is essential to remove the unnecessary information, and should satisfy the retinal needs for image processing. This is for smoothing and contrasting valuable information in the image.

For low baud rate communication protocols, the data should be compressed to achieve live streaming videos over a low baud rate data link such as Bluetooth. The data are processed to operate the stimulator. This process can be pulse modulation, to convert each frame to sub-frames and achieve the intensity level.

The general concept of the visual cortex prosthesis system is shown in Figure 1-4. The visual cortex stimulator system can be divided into two main parts: hardware and software. The hardware includes the power management system, data processing unit, data link unit, printed circuit board, and 3D printing. This system is the only example explaining how the system will engage with the stimulating part as a proof of concept.

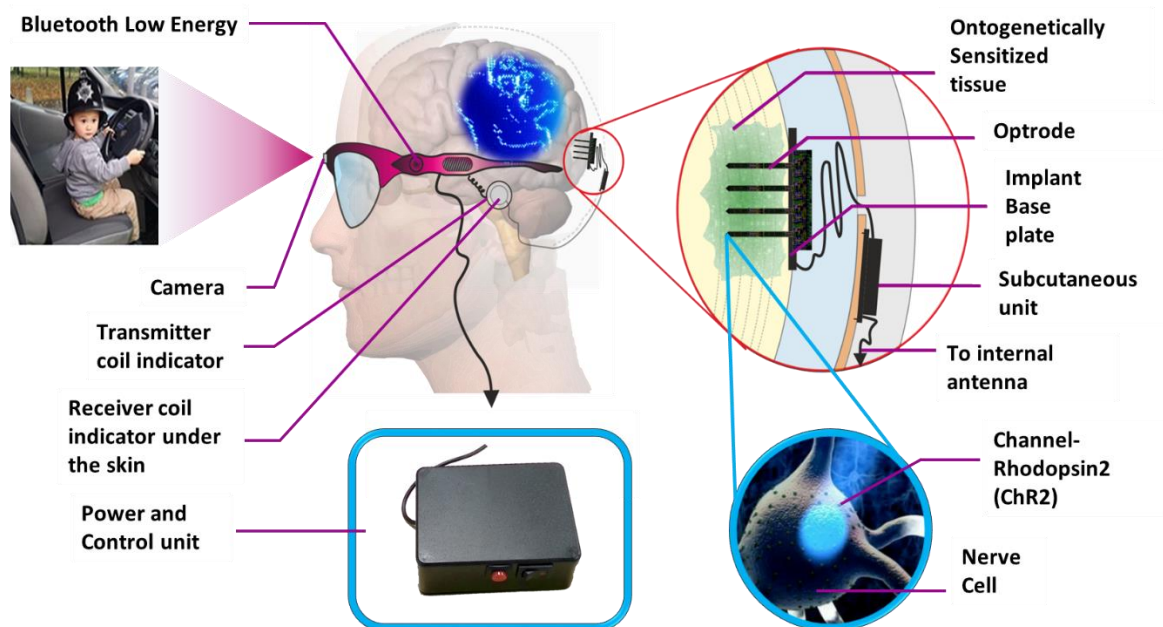


Figure 1-4: The concept of a fully wireless optogenetic visual cortex implant for restoring sight. The system comprises a wireless power delivery to the implant system, the retinal image processing and the wireless data link. The brain cells are injected with Channel-Rhodopsin2 to respond to the light stimulator.

At this stage, focusing on using light or electrodes is not essential, but a two dimensional micro Light Emitted Diode (μ LED) will be used for proof of the concept. An efficient implantable cortical prosthesis may be used for electrical or optical stimulation in the future. Also, it may be used to stimulate the retina instead of the cortical prosthesis.

1.6 Human health and safety considerations

From the wireless communication perspective, Bluetooth has been used worldwide in many industrial devices and those utilised by humans. First of all, the frequency bandwidth of the Bluetooth is in the range of the ISM boundary. Although the most common device in which it is used is mobile phones, Bluetooth is also used with medical and non-medical equipment. In other words, using Bluetooth to send images to the human brain comes under ISM limitations.

Wireless power transfer is designed to tune in to the 13.56 MHz frequency. However, the current target needs to be delivered at under 200 mA. The 3D model in the COMSOL software package was tested for the 13.56 MHz to transfer 200 mA. The results show that the heating issue with the head tissue due to electromagnetic radiation was below the limits, while the Specific Absorption Rate (SAR) was in the range of 0.01 mW/Kg [37].

1.7 Thesis

1.7.1 The motivations

Science and technology should serve the needs of the humanity. The population of the world is increasing and so is the number of people who suffer from blindness. Restoring sight is comparable to giving a second lease of life to them. However, the existing technology for restoration of the sight is insufficient, leaving a major gap in rehabilitation. The visual cortical prosthesis system can be an appropriate rehabilitative system for the restoration of the sight.

1.7.2 The aim

The aim of this PhD program was to design of a telemetry system that can control a visual cortical stimulator. This system was envisaged to have offer to features:

1. Wireless power charging.
2. Live scene streaming over wireless communication channel.

1.7.3 The objectives

In line with the aims, the transmitter side was planned to use off the shelf components for image processing and wireless communication. In contrast, it was planned that the receiver side will be designed and manufactured in house. An additional objective was that the overall system would be useful for both optical and electrical stimulation of the nervous system.

Further objectives were placed on the physical properties of the system: The implantable parts should not be power hungry 0.01 mW/Kg, it has a reasonable size 30 mm x 30 mm and to be safe according to SAR [38].

1.7.4 The achievements

The main achievements of this project are:

- The main achievements of this PhD projects are: Improved image decompression using the discrete cosine transform. I was able to transfer frames of 64x64 pixel size and 25 frames per second over a Bluetooth connection. By this means, the quality of transferred images and real time transfer streaming of scenes were improved.
- Design of a Class E power amplifier for the wireless power transfer with an efficiency of 93.43%. This level is sufficient power implantable devices.
- Design and manufacture of an efficient implantable electronic board to use in stimulation of the visual cortical neuron cells and retina. An example in this project uses a 2D μ LED as a proof of concept.

1.7.5 The outline

The thesis is structured as follows:

- Chapter 2 (Literature Review) focuses on the previous achievements of medical implant technology and visual cortical prostheses.
- Chapter 3 (Wireless power transfer) is about powering active medical implants and designing efficient wireless power transfer.
- Chapter 4 (Real time data transfer) is about the communicating with the medical implant device, and sending live streaming data to the implantable device.
- Chapter 5 (System integration and packaging) presents the main results and the system concept.
- Chapter 6 (Discussion and Conclusion) discusses the main results and design issues.
- Chapter 7 (Future work) concerns the plans for future work.

Chapter 2. Literature Review

2.1 Introduction

According to the World Health Organization (WHO), health can be defined as “a state of complete physical, mental and social well-being and not merely the absence of disease or infirmity”. Where there is an abnormality of human health, treatment will be necessary. There are many types of treatment depending on the disease and the organs involved. If we concentrate on visual disorders and more specifically blindness, the WHO reports that the number of the blind will reach approximately 80 million globally by 2020 [39]. There are different methods to restore sight, involving both preventative and restorative techniques. An example of a preventative method is saving people from blindness by reducing eye pressure (glaucoma), while restorative ways of treating the blind are to implant a retinal and visual cortical prosthesis, and stem cells.

In general, there are three categories of blindness: myopia, legal blindness, and dark blindness. Myopia is visual impairment or low vision, meaning that the person cannot see well without eyeglass or contact lenses. The range of visual impairments starts from mild to severe, and legal blindness counts as a severe impairment. A visual prosthesis is useful for those who cannot see anything at all, known as dark blindness.

Retinal prostheses have been successfully used in humans to restore sight, and Argus II from Second Sight is one such example [8]. People who benefit from retinal implant devices are those who have retinal pigmentosa (RP). In 2012, the National Organization for Rare Disorders (NORD) estimated that the number of people suffering from RP is 2.35 million people [40]. To put it another way, globally about 20% of people with RP could use a prosthesis [41]. By contrast, a retinal prosthesis is not useful for other cases of blindness [42] such as glaucoma and trauma.

Alternatively, a visual cortical prosthesis is another option for helping the blind to see again. Compared to a retinal prosthesis, the visual cortical prosthesis is more challenging. However, it can restore sight in more than 40% of cases where sight has been lost due to an accident, or glaucoma [43]. In early visual cortical prosthesis devices,

electrodes were used to stimulate neurons. In general, a visual prosthesis clearly needs a power source and communication. For this, a percutaneous wire is used, but this causes many problems. First of all, it is not comfortable for the patient, can cause infections, and there is a risk of entanglement with another object. Because of the above, a novel, efficient, fully wireless visual cortical prosthesis system is a more appropriate solution.

2.2 Neuroprosthetics history

Neuroprosthetics are used to restore the functionality of motor, sensory, and autonomic neurons which may have been damaged by disease or injury. For example, a neuroprosthesis which can restore the sense of hearing is a cochlear prosthesis [44]. Neuroprostheses for restoring vision is known as retinal (subretinal, epiretinal and optic nerve) and visual brain (visual thalamic and visual cortical) prostheses. Furthermore, brain-machine interfaces can assist those with lost limb functionality [45]. The history of nerve prostheses began in the 18th century when Galvani observed the movement of a frog's leg due to electrical stimulations. In 1924, after completing most of his initial tests on dogs, the German psychiatrist Hans recorded an electroencephalogram (EEG) from a human brain for the first time. The EEG is a means of recording the brain's electrical activity, and Hans was able to receive a signal from the brain by inserting needle electrodes under the scalp [46, 47]. To improve the quality of life people with neural disabilities, a neuroprosthesis is an option to augment or replace damaged senses [38].

In 1929, a German neurologist called Foerster found that the electrical stimulation of the visual brain led to the sensation of phosphenes [48]. The first patent for the concept of the retinal prosthesis was gained by Tassicker from Australia in 1956 [49]. In 1961, Liberson used a portable device for functional electrical stimulation for the first time. This type of stimulator employed surface stimulation to assist people with hemiparesis. After developing his invention, the device was commercialized in the 1960s in Ljubljana, led by Lojze Vodovnik [50]. The first cardiac pacemaker was developed in the early 1960s [51]. In 1980, two different research groups from Boston and North Carolina started seriously considering visual prosthesis [52].

Around 3,000 multichannel cochlear stimulators were successfully implanted worldwide in the 1990s [53]. In 1992, Humayun and colleagues reported that both normal and blind people could see “phosphenes” as light when the retina was electrically stimulated [54]. The first implanted retinal prosthesis was recorded as a human clinical trial in 2002 [55]. The next generation in 2011 became the first retinal prosthesis device by Second Sight that was approved by the Food and Drug Administration (FDA). Later, a retinal implant device called Alpha from Retinal Implant AG, Germany, was approved by the FDA and became commercially available. This was after successful implementation in the suprachoroidal space in around three patients in Australia [56]. The first approved implantable retinal prosthesis was in 2013 by Argus [8]. Compared to commercially approved retinal implant prostheses, the visual prosthesis is still in the research stage and is yet to be further developed. This is one of the principal motivations for highlighting the retinal prosthesis developed in this study, to make a difference in the next generation prosthesis market.

Neuroprosthesis devices are commonly used in experiments with animals to help researchers understand the brain and its functionality. Wireless monitoring of the brain’s electrical signal may make the results better by reducing the effects of wires. Accurate recording of the results will give a greater understanding of how the neurons are related to a specific function among its local populations [57].

2.3 Visual prosthesis

Not all kinds of blindness can benefit from a retinal prosthesis, as they can only be used in cases of RP [58]. For other cases, there are other ways to restore sight. One solution is to replace eye lenses with surgery for those with cataracts [59], or to use new pharmacological approaches [60]. Also, glaucoma can be treated by surgically reducing eye pressure or administering drugs in the early stages of rising pressure in the eye [61]. Although there is no single way to treat the wide range of causes of blindness, a visual cortical prosthesis may have the potential to do so. Figure 2-1 shows the principal components of the visual prosthesis.

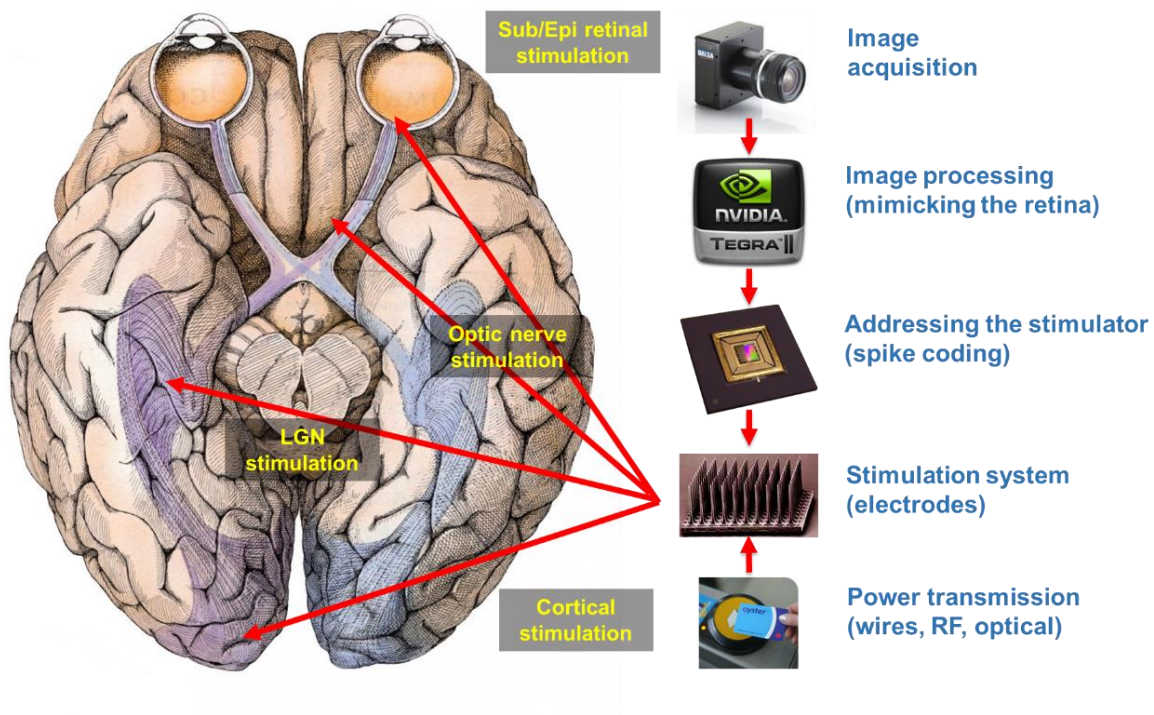


Figure 2-1: Principle components of a visual prosthesis. First, a camera captures real time images, and then the images are processed in a similar to how the retina would do so. Finally, visual cells are stimulated with electrodes/optrodes (from Degenaar lecture notes 2017).

Vision can be restored to a blind patient with a retinal prosthesis [62], and both electrical and optical retinal stimulation are possible [63]. There is another dimension to the taxonomy of the retinal prosthesis, depending on the placement of the implant [64] being on the surface of the retina, in a subretinal position or suprachoroidal one, or on the sclera. A traditional retinal prosthesis is shown in Figure 2-2.

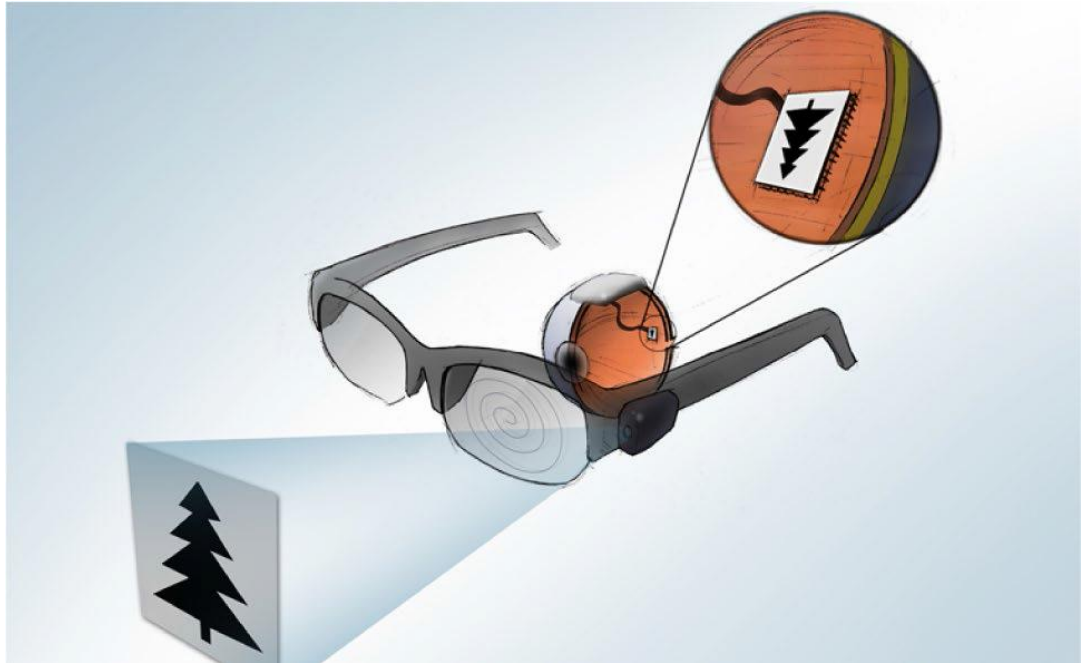


Figure 2-2: A traditional schematic of the retinal prosthesis. Real time video is wirelessly transferred to the implant part, and the received data, after being processed, are sent to electrode attached to the retina [65].

There are numerous potential applications of brain cortical implant devices, beginning with restoring sight to the blind or aiding people with dementia. However, brain implant devices are more challenging to design. The primary work of cortical stimulation for restoring vision began in 1968 [66]. Brindley and Lewin implanted stimulating electrode arrays in a female patient's brain, demonstrating that the lady was able to recognise some samples when they transferred to her visual cortex [67].

There are two common ways to interface the cortical implants with the brain: direct interfacing (intracortical) and indirect interfacing (epicortical) [68]. Stimulating the brain cells by penetrating the implant's electrodes is called intracortical, while stimulating the surface of the brain is called epicortical. Intracortical stimulation requires firm electrodes as it goes deep into the brain. However, micro-motion in the brain means that flexibility is required to prevent injury to brain tissue. Epicortical implants are more flexible compared to intracortical ones [69].

Several research groups located in different countries are working on artificial vision focus using cortical prostheses. All these groups are using electrical stimulation, except

for the neuroprosthesis group to which I belong. Table 2-1 shows existing focus groups working on cortical stimulation.

Table 2-1: Current visual cortical prosthesis working groups worldwide.

Research group	Group leader	Head office	Stimulation techniques
UVNP ¹	R. Normann	Salt Lake City, Utah	Electric
Cortivis	E. Fernandez	Universidad Miguel Hernandez; Alicante, Spain, Hernandez; Alicante, Spain	Electric
IVP ²	P. Troyk	Illinois Institute of Technology, Chicago, IL Prosthesis/Illinois Technology	Electric
PolySTIM Research Group	M. Sawan	Polystim Neurotechnologies Laboratory, Canada	Electric
OVCP ³	P. Degenaar	Neuroprosthesis lab, Newcastle University, UK	Optical
VPL ⁴	J. Pezaris	Visual Prosthesis Lab, Boston, USA	Electric

¹ Utah Visual Neuroprosthesis Programme

² Intracortical Visual Prosthesis/Illinois Institute of Technology

³ Optogenetic Visual Cortical Prosthesis

⁴Visual Prosthesis Lab

Below is a summary of each group listed in Table 2-1.

Utah Visual Neuroprosthesis Programme:

This group is also known as the Norman lab, and their work covers basic science and clinical application for improving interfaces with the peripheral and central nervous systems. They have developed two electrode arrays Utah Electrode Array (UEA) and Utah Slanted Electrode Array (USEA). The UEA consists of 100 silicon microneedles, and the USEA consists of graded needles from 0.5 mm to 1.5 mm. They use UEA for cortical applications and USEA for peripheral nervous systems. As well as these studies, they have focused on wireless power transfer and sending data to external electronic devices via a radio frequency link [70].

Cortivis:

This group is led by Dr. Eduardo Fernandez in the Universidad Miguel Hernandez, Spain. They are interested in the reforming and processing of visual information and other medical and bioengineering work. They have mainly focused on restoring sight by stimulating the periphery of the visual system using active cortical devices safely [71].

Intracortical Visual Prosthesis:

The goal of their research is to develop an intracortical visual prosthesis (ICVP). They designed 16 electrode arrays for stimulating the brain's occipital lobe. Their target is to achieve 600 to 650 electrodes for implanting in the dorsolateral surface of the occipital lobe [72].

PolySTIM Research Group:

This group are interested in the design and test of mixed-signal circuits and systems, signal and image processing, medical devices, including optical devices and implantable sensors, and integrated circuits [73]. The electrode used in their projects has 16 channels, and power is wirelessly transferred to visual cortical stimulations [74].

Visual Prosthesis Lab:

In the visual prosthesis lab in Boston, Pezaris leads a group on restoring sight by stimulating the lateral geniculate nucleus of the thalamus; that is, by implanting electrodes and sending wireless data from a camera mounted on spectacles. Pezaris argued that deep brain stimulation is an alternate pathway of restoring scene [75].

In general, the visual prosthesis includes:

- External camera
- External image processing unit
- Power supply
- Power management
- Wireless power transfer
- Wireless data

- Implantable processing unit
- Brain stimulation unit



Figure 2-3: The visual cortical implant device of Dobelle from 1978-2000. The low quality camera mounted on glasses is connected to the implant device via transcutaneous wires [76].

To stimulate neuron cells, Brindley et al. described the use of electrical stimulation in their early visual prosthesis [67], and to power the implant devices, the power is transferred wirelessly in most visual prostheses. Brindley and Lew at the University of Cambridge tested a visual cortical prosthesis on a female blind patient aged 52, and were able to create a visual sensation during examination in this patient's cerebral cortex by electrical stimulation, where the visual information appears in this part of the brain. They thought that electrically stimulating the occipital lobe of the human brain could trigger visual sensations called phosphenes, and the higher processing of visual signals occur in this part. Phosphenes are localised at the visual field, as the perception of spots of light. The results of the test were as predicted, and they also stated that

improvements to their prototype could help the blind to read and write, rather than just avoid obstacles when walking [77].

2.4 Image processing

The main objective of image processing for visual implant devices is to convert captured video to a stimulating pattern. Furthermore, the image processing unit might also implement a function to promote prosthetic vision. It is known that a retina is not only a pure photoreceptor, but also has a considerable role in image processing [78]. As the neurons are structured in a different layer in the retina [79], significant steps in image processing related to retinal processing are aimed at emulating the functionality of retinal layers. In general, the retinal processing consists of converting to:

- The greyscale levels
- Image simplification
- Zooming
- Edge enhancement

Image simplification is mainly achieved by reducing the unnecessary detail in the image; this starts by suppressing low important texture [62], handled by a minicomputer or microcontroller. Another assignment of the image processing is reducing the size of the processed data before sending. This lets the wireless communication perform its tasks easily and efficiently, and consequently the data are compressed by encoding algorithms. Therefore, the data in the implant device have to be decoded into the original information [80]. Compression of data before sending is important when the baud rate is limited.

Once received, the data needs to be decompressed, and the retrieved data on the implanted side is utilised to stimulate the visual neuron cells. In this case, an even power distributor algorithm is required to avoid a power surge [81]. This can happen when data are sent to the Micro Light-Emitting Diode (μ LED) over a very short period. Also, the data are encoded to a specific pulse mode code when transmitted to μ LED.

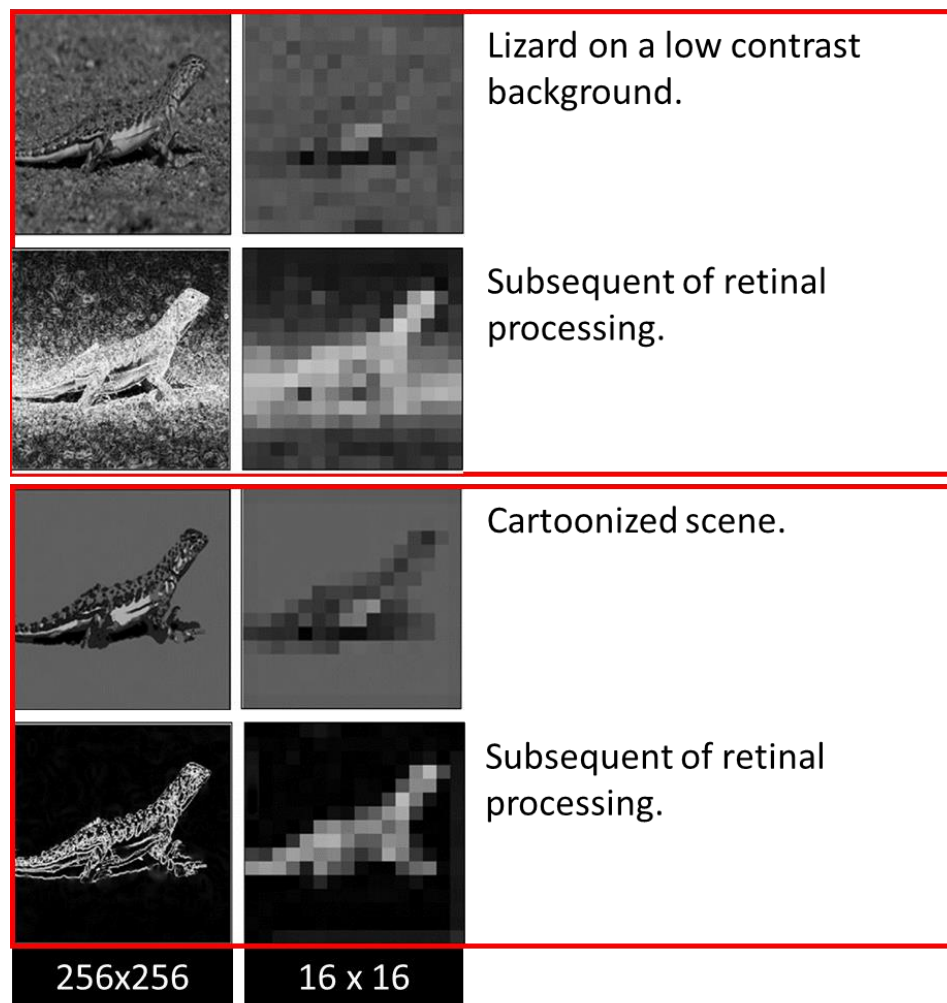


Figure 2-4: Example of image processing for the retinal prosthesis, showing the effect of scene simplification in reducing irrelevant information but leaving only the relevant objects. The left column is for an image size of 256x256 pixels, and the right columns are for an image size of 16x16 pixels Top set: is a spatial derivative image with the low contrast background. After retinal processing, the image is clearer than the lizard in the low contrast background for low quality images. Bottom set: is the simplified and edge enhanced scene [82].

2.5 Image compression

The key point of image compression is to reduce the amount of data during transmission, which in turn reduces the power consumption of the overall cortical prosthesis system. In a cortical prosthesis system, we obviously deal with a very limited amount of power which accords with legislation on health and safety requirements. Image compression is a technique used to transmit useful information in fewer bits. In the literature, different compression methods can be found such as portable network

graphics (PNG), tagged image file format (TIFF), Windows bitmap (BMP) and joint photographic experts group (JPG) [83-85]. Some of these algorithms are lossless, e.g. PNG and TIFF, whereas others are lossy. Each of these algorithms has its advantages and disadvantages, making it suitable for various applications.

The Discrete Cosine Transform (DCT) algorithm is an essential and common part of most of image compression techniques [86]. The DCT is similar to the Discrete Fourier Transform (DFT), but it depends only on the real number, and this makes it less complex than DFT [87]. DCT has eight standards, four of which are most common: type 2 DCT, simply referred to as DCT, and type 3, simply called inverse DCT (IDCT). The other two common forms of DCT are the modified discrete cosine transforms (MDCT), which particularly deals with overlapping data, and the discrete sine transform (DST) equivalent to real and odd functions of DFT [88]. DCT represents the data image regarding a sum of sinusoids with different frequencies and amplitudes. In this thesis, types 2 and 3 of the DCT were used to reduce the overhead data transmission in the visual cortical prosthesis. The most attractive part of using DCT in image compression is that the DCT preserves most of the energy of the image at low frequencies. In contrast, the spectrum in DFT is distributed in a symmetrical way, where one part is unnecessary (redundant), as shown in Figure 2-5.

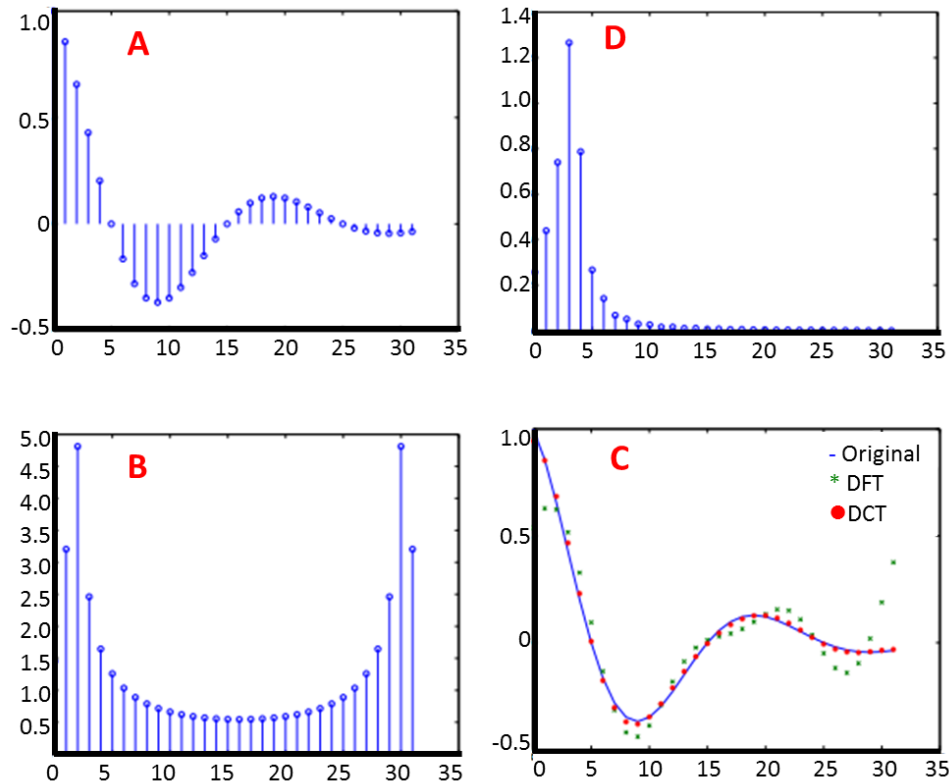


Figure 2-5: (A) Discrete signal. (B) The DFT spectrum. (C) The DCT spectrum. (D) Comparison of the DCT, DFT and the original signal $x(n)$.

2.6 Communication

There are two main protocols with the communication: Near Field Communication (NFC), and Far Field Communication (FFC).

2.6.1 Near Field Communication

NFC is a wireless communication technology at a high frequency based on a Radio Frequency Identification (RFID) system. Moreover, it is used at short distances of 10cm data and power exchange. NFC is established in mobile devices to read information from tags [89]. Because of its short distance, communication is given higher security [90] than other types of communication such as Bluetooth, ZigBee and Wi-Fi. NFC works at the frequency range 13.56 MHz, which has been chosen to reduce absorption by tissue to

stop damage [91]. Near field can be utilised for power transfer with high efficiency, but the efficiency amounts to a ratio of input power to output power [92].

2.6.2 Far Field Communication

The FFC is similar to the NFC as they are both electromagnetic waves. The speed of the magnetic field in the free spaces is equal to the speed of light ($3 \times 10^8 \text{m/sec}$) [93]. Bluetooth is an example of the FFC with a high frequency, and Amplitude Modulated (AM radio) broadcasting is an example of FFC with large distance transmission. The power of the transmitter to the receiver can be described by the following equation, known as the Friis formula:

$$\frac{P_r}{P_t} = p \cdot \frac{\eta_t D_{tmax} \eta_r D_{rmax} \lambda^2}{(4\pi r)^2} \quad (2-1)$$

Where D is the directivity, λ is wavelength, p is the account factor of misalignment of the antenna, r is the distance between two antennas and η is the input fraction power radiated in the far field to the antenna and equal to [94]:

$$\eta = \frac{R_{rad}}{R_{rad} + R_{loss}} \quad (2-2)$$

There is a different wireless communication protocol at the short range distance and low power consumption. For example, there is Bluetooth (e.g. used for mouse, keyboard and mobile to mobile), Ultra-Wide Band (UWB) (for high bandwidth multimedia), ZigBee (for controlling networks and network monitoring) and Wi-Fi (for connecting two computers). Below, Table 2-2 compares these four common communication protocols [95].

Table 2-2: Comparison between common communication protocols [95].

Standard	Bluetooth	UWB	ZigBee	Wi-Fi
Frequency band	2.4 GHz	3.1 – 10.6 GHz	868 – 2.4 GHz	2.4GHz, 5 GHz
Max Signal Rate	1 Mbps	110 Mbps	250 Kbps	54 Mbps
Distance	10 m	10 m	100 m	100 m
TX power	0-10 dBm	-41.3 dBm	(-25) -0 dBm	15 – 20 dBm
Data	16 bit	32 bit	16 bit	32 bit
VDD (volt)	1.8	3.3	3.0	3.3
TX (mA)	57	227.3	24.7	219
RX (mA)	47	227.3	27	215
Modulating	GFSK	BPSK, QPSK	BPSK (+ASK), O-QPSK	COFDM, CCK, M-QAM

Acronyms: ASK (Amplitude Shift Keying), GFSK (Gaussian Frequency Shift Keying), BPSK/QPSK (binary/quadrature phase Shift Keying), O-QPSK (offset-QPSK), COFDM (Coded OFDM (Orthogonal Frequency Division Multiplexing)), M-QAM (M-ary Quadrature Amplitude Modulation), CCK (Complementary Code Keying), CRC (Cyclic Redundancy Check).

The Packet Error Rate (PER) can be determined by finding the difference between the transmitter and receiver packets. The formula for measuring the PER is [96]:

$$PER = 1 - (1 - 0.999)^N \quad (2-3)$$

where N is the number of bits in the packet.

2.7 Data transfer

There are several design restrictions for the medical implant devices. With this, the selection or design of data link techniques is also restricted. The significant aspects that need to be considered while picking up the wireless protocol are size, data rate, low noise and security. For implant devices such as visual prosthesis, noise and accuracy are essential for transferring good quality images [97]. Moreover, the efficiency of real-time streaming is significant. In this case, the communication system will be designed or chosen from off-the-shelf industrial products. Because of their significant advantages, Bluetooth and ZigBee can be used for medical purposes [95, 98], and they are both in the range of ISM bandwidth and security. In addition to the previous points, power dissipation is important and should be considered seriously to keep the temperature

changes below the limitation, as a rise in temperature may lead to damage in the surrounding tissues [99]. The details of comparisons between Bluetooth, ZigBee, Ultra-wideband (UWB) and Wi-Fi are presented by [100, 101].

The implant devices wirelessly receive data from outside the body (called the downlink transmission). The communication with the medical implant devices is commonly achieved via radio frequency RF telemetry signals at a frequency of 402-405 MHz [102], 608-614 MHz, 1395-1400 MHz and 1427-1429.5 MHz [23] ranges, used for low rate data transmission. Also, the data can be transmitted up to 2 m distance with low power transmission [103]. From outside, the modulator circuit will modulate the binary data to be transmitted to the implanted device. The common physical properties of the modulating process are the phase, frequency and amplitude of the carrier signal, depending on the binary value that needs to be transmitted.

For high rate data transfer and high-efficiency power, a Phase Shift Keying (PSK) technique can be used instead of Amplitude Shift Keying (ASK). The data can also be transferred from implant devices to outside the body from the sensors or stimulators, known as uplink transmission. Sensors may transmit the temperature from the surrounding tissue and optical probes (optrode), or may send a data signal from the neurons. There are different objectives for the data transmission but the common performance is by Load-Shift Keying (LSK), but this depends on the load resistances of the AIMD [104].

2.8 Implant Material

For biocompatibility, common factors to consider include the host and the material from which the implant materials are made. On the host side, the standard factors are the type, genetic inheritance, location of the implementation, and the microenvironment. However, the main factors of the material itself are size, shape, coarseness, layout, porosity and morphology, structure, sterility issues, implementation duration, and degeneration. The period of the tissue response and the intensity are the responsibility of these parameters. Biocompatibility depends on the surface phenomenon, cell-cell representation, and polymer-protein interactions [105].

A biocompatible material or biomaterial is artificial, or natural materials which can replace a missing organ or function in close prolonged contact with the living tissue. In 1974, biomaterial was defined as “a systemically, pharmacologically inert substance designed for implantation within, or incorporation with, a living system” by the Clemson Advisory Board [106].

Biocompatible implant material is applied to living tissues directly, as an interface combining living and non-living substances [107]. Under this circumstance, biocompatible implant material should be compatible with the tissue and structures in the vicinity of the device and needs to be appropriately selected for their specific use. The encapsulation of the implanted medical device is quite challenging for keeping medical devices alive in the corrosive biomedical environment [108]. One of the most vital factors for the long-term success of the implant device is the appropriate selection of implant biomaterial [109].

In the last decades, extensive research work has been reported for exploring new implant biomaterial, such as silicon, amorphous aluminium oxide, polyimide, amorphous carbon, parylene [110-112]. Table 2-3 describes a partial list of frequently used biocompatible materials [113].

Table 2-3: List of biocompatible material and their applications

Material		Application
Metal	Titanium	Case/Encapsulation
	Platinum	Electrode
	Iridium	Electrode
	Zirconium	Case
	Gold	Coil/Encapsulation
Non-Metal	Ceramic	Case/Feedthroughs
	Glass	Feedthroughs
	Silicone Rubber	Carrier/ Encapsulation
	Parylene	Insulation Coating
	Teflon	Insulation Coating

The materials in the above table have shown excellent long-term performance in post-market clinical studies [114]. Some leads also have redundant insulation, typically eTFE, on each wire of the conductor coil, which additionally serves to improve hardware reliability [115].

2.9 Hermetic encapsulation

To protect the electronic system from moist conditions in the harsh environment inside the body, two strategies of packing can be used: non-hermetic and hermetic implant [116]. Packaging is essential for the long-term implant to maintain the functionality and stability of the electronic device. Protecting an active medical implant device is challenging, especially in the field of neuroprostheses [117]. For the encapsulation challenge, the biocompatibility of the used material is key [118].

Hermetic or sealed packing is maintained in a dry atmosphere, and the long term functionality of the device is guaranteed as it is normally made from low water permeability rate materials. For example, the metal housing for a cardiac pacemaker is made from titanium [119]. Two main factors may permit water to leak inside the dry interior of hermetic encapsulation, and these are cracks inside the sealing, or along the electronic feedthroughs [120].

Non-hermetic encapsulation packaging is appropriate for an electronic system fabricated discretely [121]. Medical silicon rubber is commercially available for implantable devices for non-hermetic encapsulation [122]. For short term applications, including ingenerated circuits, epoxies can be considered for well-investigated silicon rubber, as this will decrease water permeability and it has low viscosity [123].

2.10 Stimulation probes

There are many different types of stimulator architectures – flat, rod-like, and spike-like. The electrode is used in electrical stimulation, and has been used to stimulate the retina by Humayun [124], Hesse [125] and Thomas [126]. Electrode stimulation can be

achieved by Voltage Controlled Stimulation (VCS) and Current Controlled Stimulation (CCS) [127]. The electrode was used for brain stimulation by Hassan [128] and Vidaurre [129]. An optrode was used for retinal stimulation by Degenaar [130]. The optical stimulation of brain cells has been reported by Jing [131] and Kravitz [132]. Optical stimulation is performed by optogenetically engineered neurons [133, 134]. Potentially, the combination of simultaneously using electrodes with the optrode for stimulation was achieved by Veringa [135]. A stimulating technique sometimes needs extra processing, for example, in optical stimulation for specific nerve cells, the nerve cells are required to be genetically engineered, but with electrical stimulation, the cell can be executed directly without preliminary modification.

2.10.1 Electrical stimulation

There are three significant parameters in the electrical stimulation technique which need to be well programmed: voltage, pulse duration, and frequency. Electrical stimulation can be used for the treatment of disorders, including Parkinson's disease, dystonia, and essential tremor. Electrical stimulation can also be employed to study nerve behaviour. There are two kinds of controlling DBS: closed-loop and open-loop. In 2011, Santaniello argued that closed-loop performance for stimulation is significantly better than open-loop [136]. This claim is supported by other researchers such as Birdno [137].

There are very important requirements that need to be met in the electrodes and pad-electrodes for the stimulation [138]:

- Biocompatible and limited stimulation of the immune system
- No damage to tissue during stimulation and unaffected by corrosion
- No surgical gash when implanting the electrode
- Quick and easy implantation procedure of less than 20 minutes once the implant site is specified
- Lead and probes strong enough not to break during the implanting process, and stable after implantation

- Active implanting and accurate.
- Voltage should exceed the 'water window' i.e. electrolysis water to O₂ and H₂ gas. Water window means there is a critical point at which reduction and oxidation of water takes place. If the electrode potential overtakes the water window, this can damage the electrode in the form of electrode erosion, resulting in the decay of the electrode material in the electrolyte [139].
- Size, type of material and placement of electrodes impacts the current density
- Constant impedance: the controlled voltage techniques for deep brain stimulation can approximate the delivered current [140]. Overall impedance range typically varies between 500 Ω to 1500 Ω [141].

2.10.2 Optical stimulation

Channelrhodopsin-2 genetically engineered neurons were used by Boyden in 2005 to light stimulate the mammalian brain using blue light pulses which cause the depolarisation of neurons [142]. The same tests were done by Ishizuka in 2006 [143] for the action potential. The evolution of the mechanism of light delivery is important for optical stimulation for deep impact tissue, stimulating at low power energy. Moreover, more light (direct or guided) is required to penetrate the tissue in this stimulation mechanism [144]. In 2002, Nagel discovered the light sensitive channel called channel-rhodopsin [145]. When the light is supplied to the proteins, the green algae will move towards the light. It is sensitive to blue light, which causes the channel to open, and positive ions then flatten to the cell. This protein can work in membrane cells, and there is a very precise way of controlling the activity of the brain's neurons cell using the channel-rhodopsin. Genetic engineering is required to make neurons produce this protein.

Once a cell is genetically photosensitized, light needs to be delivered. For example, to assist in targeting specific neurons such as activating the neuron responsible for movement, the light can be delivered with a fibre optic cable. This makes these techniques very powerful. However, channel-rhodopsin is not the only optogenetic tool, as there is another type of protein which can switch off the neuron or mute it, such as a Halo-rhodopsin, which is sensitive to orange light.

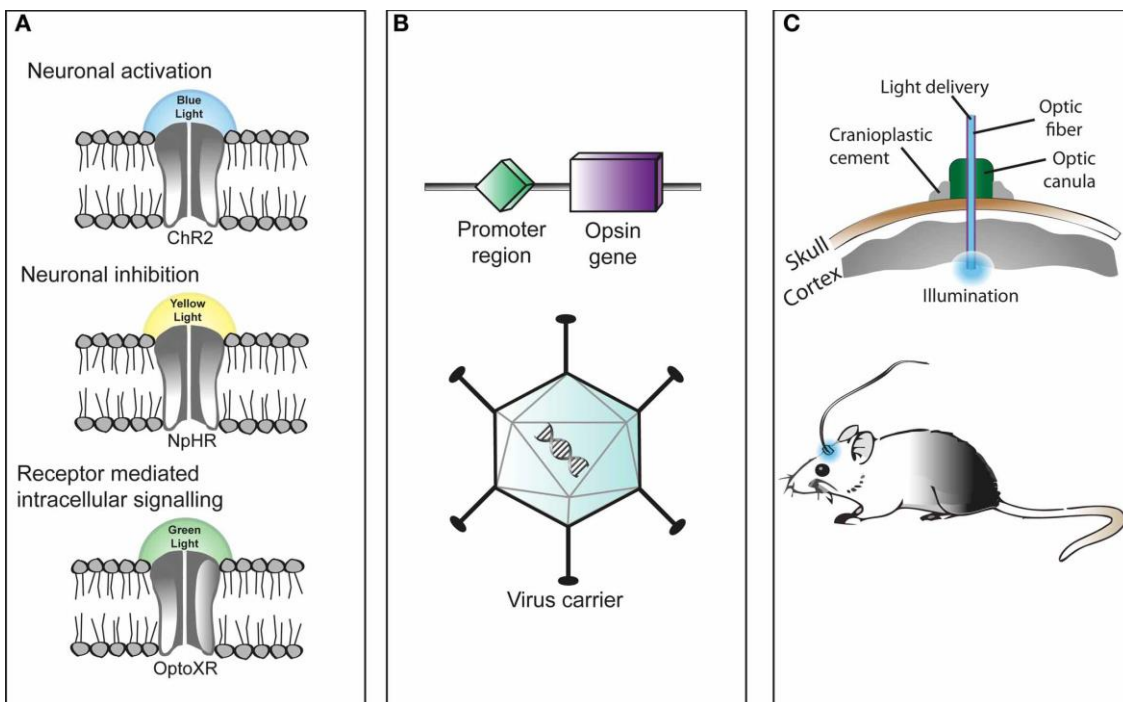


Figure 2-6: Optogenetic engineering. (A) Three types of light sensitive proteins. Top: an example of a protein sensitive to blue light, called channel-rhodopsin-2 (ChR2). Middle: a protein example sensitive to yellow light, called Natronomonas pharaonis Halorhodopsin (NpHR). Bottom: optoXRs, which responds to green light. (B) Simplified steps of optogenetic engineering, shows adding the promotor to the opsin gene then injecting it to a virus. (C) Example of light delivery to an engineered brain cell in a mouse [146].

Grossman et al. in 2009 demonstrated a $16 \times 16 \mu\text{LED}$ array as an example for optical neural stimulation. Each single μLED has the 16 mm^2 area and 0.07 mW power consumption [147]. More specifically, the power requirement for the neural stimulation was between 0.1 mW/mm^2 and 1 mW/mm^2 with existing ChR2 [148]. Continuous pulse light for stimulating the neurons is required for real-time image delivery, and this was achieved for 600 ms at 1 mW/mm^2 [133].

2.11 Powering medical implants

There are two types of medical implant devices: passive and active. Passive devices, such as vascular graft and orthopaedic devices, do not require a power source. Active implanted medical devices include cardiac pacemakers, neuron stimulators and cochlear implants [149]. These need power sources to operate. There are different ways to power the AIMD, such as percutaneous cables, battery, energy harvesting, and wireless power transfer. They have different power provision [150]. The range of the consumption for different AIMDs is shown in Figure 2-7. Battery source [151], mechanical energy harvesting [98] and the wireless power system [152] are the most efficient and common sources for powering the AIMDs.

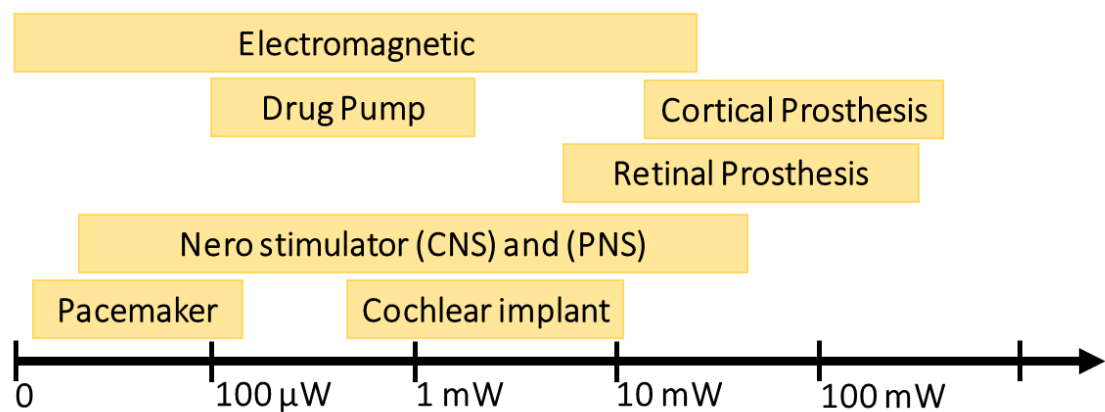


Figure 2-7: Medical implant devices and the conceptual range of power consumption. The power consumption line for Electromagnetic [152], Drug pump [153], Nero-stimulator [154] central nervous system and peripheral nerve stimulation, Pacemaker [155], Cortical prosthesis [156], Retinal prosthesis [157] and Cochlear implant [2] are presented.

To design the powering system, the following requirements need to be considered [158]:

- Temperature
- Steady operational lifetime
- Size
- Continuous power consumption
- MRI compatibility and electromagnetic interferences

- Accuracy.

The following subsections overview two examples of the power sources for the medical implant devices:

- Battery
- WPT

2.11.1 Battery

When the battery is adapted for the AIMD as a source of power, the following significant points need to be considered. First, batteries should have a long lifetime to prolong periods between the implant and surgical replacements. Next, it should satisfy the safety issue when implanted in a human. It should not have direct contact with the blood to prevent oxidation [159]. In general, implanted batteries can be divided into two groups: primary batteries (non-rechargeable) and secondary batteries (rechargeable). Primary batteries are the kind which can be used for only one period. When its lifetime is finished, the battery needs to be replaced. In Table 2-4, examples of primary batteries are presented for powering the AIMD. There are also other types which have not been mentioned here. More types of battery sources were reported by Bock [160], such as implantable batteries in the biomedical devices.

Table 2-4: Examples of the primary batteries used for the medical implant devices.

Battery types	Example of use	Ref
Lithium / ion battery	Pacemaker	[161]
Lithium / manganese dioxide	Neuron stimulator, Pacemaker and Drug delivery	[162]
Lithium / carbon monofluoride	Alternative MID	[163]
Lithium / silver vanadium oxide	Implantable cardioverter defibrillators for monitoring patient's heart continuously	[164]

Secondary batteries are also called rechargeable batteries. They have special properties like primary batteries but can be recharged. For the neuron stimulator, lithium/ion was the adopted by Lee in 2009 [165] because it is very small in size, the minimum discharge voltage is 3 V, its weight is 0.3 g to 40 g, and the charge/recharge cycle is about 1,000

times with a normal capacity of 80% [166]. Table 2-5 shows some examples and a comparison between secondary batteries. Palacin in 2009 reported that a lithium-ion battery is the most useful power on the market [167].

Table 2-5: Examples of rechargeable batteries power sources.

Battery	Application	ref
lithium/iodine	Medical Implant, Pacemaker	[168]
Nickel Cadmium	Pacemaker	[169]

Recharging batteries

There are different strategies for re-charging batteries in the AIMD. Examples of recharging the implanted battery are:

- Goto et al. in 2001 demonstrated optical uses [170]
- Radio frequency [171]
- Thermoelectric devices (e.g., radioisotope decay energy) [172]
- Electromagnetic power [173]
- Piezoelectric power, by generating electricity from motion or vibration [174] (e.g. a vibrating medium generating mechanical energy [175]).

The most common actual technique accepted widely in AIMD is radio frequency transfer. Furthermore, this is also used for data transfer. The block diagram of the wireless charging techniques is shown in Figure 2-8.

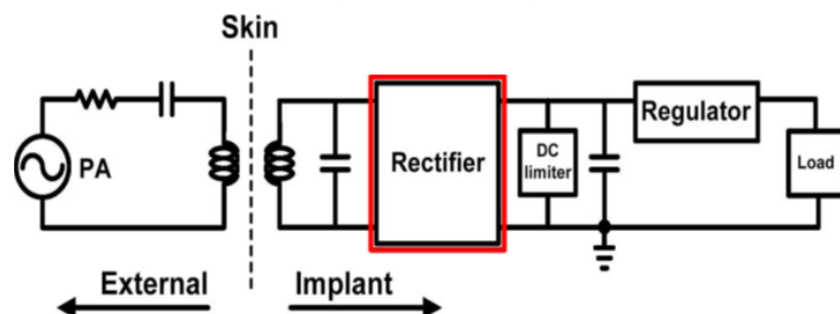


Figure 2-8: Simple schematic of wireless radio frequency for recharging an implantable battery [176].

2.11.2 Wireless power transfer

Medical implant devices can be divided into two groups according to wireless power techniques: with and without battery power sources. Extra operations are required for implanted battery sources [165], either by replacing an expired battery or recharging it. Because of power discharge and other disadvantages reported before, the use of batteries for medical implants may not be the safest option. Direct power by wireless power transfer is an alternative option which delivers sufficient power to the implant system.

Table 2-6 compares research on wireless power transfer technology. The amount of transferred power is illustrated depending on the type of implanted device. The most common and popular shape of the coil is a circle. The frequency ranges used for the wireless power are usually below 13.56 MHz. More specifically, they were in the ISM radio bands limitation condition. Consequently, the inductive links between two coils are commonly used in wireless power transfer [177, 178].

Table 2-6: Wireless power transfer for the implant device

References	f MHz	Coil shape	R1, R2 mm	Application	η %	d mm	P mW
Lin 2016 [179]	10	Circle	30,20	Brain implant	-	6	10
Xu 2016 [180]	13.56	Square	-	Cardiac pacemaker	79	50	64
Stoecklin 2016 [181]	13.56	Circle	10,4	Brain implant	-	20	190
Volk 2015 [182]	13.56	Circle	80,40	Brain implant	74	10	500
Swain 2015 [183]	0.562	Circle	-	Pressure sensor	26	30	186
Li 2015 [184]	13.56	Circle	25,9.5	Medical implant	92.6	3	102
Lee 2013 [28]	2	Circle	40,10	Brain stimulation	87	15	25
Carta 2011 [185]	1	Circle	-	Endoscopes	-	-	400
Jow 2007 [186]	5	square	20,8	Neuroprosthesis	85.8	10	-
Ghovanloo 2007	5	Circle	-	Medical implant	29.9	10	117
Sauer 2005 [188]	4	Circle	50,20	Neural implants	-	25	2.4
Kendir 2005 [189]	1	Circle	4,2	Medical implant	67	7	250

f: Frequency

P: Received power

η : Is the power efficiency

d: Distance between two coils

Coil size, R1: Radius of the primary coil, R2: Radius of the secondary coil.

2.12 Electromagnetic Radiation and Health

There are two main types of electromagnetic radiation, which are ionising radiation, and non-ionising radiation. Ionising radiation concerns a single photon of energy 10 eV and more are capable of ionising oxygen or breaking chemical bonds inside the body. For example, ultraviolet light and higher frequencies are harmful and have significant effects on health. The effect of the electromagnetic field biologically will cause dielectric heat. This effect depends on the power exposure and frequency. The Specific Absorption Rate SAR is used to measure the heating effect by knowing the rate of energy absorbed by the body. It heavily depends on the part of the body that the exposure targets and the geometry of that part. For example, for mobile phone SAR testing, the location will be the entire head. For this, the Federal Communications Commission FCC in the United States set the SAR level to below 1.6 W/Kg, and the European Committee for Electrotechnical Standardisation CENELEC has specified the limitation to below 2 W/Kg.

Each material inside the body has different and specific properties. It has been studied for 50 years for the frequency range of 10 Hz to 30 GHz [190]. The average model parameter is 45 for different tissues represented together [191, 192]. The biological tissues behave as a dielectric with losses because it is mainly water. The value of electromagnetism is known as it depends on the frequency. The dielectric permittivity is high, and it decreases with increases in frequency. For example, the relative permittivity of the blood is 435,000 at 1 Hz frequency. The electric conductivity is below 1 for the frequency range of 1 Hz to 1 GHz frequency band. The amount of water is based on whether the tissue is most lossy or least lossy. For example, wetter tissue is most lossy, and so blood could be counted as a lossiest because of its high water content, while fat is less lossy because of low water content [193].

Chapter 3. Wireless power transfer

3.1 Introduction

Power delivery to electronic medical implant devices is essential, as without power the system loses functionality. Normally, the AIMD is powered either by a battery or wireless system. The design of a wireless power transfer system requires an accurate circuit schematic and simulation to decrease power dissipation. The scheme of the wireless power transfer system is summarised as:

- a) Selecting the right tuning frequency for the system
- b) Designing the circuit for the oscillator to generate sine waves
- c) Calculating the power budget for the receiver side
- d) Choosing a proper Standard Wire Gauge (SWG) regarding the tuning frequency for coil design
- e) Adding the power amplifier to the circuit to increase up to the power on the transfer side. This allows the system to deliver power according to the power budget
- f) Rectifying the Alternating Current (AC) waves to the Direct Current (DC) wave
- g) Regulating the output voltage
- h) Finally, the system might require matching between the transmitter and receiver circuit.

The system block diagram representing the concept of the wireless power delivery is shown in Figure 3-1.

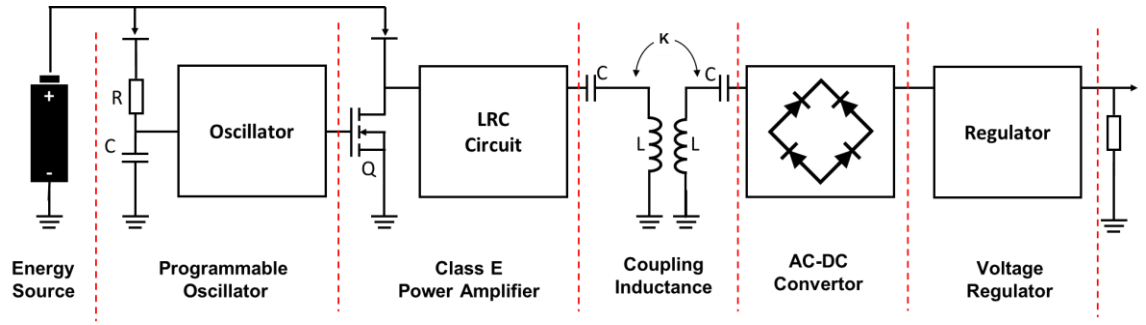


Figure 3-1: The general concept of wireless power transfer. K represents the coupling coefficient, which depends on the distance between the transmitter and the receiver coils.

3.2 Physics of wireless power transfer

There are different methods for transferring energy between the source and target using electromagnetic fields, and these are dependent on the distance between the transmitter and receiver devices, as explained below. To put it in another way, this depends on the range of energy link [194]. There are three regions according to the relation between the wavelength and distance: far-field ($\lambda \gg d$), mid-field ($\lambda \approx d$) and near-field ($\lambda \ll d$), where d is the distance between the two devices and λ is the wavelength [195]. In general, near-field is known as the non-radiative region and the far-field region is a radiative field. The wavelength can be defined as:

$$\lambda = \frac{C}{f} \quad (3-1)$$

Where C is the speed of light and f is frequency. More specifically, the details of the two main regions are as follows:

Far-field region

Examples of far-field energy transfer are microwaves, light waves and radio waves, in which the distance between the transmitter and receiver is larger than the tuning frequency [196]. This range of power transfer is also called radiative regions, and the method can be used to achieve a longer range for transferring energy.

Near-field region

Power can be transferred depending on the electric field, such as with capacitive coupling or a magnetic field in inductive coupling. Normally, the distance between the transmitter and receiver is significantly less than the tuning wavelength λ [196]. The distance $d_{tx,rx}$ between the transmitter and receiver compared to the size of coil/antenna d_{coil} , the antenna is important. If the $\lambda \ll d_{tx,rx}$, the amount of transferred power will be effective and this range is called short-range [197], but if the $\lambda \approx d_{tx,rx}$, the power cannot be transferred effectively and this range is known as the mid-field region. For this range, neither inductive nor capacitive coupling transfer sufficient power [198]. This range of power transfer is safer than the far-field, and it is radiative.

3.2.2 Magnetic field strength

A magnetic field is caused by moving a charge in a wire or space. Also, magnetic field strength H characterises the magnitude of the magnetic field and neglects the substance properties of the space. The general relation of the Magnetic Field Strength (H) is given by [199]:

$$\sum i = \oint \vec{H} \cdot d\vec{s} \quad (3-2)$$

Where i is the current. Equation (3-2) can be used for different kinds of conductor, as shown in Figure 3-2.

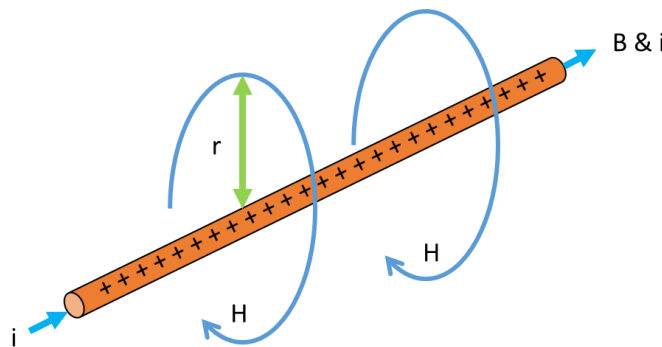


Figure 3-2: Magnetic flux surrounds the straight wire. The direction of the magnetic flux can be assigned using the right grip rule. Where i represents current flow in the wire and H is the magnetic field.

Magnetic flux strength for a straight wire in distance r is stable and can be described by the equation [200]:

$$H = \frac{1}{2\pi r} \quad (3-3)$$

The magnetic field strength of the coil with the number of turns N , the radius r , at the distance x from the centre of the coil, and current I , is as shown in Figure 3-3.

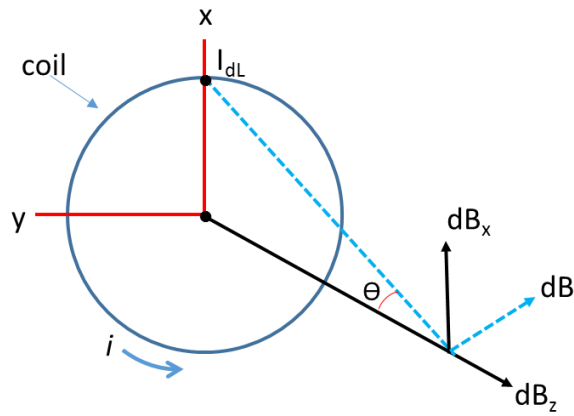


Figure 3-3: Current flows in a circular shaped wire and the magnetic field strength is the distance x from the coil.

magnetic field strength is given by [199]:

$$H = \frac{i \cdot N \cdot r^2}{2 \sqrt{(r^2 + x^2)^3}} \quad (3-4)$$

In the middle of the coil for distance x equal to zero (0), the magnetic field strength is given by:

$$H = \frac{i \cdot N}{2r} = \frac{i \cdot N}{l} \quad (3-5)$$

According to [200], the optimal radius of the coil is relative to the distance of maximum magnetic field strength given by:

$$r_1 = x \cdot \sqrt{2} \quad (3-6)$$

Where x is the distance from the coil.

3.2.3 Magnetic flux and magnetic flux density

Magnetic flux Φ is equal to the magnetic flux density B (total number of the magnetic line) in the specific cross-sectional area A.

$$\Phi = B \cdot A \quad (3-7)$$

The explanation is shown in Figure 3-4:

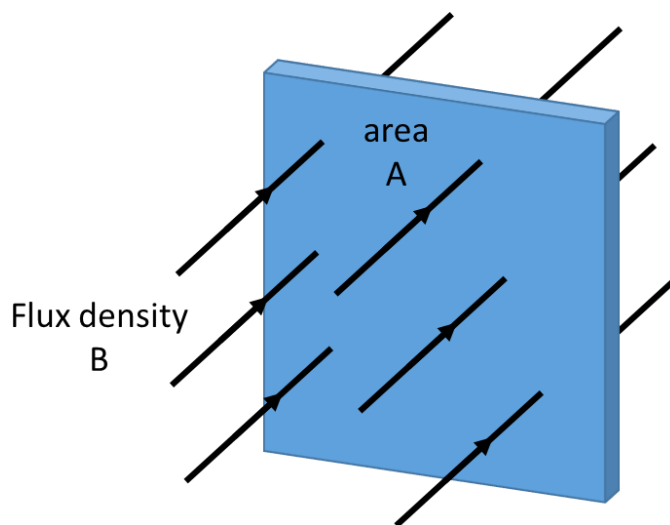


Figure 3-4: The magnetic flux and magnetic flux density modified from [201].

3.2.4 Inductance

If current passes through any form of the conductor, it will produce a magnetic field (magnetic flux). For a coil with the number of turns N and an area A, the flux linkage Ψ is:

$$\Psi = \sum_N \phi_N = N \cdot \phi \quad (3-8)$$

The inductance for the enclosed loop of wire (coil) is specified by the ratio of the total flux Ψ to the current I , which is given by [199]:

$$L = \frac{\Psi}{i} = \frac{\mu \cdot N \cdot H \cdot A}{i} \quad (3-9)$$

μ is the permeability of the human body and $\mu=\mu_0$ is the free space, which is equal to $4\pi \times 10^{-7}$ H/m. Table 3-1 shows the amount of relative permeability for 13.56 MHz and 2.45 GHz frequency for biological tissue at normal human body temperature.

Table 3-1: The relative permeability of tissue at 37 °C [202].

Material	13.56 MHz	2.45 GHz
Blood	155	60
Bone	11	4.8
Brain (white matter)	182	35.5
Brain (grey matter)	310	43
Fat	38	12
Muscle	152	49.6
Cornea	132	49
Iris	240	52
Lens cortex	175	48
Lens nucleus	50.5	26
Retina	464	56
Skin	120	44

The equations of inductance vary with coil shape, such as in this equation for a rectangular cross-sectional conductor [203]:

$$L = 0.002l \left\{ \ln \left(\frac{2l}{w+d} \right) + 0.50049 + \frac{w+d}{3l} \right\} \quad (3-10)$$

Where w is the width, t is the thickness and L is the length, shown in Figure 3-5:

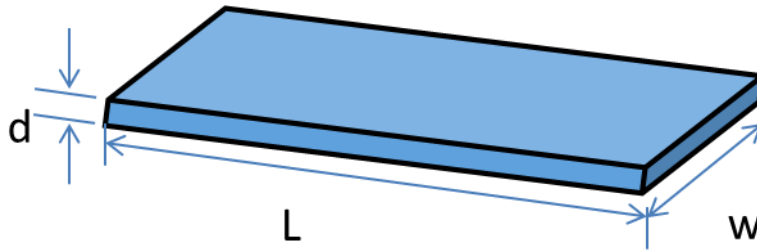


Figure 3-5: Thin film conductor.

For a flat, square coil:

$$L = 0.0467a^2N^2 \left\{ \log_{10} \left(2 \frac{a^2}{t+w} \right) - \log_{10}(2.414a) \right\} + 0.02032aN^2 \left\{ 0.914 + \left(\frac{0.2235(t+w)}{a} \right) \right\} \quad (3-11)$$

Where a is the side length, t is the thickness, w is the width and N are some turns, as shown in this Figure 3-6:

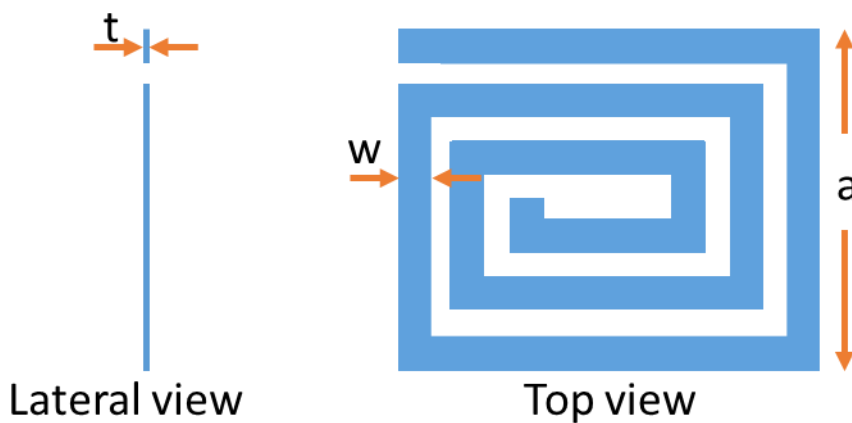


Figure 3-6: Square loop inductors. Where t trace thickness, N is the number of turns, a is the length of the first trace and W is width.

For the very thin square loop printed on printing circuit board PCB, then $t \approx 0$, and equation (11) is reduced to:

$$L = 0.0467a N^2 \left\{ \log_{10} \left(2 \frac{a^2}{w} \right) - \log_{10}(2.414a) \right\} + 0.02032a N^2 \left\{ 0.914 + \left(\frac{0.2235(w)}{a} \right) \right\} \quad (3-12)$$

There are four main factors which affect inductance [204]:

- 1) The number of turns N : an increasing number of winds will increase inductance, while a decreasing number of turns decreases inductance
- 2) Space between turns l : spacing between turns is called the length of inductance, which depends on the linear spacing
- 3) The diameter of the coil R : a small diameter has less inductance than a large diameter inductance
- 4) Core material μ (permeability): the inductance is greater when the core coil is steel or solid ferrite instead of air.

A general simplified equation for inductance with the core filled with air for the solenoid coil with the number of turns N and length l is given by:

$$L = \frac{\mu_0 \cdot A \cdot N^2}{l} \quad (3-13)$$

The schematic diagram is shown in Figure 3-7 for the solenoid coil.

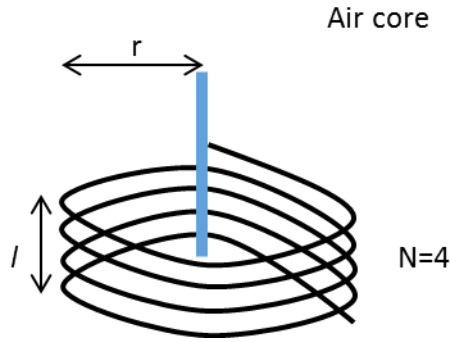


Figure 3-7: Solenoid coil.

3.2.5 Mutual inductance

The flow of current is in the first conductor and if the second conductor is placed near to the first then the magnetic flux, when produced in the first conductor, will generate current in the second. The magnetic flux of the first conductor is a function of the current $\Psi_1(i_1)$. Furthermore, the magnetic flux in the second conductor is a function of the current when applied to the first conductor $\Psi_2(i_1)$ [199].

When more than two coils are shared with the combined magnetic flux, they will have the same mutual inductance. Moreover, the mutual inductance is the fundamental operating base of the transformer and other electrical devices when they interact with another device. Mutual inductance is when the current passes through the primary coil and encourages voltage in the secondary coil; however, sometimes mutual inductance is not positive because it can cause leakage or lost inductance.

The coil site is very important for mutual inductance, as the amount of magnetic flux in the second coil, which is operated by the magnetic flux of the first coil, will be very weak. Also, the mutual inductance value will become small [205].

The mutual inductance for the two parallel circular coils can be described by [206]:

$$M_{i,o} = \frac{\mu_o \cdot \pi \cdot r_o^2 \cdot r_i^2 \cdot N_1 \cdot N_2}{2(r_o^2 + x^2)^{3/2}} \quad (3-14)$$

Where μ_0 is the permeability of free space, r_i is the radius of the inner/implantable coil, and r_o is the radius of the outer/external coil.

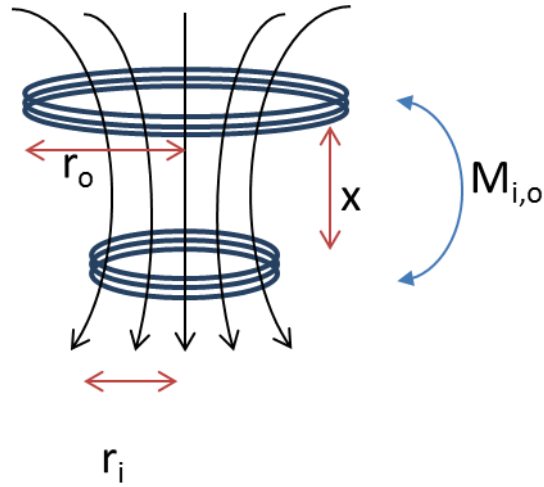


Figure 3-8: Mutual inductance between two coupled coils. The distance between the two coils is equal to x , and r represents the coil's radius.

3.2.6 Coupling coefficient

K represents the coupling coefficient or coupling factor as:

$$k = \frac{M_{12}}{\sqrt{L_1 L_2}} \quad (3-15)$$

Where L_1 is the inductance of the primary coil, L_2 is the inductance of the secondary coil, and M_{12} (when $M=M_{12}=M_{21}$) is the mutual inductance. The magnetic flux in the secondary coil operated by the magnetic flux in the primary coil is the coupling coefficient. Furthermore, it is in the range between 0 and 1 [207]. The coupling coefficient can be described as a function of the distance between two parallel coils, while the radius of the primary coil is r_o and the radius of the secondary coil is r_i , as in [199]:

$$k \approx \frac{r_o^2 r_i^2}{\sqrt{r_o \cdot r_i} (\sqrt{x^2 + r_i^2})^3} \quad (3-16)$$

3.2.7 Resonance

In basic terms, resonance in the WPT is when the secondary circuit is driven by the primary coil at the same tuned frequency. The phases of the magnetic fields between the primary and secondary coils are synchronised. Connecting a capacitor to the secondary coil optimises the power efficiency in parallel with the inductance. According to the Thomson equation, the resonance frequency can be written as [208]:

$$f = \frac{1}{2\pi\sqrt{LC}} \quad (3-17)$$

The quality factor, which is also called the unloaded quality factor, is given by the ratio of stored energy in the coil to the wasted energy in the wires. The quality factor can be described by [209]:

$$Q = \frac{\omega L}{R_2} \quad (3-18)$$

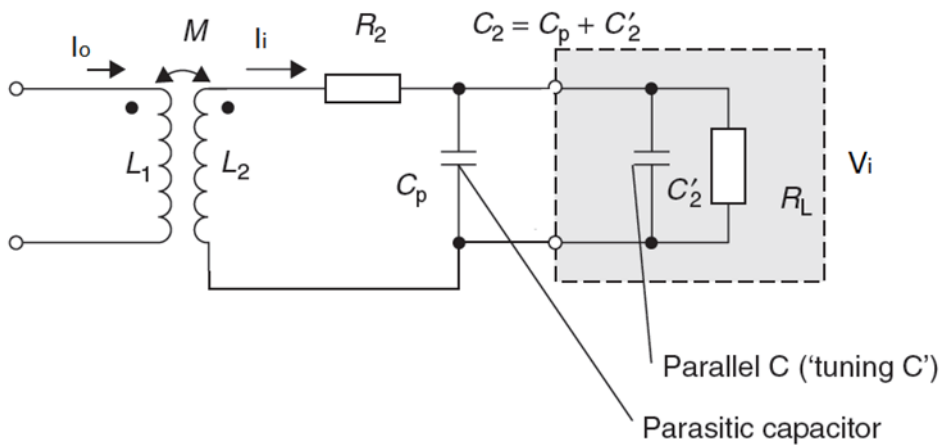


Figure 3-9: Resonant circuit after adding the capacitor C_2 in parallel with the coil.

Where R_2 is the resistance and L_2 is the inductance in the secondary coil, and ω is the angular frequency, which is equal to $2\pi f$ [199].

3.2.8 Power efficiency

The power efficiency of the wireless system, in general, can be written as [210]:

$$\eta = \frac{P_{output}}{P_{input}} \quad (3-19)$$

Where P_{input} represents the total power transferred by the load, and can be present depending on the source and load resistance:

$$\eta = \frac{i^2 R_L}{i^2 R_S + i^2 R_L} \quad (3-20)$$

Where R_L is the load resistance, R_S is source resistance, and 'i' is the total current flow in the circuit. The power efficiency can be described regarding resistance as:

$$\eta = \frac{R_L}{R_S + R_L} \quad (3-21)$$

Finally, the equation can be simplified as [211]:

$$\eta = \frac{1}{1 + \frac{R_S}{R_L}} \quad (3-22)$$

It indicates that the $R_L \gg R_S$ for the high efficiency power transfer. When the load resistance is equal to the source resistance, the maximum power efficiency will 50%.

3.2.9 Impedance matching

The impedance needs to be matched on both the transmitter and receiver side to improve the power transfer. There are different approaches for matching the circuits,

and the name of the method is classified by the shape of the circuit. For example, there are T-shape and L-shape circuits. In the L-shape, an LC matching circuit was used as shown in Figure 3-10. With the LC, L is the coil inductance, and C is the capacitance [212].

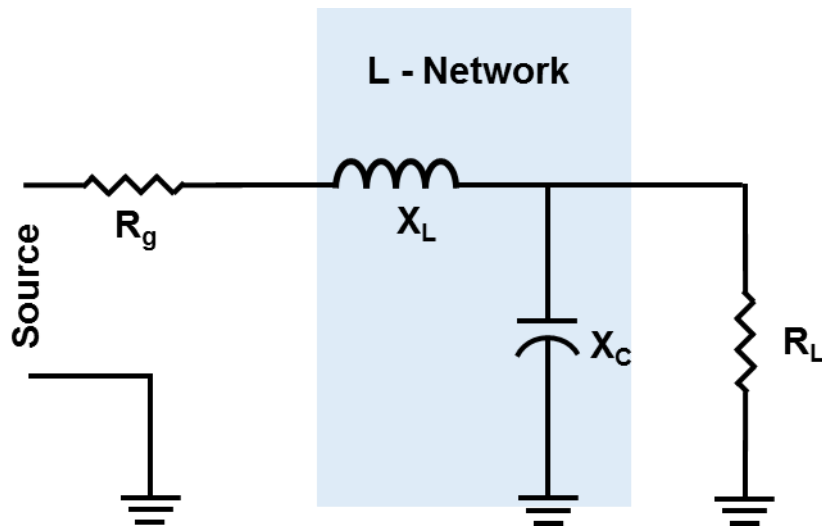


Figure 3-10: 'L' Matching Network.

To calculate the value of inductance and capacitance in the L-network matching circuit, first determine the quality factor Q by:

$$Q = \sqrt{\frac{R_L}{R_g} - 1} \quad (3-23)$$

When R_L is the load resistance, and R_g is source resistance, then the inductive reactance X_L can be described by:

$$X_L = \frac{R_L}{Q} \quad (3-24)$$

And

$$X_C = QR_L \quad (3-25)$$

The capacitance C and the inductance L can be founded by:

$$X_c = \frac{1}{2\pi fC} \quad (3-26)$$

Also, the inductive reactance X_L can be described by:

$$X_L = 2\pi fL \quad (3-27)$$

To calculate the load on the transmitter side, Matlab was used and the code is shown in Appendix A.

3.2.10 Skin effect

The phenomenon of skin effect is the electrical current displacement from the centre of the wire to its surface. This will happen especially when the AC passes through the conductor, and depends on the frequency of the source. For high frequency, the current density in the surface of the conductor will be high, while for the low frequency the current density is higher in the centre, because a higher frequency will push the majority of the current to the surface of the wire. The penetration depth δ can be described by:

$$\delta = \sqrt{\frac{2\rho}{\omega\mu}} \quad (3-28)$$

The ρ is specific resistance. Examples for δ for the 50 Hz, 100 KHz and 10 MHz respectively are 10.4 mm, 0.23 mm and 0.036 mm [213]. This result shows that the evidence of the skin effect will affect the area in which current flows. It means increasing the resistance of the conductors to the higher frequency, due to energy loss in the conductors [214].

3.2.11 Class E power amplifier

For the Class E power amplifier, there are two main factors which need to be considered after the switch transistor is assigned according to the tuning frequency. The components such as L_{ch} , $C1$, $C2$ and $L1$ need to be taken into account, as shown in Figure 3-11. The duty cycle of the circuit is about 50% for the class E amplifier. The start time can be represented as $(2n+1)\pi$, and the current in the resonant tank can be expressed by i , while the current across the inductor is L_{ch} is I_{ch} .

$$i = I \sin(\omega t + \theta) \quad (3-29)$$

Where θ is equal to (-32.5°) , then:

$$\frac{I_1}{I_{ch}} = \left(\frac{\pi^2}{4} + 1\right)^{\frac{1}{2}} \quad (3-30)$$

The peak voltage V_p across the switch transistor appears when the $d_{vc2}/dt=0$ where V_p is due to $-2\pi\theta V_{ch}$

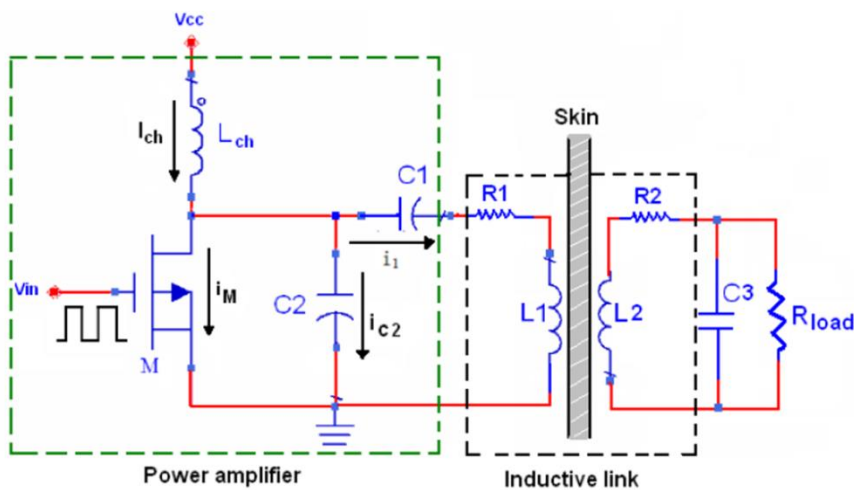


Figure 3-11: The class E power amplifier schematic example (image from [215]).

The values of the C1 can be calculated by [215]:

$$C1 = \frac{1}{\omega_o R1 (\frac{\pi^2}{4} + 1) (\frac{\pi}{2})} \quad (3-31)$$

So,

$$C1 = \frac{1}{\omega_o (5.447 R1)} \quad (3-32)$$

Where,

$$L1 = \frac{Q R1}{\omega_o} \quad (3-33)$$

Then C2 can be calculated by:

$$C2 = C1 \left[\frac{5.447}{Q} \right] \left[1 + \frac{1.42}{Q - 2.08} \right] \quad (3-34)$$

Where Q is the quality factor and R1 is on the coil used on the transmitter side.

3.2.12 Voltage rectification

After the power is wirelessly transferred, the signal is AC coupled, and this needs to be converted to a DC signal, which can be achieved with a rectifier. Various topologies for the rectifier can be used. Typically, the combination of capacitors and diodes in a simple passive circuit can be used to convert AC to DC [216]. For a low voltage rectification, there will be a drop in voltage across the diode. Normal voltage reduction across the diode is 0.7 V. This will affect the energy level in the receiver end, but there is an option to replace the normal diode with a Schottky diode. For active rectification, replacing diodes with a voltage controlled switch transistor is the best option [217].

In general, rectifiers can be divided into two groups: half-wave and full-wave. For half-wave rectifiers, the simplest circuit includes a single diode, which conducts only the positive half-cycle of the output voltage. In the negative half-cycle, the output voltage is blocked. The output voltage of the DC components can be described by:

$$V_o = \frac{1}{2\pi} \int_0^\pi V_p \sin(\omega t) d(\omega t) = \frac{V_p}{\pi} \quad (3-35)$$

Where V_p is the amplitude of received voltage. However, a half-wave rectifier is seldom used because half the power is wasted.

The simplest circuit for a full-wave rectifier is composed of two diodes. When the first diode conducts a positive half-cycle, the second diode is blocked. In both cases, the direction of the current will be the same. Also, four diodes are used in a full-wave rectifier, which is called a bridge rectifier [218].

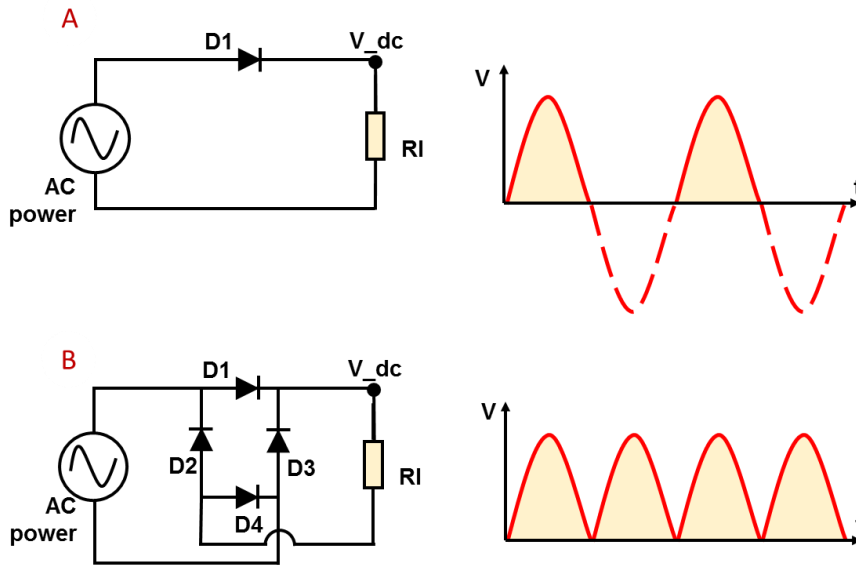


Figure 3-12: Circuit schematic and waveform of (A) the half-wave rectifier and (B) the full-wave rectifier (image from [218]).

The efficiency of the rectifier is given by:

$$\eta = \frac{P_{DC}}{P_{AC}} \quad (3-36)$$

Where P_{DC} is the output rectified voltage and P_{AC} is the input voltage.

3.2.13 Voltage Regulation

The voltage should stabilise after it is rectified and a parallel capacitor is required to be connected to the output. The capacitor will secure the output voltage from a sudden drop. An example of a voltage regulator is shown in Figure 3-13.

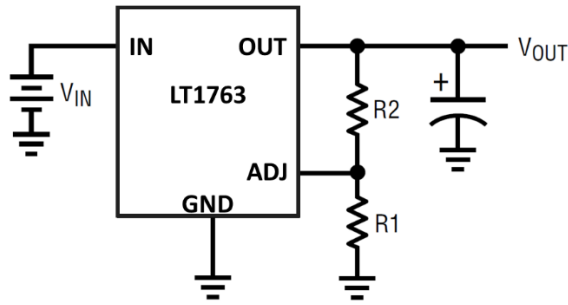


Figure 3-13: Example of the adjustable operation of the voltage regulator. LT1763 is a low dropout, low noise regulator from the Linear Technology company. It is used for fixed and adjustable output voltage.

The regulator drops the triple above the main operating voltage. The adjustable operation mode of the output voltage can be described by:

$$V_{out} = 1.22V \left(1 + \frac{R2}{R1} \right) + (I_{adj})(R2) \quad (3-37)$$

Where the $R1$ and $R2$ are the external resistors. Their ratios determine the output voltage, and a load capacitor is required to stop a sudden drop in output voltage [219].

To calculate the power efficiency of the voltage regulator, this equation can be used:

$$\eta = \frac{P_{out}}{P_{in}} \quad (3-38)$$

Where P_{out} is the output power and P_{in} is the input power after the rectification.

3.2.14 Matlab simulation for Wireless Power Transfer

For the simulation, Matlab version R2015a was used. Two figures below show the results of the calculation for the wireless power transfer using the equations presented in the previous sections. In general, the tuning frequency is set at 13.56 MHz. The relation between the magnetic field and the distance for different coil sizes is shown in Figure 3-14. The current set of 200 mA and the number of turns (N) is set to 1. For small coils with a very short distance between them, the H has the highest value, but for long distances, the larger coil radius is better. This refers to the propagation of the magnetic field in the centre of the coils.

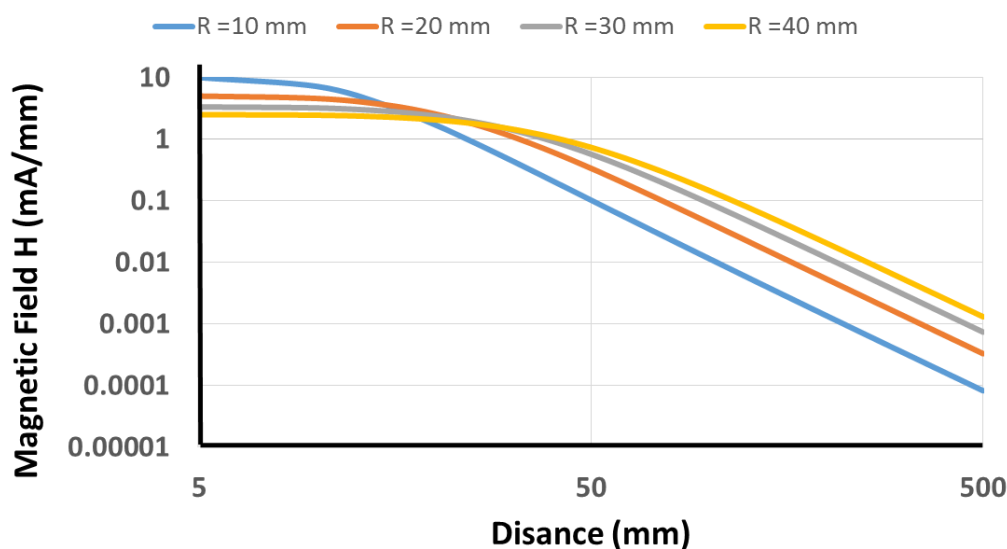


Figure 3-14: The magnetic field is proportional to the radius of the primary coil and reverse-proportional to the distance from the point of the measurement. For a distance of less than 50 mm the smaller coil is better, but for more than 50 mm the larger radius coil is better.

To understand the relationship between the change in the coil size and the magnetic field. The Matlab simulation result is shown in Figure 3-15. The current was 200 mA, and N was equal to 1. The strongest field was at the shortest distance, while the size of the smaller coil was better than the larger coil. The result was more efficient for coils sized less than 5 cm.

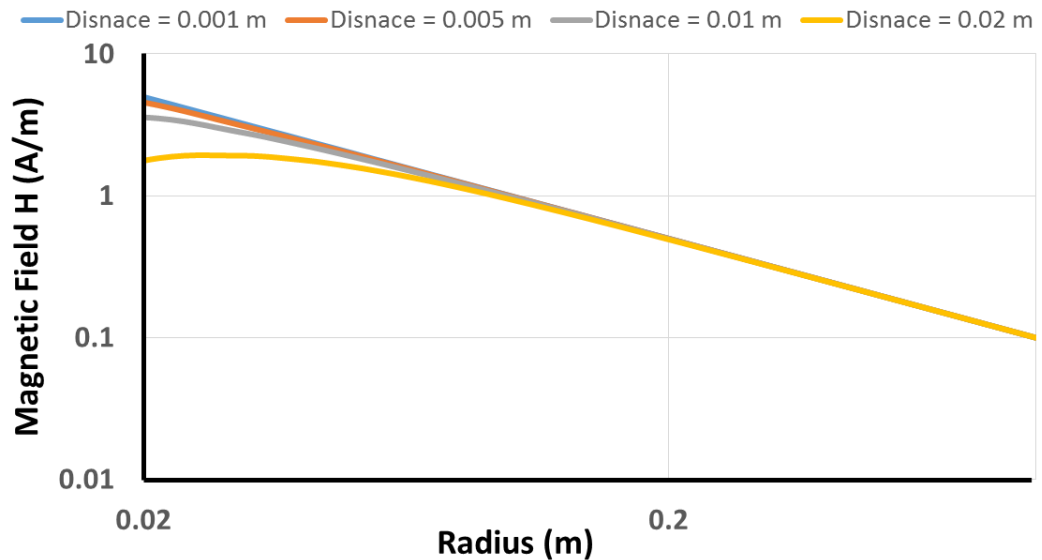


Figure 3-15: Dependency of the magnetic field on the primary coil radius. A small coil for a small distance of less than 50 mm is better than the large coil.

The current was set at 200 mA and the distance was 5 mm. There is a linear relationship between N and H , as shown in Figure 3-16. Also, when the number of turns is increased for a small coil, it will be a better than a large coil for the magnetic field.

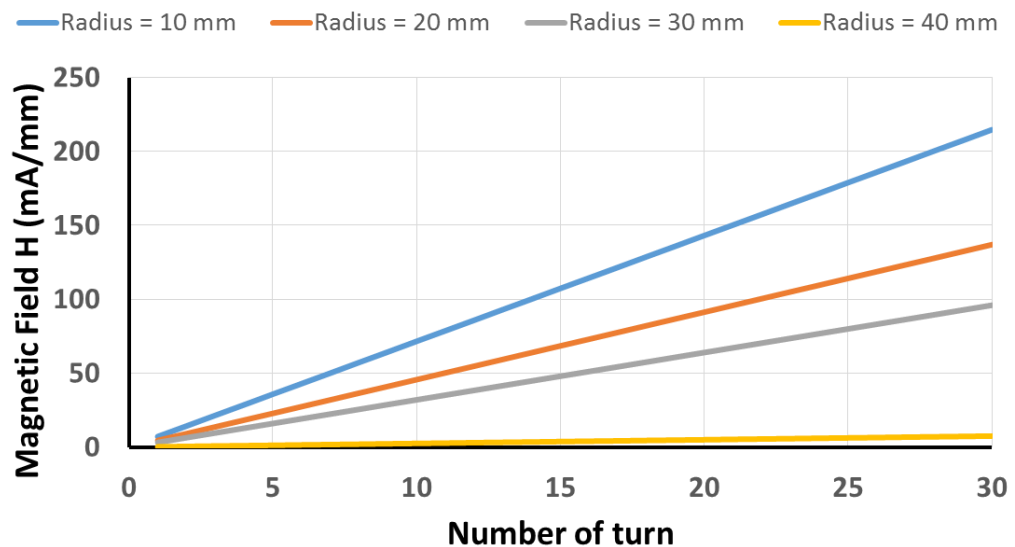


Figure 3-16: Relation between the Magnetic Field Strength (H) and the number of turns in the primary and secondary coils. A small coil is better than a large coil over small distances, and by increasing the number of turns it becomes more efficient.

Similar to the change in the number of turns, the current has a direct effect on the magnetic field. By increasing the current flow in the copper coils, the magnetic field will increase. Furthermore, the smaller size of the coil at a distance of 5 mm is better than the larger coil. The results of studying the relationship between current and H are shown in Figure 3-17.

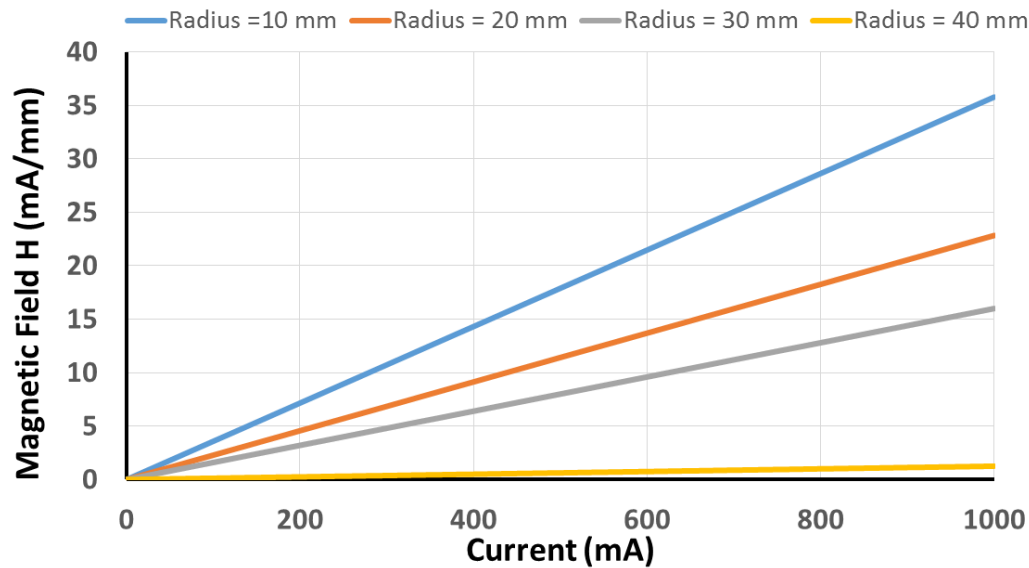


Figure 3-17: The relation between the Magnetic Field Strength (H) and change in current flow in the copper wires (coils). Increasing current flow in the small coil over a the small distance has the same effect as increasing the number of turns.

For mutual inductance, a few simulations have been tested. The result of this simulation is shown in Figure 3-18. In the top figure, the relation between the mutual inductance with the inner coil, outer coil and distance is presented. When the inner radius was changed and the outer coil remained stable and equal to 3 cm, the mutual inductance achieved the highest value when the size for the inner coil was approximately one third of the outer coil. When the size of the outer coil was changed from 0 to 4 cm, and the inner coil was fixed at 3 cm, the mutual inductance became higher by increasing the size. It is clear that increasing the distance between the two coupled coils will decrease the mutual inductance.

The bottom figure shows the relation between the power efficiency and load resistance for a range of mutual inductance levels. The power efficiency is higher when the load resistance is close to 20 ohms, in general, while the higher value of the mutual inductance of approximately 20 ohms is the best.

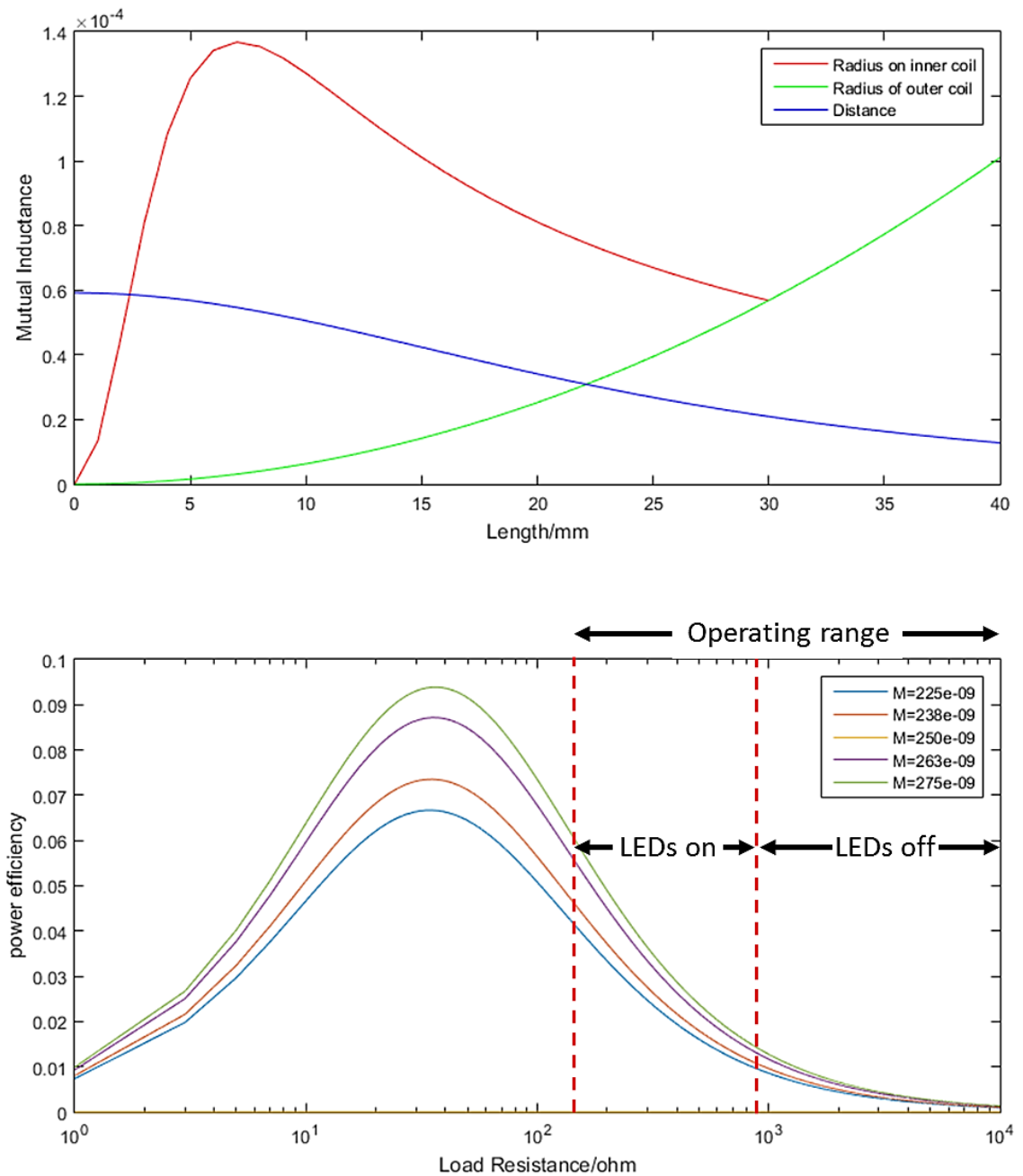


Figure 3-18: Relation between change in the radius of the inner coil, the distance between the two coils and change in radius for the implanted coil with the mutual inductance (TOP). The relation between the power efficiency and the load resistance (BOTTOM).

3.3 Power system design

For the wireless power transfer, the required components are the battery, embedded system power management, and the power of the transmitter and receiver. More details of the power system are described in the following subsections.

3.3.1 Battery

Any electronic system requires a power source. There are some important factors should the system designer consider it. These are:

1. The size of the battery and shape: this depends on where it will be used and where it will be fitted into the implant
2. Whether the type of battery is primary or secondary: if the battery is reused for a period, the secondary battery is capable of recharging and it will be the right choice
3. Capacity and discharge time: the battery will be selected according to the power consumption of the system, to cover the power budget and the required times of operating
4. Hazard: the battery should be safe and free from leakage or explosion.

In this project, a rechargeable battery of Lithium-ion polymer was selected. The technical details of the battery are listed below [220]:

- Dimensions: 60mm x 36mm x 7mm / 2.4" x 1.4" x 0.3"
- Weight: 34 g
- Nominal Capacity: 2000 mAh \pm 2%
- Nominal Voltage: 3.7 V
- Standard Charge Current: \sim 0.2 C / 0.5 A
- Recharge Voltage: 4.2 V
- Standard Discharge Current: \sim 0.2 C / 0.5 A.

Technically, this project requires a larger battery capacity to operate the system for more than 18 hrs/day. The battery should at least be capable of operating the system continually in the daytime to enable the patient to use the AIMD efficiently. The battery

charge and discharge curve are shown in Figure 3-19. The charging and discharging terminals are varied for any battery.

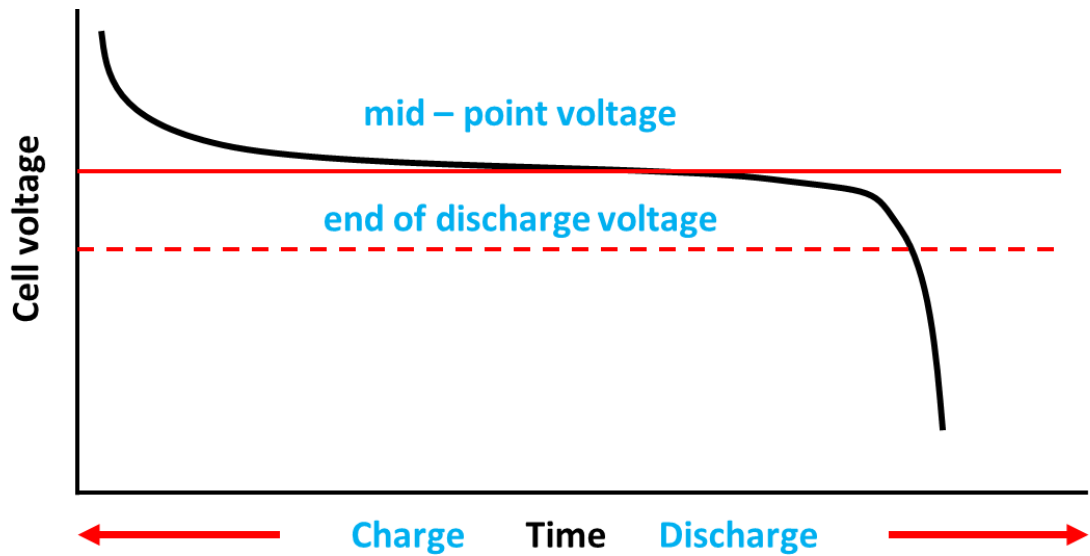


Figure 3-19: Shows battery charge and discharge (image from Texas Instruments [221]).

The midpoint line determines the charge and discharge edge, and the end of discharge voltage line shows the end of the battery life. When the battery is recharged to above the midpoint, the voltage increases its maximum peak.

3.3.2 Embedded system power management

In this project, two types of power boost were used in the external circuit, and voltage regulators were used in the internal circuit. The external components which receive power from the rechargeable battery source are a Raspberry Pi Zero and a wireless power transmitter. The Raspberry Pi Zero input voltage is 5 V. However, the selected rechargeable battery provides 3.7 V. Therefore, to convert 3.7 to 5 V, the power boost 1000C from Adafruit Company was selected, to convert battery power to supply the Raspberry Pi zero and also recharge the battery. A block diagram of the connecting network is shown in Figure 3-20. This board works as an Uninterruptible Power Supply (UPS) when the system is in running mode, and the battery can be recharging. It is useful when the battery is discharged, and it can be recharged from the external

power source. In other words, the user will not struggle to use the visual system because of an empty battery.

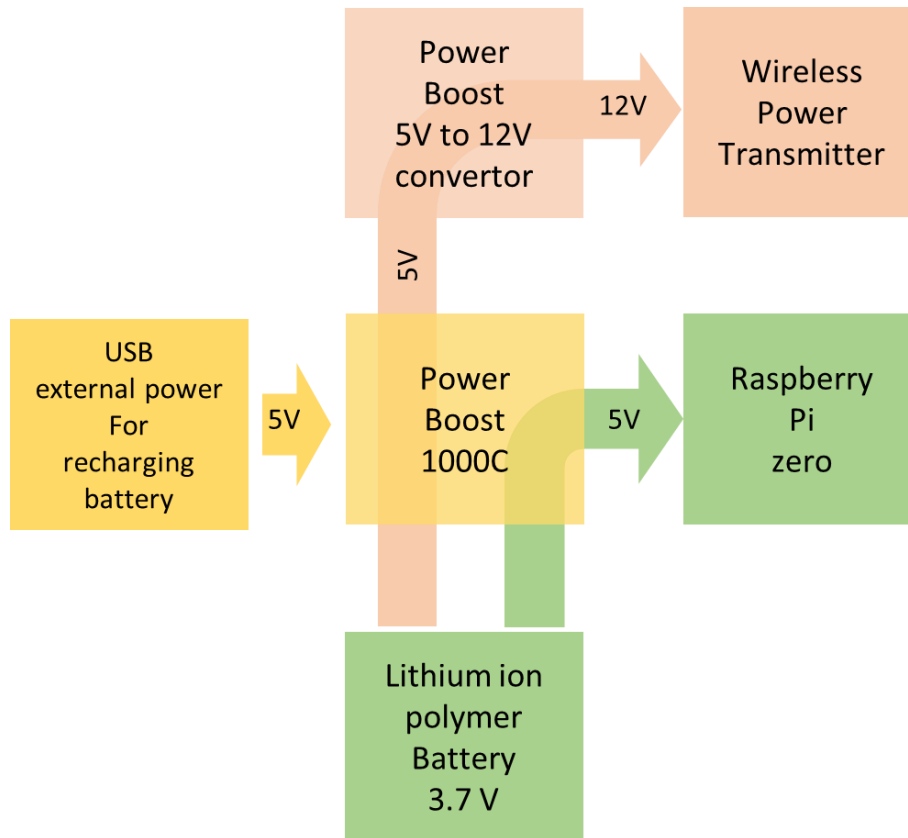


Figure 3-20: The block diagram of connecting the Raspberry Pi Zero with the step-up voltage converter (power boost). It also shows the battery connections to the system. The power boost converts the voltage from 3.7 V to 5 V (green blocks). It connects the power boost 1000C to the wireless power transmitter. The step-up voltage (designed power boost) power converter from 5 V to 12 V is put in between (orange blocks).

The second type of power boost was simulated and designed to operate the wireless power transfer system. It is designed to boost power from input 5 V to output voltage. The synchronous step-up DC-DC Converter LTC3122 from Linear Technology was used for this purpose. For the circuit schematic National Instrument (NI) Multisim and the PCB layout, NI Ultiboard, were used. The board was manufactured in the School of Electrical and Electronic Engineering at Newcastle University. The LTC3122 output current was up to 800 mA. The system schematic of the Synchronous Step-Up voltage converter is shown in Figure 3-23.

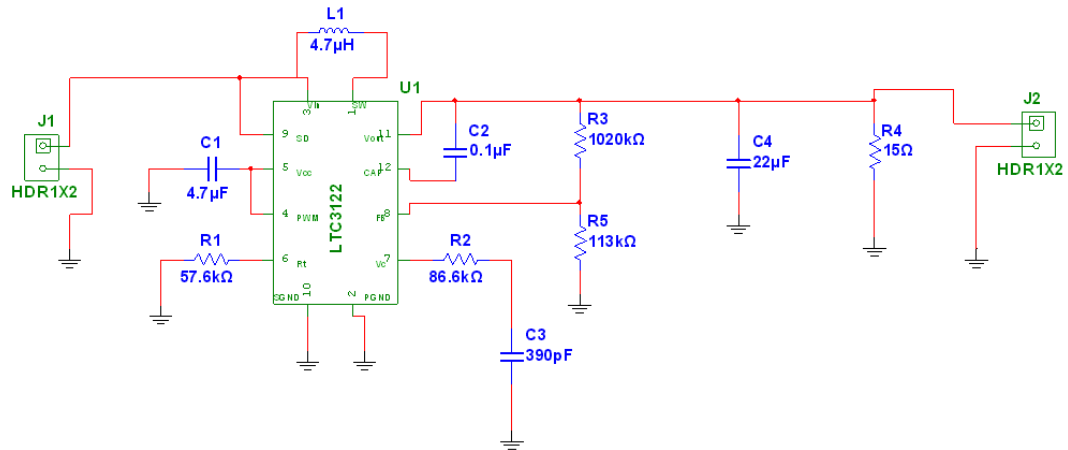


Figure 3-21: The LTC3122 Power boost, a DC-DC converter from 5 V to 12 V. The header J1 is for input 5V, and the header J2 is for the output. The schematic was provided by the Linear Technology Company.

3.3.3 Power transmitter

The details of the design of the wireless power transmitter circuit are described in the following subsections.

Oscillator

In this work, a programmable oscillator was used (DS1085L – frequency range from 8.1 kHz to 133 MHz with steps of 10 kHz). It was configured with the Arduino Uno to provide 13.56 MHz [222], and 6.78 MHz output frequency and then modified. The code script is shown in Appendix B, and the circuit schematic is shown in Figure 3-22. The circuit was used to programme and operate the microcontroller to generate the targeted frequency. The oscillator was powered by the battery, the value of R1 and R2 was 1 KΩ, and they were used as pull-up resistors.

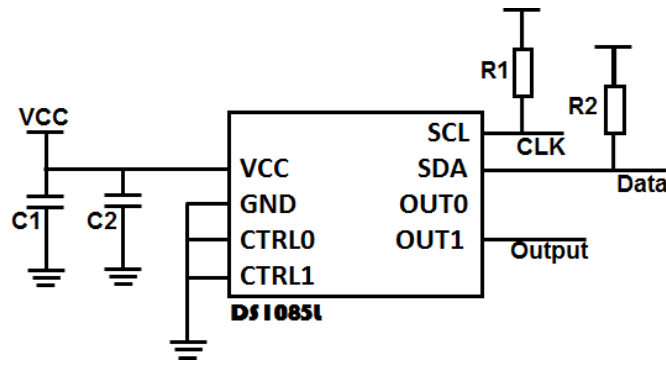


Figure 3-22: Circuit diagram of DS1085L for programing and generating the sine waves at a specific frequency.

For frequencies below 2 MHz, an NEC555 programmable oscillator was used. This timer is very common, and is widely used as a square-wave generator [223]. The circuit diagram of the 555 timer is shown in Figure 3-23. The input power supply could be any value between 5 V to 15 V. In this project, the input voltage was 12 V, and the output is in the form of square waves. The period, T , of high voltage (t_1) and low voltage (t_2) will lead to a period with 50% of the duty cycle.

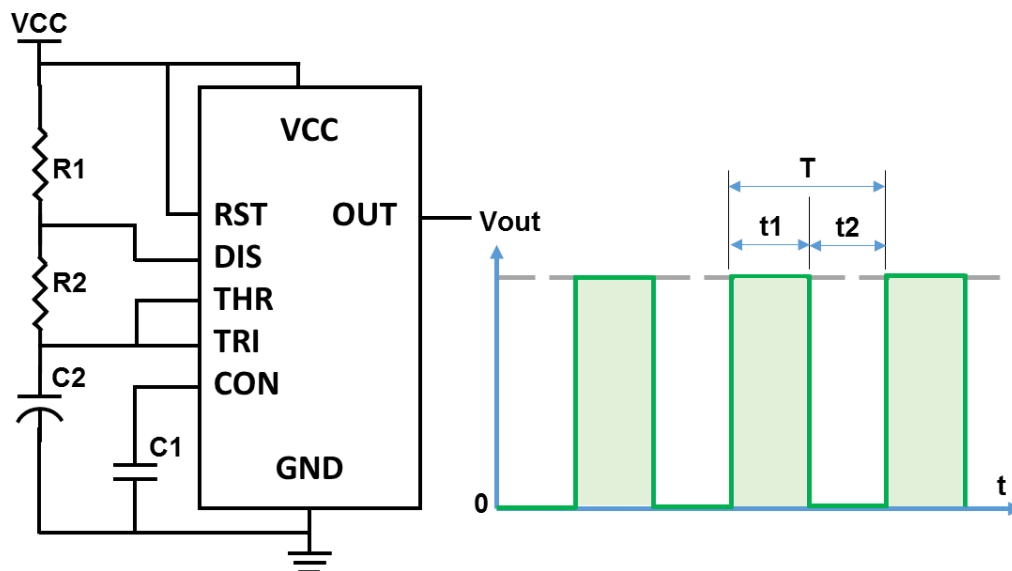


Figure 3-23: Schematic of the timer 555. The total output time is equal to t_1 plus t_2 , and output voltage depends on VCC. The two resistors R1 and R2 are used to control the output frequency.

The output voltage depends on the supply voltage, and can be described as:

$$V_{out} = VCC - 1.5 \quad (3-39)$$

The total output time period T can be calculated from:

$$T = t1 + t2 \quad (3-40)$$

Where t1 and t2 are characterised as:

$$t1 = 0.693 (R1 + R2) \times C2 \quad (3-41)$$

And

$$t2 = 0.693 \times R2 \times C2 \quad (3-42)$$

The frequency strongly depends on the R2 and C2 when the 50% duty cycle is required. In this case, the R1 should be high enough to reduce the opportunity for interference with the C2. Otherwise, it will conflict with the C2 and, as a consequence, the time cycles will not be pure. The equation of the frequency at 50% duty cycle in Hz will be [224]:

$$f = \frac{1}{1.386 \times R2 \times C2} \quad (3-43)$$

There are different options for wave generation, but the crystal oscillator was the right option because the tuning frequency is adjustable, accurate and fixed. This is why it is widely used in electronic devices such as an external clocks.

Coil inductors

Wireless medical devices have coils integrated onto cans/ceramic. In general, there are two types of coil for prototype devices: printed circuit coils (circular or square shaped), and normal copper wires on circular shaped forms. A square shaped printed circuit board (PCB) coil was designed. Nine coils were printed on one PCB, and the coils were different in some turns and this had different inductance. The middle value of the inductance for coil number five was 4.8 μ H. The PCB coil layout and the sample are shown in Appendix C.

The National Instrument (NI) Ultiboard software package was used to design the coil, which was printed at Newcastle University by the electronic technician. For the physical dimensions and calculation, the Saturn PCB toolkit version 7.02 was used. The parameters of the square printed coil are listed in Table 3-2.

Table 3-2: Parameters of the printed circuit

Some turns (N):	16
Conductor spacing (μm):	10
Conductor width (μm):	100
The outer diameter (mm):	20
Inner diameter (mm):	1.782
Fill factor (μm):	0.0576
Inductance (μH):	4.8
Tested frequency (kHz):	200
Resistance (Ω):	4.2

Coils were also designed with copper wire. For this, a circular shaped coil was selected. The diameter of the coil on the transmitter side should be greater or equal to the receiver coil for efficiency issues. On the transmitter side, again there are design limitations, since, for the current flow on the outside surface area of the wire, the thickness of the wire will affect the current flows because of wire cross sectional resistance. In this case, single core wire is one possible choice. The maximum size of the receiver coil will be 30 mm. Consequently, the transmitter coil will be 30 mm or more. Table 3-3 shows the physical parameter for the transmitter and receiver coils. The coils were fitted on transparent plastic paper.

Table 3-3: Parameters for single and multicore coils.

Properties	Single core	Multicore coil
Number of turns	7	10
Diameter (mm)	40	40
Resistance (m Ω)	112.67	421.31
Quality factor	54.98	20.75
Angle (degree)	+88.958	+87.24
Inductance (μH)	4.93	6.958

Class E power amplifier

Where the system of the WPT is designed, and the delivery was not enough, a power amplifier is required. In this project, to provide power delivery, a class E power was designed. The class E power amplifier operates as a switch rather than a current source. Ideally, current and voltage flows across the transistor and simultaneously they are nonzero. Typically, there should be no power dissipation in a switch. This concept is called soft-switching [225]. The condition of the soft-switch must satisfy the matching network components, which needs to be calculated for inductance L and capacitance C. As shown in Figure 3-24, the imaginary load R is for the transformation network [226].

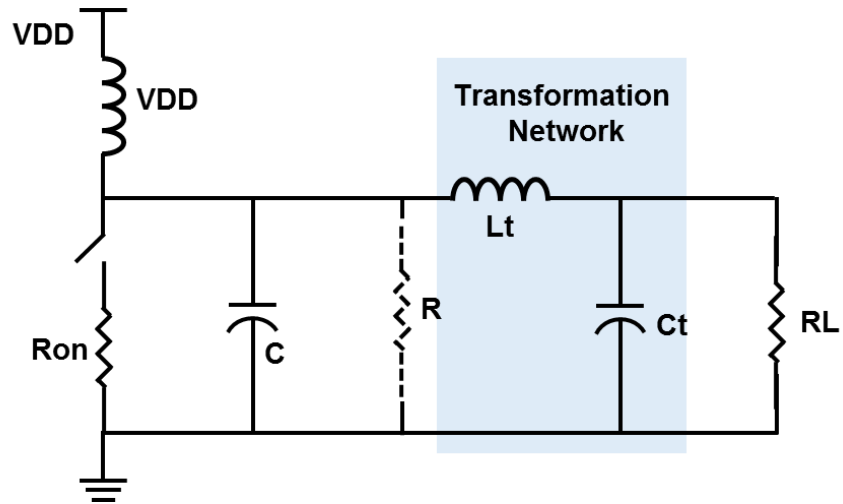


Figure 3-24: The switch performance of the class E power amplifier. The switch represents a transistor. The value of resistance R depends on Lt and Ct.

Both L and C can be described as [215]:

$$L = \frac{1.15 R}{\omega} \quad (3-44)$$

and

$$C = \frac{0.1836}{\omega \cdot R} \quad (3-45)$$

To calculate the class E power amplifier efficiency:

$$\eta = \frac{P_L}{P_L + P_{tr}} \quad (3-46)$$

Where P_L is the output power, and P_{tr} is the dissipated power of the transistor. In this case, the power loss will relate to the power of the resistor R_{on} , only when the switch is in on-mode.

3.3.4 AC to DC converter

A bridge rectifier (full wave rectifier) has been designed to convert the AC voltage to DC voltage. The bridge rectifier is realised by using four diodes as a bridge. The diodes are best connected in a series of pairs. In other words, two diodes will allow current flows in each cycle. More specifically, for the positive cycle, diode D1 and D4 conduct current, while in reverse biased diodes D2 and D3 will conduct current. Capacitor C has a significant role in the circuit, and is called a smoothing capacitor. In Figure 3-25, the red waveform shown is without the capacitor, while the black waveform is after connecting the parallel capacitor to the circuit [218].

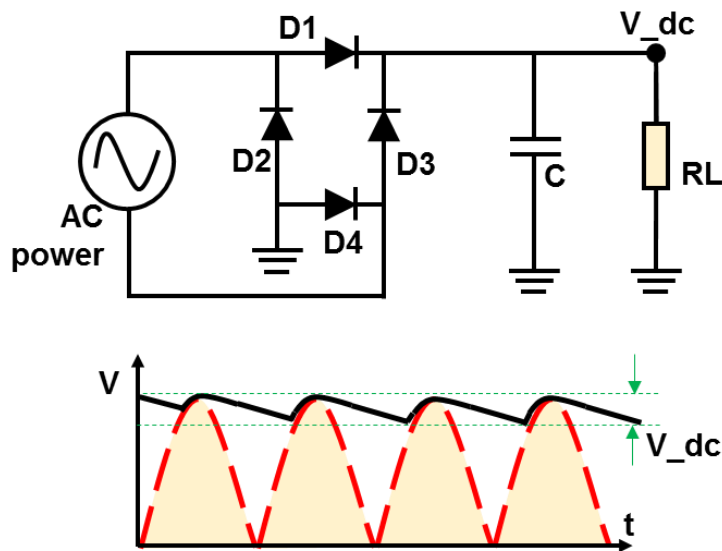


Figure 3-25: The circuit schematic of the voltage rectifier and the result of the output voltage with and without the smoothing capacitor, while the peak of the ripple voltage (V_{dc}) depends on the current across the load resistance to the frequency and smoothing capacitor (bottom waveform).

The Schottky diode was used for this design to reduce the power dissipation. The selected model was NSR05F30NRT5G from the MOUSER Company, and the specifications are listed in Table 3-4.

Table 3-4: Specification of the Schottky diodes used in the AC/DC converter circuit.

Product	Schottky Diodes
Manufacturer Part No	NSR05F30NRT5G
Mounting Style	SMD/SMT
Forward Current (mA)	500
Repetitive Reverse Voltage (V)	30
Forward Voltage (V)	0.4
Forward Surge Current (A)	10
Reverse Current (μA)	75

3.3.5 Voltage regulator

For the implant device, the LT1763CDE was chosen because of its range of input voltages. The regulator was first simulated using NI Multisim software, as shown in Figure 3-26. For the receiver side, a two on the board regulator was implemented on the circuit. Both regulators have the same model but provide a different output voltage. The LT1763CDE-3.3 and LT1763CDE-5.0 provide fixed output voltage. For the implant, 3.3 V is required to operate the microcontroller, flash memory, and JTAG programmer, while 5 V is required to operate the optrodes. The regulators allow current flows up to 500 mA. The circuit schematic for simulation using NI Multisim is shown in Figure 3-26.

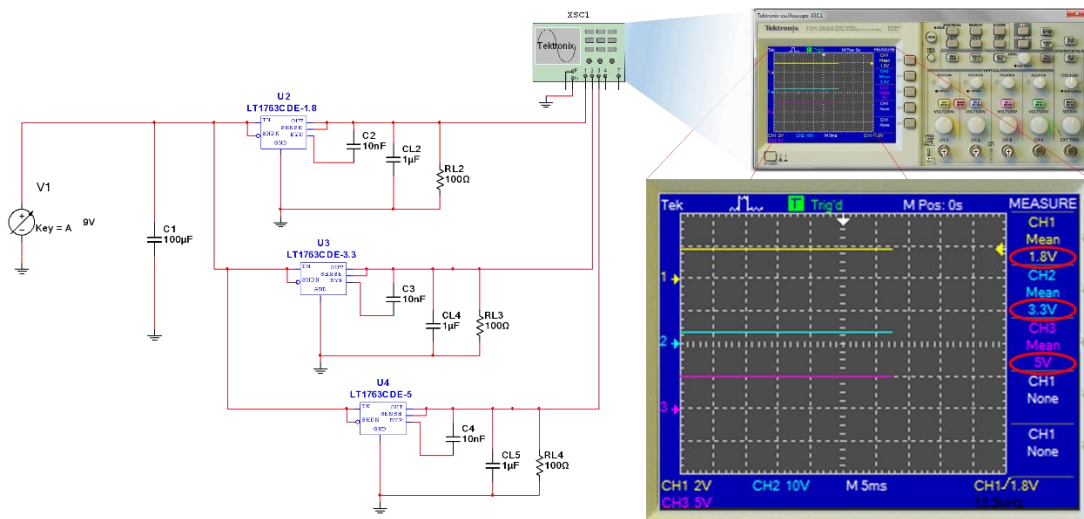


Figure 3-26: Simulation circuit schematic for LT1763CDE-1.8, LT1763CDE-3.3 and LT1763CDE-5 regulators. In this test, the circuit designed for obtaining three outputs as they are 1.8 V, 3.3 V and 5 V.

The circuit was designed to show the performance of the regulator to provide three outputs 1.8 V, 3.3 V and 5 V. The National Instrument Multisim was used for circuit simulation.

3.4 Portion of power consumption

The power consumption of the individual components is shown in Figure 3-27. The portion of the power consumption on the transmitter side is on the left, and for the receiver, the end is on the right. On the transmitter side, the most hungry power device is the Wireless Power Transfer circuit, whereas on the receiver side it is the μ LED. This version of the Raspberry Pi zero includes Bluetooth, which perhaps reduces the power consumption on the transmitter side by replacing the USB Bluetooth adapter and the USB hub.

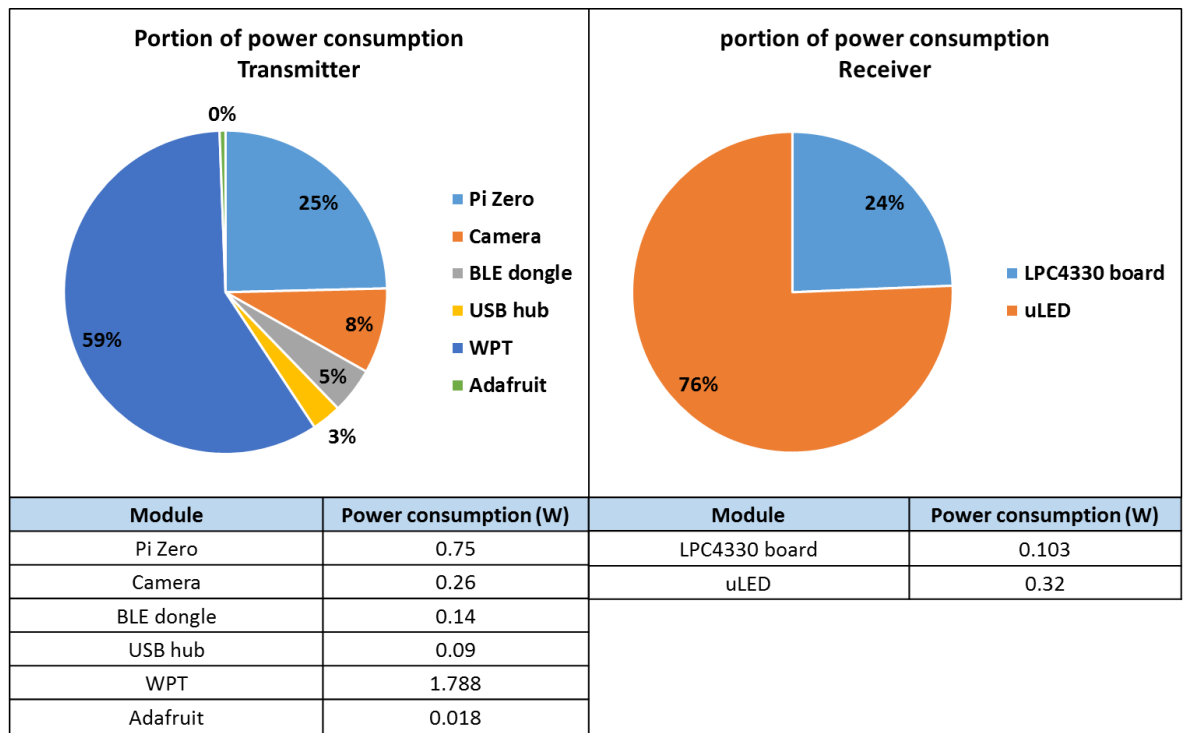


Figure 3-27: Portion of the power consumption for the transmitter side (Left) and the receiver side (right).

In future work, a three dimensional optrode will be used instead if a μ LED matrix on the receiver end for brain cell stimulation. In this case, the power consumption for the stimulator will be changed.

Chapter 4. Real time data transfer

4.1 Software design

Software design is essential in the role of the visual cortical stimulator, and includes three types programming code:

- Code for image processing: code to control and automate the system. Linux commands were used to connect the transmitter and receiver parts automatically via Bluetooth. Also, a push button was added, and a command code was written for this purpose.
- Code for data encodes and decode for communication purpose: this is for image processing in the transmitter side using Matlab Simulink. It includes capturing images from the USB camera, resizing, converting images from RGB to the intensity form, applying the algorithm of the image simplification, and image compression.
- Code for a microcontroller to control the system: on the receiver side, C code was used for receiving data, image decompression, pulse modulation and sending data to the optrodes.

The flow chart of the software design is shown in Figure 4-1. It starts with the original scene and ends with the data being sent to the stimulator.

Original scene: these are the live images captured by the USB camera. The speed of the stream of images is about 25 fps, and can be controlled by the time framing in Matlab and the number of iterations in the next step.

Scene simplification: in this stage, the scene is simplified using image cartoonization, tinted reduced outlined nature (TRON), and edge enhancement algorithms. The significant details in a scene are enhanced, whereas the high frequencies are eliminated.

Entropy: this eliminates any discontinuity in the gradient image and enhances the edge thickness by finding the difference between the current frame and the previous one.

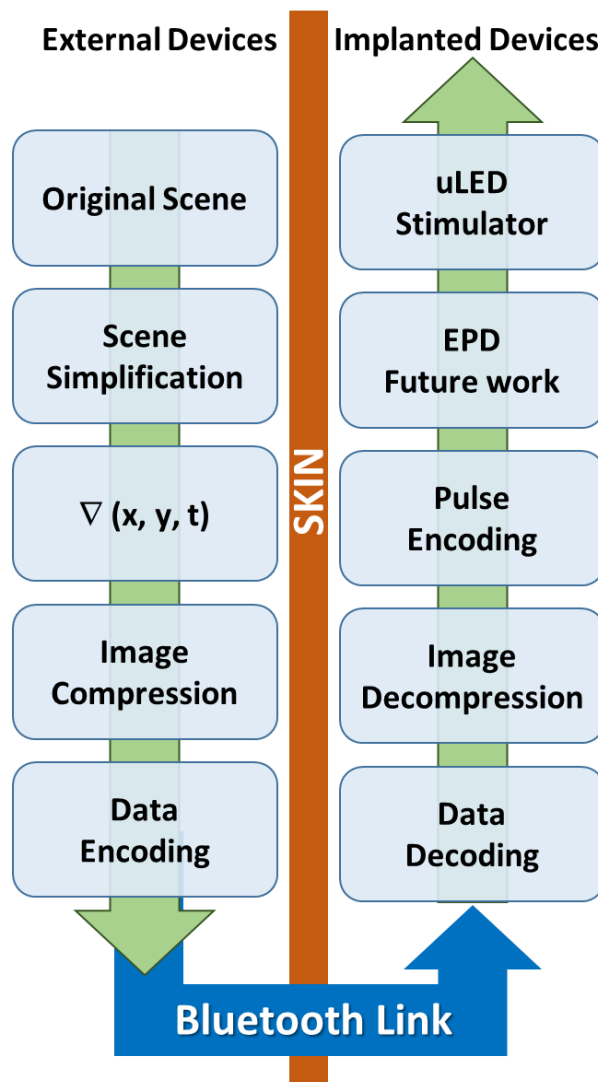


Figure 4-1: The flow of image processing. The external devices start with the camera for capturing live streaming and end with data encoding, while the implant devices start with data decoding and end with the stimulators.

Image compression: this reduces the size of the data transfer, which results in a saving in the communication bandwidth and in turn the power consumed. Basically, this block uses the most common compression technique which is the DCT. This stage of DCT discards the insignificant information so that far less are data transferred, and can be performed in two ways: block or zigzag.

Data encoding: this is rearranging data before sending it wirelessly by resequencing the data into a special format.

Data decoding: *this* is the opposite process of encoding, by converting the formatted encoded data into the original form.

Image decompression: this stage applies the IDCT to restore the image. The decompression is mainly applied to convert the compressed data to the original number of coefficients.

Pulse encoding: this converts each frame into numbers of sub-frames depending on the number of bits used to represent the pulse width modulation to derive the uLED.

Even power distributor (EPD): this represents future work to protect the system from instantaneous high peak power, and distribute power evenly to maintain continuous power delivery.

μ LED stimulator: this essential part of the implant uses 64x64 optrodes to excite (optically) the targeted cortical neurons area.

4.1.1 An overview of retinal processing

The visual processing begins with the retina's the receptive surface inside the back of the eye. Light enters the eye and passes through the layers of cells of the retina, before reaching the photoreceptors located at the back of the retina. Light activates the photoreceptors, which modulate the activity of bipolar cells. These, in turn, connect with the ganglion cells located at the front of the retina. The axons of the ganglion cells form the optic nerve, which carries information to the brain. Two other types of neurons, horizontal cells and amacrine cells, are primarily responsible for lateral interactions within the retina.

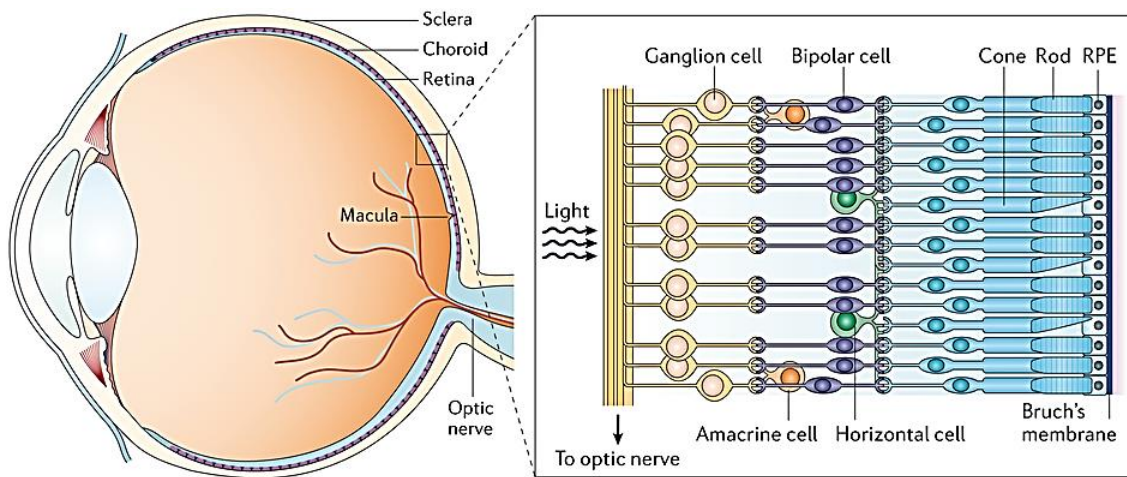


Figure 4-2: The eye and three layers of the retina, including their cell types. The light passes through the outer layer into the inner layer and starts to be absorbed in the inner layer by cones and rods. Signals are sent to the ganglion cells via the bipolar cells. From the bipolar cells, data is forwarded to the optic nerve (image from nature reviews drug discovery [227]).

The bipolar cells and ganglion cells are organised in such a way that each cell responds to a small circular patch of photoreceptors, which defines the cells receptive field. The receptive field of retinal ganglion cells is concentric and consists of a roughly circular central area and a surrounding ring. Retinal ganglion cells have two basic types of receptive fields: ON-centre OFF-surround, and OFF-centre ON-surround, as shown in Figure 4-3. The centre and its surround are antagonistic and tend to cancel each other's activity.

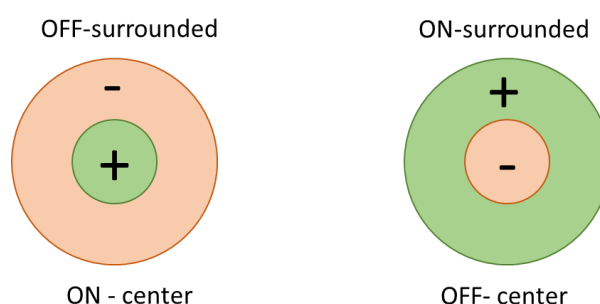


Figure 4-3: The receptive fields in the ganglion layer ON-centre and OFF-surrounded (left), OFF-centre and ON-surrounded (right).

The response of the centre of the ganglion cell to a spot of light is shown in Figure 4-4. When no light falls on the receptive field, the spontaneous level of activity is recorded from the ganglion cell.

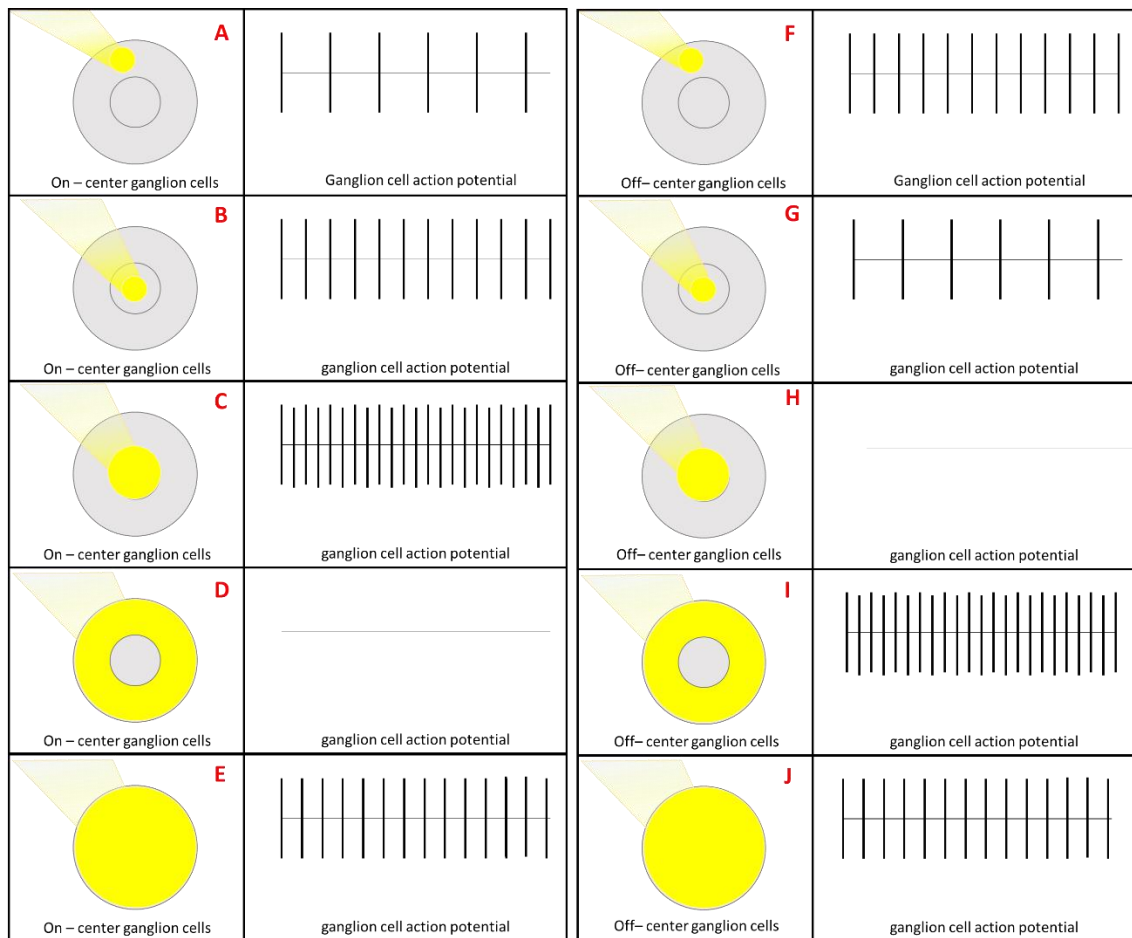


Figure 4-4: The response of an on-centre ganglion cell to a spot of light (A) The light enters the surrounding region of this on-centre ganglion cell and the level of activity in the cell will decrease. (B) A spot of light in the centre of the receptor field increases the firing rate. (C) The maximum response in the on-centre ganglion cell is achieved when the entire centre of the field is illuminated. (D) If only the surrounding of the cell is illuminated with a ring of light, the ganglion cell is maximumly inhibited. (E) Illuminating both the centre and surrounding region means the response is just above the baseline. This occurs because the centre effects are slightly stronger than the surroundings. The response of an off-centre ganglion cell: (F) The light enters the surrounding region of the off-centre ganglion cell. The level of activity recorded in the cell increases. (G) A spot of light in the centre of the receptor field decreases the firing rate. (H) If the entire centre of the off-centre ganglion cell is illuminated, the cell is maximumly inhibited. (I) Maximum response is achieved when the entire surround is eliminated by the receiving field. (J) With the centre ganglion cell, if we illuminate the centre and surrounding region, the response will change very little from a baseline (the concept of the image from neuroscience [228]).

The architecture looks for gradient and thus only differences in illumination result in outputs. To understand the importance of luminous contrast, we can contrast the boundary between light and dark regions. The response rate changes depending on the position of the receptive field, by combining information from adjacent receptive fields, and so the brain can thus construct information about edges and ultimately shapes. Figure 4-5 shows the responses of the hypothetical population on the centre ganglion cell, whose receptors fields are labelled (i) to (v) and distributed across the light-dark edge. Those cells whose activities are most affected have receptive fields whose centre region light is adjacent to the light-dark edge [228].

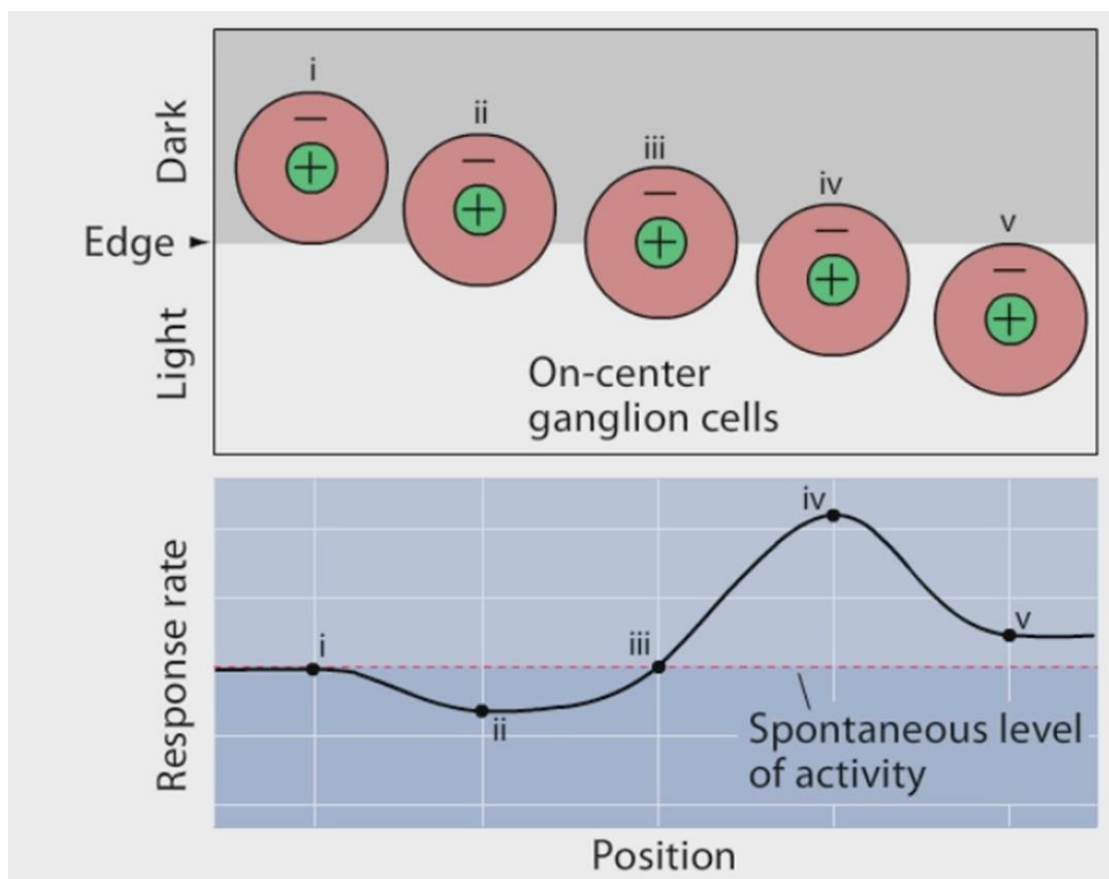


Figure 4-5: Responses of the hypothetical population on the centre ganglion cell. (i) There is no response from the receptor cell. (ii) Response rate below the spontaneous level of activity. (iii) No response. (iv) The highest response rates. (v) There is a response but it is low (image concept from neuroscience [228]).

The information supplied by the retina to the brain does not have equal weight for all parts of the visual scene, but instead emphasises features of the visual scene, such as boundary edges, which convey the most important information.

4.1.2 Image simplification and edge highlighting

The idea behind image simplification techniques is to improve image contrast. Due to the low resolutions of current retina prosthesis devices, chromatic information is not feasible at the moment, although this may change. We therefore focus on the information content of grayscale images. As the effective resolution of the stimulating array is quite small, it is better to present more primitive objects, and thus simple segmented edge weighted objects/scenes are more appropriate.

First, the images need to be simplified by suppressing low importance textures. To achieve this, anisotropic smoothing is used. This algorithm iteratively eliminates noise and low importance textures. However, unlike Gaussian blurring, it reduces the diffusivity at those locations with a larger likelihood of being an edge, i.e. it does not blur them. Mathematically, the process is defined as follows:

$$I(x, y)^{n+1} = I(x, y)^n + \Delta t [(C \cdot \nabla I(x, y)_H) + \nabla(C \cdot I(x, y)_V) + \nabla(C \cdot \nabla I(x, y)_{D1}) + \nabla(C \cdot \nabla I(x, y)_{D2})] \quad (4-1)$$

Where I is the initial unprocessed image pixel value, ∇ is the gradient operator, and C is the diffusion coefficient. n is the iteration number, Δt is the time step which controls the accuracy and speed of smoothing, and ∇I_H and, ∇I_V , ∇I_{D1} , and ∇I_{D2} represent the horizontal (H), vertical (V), and two diagonal (D) gradients of the image pixel. The simplification process is continuous until the following equation is satisfied:

$$D = \sum_{k=1}^n a_k - PT \quad (4-2)$$

Where D is the energy deficit in an image, a_k is the intensity of k^{th} led, P is the power budget (number of LEDs in ON state at the same time) and T is the frame time. As can be observed from (eq 2), if D is positive it means more simplification is required unless the image fits into the energy budget.

As with most detailed image processing algorithms, optimal parameters will vary with user preference. In the case of anisotropic diffusion, the key parameters are the number of iterations n . Smaller n results in more textures remaining; larger n leads to greater smoothing, which eventually also removes larger edge components, i.e. the image becomes blurred. However, eventually increasing n will consequentially increase the energy deficiency of the image, and so equation two controls this process.

Once the anisotropic simplification is complete, we extract the spatio-temporal gradients of the image:

$$\nabla I(x, y) = \sqrt{(\nabla_H I(x, y)_s)^2 + (\nabla_V I(x, y)_s)^2} \quad (4-3)$$

Where I_s is the simplified image. For still images, we simply use the spatial derivatives. To increase edge thickness and remove any discontinuity in the gradient image, we convolve it with a Gaussian filter and normalise it between 0 and 1. We then define two threshold values, τ_{min} , τ_{max} and set all pixels of the normalized gradient image below τ_{min} to 0 and all the pixels above τ_{max} are set to 1 according to how much denser the edges need to be.

To generate an edge-weighted image, we define a threshold value K below which all the pixels in the normalised gradient image will be raised to K . The value of K determines how much of the background information of the image needs to be reserved, and this can be determined according to patient preference. The gradient image now becomes a weighting matrix W , which will determine how many details of the visible image will be reserved while also increasing the brightness of the relevant edges. The edge-weighted image is then defined as the multiplication of W by the anisotropically simplified image:

$$\text{Edge weighted} = W * I^{n+1}$$

(4-4)

Raspberry Pi Zero was programmed and deployed with Matlab Simulink for this purpose. Matlab function code is shown in Appendix number missing for image processing by Al-Atabany, with some improvement [82]. Then the code was modified after adding a compression algorithm for the image compression. The code was written to print the outcomes on the screen in Raspberry Pi. The result was redirected by writing some codes in Linux to send it via Bluetooth.

4.1.3 Image compression

The system is designed to deliver live streaming and real time images to the brain cells. For live streaming, 25 frames per second are normally required [229]. An example of the image size is 64x64 pixels. In other words, the size of images is approximately 4,000 pixels, equivalent to 4 Kbyte of data. This number is limited to the lowest visual perception for the human eye. The achieved baud rate for the Bluetooth was 170 Kbps, and so the 25 fps of the 4 KB image are equal to 100 KB, which is higher than the capability of Bluetooth. For this reason, the images should be compressed up to 61%. Effectively, this is a simplified motion JPEG method.

There are two techniques which can be used for image compression. The two algorithms are DCT-block and DCT-Zigzag. As shown in Figure 4-6, after the image has been simplified, the steps of image compression using the DCT-block are as follows:

- a) Reduce the size of the simplified image to 64x64
- b) Divide the image into 8x8 blocks
- c) Rearrange the 8x8 blocks from 2D sequence to 1D
- d) Apply the DCT algorithm to each 8x8 block
- e) Select 5x5 blocks from the low frequency level
- f) Reshape the 5x5 blocks from 1D sequence to 2D
- g) End with a 40x40 pixel compressed image.

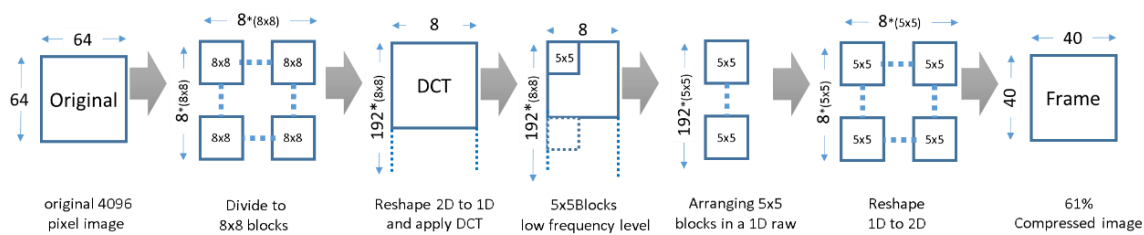


Figure 4-6: The steps of the image compression using the DCT-block. Matlab Simulink was used to implement the code to the LPC4330 microcontroller. This example is for 61% compression ratio.

The special header will be added to the compressed image for the design purpose. Then the data were printed on the screen in the Raspberry Pi Zero. Later, the data will be redirected and sent to the implant device over the Bluetooth. For this, the Linux command was written. In the command was linked to the push button for turning the system on/off. When the button is pressed and then released, the Raspberry is powered, and then the Bluetooth connects automatically to the implanted Bluetooth. Finally, the camera starts capturing real time images and sends over Bluetooth.

4.1.4 Image decompression

After the data has been delivered to the implanted device, the compressed information needs to decompress to restore the simplified image. Figure 4-7 shows the decompressed image, and the details are as follows:

- The 40x40 compressed image is collected over Bluetooth
- The image is divided into 5x5 blocks
- The 5x5 block sequence is reshaped from 2D to 1D
- Each 5x5 block is completed with zeros to make 8x8 blocks
- The IDCT is applied to each 8x8 block

f) The 8x8 block sequence is reshaped from 1D to 2D

g) The 64x64 image is the restored image.

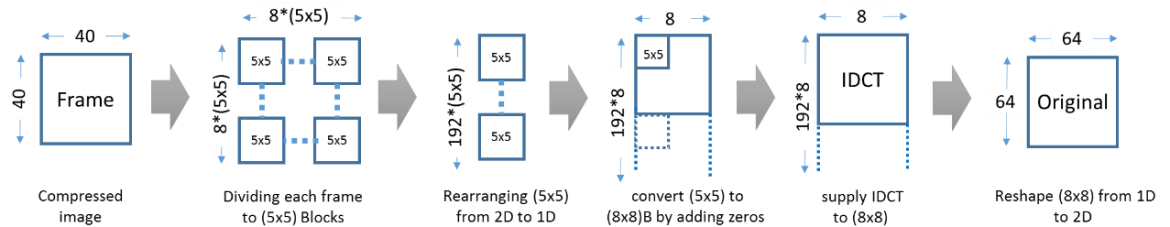


Figure 4-7: Image decompression steps using the DCT-block. Matlab Simulink was used to implement the code in the LPC4330 microcontroller. This example is for 61% of the compression ratio.

The images need to be converted to sub-frames and sent to the optrodes; the number of sub-frames will determine the intensity level of the optrodes.

4.1.5 Pulse modulation

Rather than the activation of the on-off LED, the pulse coding stage offers different levels of intensity to evoke a pixel in the visual space. It suggests that the intensity modulation should be varied using a pulse width modulation technique. The pulse width is subject to the efficiency of the μ LED and the Channel-rhodopsin 2 (ChR2). In fact, this is important because it gives us the flexibility to control the LED's brightness when conducting clinical trials. In other words, it allows us to determine how bright (and consequently how much current) a spot has to be so that the subject can observe it.

The value of each pixel varies between 0-255 characters. This value represents the intensity level. For pulse modulation, the number of sub-frames determines the intensity level of the optrodes, and the number of frames can be found by:

$$\text{Number of subframes} = 2^n \quad (4-5)$$

where n is the number of bits for each pixel.

For example, for $n=5$, the number of subframes is 32. The maximum number of subframes is 256, which creates the highest intensity level that can be sent to the μ LED/optrodes.

4.2 Visual information system

For the visual information system, the hardware components include the USB camera, the embedded processor, and the data link. The block diagram for this is shown in Figure 4-8.

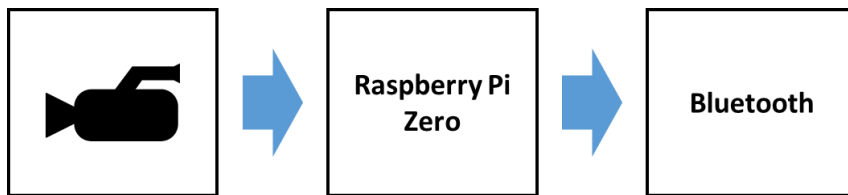


Figure 4-8: The block diagram of the hardware of the transmitter part for the visual information system. The system consists of a camera, Raspberry Pi Zero, and Bluetooth.

The details of the components of the transmitter are explained in the following subsections.

4.2.1 Camera

The camera has a significant role in this project, and quality and power consumption are two important factors in selecting the right camera. A good quality camera will give the designer a wide selection of lower level image quality, while low power consumption will keep the overall power consumption of the system down. The camera needs to be small to allow the user to mount the camera in a headset, and so a lightweight one is preferred. For this project, the Logitech C270 720p HD Webcam camera model was selected. The maximum power consumption for the camera is 260 mW in running mode,

and it is compatible with the Raspberry Pi Zero. It supports face tracking, which may be useful in future work. The main useful feature of the camera is that it works in dim light. The camera is shown in Figure 4-9.



Figure 4-9: Logitech C270 720p HD Webcam is used on the transmitter side for live video streaming.

In the assembly step, the original cover of the camera was removed to mount the camera in the eyeglass designed for this project.

4.2.2 Embedded processor

On the transmitter side, the mini processor plays an important role in image processing and data transmission. It should be able to hold the algorithm of the image processing and send data to the serial port at the same meantime. Normally, the mini processor will consume high power in visual prosthetic systems, and so selecting a low power consumption and an efficient device is a major choice. The Raspberry Pi Zero is shown in the Appendix – J was the right choice for this. The general specifications are as follows [230]:

- Generation: PCB version 1.3
- Architecture: ARMv6Z (32-bit)
- System on chip: Broadcom BCM2835
- Central Processing Unit: 1 GHz single-core ARM1176JZF-S
- Size: 65 mm × 30 mm × 5 mm

- Weight: 9 g
- USB 2.0 ports: 1 Micro-USB (direct from BCM2835 chip)
- Power rating: 700-800 mW.

At the end of this PhD, a new version of the Raspberry Pi Zero became available with built in Bluetooth, and this will miniaturise the board further.

The Raspberry Pi supports Matlab for programming. Matlab Simulink was used to implement the image processing code. The required components connected to the Raspberry Pi for image processing were the USB Bluetooth and camera modules.

4.2.3 Microcontroller

A microcontroller is defined as a microcomputer fabricated on a single chip [231]. Furthermore, like a microprocessor, it is available in different word lengths from 4 bit to 128 bit. Today, most electronic devices have microcontrollers to operate components such as storage and communication, and are on display. Moreover, they are widely used in industry in cars and also in computer hardware devices such as a mouse and keyboard.

The microcontroller usually contains the following components: a central processing unit, random access memory, read only memory, input/output ports, analogue to digital converters, interrupt controls, serial interfacing ports, oscillatory circuits and timers and counters. Figure 4-10 shows the block diagram and the basic structure of the microcontroller [232].

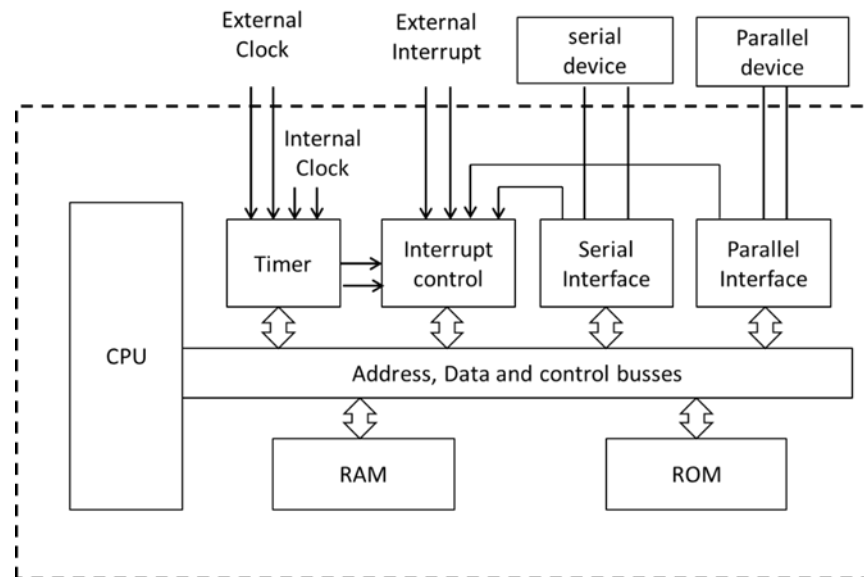


Figure 4-10: Block diagram of the microcontroller architecture. In general, microcontrollers consist of a central processing unit (CPU), random access memory (RAM), read only memory (ROM), internal clock and port interfacing with external devices (image from eBook titled Digital System Design –Use of Microcontrollers [233])

For the development of medical implant devices, selecting the right microcontroller is a critical phase. The wrong microcontroller can result in a long development time and complicated firmware. Therefore, different microcontrollers from different companies were investigated and studied. These include OMAP138, XMOS, SAMA5D4, BCM2836 SoC, ARM Cortex M0 and MK64FN1M0VLL12 MCU. Table 4-1 shows a comparison of the factors between these microcontrollers. As we can see from the table, ARM-Cortex-M0 and SAMA5D4 have the lowest power consumption. However, these microcontrollers do not support DSP processing, which means they are not powerful enough to perform image processing algorithms. On the other hand, OMAP138, XS1-L4A-64-TQ48, and BCM2835 have high power consumption, even though they have a DSP processor. This leaves us with MK64FN1M0VLL12, which seems a good compromise that includes DSP and has relatively low power consumption. The main features of this microcontroller are 1 MB Flash memory, 256 kB SRAM and 66 input/output GPIOs [234].

Table 4-1: Comparison between highlighted microcontrollers for MID purpose

Microcontroller	Processor dimensions (mm)	System CLK (MHz)	Power consumption (mW)	DSP	Core
OMAP138 [235]	16x16	375	479.73	Yes	ARM926EJ-S
XS1-L4A-64-TQ48	9x9	400	660	Yes	XMOS
SAMA5D4 [237]	16x16	500	150	No	ARM Cortex-A5
BCM2836 [238]	12.3x12.3	900	700	No	ARM Cortex-A7
ARM Cortex M0 [239]	7x7	48	29.7	No	ARM
MK64FN1M0VLL12	14x14	120	160	Yes	ARM
LPC4330 [241]	9x9	204	80	Yes	ARM

In the first design for version one, the MK64FN1M0VLL12 microcontroller was used and tested. The result is shown in chapter 5. Then, for the second version, the LPC4330 was adopted because its advantages. The details of designing the PCB, compared with both microcontrollers, and highlighting the advantage of LPC4330, are described in the next chapter.

4.2.4 Data link

Bluetooth is a common communication protocol used for medical purposes. Numerous medical devices use Bluetooth as a data link protocol. Table 4-2 gives examples of the medical devices that use Bluetooth and their manufacturers.

Table 4-2: Examples of available medical devices communicating with Bluetooth [37]

Device types	Manufacturer	Models
Blood Pressure	A&D	UA-767PBT-C
	Omron	Home Blood Pressure
Glucose Meter	Roche	Accu-Check Smart Pix
Pedometer	Omron	Pedometer with Bluetooth docking
Pulse oximeter	Nonin	PalmSAT 2500
	Nonin	Onyx II 9560 Fingertip
Weighing Scales	A&D	UC-321PBT-C
	Omron	Weighing scales with body composition

Bluetooth was selected for communication with the implant. On the transmitter side, a Plugable USB Bluetooth Adapter was used, and on the receiver side the HC05 Bluetooth module was used. On the transmitter side, a USB dongle was connected via the USB hub to the Raspberry Pi Zero because it has only one USB connection for data, while the HC05 was directly soldered to the implanted board. The connections between the two modules were configured by writing a command line in Linux.

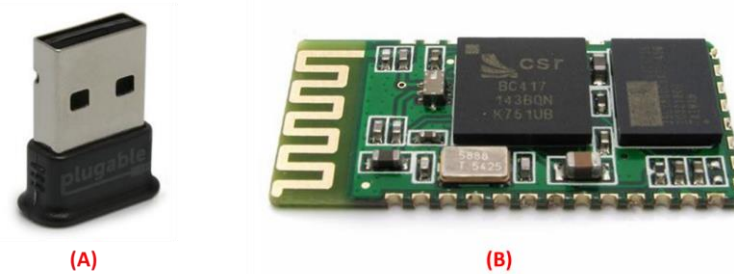


Figure 4-11: (A) Bluetooth 4.0 adapter model Plugable USB 2.0. It is used on the transmitter side, and it supports all Raspberry Pi models. It is compatible with classic Bluetooth [242]. (B) The HC05 Bluetooth module for the receiver side. The board is soldered to the implanted board.

The Bluetooth module on the transmitter side is programmed to connect and send data automatically. The Linux command code is written to search and connect to the receiver coil. Then the Raspberry Pi Zero is programmed to send data over Bluetooth.

4.3 Software configuration

In this section, the details of live video streaming over Bluetooth are presented. This consists of live scene capturing, image simplification, image compression, data transfer over BLE, image decompression, an even power distributor and image encoding, to be displayed on the μ LED. Image encoding will be used later for optogenetic brain cell stimulation.

First, the real-time images were captured by the camera mounted on the glasses. The standard resolution for the coloured images was set at 640x480. Then, the images were resized to 64x64, and after separating the RGB colours were converted to the grayscale intensity level. Matlab Simulink was used to programme the transmitter side for image processing, as shown in Figure 4-12.

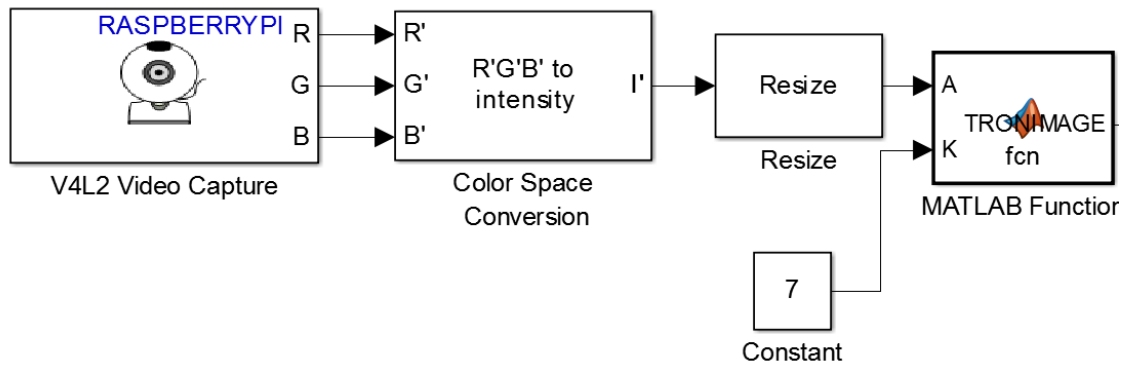


Figure 4-12: The images are converted to grayscale intensity after being captured by the USB camera. Then, the image is resized to 64x64 pixel size and simplified according to the retinal processing.

The images were simplified, compressed and sent over Bluetooth. Image processing and transfer protocol are illustrated in the block diagram shown in Figure 4-13.

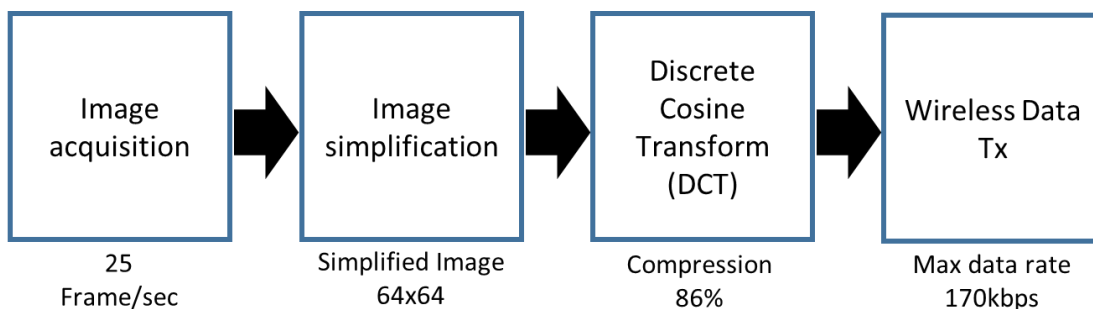


Figure 4-13: Block diagram showing the image processing on the transmitter side.

On the receiver side, the compressed images are received via Bluetooth connection to the microcontroller. Then, the compressed images are decompressed and returned to

their original state. The image processing steps are presented as a block diagram shown in Figure 4-14. The images are converted to sub-frames to perform pulse modulation, and the sub-frames vary from 0 to 255.

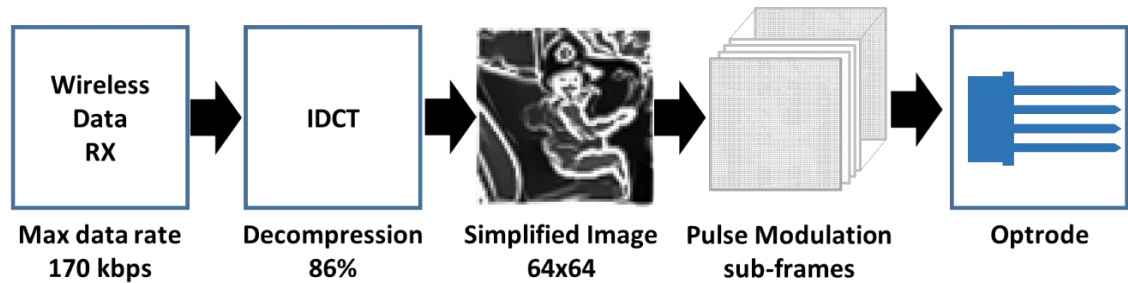


Figure 4-14: Block diagrams of the image processing on the receiver side. The compressed images restored to the simplified image. Then, conversion of an individual image to pulse mode, and transition to the optrode.

4.3.1 Image acquisition

The size of coloured images is 640x480 pixels after capture. The RGB images are converted into grayscale intensity using Matlab Simulink to Intensity. Then, they are resized to 64x64 pixels.

4.3.2 Image simplification

Live streaming of 25 frames per second is captured from the Logitech camera mounted on the glasses. Raspberry Pi Zero is used for image processing on the transmitter side. The image was resized into 64x64 before applying the algorithm of image simplification. A few stages are applied for image simplification and retinal processing. Examples of image simplification are shown in Figure 4-15, including cartoonization and edge highlighting.

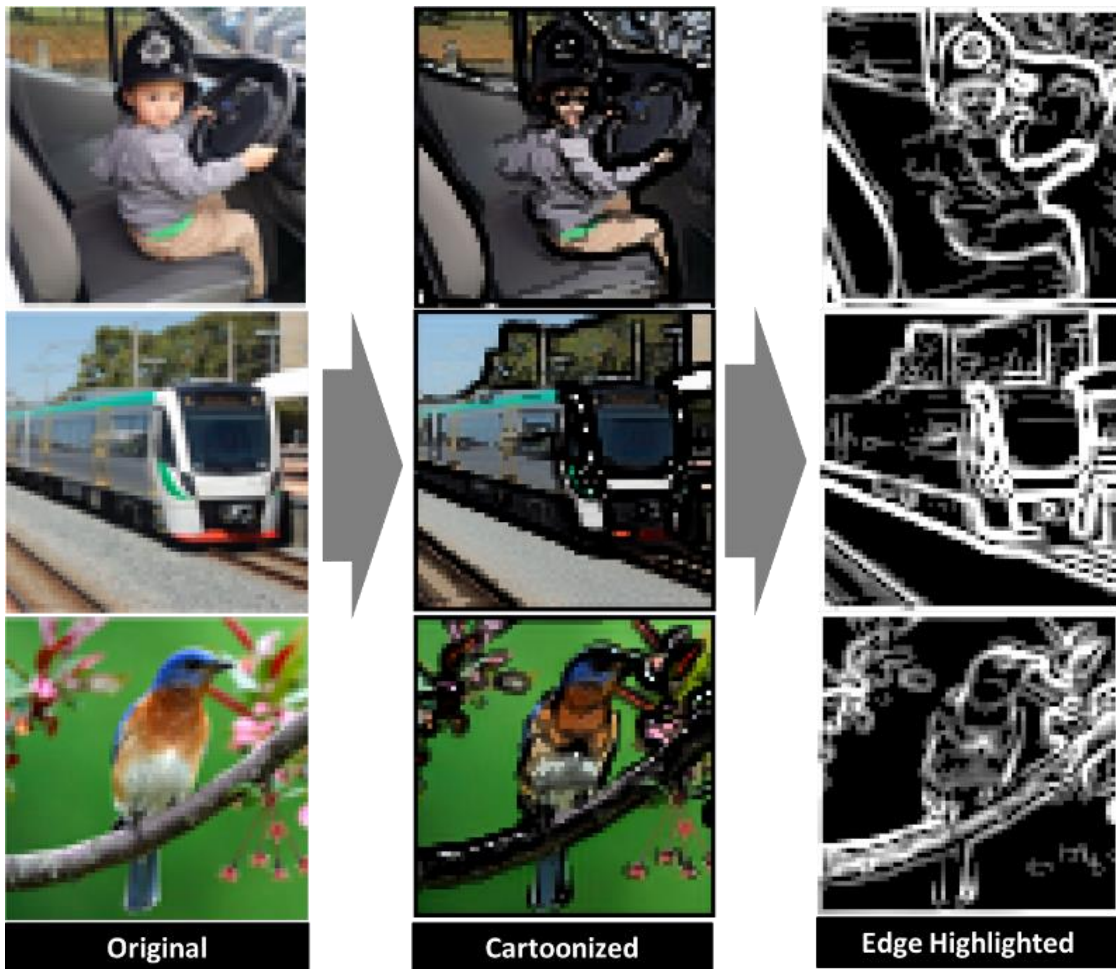


Figure 4-15: Example of image processing steps on the transmitter side, consisting of image simplification that includes image cartoonization and edge highlighting. The size of the images is 4096 bytes, which means 64x64 pixels.

The iteration level was adjusted to obtain a better quality of image and stream of 25 fps. There is a significant relation between frames per second, number of iterations and the quality of the image, as shown in Figure 4-16.

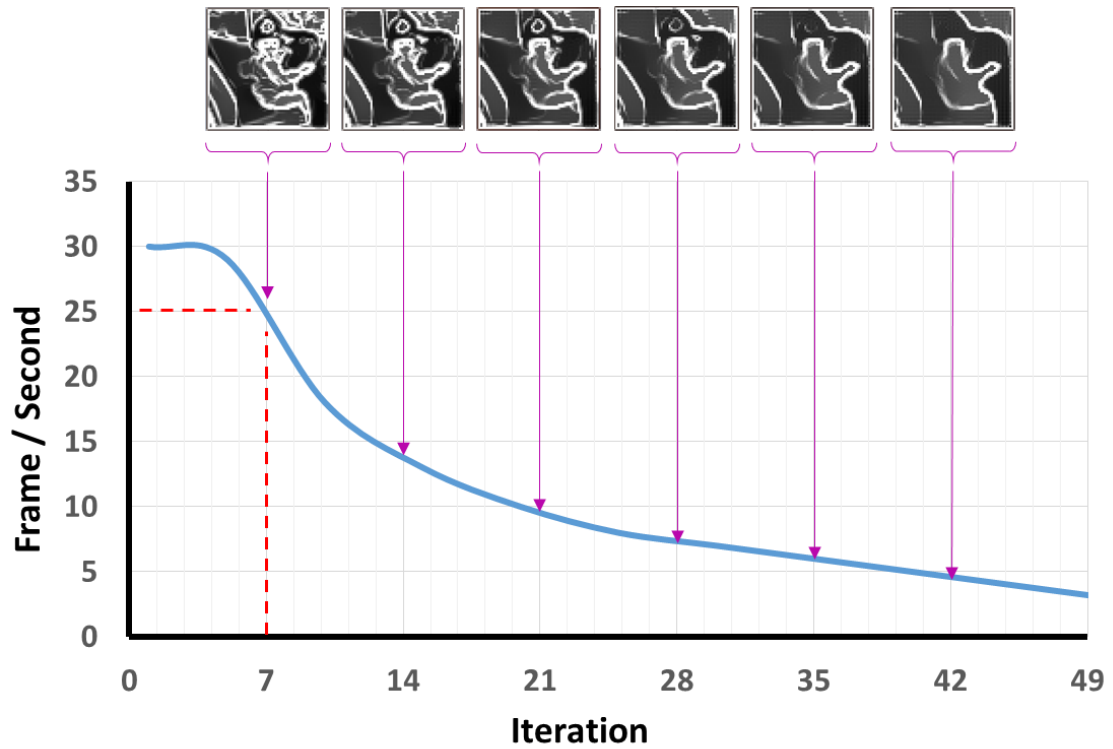


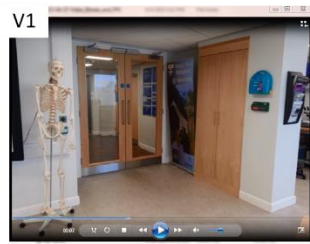
Figure 4-16: Relationship between the number of iterations, the number of images per second, and the quality of images. Better quality is in the lower number of iterations region, and for the 25 frames per second, the number of iterations is equal to 7.

4.3.3 Data analysis

The purpose of the visual cortical implant device is to restore the sight of blind people, who will carry the device around. Different and mixed scenes were expected for AIMD to be captured in the streaming videos. Certainly, users will wear it everywhere in their daily life. Five different videos were recorded as exemplary scenes:

1. in the biomedical lab to show natural light sources mixed with the electrical light source for different backgrounds
2. in the corridor, which represents only industrial light source
3. inside a lift, representing a dim light background
4. a location with a complex background of nature
5. a normal video for the nature of various backgrounds

Screenshot samples of these video types are shown in Figure 4-17.



V1 was taken in the lab
(light bulb and natural light are exist)
21sec, 8.13 MB



V2 was taken in the corridors
(near to your office) just light bulb
21sec, 8.36 MB



V3 was taken inside the elevator
(was dark with dim light)
21sec, 8.84 MB

640X480



V4 was taken for green area and
flowers only (natural outside)
21sec, 8.26 MB



V5 was taken in the garden
(garden, trees and sky , more general)
21sec, 8.32 MB

Figure 4-17: Five videos for data analysis. They were taken with different backgrounds and different light sources. The length of each video is 21 sec. A mobile phone Samsung Galaxy Note II was used to capture these scenes.

The purpose of recording different scenes was to obtain a better understanding of the data rate. The Bluetooth data link is limited to below 170 Kbps for sustained signals. The original frame size of the recorded coloured videos was 640x480 pixels. First, they were converted to the grayscale level, and then the frame size was resized to different frame sizes of 256, 1024, 4096, 9216, 17424 and 65536 pixels, as shown Figure 4-18.

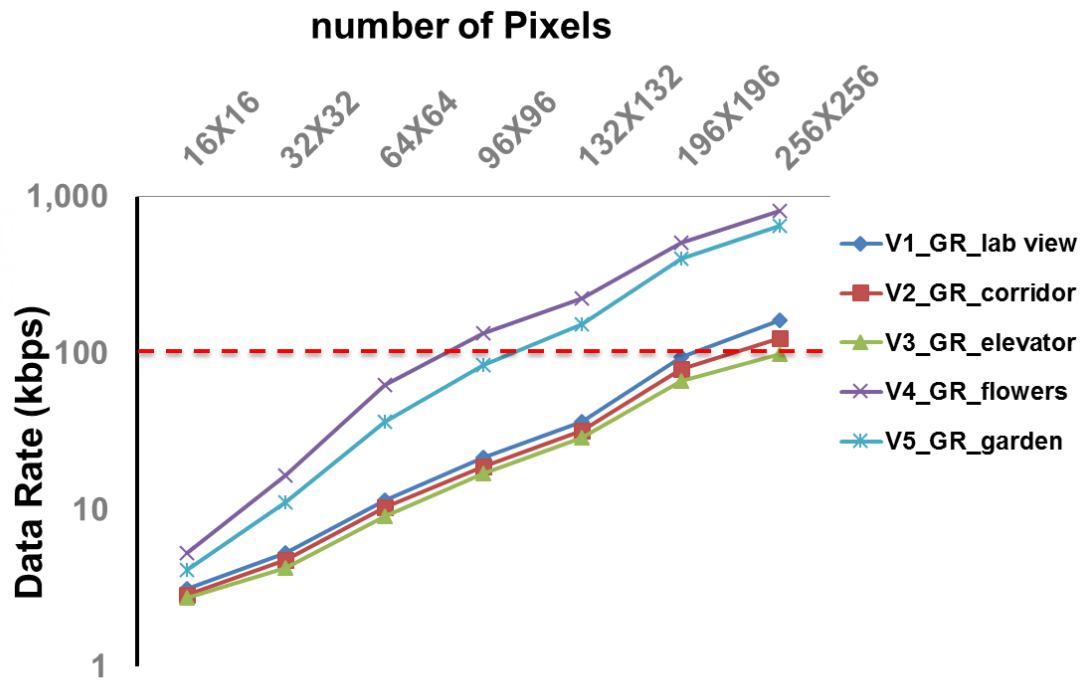


Figure 4-18: Relationship between the data rate and the number of pixels for different backgrounds. There is a noticeable shift for the videos with natural light backgrounds.

Both natural background and sunlight limit the acceptable size for image transmission via Bluetooth to 4,096 pixels and lower. Other video frame sizes can increase up to 17,424 pixels. The data reported here appear to support the assumption that sunlight affects the size of data. As a result, sunlight has a direct effect on the size of images.

4.3.4 Image compression

The images are compressed after they have been simplified at a ratio of 86%. For image compression, images are divided into 8x8 blocks, and DCT_BLOCKS is applied to each block in one image. Later, from each 8x8 block, a 3x3 matrix is adopted in the low-level frequency region. By using this technique, the original image is compressed from 64x64 pixels into the 24x24 pixels, at a ratio of 86%. The data in each image after the previous process is shifted and sequenced into character codes in the range [44, 253]. Then, in each frame, the first pixel is replaced from the original character number into the specific character number 254 as the special header in this case.

Table 4-3: Examples of the image compression.

Case of study	Size of image before compression (Byte)	Size of image after compression (Byte)	CR %
1	4096	4096	0
2	4096	1024	75
3	4096	576	86
4	4096	256	93

CR: Compression Ratio

Details of image compression using Matlab Simulink are shown in Appendix E.

4.3.5 Data link

Bluetooth was used to communicate with the implant device, and the maximum data rate achieved was 170 Kbps. The bit error was checked between the transmitter and receiver end, and had a range of approximately 10 cm as a proof of concept. The result shows no difference between the transmitted and received data, as shown in Appendix F. The test bench setup for two-way communication between the Tx and Rx is shown in Figure 4-19.

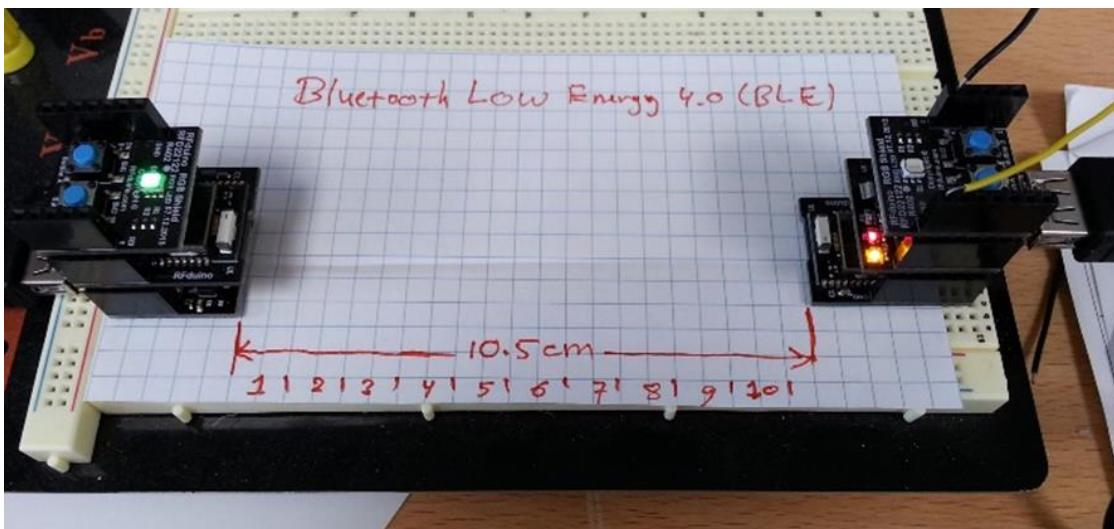


Figure 4-19: The novel two-way communication through the air using Bluetooth between two RFduino. RFduino is an example of Bluetooth 4.0 and Bluetooth Low Energy (BLE). The test was repeated by sending the data through water and pork.

The experimental rig was used to test communication through pork and water, as shown

in Figure 4-20. The data are sent from the transmitter board (Tx) fixed on a stainless steel rod. When the receiver board (Rx) inside a Faraday cage receives the data, it sends the data back outside. The data are then gathered by the Tx. From the result, there is no data loss for the distance of up to 35 mm.

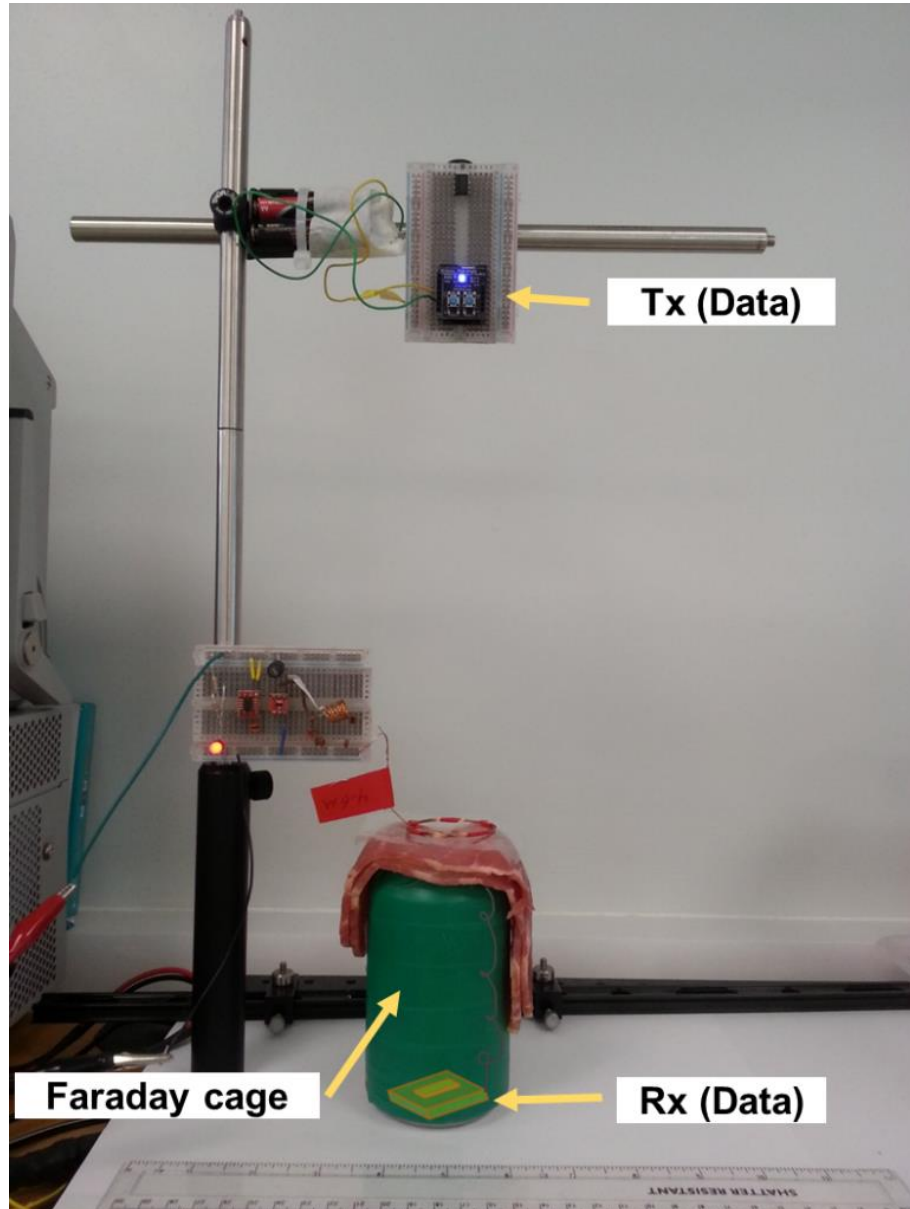


Figure 4-20: Experimental rig with Faraday cage to measure wireless data and power transfer through pork. The implanted device (inside the cage) is powered wirelessly. The Transmitter RFduino is fixed on a rod at 25 cm distance from the Rx, and it is powered by a battery source.

Three different communication protocols in three different devices were tested: the USB Bluetooth model was Plugable, the nRF9E5 from the NORDIC company was run at 868/915 MHz, and the CC2430EM from Texas Instruments was run at 2.45 GHz. The practical result for the maximum baud rate using Plugable was 170 kbps, which is higher than others, as shown in Table 4-4.

Table 4-4: Comparison results for different communication protocols.

Parameter	Plugable	nRF9E5	CC2430EM
Packet size (Byte)	1-32	1-32	1-32
Tx Output power (dBm)	21	-(10) – 20	(-2) – 10
Modulation	GFSK	FSK, MSK, GFSK	GFSK
Baud Rate (Kbps)	170	80	50
Average BER %	0.1%	0.1%	0.1%

4.3.6 Image decompression

Compressed data sized 576 pixels are decompressed into 4,096 pixels using C programming language cross-compiled for the microcontroller. The decompression procedure is applied to each frame by dividing it into 3x3 blocks; then each block is converted to 8x8 by adding zeros. The IDCT is applied to 8x8 blocks to obtain the normal pixels. Later, the blocks are combined to reconstruct the original frame. To test the quality of images at the receiver end, examples from the live streaming were captured for different compression ratios, as shown in Figure 4-21. Square patterns are chosen as an example for image compression and decompression, while the triangular zig-zag patterns are normally used in DCT-jpeg compression.

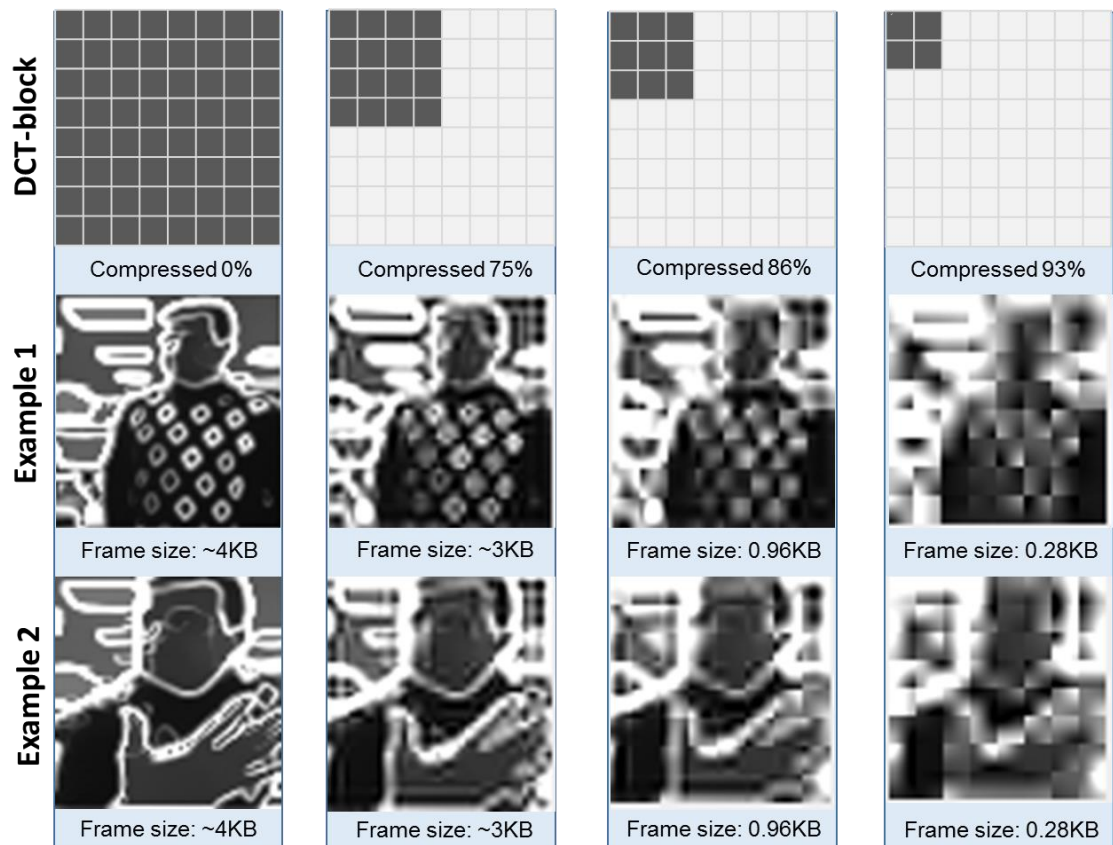


Figure 4-21: Screenshot captured from live streaming for different compression ratios. The DCT-blocks were implemented for image compression. The 2x2 blocks for the 93% compression, 3x3 for the 86% compression and the 4x4 for the 75% image compression.

The five recorded videos were used as an example of image simplification and image compression/decompression. Samples from each video were captured for different compression ratios, as shown in Figure 4-22. For video numbers 1, 2 and 5, the scene was clear for compression rates up to 86%. In videos 3 and 4, the scene was clear for compression rates up to 75%.

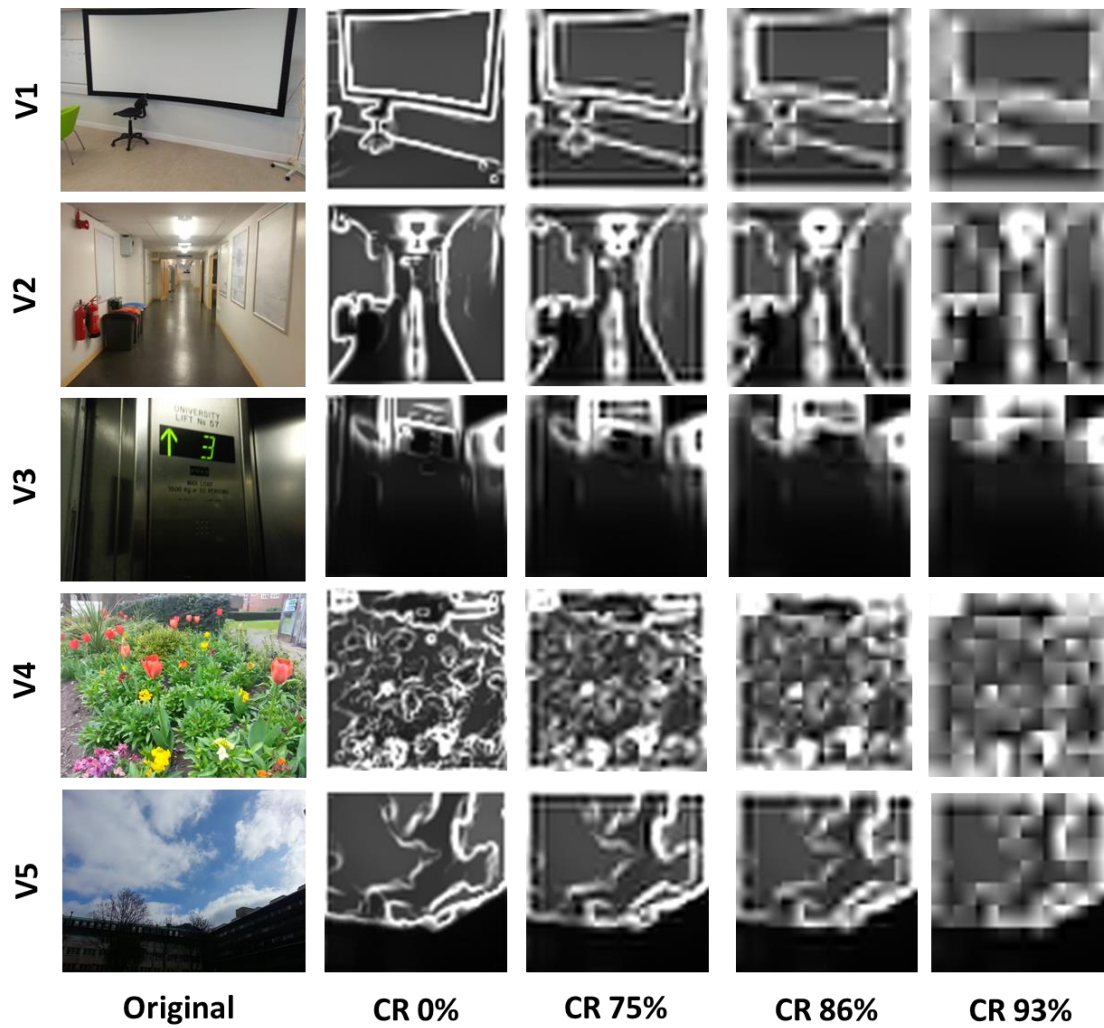


Figure 4-22: The result of image simplification and compression for five recorded videos. V1 was in the lab, V2 was in the corridor, V3 was in the elevator, V4 was in the garden, and V5 was a mixed natural background. In V1, V2 and V5, the scenes can be recognised, with a compression ratio of up to 86%. In V3 and V4, it is clear for up to 75%.

4.3.7 Pulse modulation

The original simplified image was grayscale, where each pixel was represented by 256 intensity levels. If the full range of intensity levels had been chosen, the number of sub-frames would have been 256. However, the microcontroller limitation reduced the intensity level to bits, and in this case the number of sub-frames was 16.

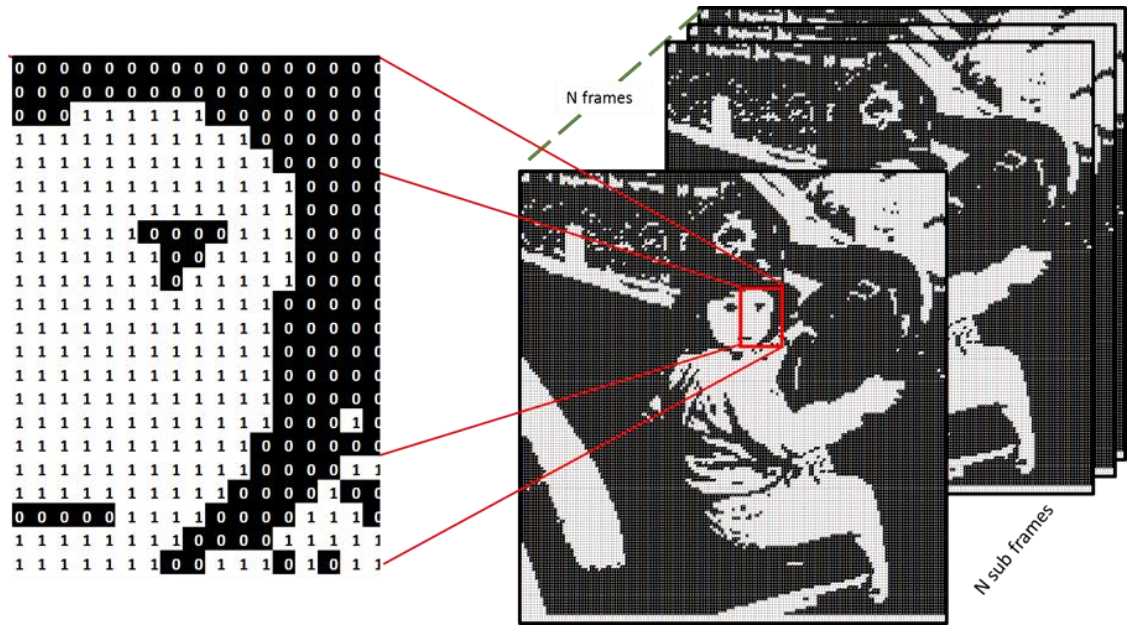


Figure 4-23: Example of sub-frames for pulse-modulation. The number of sub-frames depends on the intensity level requirement for the display on the μ LED matrix/optrodes. In this example, 16 sub-frames were subtracted from 255 frames.

4.3.8 μ LED display

The result of the processed images on the receiver side was sent to the optrode. In this work, a testing μ LED matrix was used as a replacement for the target optrode. The images were displayed on 90x90 matrix size. The original size of the images was 64x64 pixels, but this was resized to 90x90 pixels for showing on the μ LED matrix. Figure 4-24 shows a sample of displayed images tested on the μ LED matrix. To stimulate the brain cells, we will use 3D optrodes.

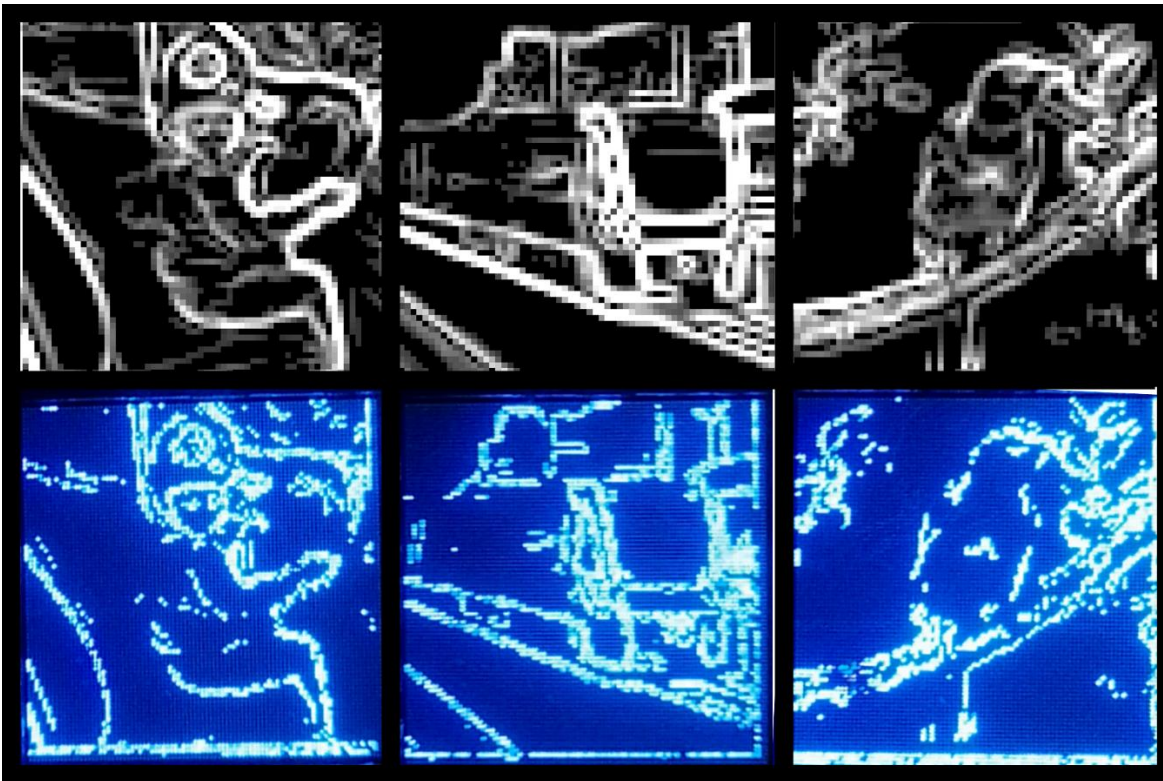


Figure 4-24: A μ LED matrix of 90x90 pixels displaying three examples of images. For testing, the μ LED display was used instead of 3D optrodes. The top row is imaged after simplification and the bottom row shows the examples taken from the μ LED matrix. The images are (Left column) a boy in a fire engine. (Middle column) A train. (Right column) A bird.

4.3.9 Processing requirement

The image processing at the transmitter and receiver side takes time. On the transmitter side, the image processing consists of image simplification and compression. On the receiver end, the following tasks are performed: collecting data from Bluetooth, image decompression, pulse modulation and transfer to the optrodes for display. Figure 4-25 shows a distribution of the total elapsed time for image processing per frame on both sides.

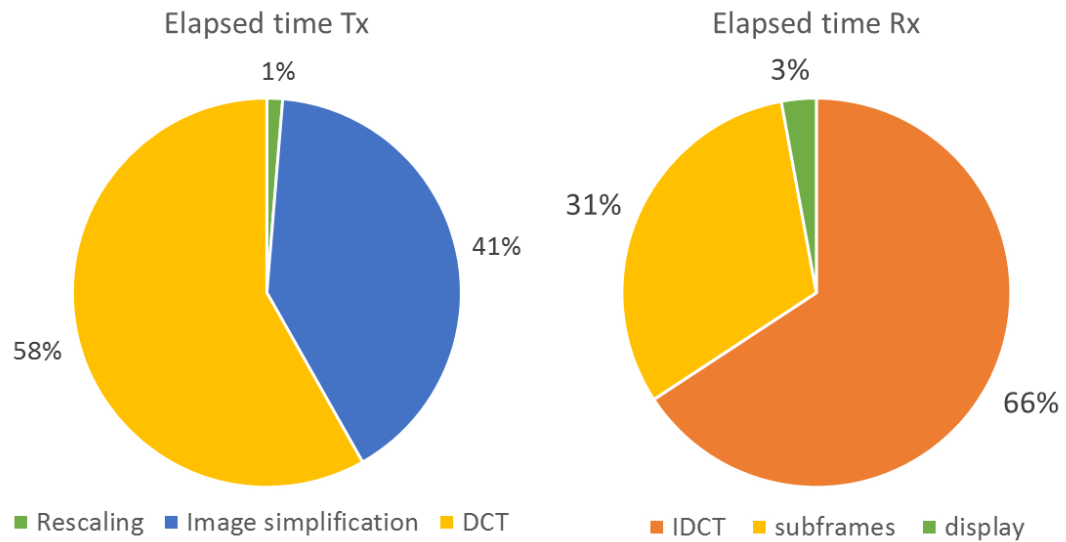


Figure 4-25: Portion of the elapsed time for image processing at the transmitter and receiver side. In the front end processes, the image compression takes longer, and at the receiver, end decompression takes longer.

The transmitter image compression takes more than half the total time, while image rescaling takes less time. Image decompression time is nearly three-quarters of the total time at the receiver side, but less time is needed to send data to the display. The absolute time for each frame it should be no more than 40 ms, for the average of 25 fps.

4.3.10 Implantable microcontroller unit

Medical implant devices in general and especially visual cortical prostheses have necessitated the use of a controller, either on the transmitter side, on the receiver side, or both. On the transmitter side there is no serious limitation, but there is on the receiver side. For this project, numerous microcontrollers were studied and tested for the receiver end. In this case, two microcontrollers from the ARM Company were allocated. The first microcontroller selected was the ARM Cortex M4 MK64FN series. After careful testing, it proved to be insufficient for the final design. Later, a dual-core microcontroller was chosen from the ARM Company of the LPC43xx series, comprising M4 and M0 cores, and this design was more efficient in terms of lower power consumption.

MK64FN1MOVLL12

For primary testing, the ARM microcontroller (MK64FN1MOVLL12) was selected. A further practical step related to fabrication was taken by manufacturing a round-shaped two-layered PCB, using Altium 16.0 software, as shown in Figure 4-26. The diameter and thickness of this PCB are 30 mm and 2.68 mm respectively, and the weight is less than 3 g. At this stage, the wireless power receiver was not added to the board. Figure 4-26 shows the first version of the PCB which only contains the microcontroller.

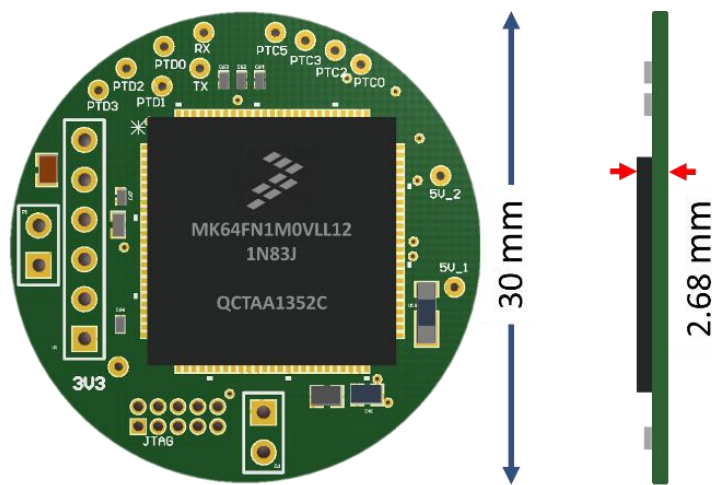


Figure 4-26: The PCB layout for MK64FN1MOVLL12 using the Altium designer 16.1. It is only two layers, and the diameter of the board is 30 mm, the width is 2.68 mm, and the weight is less than 3g. There is no communication or power link.

The microcontroller was programmed with the Kinetis® Design Studio (KDS) using C language. As the K64F supports the Digital Signal Processing (DSP), the power consumption of the microcontroller, with and without DSP library, was obtained and is presented graphically in Figure 4. To keep the power consumption low for the implant device, frequencies below 40 MHz were utilised.

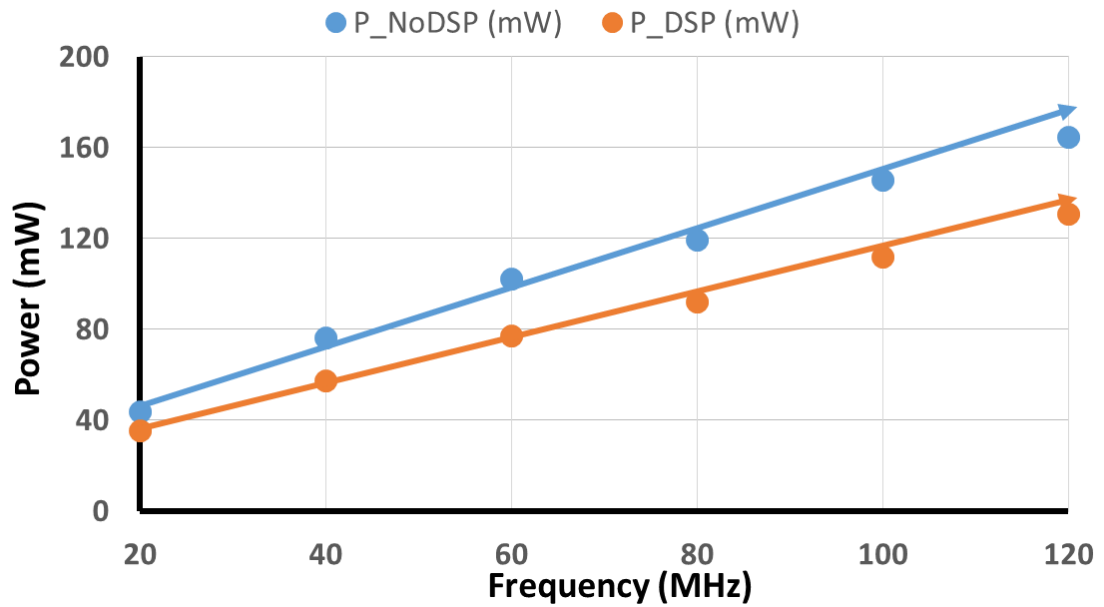


Figure 4-27: Microcontroller power consumption varies almost linearly with the frequency. The limit of power consumption is below 76.56 and 57.59 mW with and without DSP, respectively.

The microcontroller performs image decompression algorithm and pulse width modulation that stimulates the optrodes\electrodes. The image compression and decompression ratios were tested with different microcontroller frequencies. With an increase in the image compression ratio, the processing time of decompression will decrease. For the 40 MHz frequency, the fastest decompression time was 40 ms at CR 98%, as shown in Figure 4-28. As the compression technique was lossy, the image quality of the 98% compression ratio was poor compared to the 86% compression. In other words, the number of frames per second will increase for a high compression ratio.

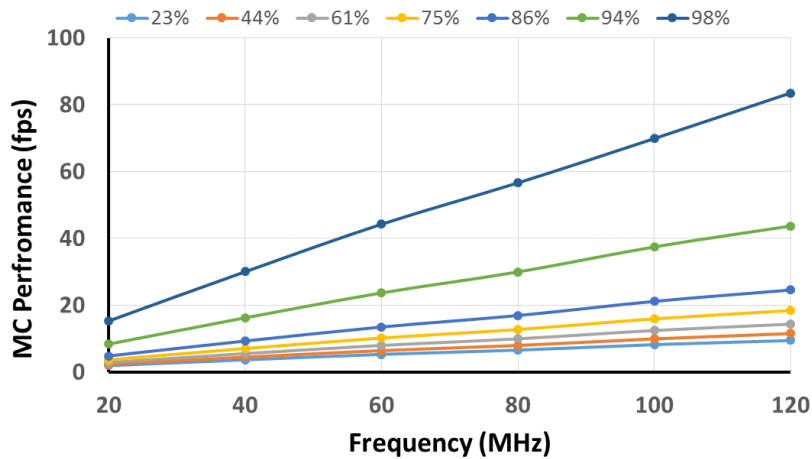


Figure 4-28: Performance of the microcontroller in clock several frequencies with different compression ratios. With a higher compression rate, more frames per second are achieved, which means that the microcontroller can perform faster.

To improve the quality of images and performance of the microcontroller, the DSP library was utilised. After adding the DSP library, the performance of the microcontroller was again tested with changes in the frequency of the microcontroller from 20 MHz to 120 MHz, as shown in Figure 4-29. As expected, the elapsed time for 86% CR with DSP was reduced from 107 ms to 19.55 ms.

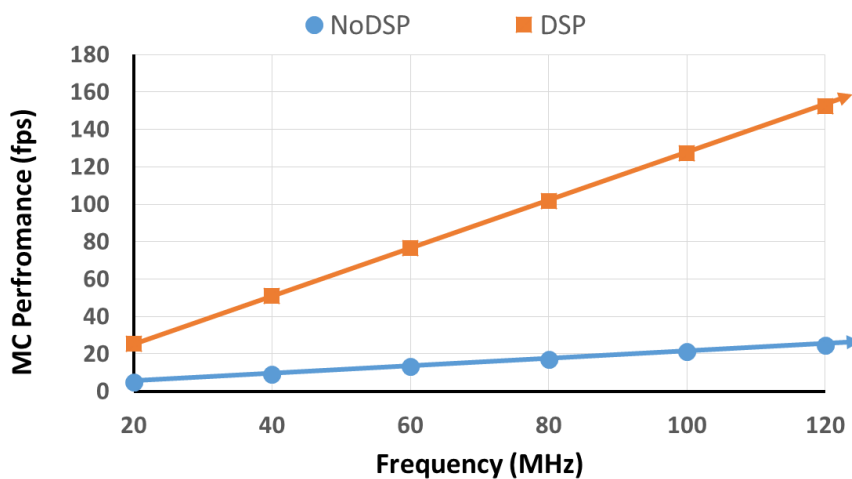


Figure 4-29: Performance of the microcontroller for 86% CR with and without DSP. With the DSP, the microcontroller can run at a lower frequency with high performance. The microcontroller running at 120 MHz without DSP has the same performance at 20 MHz with the DSP.

Figure 4-30 shows the results of the energy consumed with and without DSP. As can be seen, at 40 MHz the energy consumed to perform IDCT with 86% CR was 10 mJ. The use of DSP reduced the energy to 1.8 mJ to perform the same task.

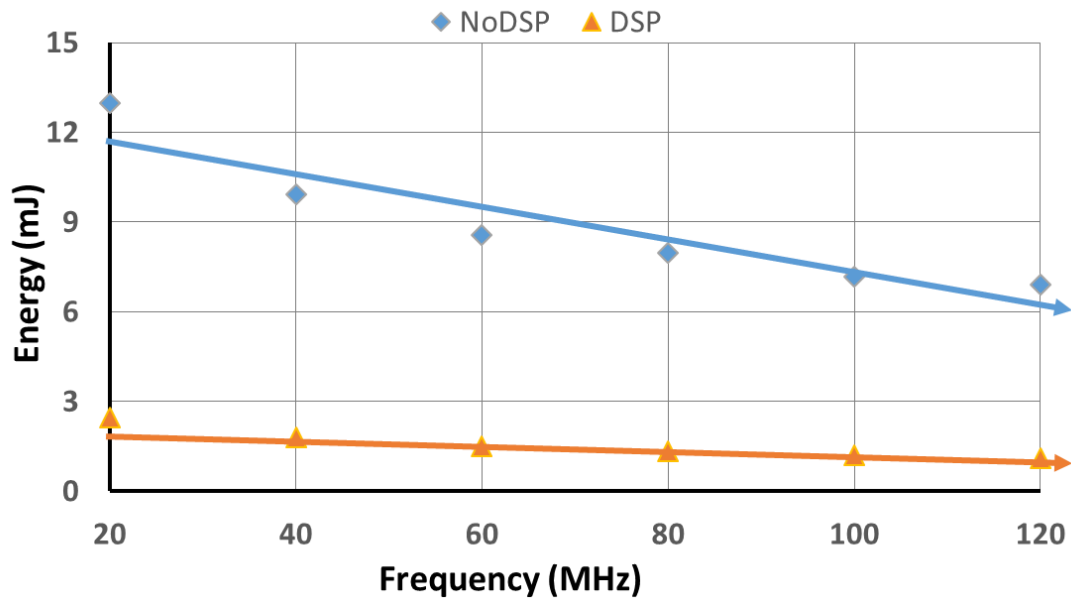


Figure 4-30: Energy efficiency for the microcontroller with and without DSP for different clock frequencies at 86% CR. Using the DSP is up to four times more energy efficient than if it is run without the DSP.

ARM Cortex LPC4330 microcontroller

There were some disadvantages in using the MK64FN1M0VLL12 microcontroller. For better results, we switched to using the LPC4330 instead. Both are from ARM Cortex M4 microcontroller series. However, LPC4330 was better because of several features. First, the size is smaller: MK64FN is 14x14 mm, LPC4330 is 9x9 mm. Second, it has slightly lower power consumption, as shown in Figure 4-31. The maximum clock frequency for the previous one was 120 MHz, but for this microcontroller, it was 204 MHz, and therefore we prefer LPC4330 as a dual-core microcontroller. It has a built-in ARM Cortex M0 and M4F which allows the microcontroller to be programmed as a dual-core for better performance.

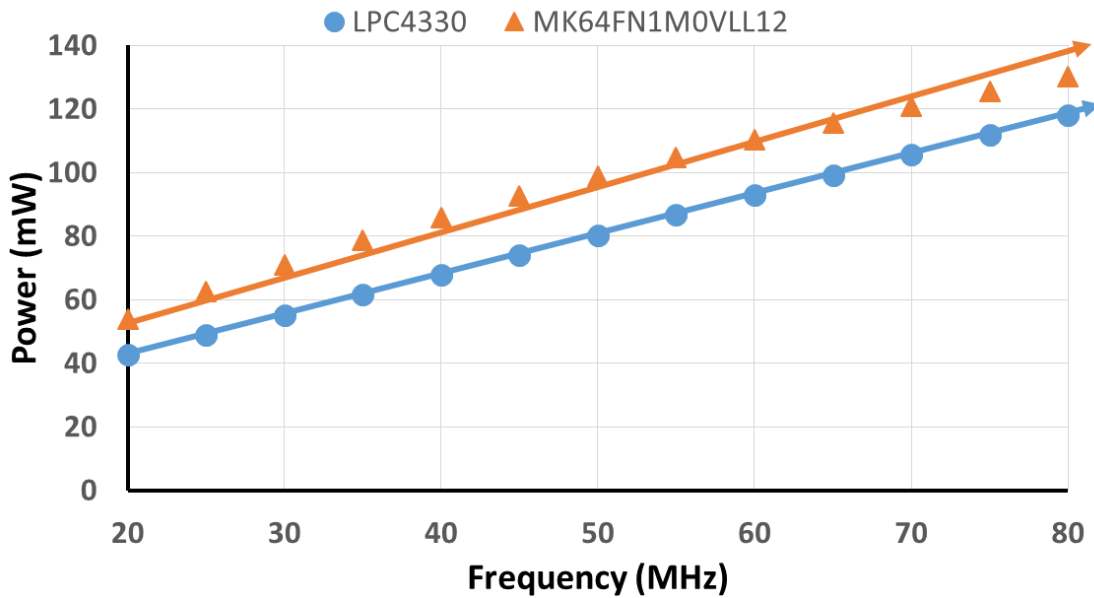


Figure 4-31: Comparison between MK64FN1M0VLL12 and LPC4330 power consumption at different frequencies. Basically, the power consumption of the LPC4330 is lower than the MK64FN1M0VLL12 by approximately 10 mW in each frequency range.

A six layer and double-sided PCB was designed and fabricated for the LPC4330 microcontroller. The weight of the board is less than 3 g, and the diameter is 30 mm. The top side of the board contains a flash memory, wireless power transfer circuit, power management, JTAG programmer pins, external oscillator and serial pins to drive the optrode. The bottom side of the board contains only the Bluetooth module. The printed circuit board is shown in Figure 4-32. For wireless power, the circuit perspective contains the AC-DC converter and dual DC-DC regulator. The two regulators provide 3.3 V and 5 V output voltage for the implanted system.

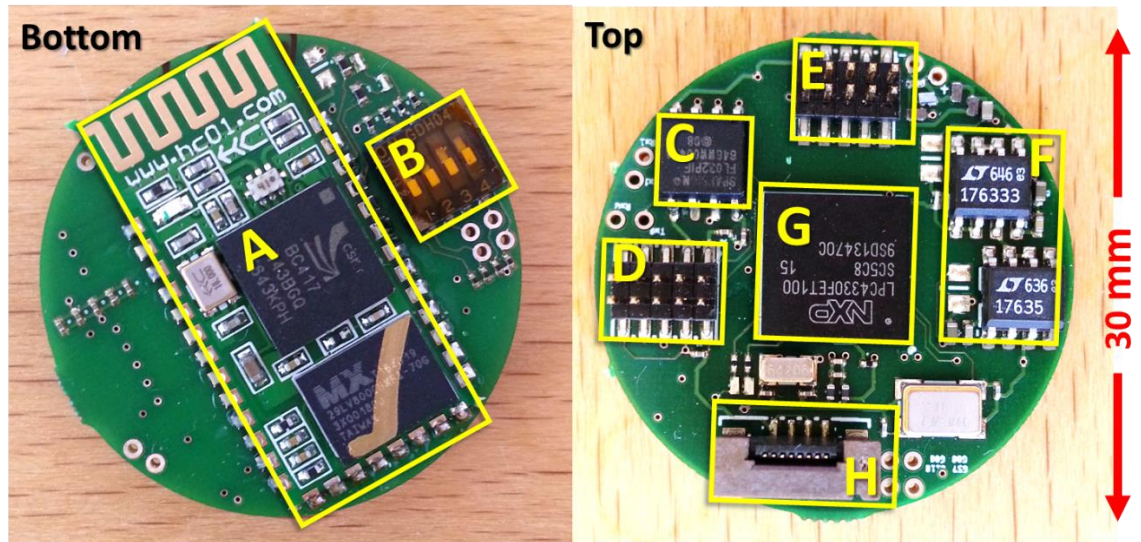


Figure 4-32: The final implanted board using LPC4330 ARM cortex M4F&M0 dual-core microcontroller. The board is six layers and double-sided. (A) The Bluetooth module. (B) Switch for boot selection. (C) External flash memory. (D) Serial Peripheral Interface header. (E) Joint Test Action Group (JTAG) interface connection port. (F) The 3.3 V and 5 V voltage regulators. (G) Dual-core LPC43xx series microcontroller. (H) Ribbon cable header to control the optrodes.

4.4 Comparison between DCT-Blocks and DCT-Zigzag

The data compression or more specifically image compression is essential, as the image size was higher than the limitation requirement for the data link. DCT-blocks were used to compress the images, but later DCT-Zigzag was also tested for image compression and compared with the DCT-Blocks. Different compression ratios were examined for DCT-Zigzag and DCT-Blocks. For example, 94%, 86%, 75% and 61% compression ratios were used to compare the quality of the original image and the compressed image for both the DCT-blocks and DCT-Zigzag algorithm. The ratio of the maximum possible power of the signal to the power of corrupting noise that affects the fidelity of its representation was tested, known as Peak Signal to Noise Ratio (PSNR). The results are presented as images for visual comparison, and as a graph. As shown in Figure 4-33, the top line shows decompression images using DCT-blocks, while the bottom line shows the decompression images using DCT-Zigzag. Apparently, there is almost no difference between the images using DCT-blocks and DCT-Zigzag in the compression ratios used.

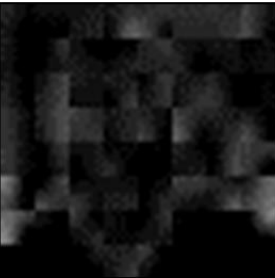



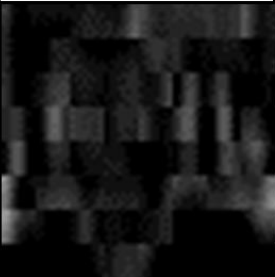



			
DCT_CR94% PSNR 17.11 dB	DCT_CR86% PSNR 17.49 dB	DCT_CR75% PSNR 17.76 dB	DCT_CR61% PSNR 17.93 dB
			
ZZ_CR94% PSNR 17.22 dB	ZZ_CR86% PSNR 17.55 dB	ZZ_CR75% PSNR 17.84 dB	ZZ_CR61% PSNR 17.97 dB

Figure 4-33: Peak signal-to-noise ratio that illustrates visual views comparing DCT-blocks and DCT-Zigzag. There is a slight difference between the two methods, which can be ignored.

In another way, as shown in Figure 4-34, the quality of the reconstructed images using DCT-Zigzag is better than DCT-blocks because PSNR is high. The result is as we predicted because with normal compression when using DCT-blocks some of the important pixels may be lost.

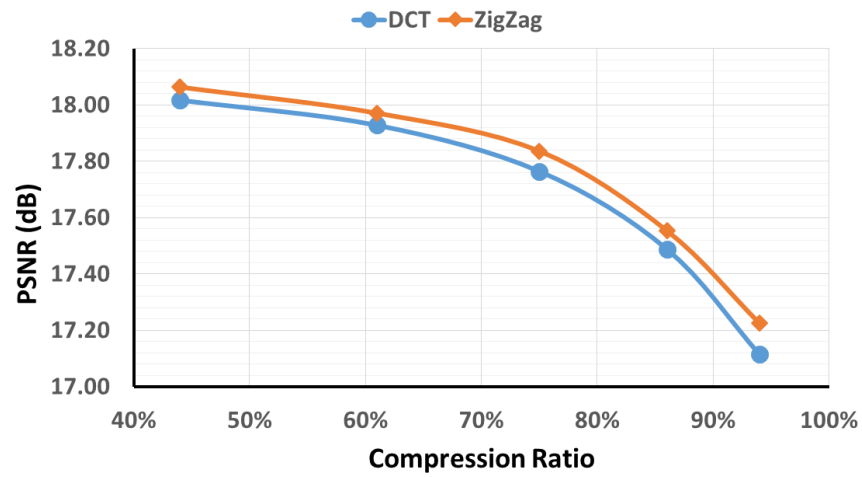


Figure 4-34: Peak signal-to-noise ratio between the original and compressed images. DCT-Zigzag is better quality than DCT-blocks but there is no significant difference.

Then, to calculate the cumulative squared error between the original and compressed images, the mean-square error (MSE) for both algorithms was used. The results show that the DCT-blocks is better than DCT-Zigzag because the MSE for DCT-blocks is lower than MES for DCT-Zigzag. A comparison of MSE values between DCT-blocks and DCT-Zigzag for all the compression ratios is shown Figure 4-35.

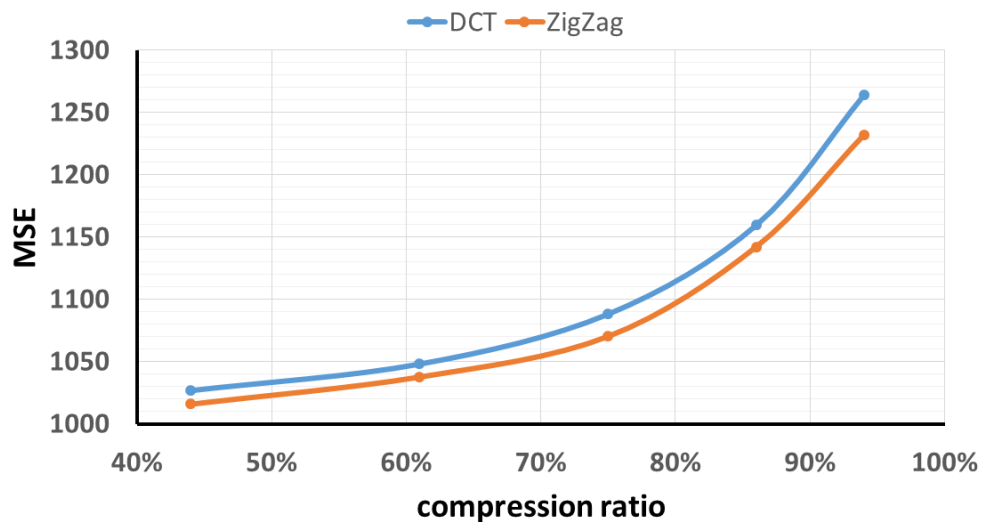


Figure 4-35: The Mean Square Error (MSE) for DCT-blocks and DCT-Zigzag. DCT-block compression is better than DCT-Zigzag because it has a lower value of MSE.

The average differences in the number of pixels between the original and compressed images are shown in Figure 4-36. DCT-blocks have less difference in the number of pixels than DCT-Zigzag for compression ratios of up to 75%. However, DCT-Zigzag is better at higher compression ratios.

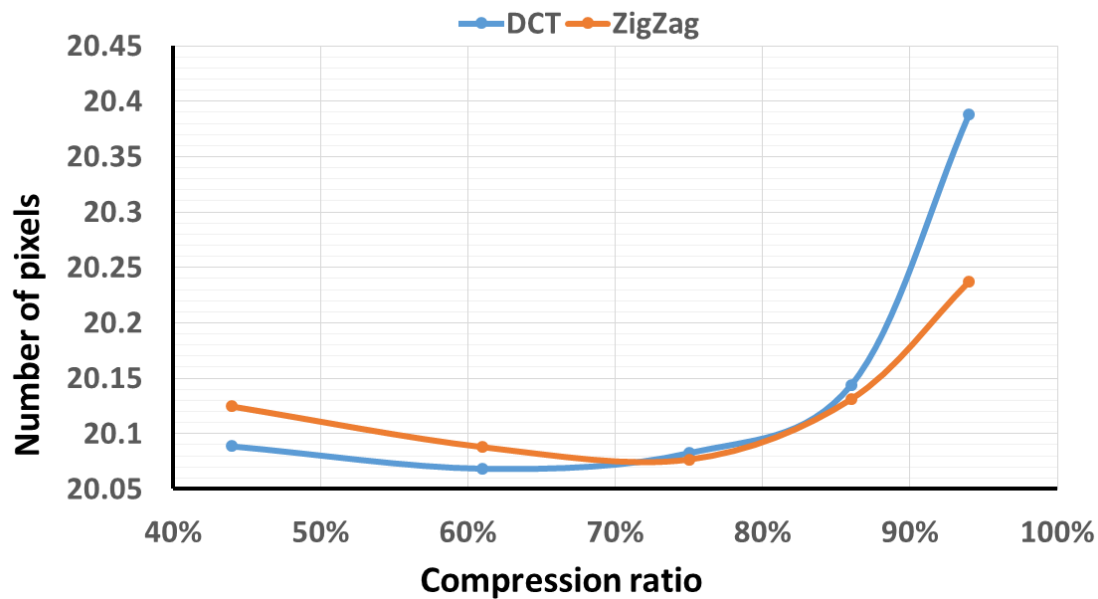


Figure 4-36: Average difference in the number of pixels between the original and compressed images. DCT-blocks are better than DCT-Zigzag for compression ratios of up to 75%, whereas at 75% they are more similar.

Finally, the maximum differences in the number of pixels between the original and compressed images were calculated. The calculation was made for DCT-blocks and DCT-Zigzag to compare them. The outcome of maximum differences is shown in Figure 4-37. The results show that DCT-block compression is better than DCT-Zigzag, with only a slight difference between them.

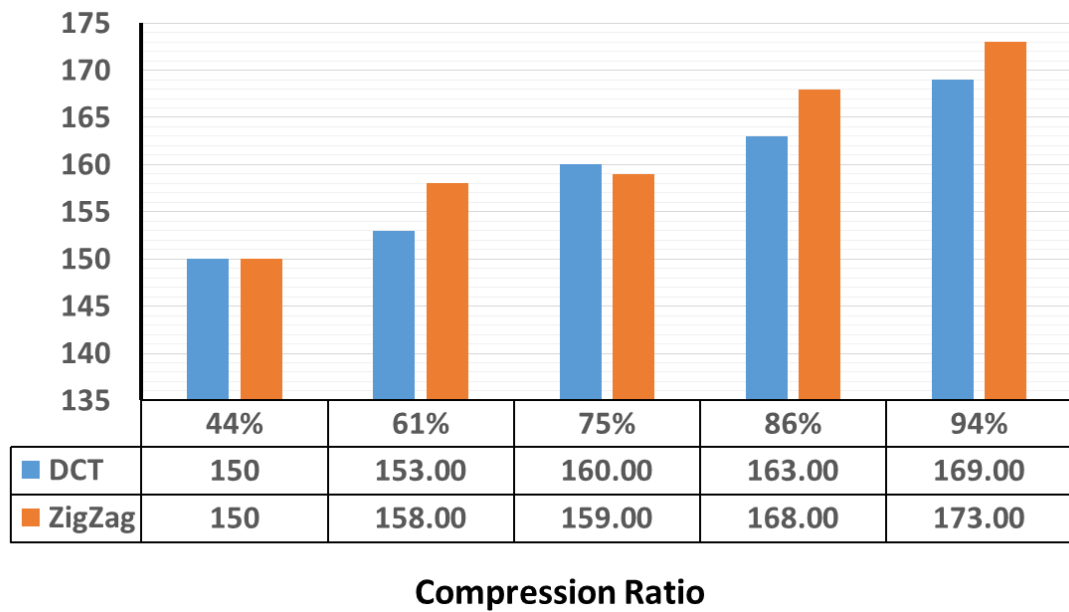


Figure 4-37: Maximum differences between the number of pixels in the original and compressed images. In general, both methods have closer similarity at 75% compression ratio.

Overall, there were no significant differences between the DCT-blocks and DCT-Zigzag. Therefore, in this work, DCT-blocks as a method of compression technique was used.

4.4.1 Embedded system integration

A bench system for the power transmitter and receiver side was tested. After achieving the objective results, the next step was the PCB design and manufacture. There are numerous aspects to consider in PCB design. On the transmitter side, there is a wireless power system and power boost, while on the receiver side there is only the implanted board.

In the external part, two boards were designed and manufactured. The first board was for the power boost; to step up the DC voltage, the voltage was converted from 5 to 12 V. This was only a single layer board and it was manufactured at Newcastle University, while the Wireless Power Transfer board was designed after the final

implanted board had arrived. As there was insufficient time to send the layout of the board to be printed in the factory, the final WPT board was soldered on Veroboard, as shown in Figure 4-38.

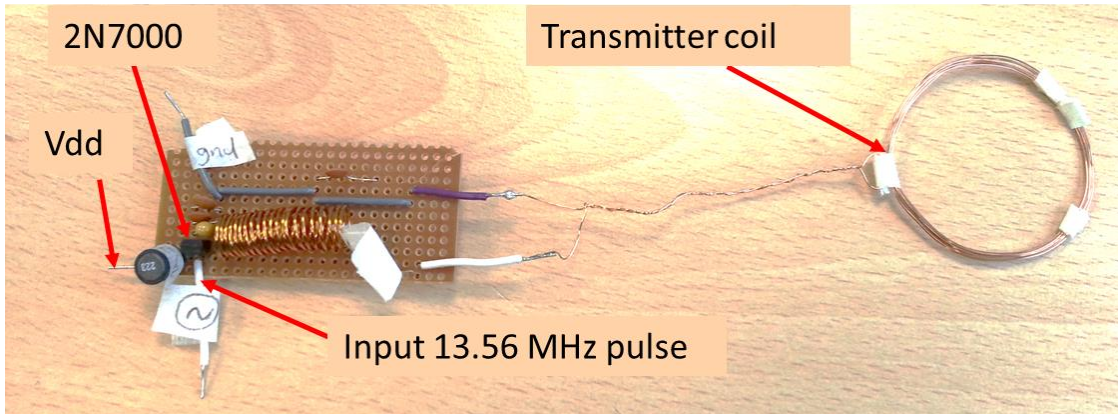


Figure 4-38: The wireless power transfer board was tuned at a frequency of 13.56 MHz. The 2N7000 used a switch transistor.

The wireless power transfer circuit schematic was drawn using National Instrument Multisim.

4.4.2 Implantable system integration

The MK64FN1M0VLL12 microcontroller was selected, and the Altium designer was used to design the PCB. The first board was a single, double layer. On the board, there was no external flash memory or Bluetooth. The board was printed in Newcastle University. The LPC4330 microcontroller, for the PCB version 1 and version 2, the NI Ultiboard was used. The board consists of six layers. The type of the LPC4330 package was TFBGA100, and it is described as follows:

- Plastic thin fine-pitch ball grid array package
- Package of 100 Low Profile Quad Flat Pack (LQFP)
- Body 9 x 9 x 0.7 mm
- The version was SOT926-1.

The LPC4330 PCB is a multilayer board, and it includes:

- Bluetooth
- Wireless power receiver circuit
- External flash memory
- JTAG header
- μ LED header
- SPI header
- Boot switch.

The external flash handles the program to bring the board to the standalone mode. The JTAG header allows programming via LPC_Link2 debugger. However, the μ LED header controls the optrode/ μ LED matrix. Finally, the SPI header can be used for general purposes. On the board, there are two UART pinouts, the UART0 and UART1. Also, there are four GPIO out on the board for general purpose programming. The board pinout for the LPC4330 can be seen in Appendix D.

The LPC4330 body size was 9 mm x 9 mm, and it consists of BGA. To connect the chip to the other components was quite challenging because of the manufacturer's capability and the size of the chip. The VIAs were used to connect it to other components. For this, the trace was passed in between different layers. Moreover, the smallest size of the VIAs was used. Also, the BGA pad and VIA's pad was overlapped to prevent a design error check in the system.

The inner layers were set for the ground and power purposes. Also, the first layer was set for the ground, and the third layer was set for the power. This was to reduce the number of traces and minimise the interference between traces.

Chapter 5. System integration and packaging

5.1 Hardware overview

In this section, the wireless power transfer (WPT) results are presented. The rate of power delivery to the receiver end was carefully calculated. In general, a wireless power system consists of a transmitter and receiver parts. The techniques for designing the WPT can be performed by focusing either on the transmitter or receiver side. The total power consumption in the receiver end has a significant effect on the system design because of safety requirements. The transferred power is bounded by the IEEE and FCC standard exposure limitations [243, 244]. Additionally, the implant should not heat the tissue by more than 2°C. For these reasons, the receiver side was explored. The total power budget was calculated for the AIMD, and its subcomponents. Figure 5-1 shows the general concept of the wireless implantable system.

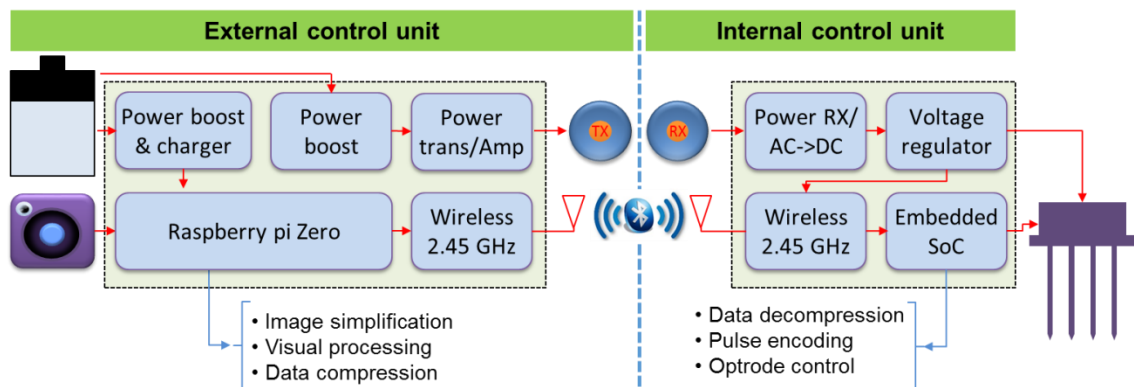


Figure 5-1: The system is divided into two parts, the transmitter and receiver. The external parts are placed on the glasses and the case. The internal parts are collected on the implantable board.

The result of designing the wireless power system and testing it are described in the following order: (1) the outcome of the coil design; (2) increasing the budget of input power for the wireless power system by adding an class E amplifier to the system; (3) matching the impedance for both sides of the circuits; (4) the AC-DC circuit and (5) regulating the voltage. Also, some examples are presented for testing the WPT systems.

5.1.1 External power management unit

An Adafruit Power boosts 1000C (TPS61090) was used to operate the Raspberry Pi Zero and recharge the battery. It can be powered by a Lithium Ion 3.7 V rechargeable battery, and will provide 5 V output voltage. Its efficiency is above 90%, and it can supply up to 1 A of output current. The board has load-sharing, which helps users to charge and boost the power without obstructing the output voltage, and it is therefore an uninterruptible power supply. The power boost board is shown in Figure 5-2. The board consumes 5 mA when it is enabled, and it consumes 20 μ A when disabled.

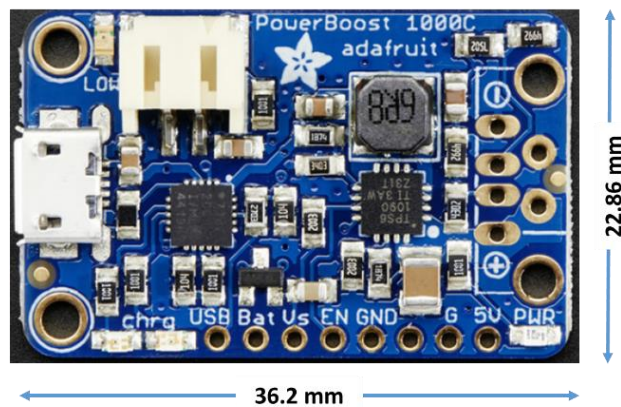


Figure 5-2: Adafruit Power boosts 1000C. While it is converting from 3.7 V to 5 V output voltage, it can be used to recharge a battery. The weight of the boards is 6 g. The power consumption of the board is approximately 18.5 mW (image from Adafruit web page [245]).

The next boost converter was added to the system to operate the wireless power transfer system on the transmitter side. The aim of using this is to convert the 5 V output voltage from the power boost 1000C to 12 V. For the circuit schematic and the PCB layout, the National Instrument (NI) Circuit Design suite 13.0 was used. The PCB is shown in Figure 5-3. The size of the board was 28.5 mm x 9.63 mm and its weight is 1.1 g.

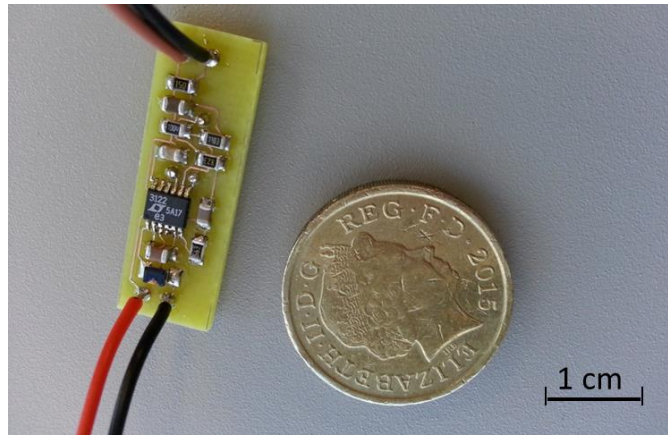


Figure 5-3: LTC3122 power boost board for regulating voltage 5 V to 12 V.

To simulate the LTC3122, LTspice software from Linear Technology was utilised, and the results are shown in Figure 5-4. The microcontroller took only 11 ms to adjust the output voltage. Also, the output current was up to 800 mA.

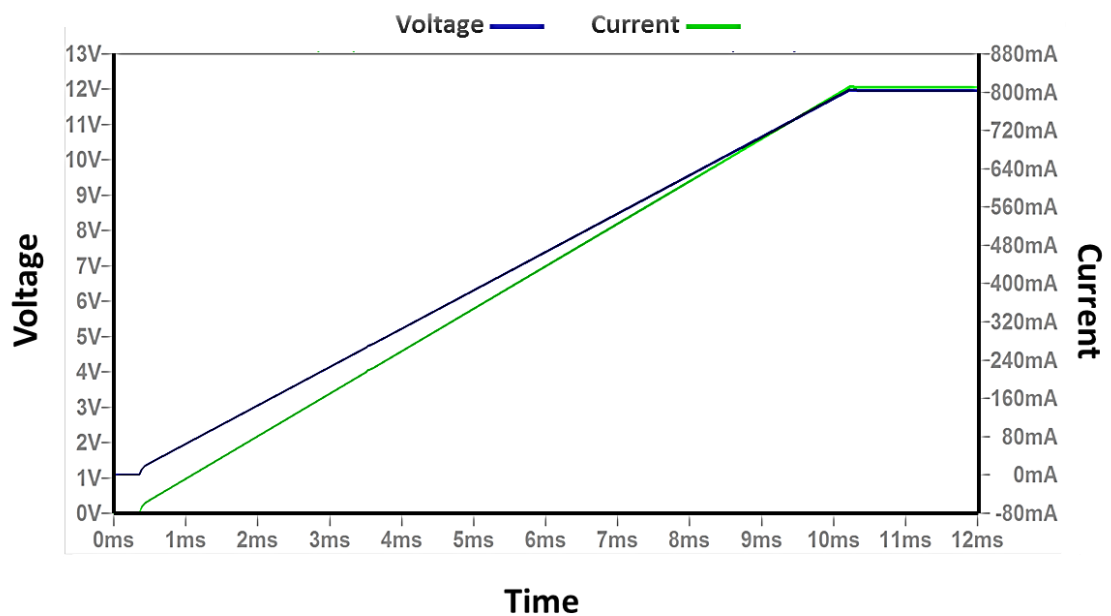


Figure 5-4: Simulation results for the 12 V and 800 mA output from the LTC3122 regulator. The input voltage is 5 V for the regulator. The output current (left y-axis) and the output voltage (right y-axis).

5.1.2 Power Transmitter

The purpose of a wireless power transfer circuit is to transmit power wirelessly. The main components of the transmitter side include a pulse generator, a power amplifier and a coil. In the power amplifier circuit, the transistor functions as a switch. To turn the turning switch on/off automatically, a square wave is required. For this, the pulse generator is required in the circuit as an input wave to operate the transistor. In other words, the transistor speed should be equivalent to the pulse. In Figure 5-5, the fundamental diagram of the wireless power in the transmitter is presented.

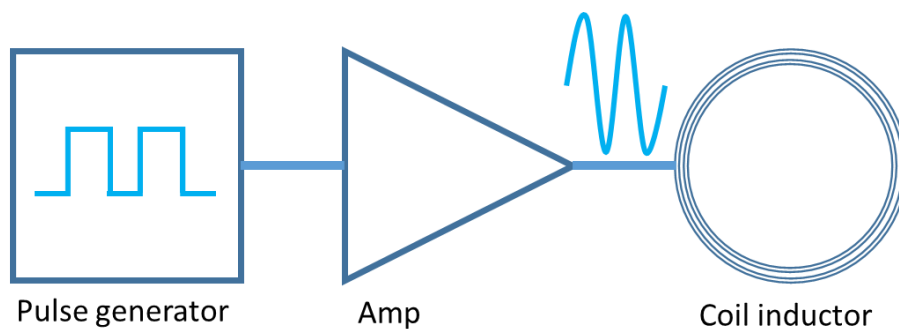


Figure 5-5: The basic block diagram of the wireless power transmitter. The pulse generator operates the switch BJT/MOSFET transistor. Then, the transistor increases the power to the system.

Pulse generator

To generate 13.56 MHz and 6.78 MHz frequencies, a programmable oscillator was used. The output pin was connected to the Agilent InfiniiVision model MSO-X-4034A. The result of the generated wave is shown in Figure 5-6. The wave is supposed to be a square wave, but the signal was affected by the capacitor in the probe. When the programmable oscillator is programmed to achieve 6.78 MHz, the archived result was 6.68 MHz, and for 13.56 MHz the closest result achieved was 13.74 MHz. Later, for the final design, a crystal oscillator was used to generate 13.5 MHz as it is very precise. To generate frequencies below 2 MHz, a 555 timer integrated circuit (IC) was used. The output pulse from the timer is more stable than the programmable oscillator. The waveform of the 555 timers oscillating at 1.63 MHz is shown in Figure 5-6.



Figure 5-6: Oscilloscope screenshot for 6.78 MHz and 13.56 MHz frequencies for the programmable oscillator DS1085L and Oscilloscope screenshot of 555 timers at 1.63 MHz frequency.

In the bench test for the wireless power transfer, the waveform generator from the Agilent oscilloscope was used for all frequency ranges. However, for the final design of the wireless power transfer, the crystal oscillator was employed and tuned at 13.5 MHz.

Class E power amplifier

The observed power in the transmitter circuit of the wireless power system was 4.63 mW. This was produced directly by the programmable oscillator. The output power measured at the output pin was 14.4 mW which is low. The power loss between transmitter and receiver is 32.15% because the impedance matching for the system at that stage was not considered. To increase the power level on the transmitter side, a class E power amplifier was designed with an efficiency of 93.43%. The N-Channel Logic Level Enhancement Mode Field Effect Transistor 2N7000 was implemented as a switch controller. The basic schematic of the class E amplifier is shown in Figure 5-7.

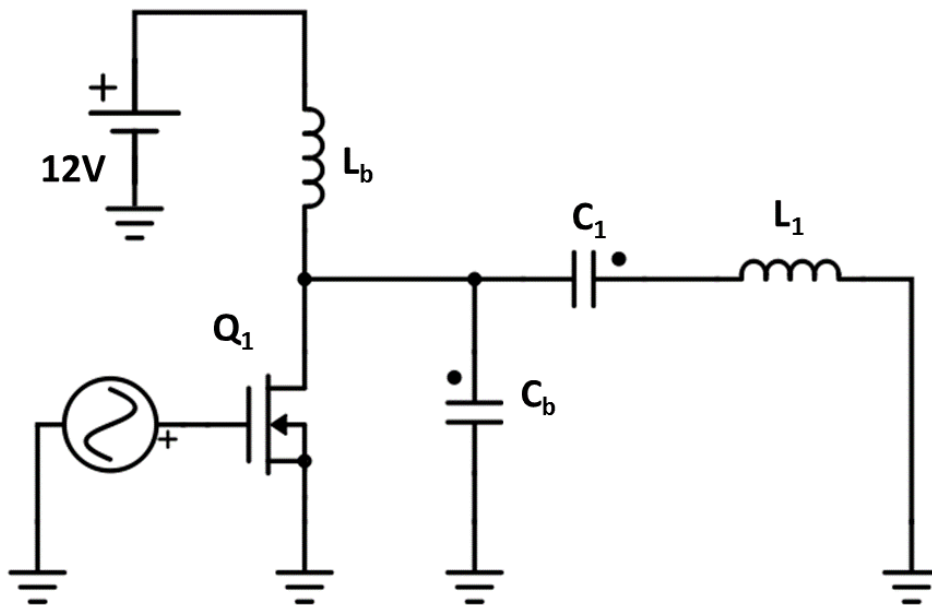


Figure 5-7: Class E power amplifier schematic circuit. The main significant factors in the circuit are C_b and C_1 . The transistor acts as a switch and should satisfy the required speed of the system as the frequency is 13.56 MHz.

The detailed specifications for the design of the class E amplifier tuned in the range of 13.56 MHz frequency are listed in Table 5-1.

Table 5-1: List of parameters/components used in the Class E power amplifier.

Q_1	V_{dd} (V)	L_b (μ H)	C_b (pf)	C_1 (pf)	L_1 (μ H)	R_1 (Ω)	Efficiency
BSS138	12	8.8	126	81	2	100	87.3%
IRF540	12	0.5	250	50	2.5	39	20.4%

5.1.3 Coil Inductors

Two sets of coils were designed and tested for wireless power transfer. First, copper wire was selected for the transmitter (Tx) coil with a Tx diameter of 40 mm. The coil wire was wound in the form of a planar coil, as shown in Figure 5-8. Specifications of both coils are listed in Table 4-2. For the coil on the transmitter side, single core copper wire was used because it is better than multicore wires, since single core wire has a larger outside surface area and low resistance compared with multi-core wires. In the final design, the single core Litz wire was selected for the transmitter side.

The implant device will be placed outside the skull and connected directly to the RX coil. Keeping the receiver coil outside the skull has two main benefits: i) it prevents the brain from being damaged; ii) the distance from the transmitter coil will be kept short. In order to transfer power efficiently, a short distance should be kept from the transmitter. However, keeping the Rx coil far from the brain is required to prevent the tissue being damaged, because the temperature may rise in the RX coil during long periods of operation. The proposed design of the receiver coil is a printed circuit coil, and example of which is shown in Figure 5-8.

The geometric size and parameters of the printed coil inductor are listed in Table 4-1. Although the printed coil was a good candidate, it was eliminated because of the high complexity of the implanted board, which left no space for the printed coil.

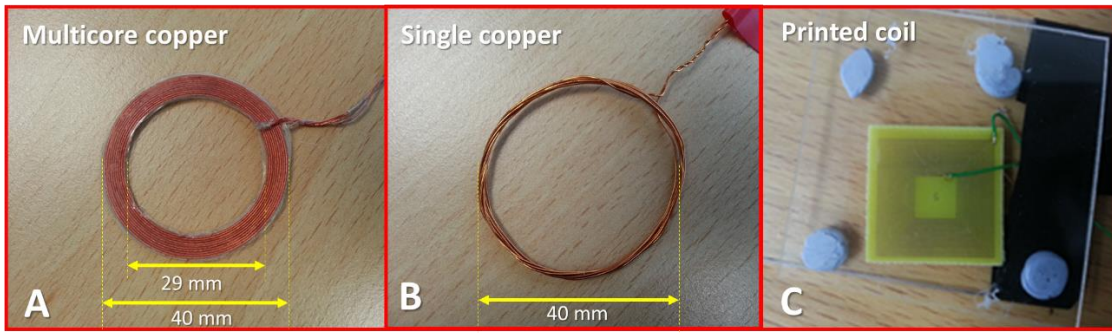


Figure 5-8: Planer flat coil at the front end (A), a planar coil at the front end and receiver side (B), and printed coil on the board just for the receiver side (C).

5.1.4 Power receiver

On the receiver side, after the electromagnetic wave has been received, it is sent to the full bridge rectifier to rectify the sine wave shape. The capacitor needs to be connected in parallel with the full wave bridge rectifier to smooth the wave and reduce the effect of the ripple wave. Finally, a voltage regulator is necessary to stabilise and fix the output voltage.

Rectifier

For the AC-DC conversion, a normal bridge rectifier was used. In this stage, the Schottky diode NSR05F30NRT5G was selected. The maximum supply current allowance for the circuit is 10 A, and the repetitive reverse voltage is 30 V. The tuning frequency is 13.56 MHz, and the ripple voltage (ΔV) was calculated for the full wave rectifier as:

$$\Delta V = \frac{I_{load}}{2fC} \quad (5-1)$$

Where C is the parallel capacitor, it is connected with the load resistance. When the load of the implant device is approximately 100 Ω , 10 μf capacitors are chosen. Then, the value of the ripple is 0.055 V. The rectifier circuit did not affect the received current, but the voltage dropped by a factor of 0.35-0.44 V. This means that in theory if the delivered voltage to the receiver coil was 10 V, then the result is 9.2 V on average after the rectifier.

Figure 5-9 shows an experimental example of full-wave rectification, for the received voltage of 10.18 V peak to peak (maximum voltage 5.09) on the receiver side. After the rectifier, the positive and negative rectified voltage is highlighted. In this example, the maximum voltage was 4.95 V at the tuning frequency of 13.5 MHz. This was before connecting the capacitor in parallel with the output voltage.

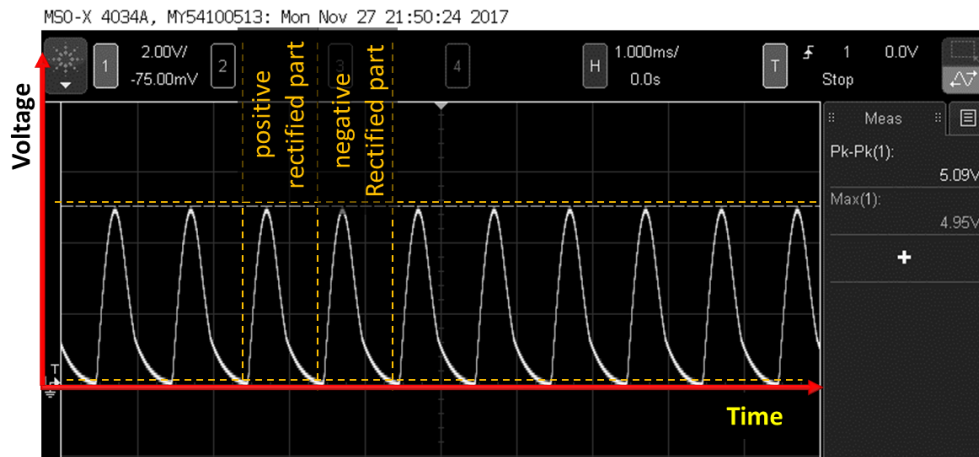


Figure 5-9: Example of the full wave voltage rectification on the receiver side before adding the smoothing capacitor.

After adding the capacitor, the rectified signal becomes smooth, and DC voltage was 4.81 V, as shown in Figure 5-10. The measured ripple voltage on the oscilloscope was 55 mV.

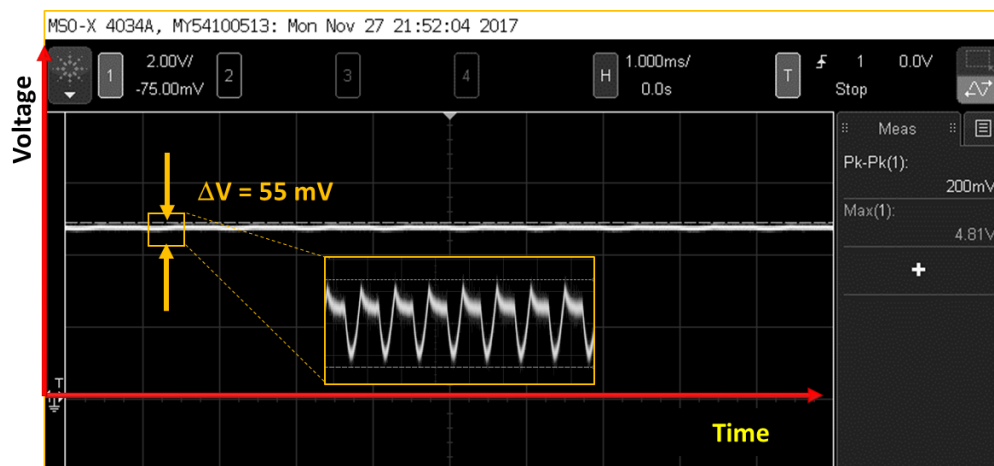


Figure 5-10: Voltage rectifier example after connecting the smoothing capacitor in parallel.

Regulator

Different approaches have been attempted for the DC-DC converter for the transmitter and receiver parts. For the receiver end, the LT1763CDE DC-DC converter was supplied to fix the output voltage. Experimental data were measured with different resistance loads. As shown in Figure 5-11, the output voltage was stable and fixed at 3.3 V for the specific test. This test was performed to show the capability and stability of the regulator. The current decreased when more resistance load was added to the output. The power line increased from zero load resistance up to 100 Ω and then it decreased from 100 Ω to 1 k Ω . The peak value for the power was more than 80 mW at the receiver end at 100 Ω resistance load. The regulator starts working on the threshold value of the resistor. For each design regardless of the load, there should be a threshold value of resistance load connected to the regulator. The extra load will not make a difference after this.

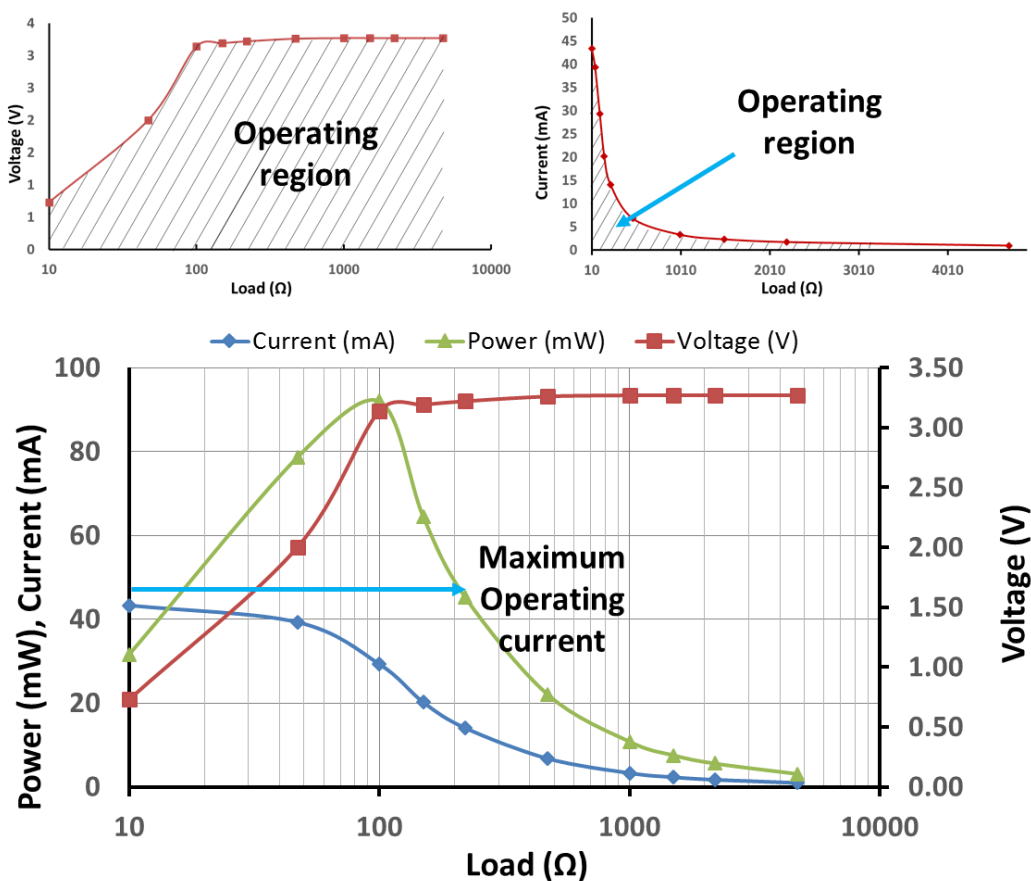


Figure 5-11: The relation between power, current and regulated voltage output with different loads. The key issue is to maintain the required voltage across the load. Below 100 ohms, the voltages drop off because the power management cannot supply sufficient current to the load.

5.2 Camera

Still images with a quality of 640 x 480 pixels were captured using a Logitech C270 720p HD webcam. There are two useful specifications in this camera: it is capable of adjusting the image automatically in dim light, and it has a wide-angle lens that provides a 60° field of view. The camera was disassembled to fit in the 3D glasses model. The power consumption of the camera is about 260 mW.

5.3 PCB Layout consideration

There are some basic rules which need to be considered before starting to design a PCB. Some of these rules are related directly to the PCB designer, and some are related to the manufacturer's technical capability. The PCB designer should pay attention to the power trace line because the wrong calculation causes the temperature to rise on the board, and this will increase the risk from the implant device.

The PCB manufacturer company will limit the minimum design rule according to their capability. For example, the PCBTrain Company limits the trace width to no less than 0.127 mm [246]. To make the PCB routing easier and more efficient regarding the power line, adding the power in a single layer is recommended. The PCB will be very small because of the implanting issue. Vertical Interconnect Access (VIA) is the most significant factor to consider, as techniques to connect two traces between two layers. Normally, it should cover the solder mask to protect it from being soldered. Moreover, the company will limit their minimum size. In this case, for using the BGA footprint microcontroller types, the smallest capacity of VIA is the best option.

5.4 Security and safety

The two main significant topics that need to be considered are security and safety. From the perspective of security, Bluetooth was used in the system for communication. Bluetooth is known as a secured protocol for communication. It is very common and used in many useful devices such as mobile phones, tablets, computers and medical

devices. In projects such as a pacemaker, a secure data link is permanent, but in this project it is not necessary because if the system is hacked nothing serious will affect the user. However, security is still considered to be essential and so Bluetooth was nominated as the communication protocol.

The main potential problem during the operation of the AIMD is the probability of the device overheating the body parts in which it is located. This is likely to raise the temperature which could damage the tissue surrounding the device. The normal body temperature is 37°C. The International Organization for Standardization (ISO) 14708-1:2014 limits the temperature increase by the AIMD to no more than 2°C [247], and therefore the AIMD in this project takes this into consideration. The size of the board is calculated taking into account the temperature changes, as smaller PCB implants are more likely to raise the temperature, especially with high power consumption devices. Devices of 3 cm² and greater physical size are more likely to keep the temperature rise below 1°C. In this project, the physical dimension of the implant device is 7.686 cm².

The maximum allowance for the power consumption is 480 mW for this work, as shown Figure 5-12. Interestingly, the measured power consumption for the implant system was below 300 mW.

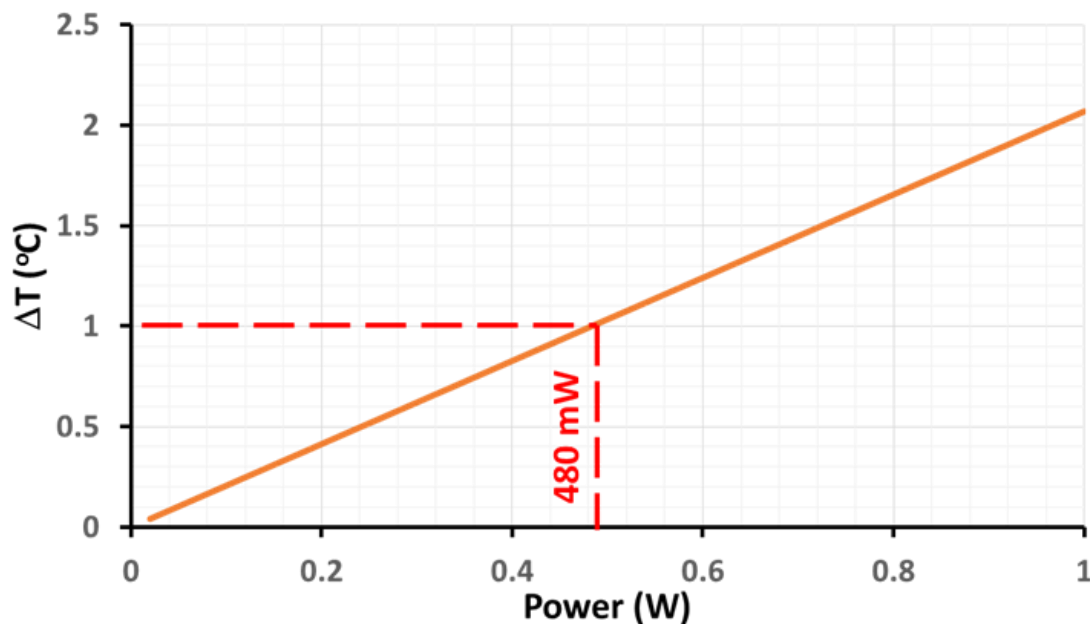


Figure 5-12: Power consumption allowance is below the temperature change limitation. For a board size of 30 mm, the limitation of power consumption is around 480 mW. The power consumption of the implanted board is approximately 300 mW.

It states that the designed implanted device is safe and can be implanted with low risk. The size of the implant is thus helpful for reducing the risk.

5.5 System level testing

Vertical distance and horizontal alignment

The regulator was designed to provide 3.3 V output voltage. This test is just to display the performance of the voltage regulation. The output voltage for the test bench was fixed at 3.3 V. The test of the WPT system is made by varying the horizontal alignment and the change in distance between the two coils. According to the experiment, the limited range of the output voltage was observed to be unconditionally stable. Also, the distance between the coils was 0, 5, and 10 mm. The results show that there was no change in voltage, as shown in Figure 5-13. Plastic sheets of 4.9 mm thickness were used between the coils to organise the specific distances.

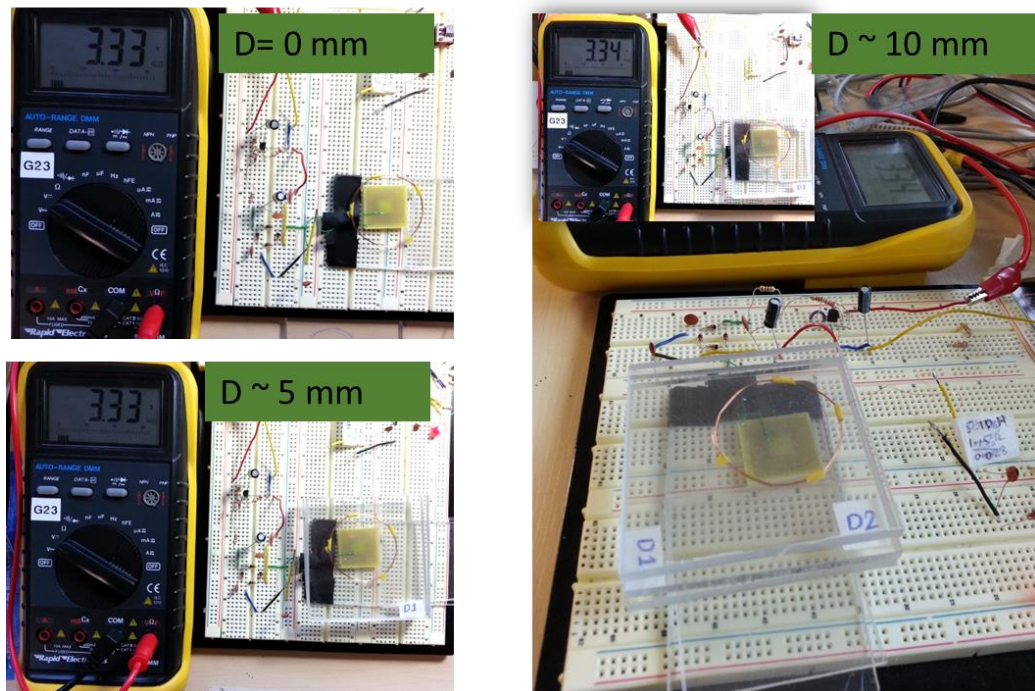


Figure 5-13: Vertical distance between two coils. The two coils are contacted (top left), 5 mm distance between two coils (bottom left) and the distance between two coils is 10 mm (right).

For horizontal alignments, the primary coil was moved slowly till the edge fit the centre of the implanted coil. The result is shown in Figure 5-14, where the measured output voltage was stable [152]. The output voltage was stable, and there was no degradation.

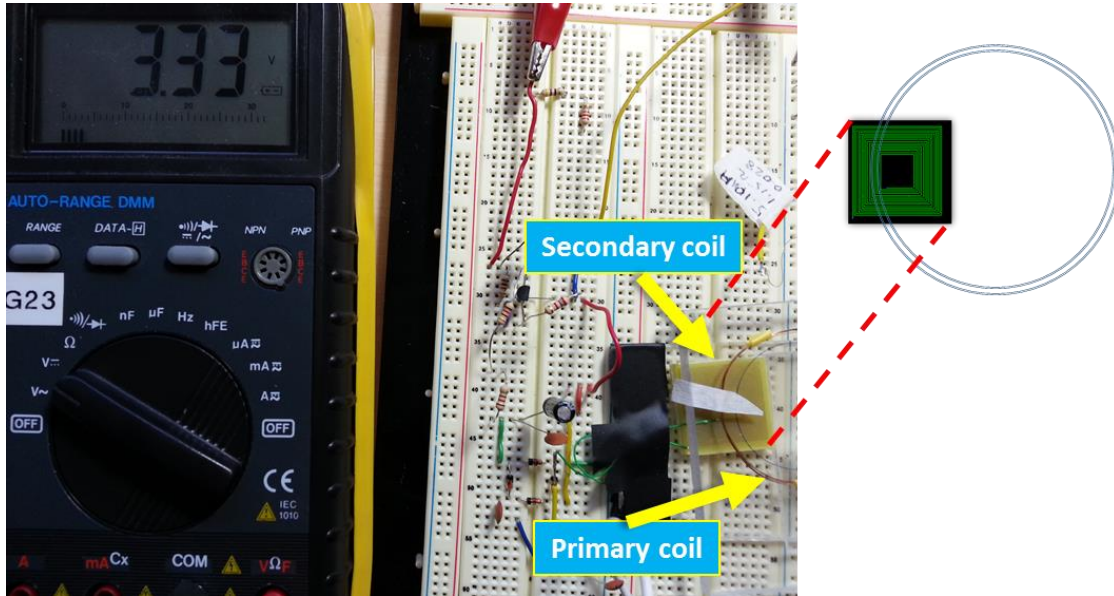


Figure 5-14: Maximum horizontal alignment between the two coils shows that the voltage is stable after moving the Tx coil to the centre of the Rx coil. The voltage was stable, and there were no changes.

In-vitro test

The circuit was characterised by transferring power through three different physical mediums: the air, water, and fresh pork. This temperature was chosen because of normal human body temperature. In this experiment, the test bench of wireless power transfer circuit consists of the power supply, programmable oscillator, Class E amplifier, matching circuit, transmitter and receiver coils, and the rectifier. The schematic of the wireless power transfer system circuit is shown in Figure 5-15.

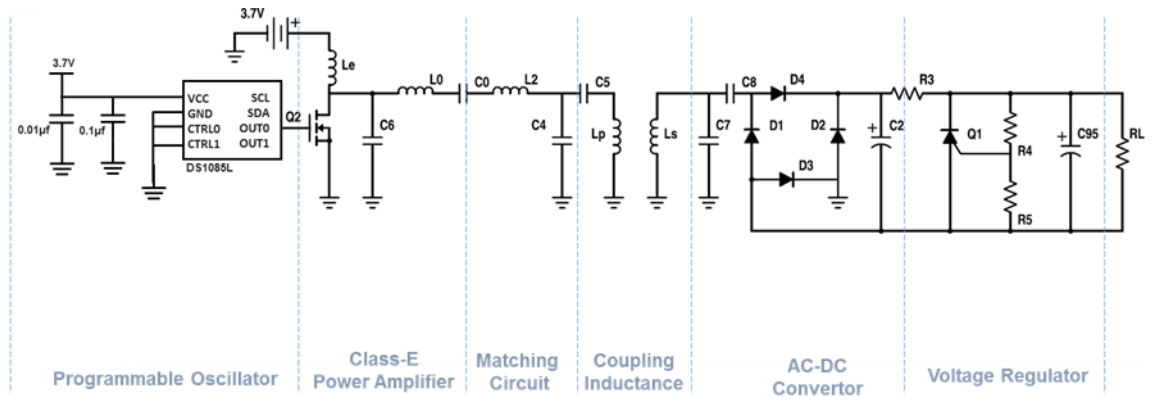


Figure 5-15: WPT circuit schematic used for transferring power through air, water, and pork. The programmable oscillator was set to 13.56 MHz. The power source of the device was from KESIGHT E3648A Dual output DC power supply.

The measured results are illustrated in Figure 5-16.

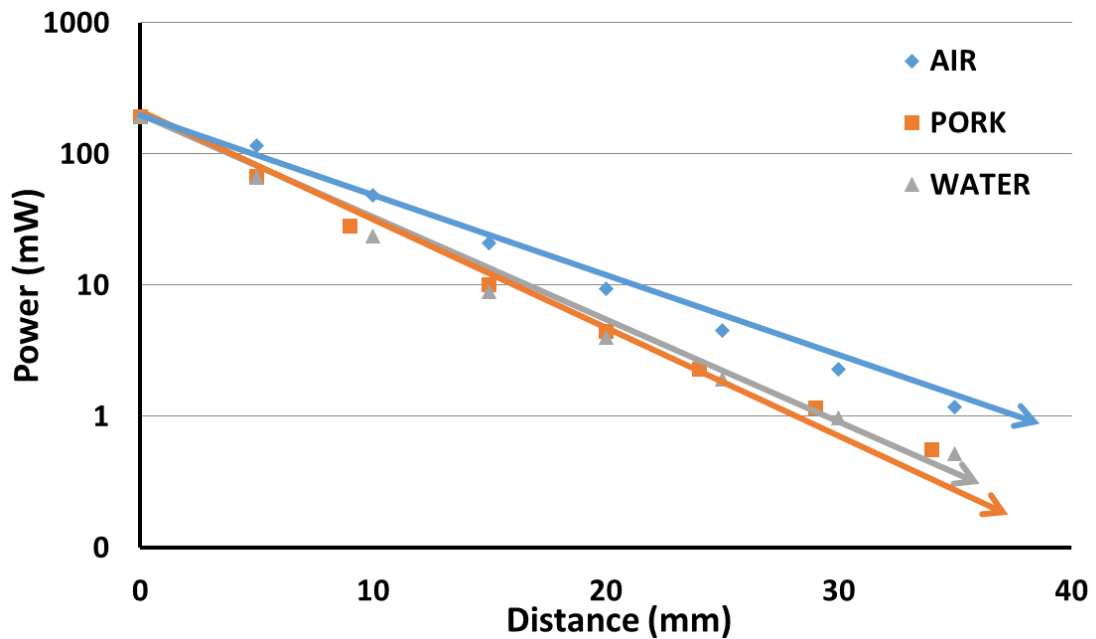


Figure 5-16: Received DC power through the air, water, and pork. At the 5 mm distance between two coils after transfer through the physical mediums, the power-degraded around 40%.

There was a significant variation in power on changing medium. In fact, the power reduced to 40% of its original value when the medium was changed from air to pork and water. Because of its similarity to human tissue, the tissue experiment was conducted

in-vitro with pork. The experimental base for power transmission through fresh meat is shown in Figure 5-17.

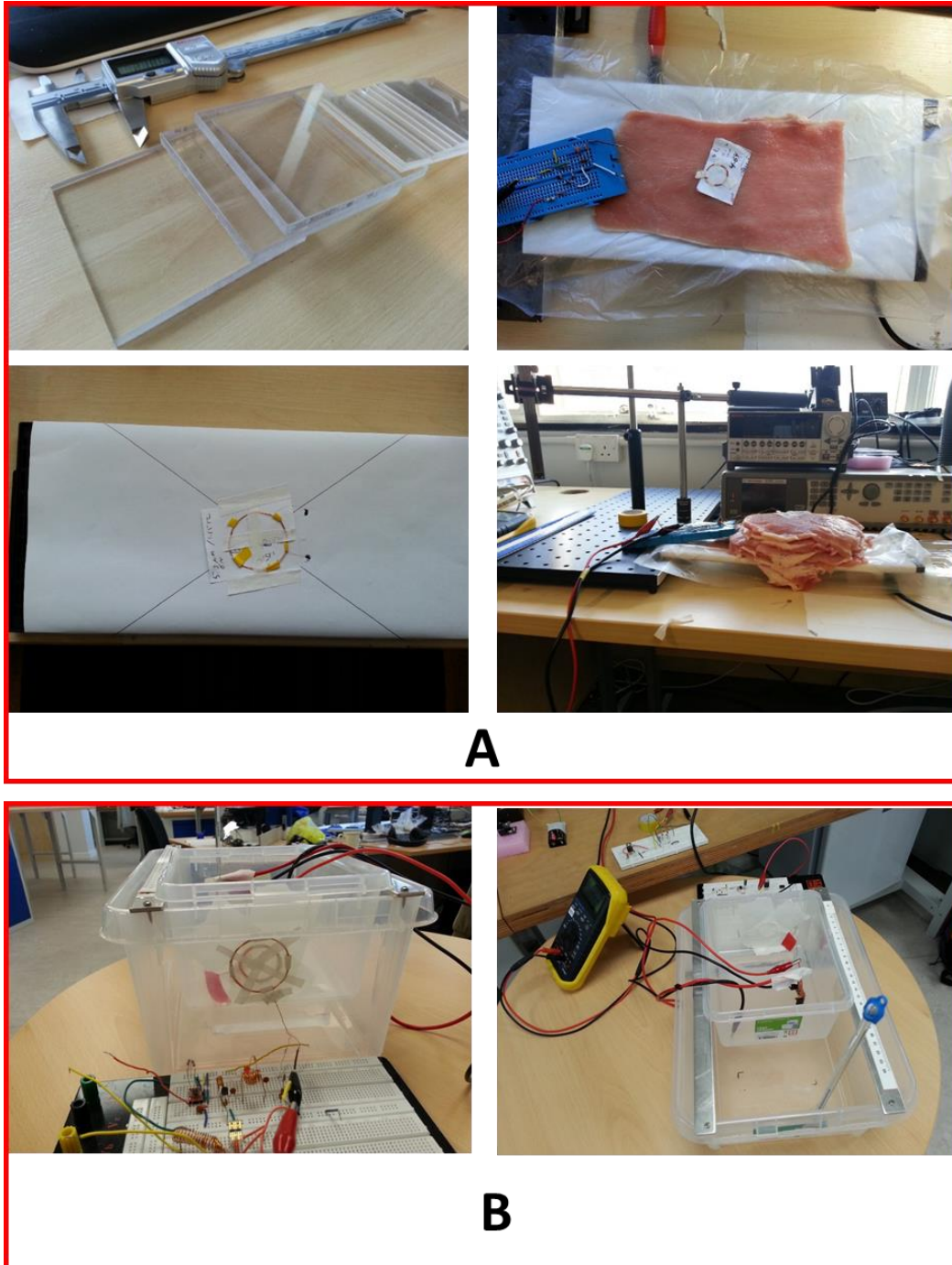


Figure 5-17: (A) Top left, plastic for spacing between two coils for the air gap, and the rest is the experimental rig for the wireless power transfer through pork. (B) The box is labelled on top and the bottom is filled with water. This illustrates the power transmission through warm water.

5.5.2 Optrodes

The μ LED matrix employed in this work was 90x90 pixel as a proof of concept. It was designed and manufactured by Degenaar from Newcastle University. The purpose of this was for the retinal prosthesis, but it is used here to test and demonstrate the PhD work. Its power consumption is below the 320 mW for maximum brightness. An example of the μ LED matrix is shown in Figure 5-18.

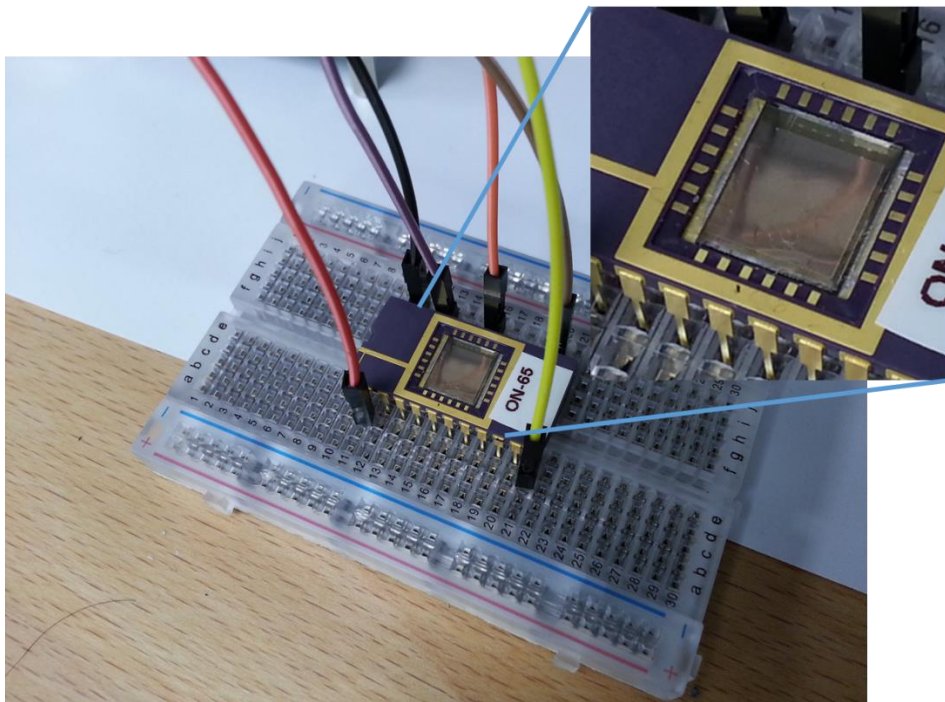


Figure 5-18: The 90x90 μ LED matrix used to illustrate the visual cortical stimulator.

The μ LED matrix requires an input voltage of 5 V. It has 4 input ports: clock, activate, column and row.

5.6 Assembly of visual cortical prosthesis

The overall system of a medical implant device for a visual cortical prosthesis is prepared after the assembly of all the parts. The main parts of the system are the transmitter and receiver. At the transmitter, there is a USB camera, 3D printed model glasses, a

rechargeable battery, a power management unit, a wireless power transmitter, the Raspberry Pi Zero minicomputer and Bluetooth. The transmitter components after being assembled are shown in Figure 5-19. There are two switches in the black box where most components are installed. The first switch (red colour) is for switching power off the system. By doing this, the battery will be disconnected from the system. The second switch (black colour) is for turning on and off the Raspberry Pi Zero. When the Raspberry Pi is switched on, it is programmed to capture the video and send it automatically over the Bluetooth. Also, the black box can either be attached to a belt or put in a pocket. The dimensions of the box are as follows: width 10 cm, length 7.5 cm and height 4 cm. Its weight including the parts is 180.7 g, and the weight of the printed glasses is 96.3 g, with a total weight for the transmitter of 277 g.

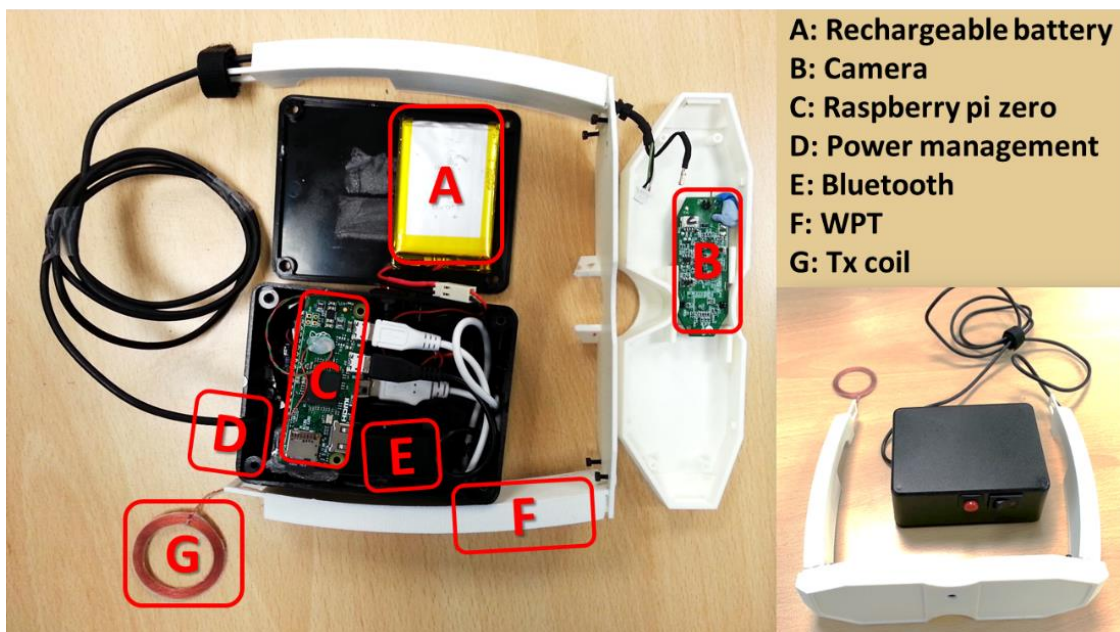


Figure 5-19: The transmitter parts of the wireless visual cortical stimulator are divided into two parts, case and glasses. The wireless power transmitter circuit, transmitter coil and the camera are mounted on the glasses. The Raspberry Pi Zero, rechargeable battery, power boost 1000C, a power boost for WPT, USN hub and Bluetooth adapter are placed in the case.

The implanted receiver contains a PCB and a stimulator. The printed circuit board consists of a wireless power receiver, power management unit, flash memory, JTAG

programmer, LPC4330 microcontroller, Bluetooth, and switch for selecting an operating mode of the microcontroller. For the stimulator, in this stage of design, a μ LED 90x90 matrix was used. However, in a future design, a 3D model of the optrode will be used to stimulate visual neuron cells. The target and test purpose stimulators on the receiver side are illustrated in Figure 5-20.

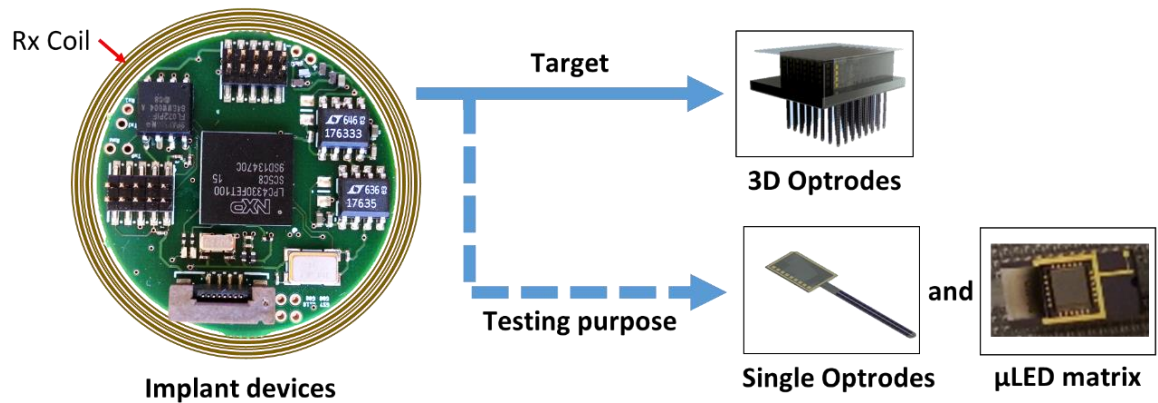


Figure 5-20: The receiver parts of the wireless visual cortical stimulator. The targeted 3D optrode will be used in future work. μ LED 90x90 is used to illustrate the result and single optrode for the blinking test.

Chapter 6. Discussion and Conclusion

In this chapter, all aspects of the system design and results are discussed. After concluding the outcome of this chapter, potential future work will be presented.

6.1 Wireless power transfer

Neither the primary nor secondary type of battery sources were selected to power the implant devices. The primary battery does not provide enough power for the visual prosthesis. For example, the Lithium metal battery CR2032 is coin shaped and can provide 250 mAh and 3 V output. The dimension of the battery is 20 mm x 3.2 mm [248]. This battery can operate the system for only 26 minutes if the total power consumption of the system is 2 Watts, and so these types of batteries are not valid. Although the secondary batteries can be recharged, they have the same problem as the primary batteries in that they can provide power for a very short time and then require recharging. Thus, the most significant factor in using the secondary batteries in brain implant devices is size and related capacity. For this, the Wireless Power Transfer technique is designed and simulated to deliver efficient power to the implant devices.

The main parts in the design of the WPT circuit are an oscillator, coils, power amplifier, AC-DC convertor and regulator. Three type of protocols are designed and tested to generate a square waveform: DS1085L programmable oscillator, 555 timers and crystal oscillator. The DS1085L can be programmed from 8.1 KHz to 133 MHz, but it is not stable. The 555 timer is more stable but cannot be programmed for a frequency higher than 2 MHz. At this stage, the crystal oscillator was the best option because it is stable and can provide the required frequency.

Two types of coils were designed for the receiver side: a circular copper wire and square printed coil. The result of the square printed coil was better than the circle coil, but because of the complexity of the implanted PCB, there was no space to implement the printed coil. As a result, the simple circular copper wire was used on the receiver side. To improve the efficiency of the transferred power, the size of the transmitter coil is designed to be approximately equal to the receiver coil.

To increase the power on the transmitter side, there were two options: a class D amplifier and a class E amplifier. The class D power amplifier is good for frequencies of less than 10 MHz [249], but because the target frequency in this project was 13.56 MHz, the class E power amplifier was selected. This frequency was chosen for this project because of its compatibility with the NFC frequency range and its compliance with ISM bandwidth range.

There are different types and strategies for AC-DC signal conversion, but for simplicity, a full bridge voltage rectifier was selected in this project. The Schottky diodes were used to reduce the power lost on the receiver side. A proper capacitor was connected in parallel with the bridge to reduce the ripple voltage.

The output voltage should be fixed at a specifically required voltage, which should be stable for a small change in distance between the two coils. Several methods have been studied and tested to regulate the voltage. An example of the design of the voltage regulator step by step is shown in Appendix G. Two types of LT1763CDE voltage regulator from Linear Technology were selected to provide 3.3 V and 5 V in the implanted board. For the transmitter side, two DC-DC voltage converters were required, the first to convert 3.7 V to 5 V to operate the Raspberry Pi Zero and related components, and the second to convert 5 V to 12 V to operate the WPT circuit. For the first case, the Adafruit power boost 1000C was purchased, but for the second, the LTC3122 from Linear Technology was selected. The circuit was simulated in NI Multisim, and the PCB layout was designed in NI Ultiboard.

The power transferred was tested through different mediums, namely air, water, and pork. The result was normal for transfer of the power through air. However, there was a reduction in power when it passed through water and pork. The average of the power reduction was approximately 40%.

The targeted range for delivering power to the implanted devices is less than 10 mm. To fix the output voltage, a voltage regulator is used. When the distance between the two coils was increased from 0 to 10 mm, there was no change in voltage on the receiver side. Later, the horizontal alignment between the coils was changed. The edge of the transmitter coil was aligned to the centre of the receiver coil. The result showed no changes in the voltages when the output voltage was fixed at 3.3 V.

6.2 Image processing

This section is divided into two parts, the hardware used for image processing and program code for image processing.

6.2.1 Hardware

On the transmitter side, the Raspberry Pi Zero was used. It is a minicomputer, efficient for image processing because its operating frequency is 1 GHz. Power consumption is significant for the visual prosthesis, especially for the implanted devices. Battery life is an issue for the implanted devices. For low power consumption devices, the battery will run for a longer time. Raspberry Pi Zero is not power hungry compared to other versions of the Raspberry Pi and minicomputer models, as its maximum power consumption is 750 mW. The weight of the external parts is not a problem, but being lightweight it is more convenient to carry. Its weight is only 9 g and the size of the board is acceptable. The Raspberry Pi Zero supports a USB Bluetooth dongle and a USB camera, and it can be programmed in Matlab Simulink, so the code can be easily deployed to it.

The microcontroller ARM Cortex dual core M0&M4F LPC4330 is used at the receiver end. The advantages of the microcontroller are small size, light weight, low power and speed. The round shape PCB is designed to be easy for implanting. The spaces between components on the PCB were decreased to a minimum to keep the overall board size small. There was some extra space on the LPC4330 board, but the size of the HC05 board is too big to fit. The Bluetooth module will be changed to a smaller package in the 3rd version of the LPC4330 board. Therefore, the new board will be slightly smaller.

6.2.2 Software

As well as the retinal processing, other image processing is compiled for both the transmitter and receiver sides. Image simplification is essential to increase the useful information and reduce or decrease the unnecessary information. For this, image smoothing using image cartoonization and edge highlighting is used. The targeted frame size of 64x64 is used. For 25 fps, the total baud width is about 800 kbps, which is much higher than the capability of the Bluetooth link. The maximum baud rate was achieved

at 170 kbps. Image compression is required to reduce the size of the images. The best option at this stage for image compression was an 86% compression ratio. The discrete cosine transform (DCT) was used to convert images to the frequency domain. Normally, DCT is applied to the 8x8 blocks. For the compression ratio of 86%, the 3x3 block was selected from each 8x8 block. This technique is named the DCT_block. Another method used for image compression was Zigzag diagonal scanning to select the required frequency domain elements. Both methods, DCT_block and DCT_Zigzag were compared, and the result was very close. Matlab Simulink was used for the image processing on the transmitter side. The code was deployed to the Raspberry Pi Zero. The result of the processed data was printed to the standard output and then redirected to send over Bluetooth using the Linux commands.

In the receiver side, C code is used to retrieve the original data. The received data for each frame were decompressed after being collected. The LPC4330 is efficient and fast at processing these data when the core frequency is high, but running the microcontroller at a high frequency consumes high power. Using the Digital Signal Processing (DSP) library reduces the power consumption because the microcontroller can run at a low frequency.

Each pixel in a 64x64 frame is in the character format ranges [0, 255] of intensity level. To operate the μ LED, if the whole range is used, the number of sub-frames will be 256. This process is known as pulse modulation. In this project, only 16 levels were used for the intensity level. The μ LED matrix is used as an example of stimulator optrodes. In the portion of the power consumption graph, the μ LED power consumption is three times higher than the LPC4330 board. The power consumption of the targeted 3D optrode should be lower than the μ LED matrix. This means that the total power consumption of the implant devices will decrease.

6.3 Safety

The maximum change in temperature by implanted devices is limited to no more than 2°C. The total power consumption was below 300 mW. The maximum allowance of the power consumption for the implant devices of 30 mm diameter is approximately

480 mW. For this range, the change in temperature was 1°C, which is within the permitted change, as calculated and compared with the literature. This means that the device can be implanted under the skin outside the skull with low risk.

6.4 Conclusion

Blindness is unlike other disorders, as people who cannot see cannot manage their daily needs independently. With the increasing global population, blindness will also increase, and advanced medical electronic devices are one potentially successful method for helping the blind to see again. However, the approved retinal prosthesis can only aid people with retinal pigmentosa. To help a wider range of people by optical stimulation approaches, a visual cortical prosthesis will be an alternative option for restoring sight.

In this work, a wireless visual cortical prosthesis was designed to help blind people to see again. This device consists of hardware and software parts. For hardware achievements, a wireless power system designed and printed on a board to deliver up to 200 mA to the implant part. To increase power on the transmitter side, a class E power amplifier was simulated and designed with an efficiency of 93.43%. There was approximately 40% reduction of power when it was transferred through water and pork. The DC-DC converter board was designed to power the WPT system. In the implantable side, a six-layer PCB was designed to handle the received power and data. The ARM Cortex LPC4330 microcontroller was used for image processing in this board.

For software, on the transmitter side, the Raspberry Pi Zero was programmed using Matlab Simulink. The code includes capturing live streaming images, image implication, image compression and data encoding. On the receiver side, the designed LPC4330 board was programmed using C code for data decoding, image decompression, pulse modulation and operating the μ LED matrix. DSP library is used to reduce the power consumption. The 64x64 image is compressed with the ratio of 86% to allow it to be transferred over Bluetooth as the maximum achieved baud rate of Bluetooth was 170 kbps. There was no change in data with transfer through water and pork. Two techniques of compression were tested, DCT_block and DCT_Zigzag, and there was no great difference between them. The board is safe for implant according to health and

safety limitations because the temperature increase for the implanted board was below 1°C. For the assembly the transmitter parts, the glasses were designed and printed to hold the camera, wireless power transmitter and transmitter coil. Also, an off the shelf box was used to assemble the power management system to recharge the battery and power the transmitter devices, battery, USB hub, Raspberry Pi Zero and Bluetooth.

In conclusion, the wireless optogenetic visual cortical stimulator is designed to restore sight to a wide range of causes of blindness. The prototype version of the system was tested with the μ LED matrix. The future target stimulator is a 3D optrode designed by the CANDO group.

Chapter 7. Future work

Regarding future work, there will be some development of, and improvement in, the existing wireless visual cortical prosthesis project, and other work related to this project. The ideas for developing and improving work are as follows:

1. Use of frame techniques to reduce the size of the image and improve the quality of images. For image compression at 86%, the quality of images is acceptable, but reducing this ratio to 60% compression ratio would be better. However, when the compression ratio is decreased, the size of the images is increased. In this case, a frame to frame compression technique will be useful. This technique was invented by Patrick Degenaar and programmed and tested by Sabah Nayyef. The idea was to compare the two frames and select their similarities. The comparison is made between a frame sent and a frame that needs to be sent, so that similar pixels are not sent. The result of the frame to frame concept is shown in Figure 7-1.

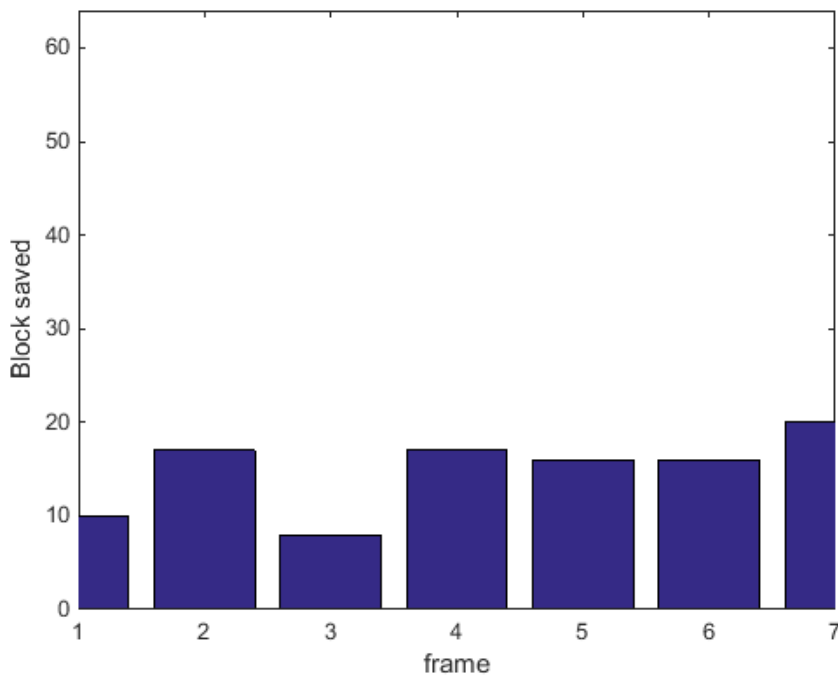


Figure 7-1: The frame to frame technique shows the number of saved blocks. Each block is 8 x 8 pixels, and the total number of blocks in each frame is 64 blocks for the frame size of 64 x 64 pixels [work by Sabah Nayyef].

2. The only step that is not included in this system is the even power distributor (EPD). This is another challenging work to reduce the power consumption in the implanted parts. The idea of the EPD was invented by Patrick Degenaar and the mathematical implementation was performed by Andrew Mokhov at Newcastle University. There is a plan to develop the visual cortical implant system in the future, and the EPD will be one of the targeted projects for this purpose.

3. Use of a smartphone in the transmitter part for image processing. The code for image simplification and image compression written in Matlab will be translated to Java code. The graphics interface will be compatible with both Android and Apple operating systems. The entire code will be connected with the volume button for switching the application on and off. The camera of the mobile phone will be used to capture live streaming videos, and the Bluetooth on the mobile will be used to transfer the data. Bluetooth in the wireless visual cortical implant device is used for this work, and that was another reason Bluetooth was used in this research project.

4. Testing wireless power transfer through water in different temperature ranges, from 0 to 100°C.

5. Testing wireless power transfer through pork using different tuning frequencies. The operating frequencies for this test will be 200 KHz, 2 MHz, 6.78 MHz and 13.56 MHz.

6. The stimulator part is an optrode or μ LED matrix. The optrode was developed by the Controlling Abnormal Network Dynamics using Optogenetics (CANDO) team at Newcastle University. The aim of designing this optrode was to aid people with epilepsy, but the 3D matrix of that optrode can be used to deliver data to the visual cortex to restore sight. The 3D model of the optrode is shown in Figure 7-2, and a three dimensional optrode will be the target for stimulating the brain nerve cells in the future.

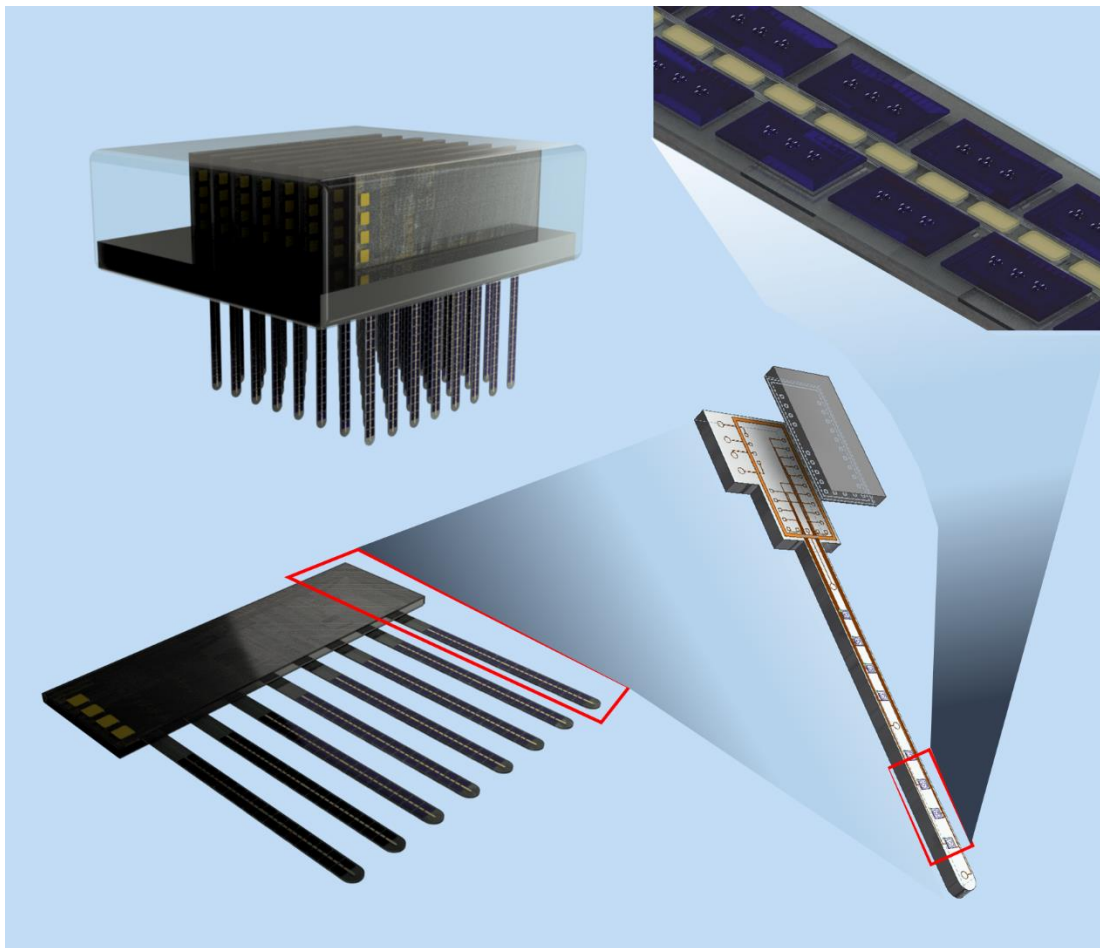


Figure 7-2: The three dimensional optrode exemplar designed by Patrick Degenaar for the CANDO project. This will be used for a visual cortical prosthesis in future work.

References

- [1] R. S. Ramchandran, H. B. Hindman, and S. Sørensen, "16 Vision Impairment and Its Management in Older Adults," in *Geriatric Rehabilitation: From Bedside to Curbside*, ed: CRC Press, 2017, pp. 293-314.
- [2] X. Wei and J. Liu, "Power sources and electrical recharging strategies for implantable medical devices," *Frontiers of Energy and Power Engineering in China*, vol. 2, pp. 1-13, 2008.
- [3] J. G. Webster and H. Eren, *Measurement, instrumentation, and sensors handbook: electromagnetic, optical, radiation, chemical, and biomedical measurement*: CRC press, 2014.
- [4] F.-G. Zeng, "Trends in Cochlear Implants," *Trends in Amplification*, vol. 8, pp. 1-34, 2004.
- [5] C. Hsiao-Chin, Y. Ming-Yu, W. Qi-Xiu, C. Kuo-Jin, and W. Li-Ming, "Batteryless Transceiver Prototype for Medical Implant in 0.18um CMOS Technology," *IEEE Transactions on Microwave Theory and Techniques*, vol. 62, pp. 137-147, 2014.
- [6] A. Rosengren, L. Wallman, N. Danielsen, T. Laurell, and L. M. Bjursten, "Tissue reactions evoked by porous and plane surfaces made out of silicon and titanium," *IEEE Transactions on Biomedical Engineering*, vol. 49, pp. 392-399, 2002.
- [7] D. Hodgins, A. Bertsch, N. Post, M. Frischholz, B. Volckaerts, J. Spensley, *et al.*, "Healthy Aims: Developing New Medical Implants and Diagnostic Equipment," *IEEE Pervasive Computing*, vol. 7, pp. 14-21, 2008.
- [8] Y. H.-L. Luo and L. da Cruz, "The Argus® II Retinal Prosthesis System," *Progress in Retinal and Eye Research*, vol. 50, pp. 89-107, 2016.
- [9] H. Kolb, E. Fernandez, and R. Nelson, *Webvision: The Organization of the Retina and Visual System*: University of Utah Health Sciences Center, 2016.
- [10] L. Zhang, J. Du, S. Justus, C.-W. Hsu, L. Bonet-Ponce, W.-H. Wu, *et al.*, "Reprogramming metabolism by targeting sirtuin 6 attenuates retinal degeneration," *The Journal of Clinical Investigation*, vol. 126, 2016.
- [11] (2017). *Blindness: Vision 2020 - The Global Initiative for the Elimination of Avoidable Blindness*. Available: <http://www.who.int/mediacentre/factsheets/fs213/en/>
- [12] P. M. Lewis and J. V. Rosenfeld, "Electrical stimulation of the brain and the development of cortical visual prostheses: An historical perspective," *Brain Research*, vol. 1630, pp. 208-224, 2016.
- [13] K. Nikolic, N. Grossman, M. S. Grubb, J. Burrone, C. Toumazou, and P. Degenaar, "Photocycles of Channelrhodopsin-2," *Photochemistry and photobiology*, vol. 85, pp. 400-411, 2009.
- [14] G. Calvert, C. Spence, and B. E. Stein, *The handbook of multisensory processes*: MIT press, 2004.
- [15] M. C. Meilgaard, B. T. Carr, and G. V. Civile, *Sensory evaluation techniques*: CRC press, 2006.
- [16] Margaret. (2017). *Parts and Functions of the Eyes*. Available: <http://www.globaleyecare.org/2015/05/09/parts-and-functions-of-the-eyes/>
- [17] A. Dahl. (2016). *Blindness*. Available: <http://www.medicinenet.com/blindness/article.htm>

- [18] S. R. Platt, S. Farritor, K. Garvin, and H. Haider, "The use of piezoelectric ceramics for electric power generation within orthopedic implants," *IEEE/ASME Transactions on Mechatronics*, vol. 10, pp. 455-461, 2005.
- [19] P. D. Mitcheson, "Energy harvesting for human wearable and implantable bio-sensors," in *Annual International Conference of the IEEE Engineering in Medicine and Biology Society (EMBC)*, 2010, pp. 3432-3436.
- [20] A. Sudano, D. Accoto, M. T. Francomano, F. Salvinelli, and E. Guglielmelli, "Optimization of kinetic energy harvesters design for fully implantable Cochlear Implants," in *Annual International Conference of the IEEE Engineering in Medicine and Biology Society (EMBC)*, 2011, pp. 7678-7681.
- [21] K. Dongwon, G. A. Rincon-Mora, and E. O. Torres, "Harvesting Ambient Kinetic Energy With Switched-Inductor Converters," *IEEE Transactions on Circuits and Systems I: Regular Papers*, vol. 58, pp. 1551-1560, 2011.
- [22] K. Murakawa, M. Kobayashi, O. Nakamura, and S. Kawata, "A wireless near-infrared energy system for medical implants," *IEEE Engineering in Medicine and Biology Magazine*, vol. 18, pp. 70-72, 1999.
- [23] D. Panescu, "Emerging Technologies [wireless communication systems for implantable medical devices]," *IEEE Engineering in Medicine and Biology Magazine*, vol. 27, pp. 96-101, 2008.
- [24] A. M. Sodagar and K. Najafi, "Wireless Interfaces for Implantable Biomedical Microsystems," in *49th IEEE International Midwest Symposium on Circuits and Systems (MWSCAS)*, 2006, pp. 265-269.
- [25] W. E. Finn and P. G. LoPresti, *Handbook of Neuroprosthetic Methods*: CRC Press, 2002.
- [26] F. Shahrokhi, K. Abdelhalim, D. Serletis, P. L. Carlen, and R. Genov, "The 128-Channel Fully Differential Digital Integrated Neural Recording and Stimulation Interface," *IEEE Transactions on Biomedical Circuits and Systems*, vol. 4, pp. 149-161, 2010.
- [27] S. K. Moore, "Psychiatry's shocking new tools [brain stimulation techniques]," *IEEE Spectrum*, vol. 43, pp. 24-31, 2006.
- [28] L. Hyung-Min, P. Hangue, and M. Ghovanloo, "A Power-Efficient Wireless System With Adaptive Supply Control for Deep Brain Stimulation," *IEEE Journal of Solid-State Circuits*, vol. 48, pp. 2203-2216, 2013.
- [29] Tianjia Sun, Xiang Xie, and Z. Wang. (2013). *Wireless Power Transfer for Medical Microsystems* [eBook].
- [30] X. Qi, G. Zhaolong, W. Hao, H. Jiping, M. Zhi-Hong, and S. Mingui, "Batteries Not Included: A Mat-Based Wireless Power Transfer System for Implantable Medical Devices As a Moving Target," *IEEE Microwave Magazine*, vol. 14, pp. 63-72, 2013.
- [31] A. Eusebio, W. Thevathasan, L. Doyle Gaynor, A. Pogosyan, E. Bye, T. Foltynie, *et al.*, "Deep brain stimulation can suppress pathological synchronisation in parkinsonian patients," *Journal of Neurology, Neurosurgery & Psychiatry*, vol. 82, pp. 569-573, 2011.
- [32] P. Boon, K. Vonck, V. De Herdt, A. Van Dycke, M. Goethals, L. Goossens, *et al.*, "Deep brain stimulation in patients with refractory temporal lobe epilepsy," *Epilepsia*, vol. 48, pp. 1551-1560, 2007.
- [33] B. Gordon, R. P. Lesser, N. E. Rance, J. Hart Jr, R. Webber, S. Uematsu, *et al.*, "Parameters for direct cortical electrical stimulation in the human: histopathologic confirmation," *Electroencephalography and Clinical Neurophysiology*, vol. 75, pp. 371-377, 1990.

- [34] T. Whitehead. (2013). *Deep Brain Stimulation for Tic Disorders: Fad Therapy or Good Medicine?*. Available: <http://www.skepticink.com/gps/>
- [35] P. D. Bradley, "Wireless medical implant technology—Recent advances and future developments," 2011, pp. 37-41.
- [36] G. Lerosey, "Applied physics: Wireless power on the move," *Nature*, vol. 546, pp. 354-355, 2017.
- [37] K. S. Nikita, *Handbook of biomedical telemetry*: John Wiley & Sons, 2014.
- [38] N. R. F. Al-Rodhan, "The Science and Technology of Human Enhancement," in *The Politics of Emerging Strategic Technologies*, ed: Springer, 2011, pp. 208-223.
- [39] "World Health Organization (WHO): Definition of Health " vol. 2, ed. New York: Official Records of the World Health Organization, 1948, p. 100.
- [40] (2012). *Retinitis Pigmentosa*. Available: <https://rarediseases.org/rare-diseases/retinitis-pigmentosa/>
- [41] J. F. Rizzo, D. B. Shire, S. K. Kelly, P. Troyk, M. Gingerich, B. McKee, *et al.*, "Development of the boston retinal prosthesis," in *Annual International Conference of the IEEE Engineering in Medicine and Biology Society*, 2011, pp. 3135-3138.
- [42] L. S. Theogarajan, "A low-power fully implantable 15-channel retinal stimulator chip," *IEEE Journal of Solid-State Circuits*, vol. 43, pp. 2322-2337, 2008.
- [43] WHO. (2017). *Blindness: Vision 2020 - The Global Initiative for the Elimination of Avoidable Blindness*. Available: <http://www.who.int/mediacentre/factsheets/fs213/en/>
- [44] V. H. H. Gonzalez and T. Moser, "30 Optogenetic Stimulation for Cochlear Prosthetics," *Optogenetics: From Neuronal Function to Mapping and Disease Biology*, p. 442, 2017.
- [45] K. Nazarpour, A. Barnard, and A. Jackson, "Flexible cortical control of task-specific muscle synergies," *Journal of Neuroscience*, vol. 32, pp. 12349-12360, 2012.
- [46] M. Tudor, L. Tudor, and K. I. Tudor, "Hans Berger (1873-1941)--the history of electroencephalography," ed, 2004.
- [47] L. F. Haas, "Hans Berger (1873–1941), Richard Caton (1842–1926), and electroencephalography," *Journal of Neurology, Neurosurgery & Psychiatry*, vol. 74, p. 9, 2003.
- [48] W. Penfield, "The electrode, the brain and the mind," *Zeitschrift für Neurologie*, vol. 201, pp. 297-309, 1972.
- [49] P. Degenaar, "Retinal Prosthesis," in *Encyclopedia of Biophysics*, G. C. K. Roberts, Ed., ed Berlin, Heidelberg: Springer Berlin Heidelberg, 2013, pp. 2227-2231.
- [50] W. T. Liberson, H. J. Holmquest, D. Scot, and M. Dow, "Functional electrotherapy: stimulation of the peroneal nerve synchronized with the swing phase of the gait of hemiplegic patients," *Archives of physical medicine and rehabilitation*, vol. 42, pp. 101-105, 1961.
- [51] R. Tashiro, N. Kabei, K. Katayama, E. Tsuboi, and K. Tsuchiya, "Development of an electrostatic generator for a cardiac pacemaker that harnesses the ventricular wall motion," *Journal of Artificial Organs*, vol. 5, pp. 0239-0245, 2002.
- [52] J. F. Rizzo, "Update on Retinal Prosthetic Research: The Boston Retinal Implant Project," *Journal of Neuro-Ophthalmology*, vol. 31, 2011.
- [53] D. K. Kessler, "The Clarion® Multi-Strategy™ Cochlear Implant," *Annals of Otology, Rhinology & Laryngology*, vol. 108, pp. 8-16, 1999.

- [54] M. S. Humayun, E. de Juan, Jr, G. Dagnelie, R. J. Greenberg, R. H. Propst, *et al.*, "Visual perception elicited by electrical stimulation of retina in blind humans," *Archives of Ophthalmology*, vol. 114, pp. 40-46, 1996.
- [55] A. C. Ho and C. D. Regillo, *Age-related macular degeneration diagnosis and treatment*: Springer Science & Business Media, 2011.
- [56] L. N. Ayton, P. J. Blamey, R. H. Guymer, C. D. Luu, D. A. X. Nayagam, N. C. Sinclair, *et al.*, "First-in-Human Trial of a Novel Suprachoroidal Retinal Prosthesis," *PLOS ONE*, vol. 9, p. e115239, 2014.
- [57] R. R. Harrison, P. T. Watkins, R. J. Kier, R. O. Lovejoy, D. J. Black, B. Greger, *et al.*, "A low-power integrated circuit for a wireless 100-electrode neural recording system," *IEEE Journal of Solid-State Circuits*, vol. 42, pp. 123-133, 2007.
- [58] E. Zrenner, "Will Retinal Implants Restore Vision?," *Science*, vol. 295, p. 1022, 2002.
- [59] J. R. Soohoo, S. S. Lane, R. J. Cionni, J. P. Berdahl, G. R. Sussman, and M. Y. Kahook, "Comparison of stability between a modular intraocular lens system and a single-piece hydrophobic acrylic intraocular lens," *Journal of Cataract & Refractive Surgery*, vol. 42, pp. 1821-1825, 2016.
- [60] C. Skinner and V. Miraldi Utz, "Pharmacological approaches to restoring lens transparency: Real world applications," *Ophthalmic Genetics*, pp. 1-5, 2016.
- [61] R. Chandrawati, J. Y. H. Chang, E. Reina-Torres, C. Jumeaux, J. M. Sherwood, W. D. Stamer, *et al.*, "Localized and Controlled Delivery of Nitric Oxide to the Conventional Outflow Pathway via Enzyme Biocatalysis: Toward Therapy for Glaucoma," *Advanced Materials*, 2017.
- [62] E. Margalit, M. Maia, J. D. Weiland, R. J. Greenberg, G. Y. Fujii, G. Torres, *et al.*, "Retinal Prosthesis for the Blind," *Survey of Ophthalmology*, vol. 47, pp. 335-356, 2002.
- [63] S. B. David C Ng, Jiawei Yang, Nhan Tran and Efstratios Skafidas, "Wireless technologies for closed-loop retinal prostheses," *Journal of Neural Engineering*, vol. 6 2009.
- [64] J. D. Weiland, W. Liu, and M. S. Humayun, "RETINAL PROSTHESIS," *Annual Review of Biomedical Engineering*, vol. 7, pp. 361-401, 2005.
- [65] H. Ko and S. Lee, "Electrical characterization of 2D and 3D microelectrodes for achieving high-resolution sensing in retinal prostheses with in vitro animal experimental results," *Microsystem Technologies*, vol. 23, pp. 473-481, 2017.
- [66] R. A. B. Fernandes, B. Diniz, R. Ribeiro, and M. Humayun, "Artificial vision through neuronal stimulation," *Neuroscience letters*, vol. 519, pp. 122-128, 2012.
- [67] G. S. Brindley and W. S. Lewin, "The sensations produced by electrical stimulation of the visual cortex," *The Journal of Physiology*, vol. 196, pp. 479-493, 1968.
- [68] P. Konrad and T. Shanks, "Implantable brain computer interface: Challenges to neurotechnology translation," *Neurobiology of disease*, vol. 38, pp. 369-375, 2010.
- [69] C. Hassler, T. Boretius, and T. Stieglitz, "Polymers for neural implants," *Journal of Polymer Science Part B: Polymer Physics*, vol. 49, pp. 18-33, 2011.
- [70] R. Normann. (2017). *profile page*. Available: <http://neuroscience.med.utah.edu/faculty/normann.php>
- [71] Cortivis. (2002). *Partners*. Available: <http://cortivis.umh.es/partners.htm>
- [72] (2017). *Intracortical Visual Prosthesis*. Available: <http://neural.iit.edu/research/icvp/>
- [73] M. SAWAN, "NEUROTECHNOLOGY LABORATORY (POLYSTIM)," 2017.

- [74] M. Sawan, B. Gosselin, and J. Coulombe, "Learning from the Primary Visual Cortex to Recover Vision for the Blind by Microstimulation," in *NORCHIP*, 2008, pp. 1-4.
- [75] J. Pezaris. (2017). *Visual Prosthesis Lab*. Available: <http://www.massgeneral.org/neurosurgery/research/researchlab.aspx?id=1466>
- [76] P. M. Lewis and J. V. Rosenfeld, "Electrical stimulation of the brain and the development of cortical visual prostheses: An historical perspective," *Brain Research*, vol. 1630, pp. 208-224, 2016.
- [77] J. B. Troy, "Visual Prostheses: Technological and Socioeconomic Challenges," *Engineering*, vol. 1, pp. 288-291, 2015.
- [78] J. J. Atick and A. N. Redlich, "What does the retina know about natural scenes?," *Neural computation*, vol. 4, pp. 196-210, 1992.
- [79] W. Liu, W. Fink, M. Tarbell, and M. Sivaprakasam, "Image processing and interface for retinal visual prostheses," in *IEEE International Symposium on Circuits and Systems (ISCAS)*, 2005, pp. 2927-2930.
- [80] L. Schwiebert, S. K. S. Gupta, and J. Weinmann, "Research challenges in wireless networks of biomedical sensors," in *7th annual international conference on Mobile computing and networking*, 2001, pp. 151-165.
- [81] M. A. Yaman and P. Degenaar, "FPGA design of an even power distributor for optoelectronic neural stimulation," in *IEEE Jordan Conference on Applied Electrical Engineering and Computing Technologies (AEECT)*, 2013, pp. 1-4.
- [82] W. Al-Atabany, B. McGovern, K. Mehran, R. Berlinguer-Palmini, and P. Degenaar, "A Processing Platform for Optoelectronic/Optogenetic Retinal Prosthesis," *IEEE Transactions on Biomedical Engineering*, vol. 60, pp. 781-791, 2013.
- [83] R. C. Gonzalez and R. E. Woods, "A text book on "Digital Image Processing"," *Publications of Pearson*, 2002.
- [84] A. Nosratinia, "Enhancement of JPEG-compressed images by re-application of JPEG," *The Journal of VLSI Signal Processing*, vol. 27, pp. 69-79, 2001.
- [85] W. A. Pearlman and A. Said, *Digital Signal Compression: principles and practice*: Cambridge University Press, 2011.
- [86] M. Puschel, "Cooley-Tukey FFT like algorithms for the DCT," in *IEEE International Conference on Acoustics, Speech, and Signal Processing (ICASSP'03)*, 2003, pp. II-501.
- [87] N. Ahmed, T. Natarajan, and K. R. Rao, "Discrete cosine transform," *IEEE transactions on Computers*, vol. 100, pp. 90-93, 1974.
- [88] X. Shao and S. G. Johnson, "Type-II/III DCT/DST algorithms with reduced number of arithmetic operations," *Signal Processing*, vol. 88, pp. 1553-1564, 2008.
- [89] Y.-S. Chang, W.-J. Wang, and Y.-S. Hung, "A near field communication-driven home automation framework," *Personal and Ubiquitous Computing*, vol. 17, pp. 169-185, 2013.
- [90] E. Schnell, "Near Field Communications: Features and Considerations," *Journal of Electronic Resources in Medical Libraries*, vol. 10, pp. 98-107, 2013.
- [91] P. Vaillancourt, A. Djemouai, J. F. Harvey, and M. Sawan, "EM radiation behavior upon biological tissues in a radio-frequency power transfer link for a cortical visual implant," in *19th Annual International Conference of the IEEE Engineering in Medicine and Biology Society*, 1997, pp. 2499-2502 vol.6.

- [92] K. F. Warnick, R. B. Gottula, S. Shrestha, and J. Smith, "Optimizing Power Transfer Efficiency and Bandwidth for Near Field Communication Systems," *IEEE Transactions on Antennas and Propagation*, vol. 61, pp. 927-933, 2013.
- [93] L. Frenzel. (2012). *What's The Difference Between EM Near Field And Far Field?* Available: <http://electronicdesign.com/>
- [94] D. C. Yates, A. S. Holmes, and A. J. Burdett, "Optimal transmission frequency for ultralow-power short-range radio links," *IEEE Transactions on Circuits and Systems I: Regular Papers*, vol. 51, pp. 1405-1413, 2004.
- [95] L. Jin-Shyan, S. Yu-Wei, and S. Chung-Chou, "A Comparative Study of Wireless Protocols: Bluetooth, UWB, ZigBee, and Wi-Fi," in *33rd Annual Conference of the IEEE Industrial Electronics Society (IECON)*, 2007, pp. 46-51.
- [96] R. Khalili and K. Salamatian, "A new analytic approach to evaluation of packet error rate in wireless networks," in *3rd Annual Communication Networks and Services Research Conference (CNSR'05)*, 2005, pp. 333-338.
- [97] P. Walter, Z. F. Kisvárdy, M. Görtz, N. Alteheld, G. Rossler, T. Stieglitz, *et al.*, "Cortical activation via an implanted wireless retinal prosthesis," *Investigative ophthalmology & visual science*, vol. 46, pp. 1780-1785, 2005.
- [98] S. Priya and D. J. Inman, *Energy harvesting technologies* vol. 21: Springer, 2009.
- [99] M. H. Maghami, A. M. Sodagar, A. Lashay, H. Riazi-Esfahani, and M. Riazi-Esfahani, "Visual Prostheses: The Enabling Technology to Give Sight to the Blind," *Journal of Ophthalmic & Vision Research*, vol. 9, pp. 494-505, 2014.
- [100] T. Nolte, H. Hansson, and L. L. Bello, "Wireless automotive communications," in *Euromicro Conference on Real-Time Systems*, 2005, pp. 35-38.
- [101] D. Karia, J. Baviskar, R. Makwana, and N. Panchal, "Performance analysis of ZigBee based Load Control and power monitoring system," in *2013 International Conference on Advances in Computing, Communications and Informatics (ICACCI)*, 2013, pp. 1479-1484.
- [102] M. N. Islam and M. R. Yuce, "Review of Medical Implant Communication System (MICS) band and network," *ICT Express*, vol. 2, pp. 188-194, 2016.
- [103] K. Y. Yazdandoost and R. Kohno, "Wireless Communications for Body Implanted Medical Device," in *Asia-Pacific Microwave Conference (APMC)*, 2007, pp. 1-4.
- [104] A. Kiourti, "Between Telemetry: Communication Between Implanted Devices and the External World," *Opticon*, vol. 1826 2010.
- [105] E. Fournier, C. Passirani, C. N. Montero-Menei, and J. P. Benoit, "Biocompatibility of implantable synthetic polymeric drug carriers: focus on brain biocompatibility," *Biomaterials*, vol. 24, pp. 3311-3331, 2003.
- [106] E. Pandey, K. Srivastava, S. Gupta, S. Srivastava, and N. Mishra, "SOME BIOCOMPATIBLE MATERIALS USED IN MEDICAL PRACTICES-A REVIEW," *INTERNATIONAL JOURNAL OF PHARMACEUTICAL SCIENCES AND RESEARCH*, vol. 7, pp. 2748-2755, 2016.
- [107] T. Yuen, W. F. Agnew, L. Bullara, and D. B. McCreery, "Biocompatibility of electrodes and materials in the central nervous system," *Neural Prostheses: Fundamental Studies*, W. Agnew, and D. McCreery, eds (Englewood Cliffs, NJ, Prentice Hall), pp. 171-321, 1990.
- [108] D. D. Zhou, X. T. Cui, A. Hines, and R. J. Greenberg, "Conducting polymers in neural stimulation applications," in *Implantable Neural Prostheses 2*, ed: Springer, 2009, pp. 217-252.
- [109] M. Saini, Y. Singh, P. Arora, V. Arora, and K. Jain, "Implant biomaterials: A comprehensive review," *World Journal of Clinical Cases: WJCC*, vol. 3, p. 52, 2015.

- [110] S. R. Montezuma, J. Loewenstein, C. Scholz, and J. F. Rizzo, "Biocompatibility of materials implanted into the subretinal space of Yucatan pigs," *Investigative ophthalmology & visual science*, vol. 47, pp. 3514-3522, 2006.
- [111] C. Scholz, "Perspectives on: Materials aspects for retinal prostheses," *Journal of Bioactive and Compatible Polymers*, vol. 22, pp. 539-568, 2007.
- [112] R. Sweitzer, C. Scholz, S. Montezuma, and J. F. Rizzo Iii, "Evaluation of subretinal implants coated with amorphous aluminum oxide and diamond-like carbon," *Journal of bioactive and compatible polymers*, vol. 21, pp. 5-22, 2006.
- [113] F.-G. Zeng, S. Rebscher, W. V. Harrison, X. Sun, and H. Feng, "Cochlear implants," in *Implantable Neural Prostheses 1*, ed: Springer, 2009, pp. 85-116.
- [114] R. McVenes and K. Stokes, "Implantable cardiac electrostimulation devices," in *Implantable Neural Prostheses 1*, ed: Springer, 2009, pp. 221-251.
- [115] H. Schüller, T. Fahraeus, and L. Thuesen, "First clinical experience with an automatic output adaption pacemaker based on evoked response," *PACE*, vol. 18, p. 824, 1995.
- [116] J. R. S. Louis, M. Thumm, and G. N. Gale, "Hermetic and non-hermetic packaging of devices," ed: Google Patents, 1980.
- [117] M. F. Nichols, "The challenges for hermetic encapsulation of implanted devices—a review," *Critical reviews in biomedical engineering*, vol. 22, pp. 39-67, 1994.
- [118] Y. Kanda, R. Aoshima, and A. Takada, "Blood compatibility of components and materials in silicon integrated circuits," *Electronics Letters*, vol. 17, pp. 558-559, 1981.
- [119] R. Traeger, "Nonhermeticity of polymeric lid sealants," *IEEE Transactions on Parts, Hybrids, and Packaging*, vol. 13, pp. 147-152, 1977.
- [120] R. Thomas, "Moisture, myths, and microcircuits," *IEEE Transactions on Parts, Hybrids, and Packaging*, vol. 12, pp. 167-171, 1976.
- [121] D. Zhou and E. Greenbaum, "Implantable neural prostheses 1," *Biological and Medical Physics, Biomedical Engineering, Springer Science Business Media, LLC*, 2009.
- [122] G. S. Brindley, "The first 500 patients with sacral anterior root stimulator implants: general description," *Spinal Cord*, vol. 32, pp. 795-805, 1994.
- [123] A. Vanhoostenberghe and N. Donaldson, "Corrosion of silicon integrated circuits and lifetime predictions in implantable electronic devices," *Journal of neural engineering*, vol. 10, p. 031002, 2013.
- [124] M. S. Humayun, E. de Juan Jr, J. D. Weiland, G. Dagnelie, S. Katona, R. Greenberg, et al., "Pattern electrical stimulation of the human retina," *Vision Research*, vol. 39, pp. 2569-2576, 1999.
- [125] L. Hesse, T. Schanze, M. Wilms, and M. Eger, "Implantation of retina stimulation electrodes and recording of electrical stimulation responses in the visual cortex of the cat," *Graefe's Archive for Clinical and Experimental Ophthalmology*, vol. 238, pp. 840-845, 2000.
- [126] T. M. O'Hearn, S. R. Sadda, J. D. Weiland, M. Maia, E. Margalit, and M. S. Humayun, "Electrical stimulation in normal and retinal degeneration (rd1) isolated mouse retina," *Vision Research*, vol. 46, pp. 3198-3204, 2006.
- [127] J. Vidal and M. Ghovanloo, "Towards a Switched-Capacitor based Stimulator for efficient deep-brain stimulation," in *Annual International Conference of the IEEE Engineering in Medicine and Biology Society (EMBC)*, 2010, pp. 2927-2930.

- [128] A. Hassan and M. S. Okun, "Emerging Subspecialties in Neurology: Deep brain stimulation and electrical neuro-network modulation.," *Neurology*, vol. 80, pp. e47-e50, 2013.
- [129] C. Vidaurre, J. Pascual, A. Ramos-Murguialday, R. Lorenz, B. Blankertz, N. Birbaumer, *et al.*, "Neuromuscular electrical stimulation induced brain patterns to decode motor imagery," *Clinical Neurophysiology*, vol. 124, pp. 1824-1834, 2013.
- [130] P. Degenaar, N. Grossman, M. A. Memon, J. Burrone, M. Dawson, E. Drakakis, *et al.*, "Optobionic vision—a new genetically enhanced light on retinal prosthesis," *Journal of neural engineering*, vol. 6, p. 035007, 2009.
- [131] W. Jing, W. Fabien, A. B. David, Z. Jiayi, O. Ilker, D. B. Rebecca, *et al.*, "Integrated device for combined optical neuromodulation and electrical recording for chronic in vivo applications," *Journal of Neural Engineering*, vol. 9, p. 016001, 2012.
- [132] A. V. Kravitz, S. F. Owen, and A. C. Kreitzer, "Optogenetic identification of striatal projection neuron subtypes during in vivo recordings," *Brain Research*, vol. 1511, pp. 21-32, 2013.
- [133] N. Grossman, K. Nikolic, C. Toumazou, and P. Degenaar, "Modeling Study of the Light Stimulation of a Neuron Cell With Channelrhodopsin-2 Mutants," *IEEE Transactions on Biomedical Engineering*, vol. 58, pp. 1742-1751, 2011.
- [134] R. Pashaie, P. Anikeeva, J. H. Lee, R. Prakash, O. Yizhar, M. Prigge, *et al.*, "Optogenetic brain interfaces," *IEEE reviews in biomedical engineering*, vol. 7, pp. 3-30, 2014.
- [135] F. Veringa, "Electro-optical stimulation of the human retina as a research technique," *Documenta Ophthalmologica*, vol. 18, pp. 72-82, 1964.
- [136] S. Santaniello, G. Fiengo, L. Glielmo, and W. M. Grill, "Closed-Loop Control of Deep Brain Stimulation: A Simulation Study," *IEEE Transactions on Neural Systems and Rehabilitation Engineering*, vol. 19, pp. 15-24, 2011.
- [137] M. J. Birdno, S. E. Cooper, A. R. Rezai, and W. M. Grill, "Pulse-to-Pulse Changes in the Frequency of Deep Brain Stimulation Affect Tremor and Modeled Neuronal Activity," *Journal of Neurophysiology*, vol. 98, pp. 1675-1684, 2007.
- [138] A. Scheiner, G. Polando, and E. B. Marsolais, "Design and clinical application of a double helix electrode for functional electrical stimulation," *IEEE Transactions on Biomedical Engineering*, vol. 41, pp. 425-431, 1994.
- [139] S. Negi, R. Bhandari, L. Rieth, R. Van Wagenen, and F. Solzbacher, "Neural Electrode Degradation from Continuous Electrical Stimulation: Comparison of Sputtered and Activated Iridium Oxide," *Journal of neuroscience methods*, vol. 186, p. 8, 10/28 2010.
- [140] W. G. David Brocker *Brain Stimulation: Chapter 1. Principles of electrical stimulation of neural tissue*: Elsevier Inc, 2013.
- [141] X. F. Wei and W. M. Grill, "Impedance characteristics of deep brain stimulation electrodes in vitro and in vivo," *Journal of neural engineering*, vol. 6, p. 046008, 2009.
- [142] E. S. Boyden, F. Zhang, E. Bamberg, G. Nagel, and K. Deisseroth, "Millisecond-timescale, genetically targeted optical control of neural activity," *Nat Neurosci*, vol. 8, pp. 1263-1268, 2005.
- [143] T. Ishizuka, M. Kakuda, R. Araki, and H. Yawo, "Kinetic evaluation of photosensitivity in genetically engineered neurons expressing green algae light-gated channels," *Neuroscience Research*, vol. 54, pp. 85-94, 2006.

- [144] T. V. F. Abaya, S. Blair, P. Tathireddy, L. Rieth, and F. Solzbacher, "A 3D glass optrode array for optical neural stimulation," *Biomedical Optics Express*, vol. 3, pp. 3087-3104, 2012.
- [145] G. Nagel, D. Ollig, M. Fuhrmann, S. Kateriya, A. M. Musti, E. Bamberg, *et al.*, "Channelrhodopsin-1: A Light-Gated Proton Channel in Green Algae," *Science*, vol. 296, p. 2395, 2002.
- [146] E. A. C. Pama, L. Colzato, and B. Hommel, "Optogenetics as a neuromodulation tool in cognitive neuroscience," *Frontiers in Psychology*, vol. 4, p. 610, 2013.
- [147] N. Grossman, V. Poher, M. Grubb, G. Kennedy, K. Nikolic, B. McGovern, *et al.*, "Multi-site optical excitation using ChR2 and micro-LED array," *Journal of Neural Engineering*, vol. 7, 2010.
- [148] B. McGovern, R. Berlinguer Palmi, N. Grossman, E. Drakakis, V. Poher, M. A. A. Neil, *et al.*, "A New Individually Addressable Micro-LED Array for Photogenetic Neural Stimulation," *IEEE Transactions on Biomedical Circuits and Systems*, vol. 4, pp. 469-476, 2010.
- [149] V. K. Khanna, *Implantable Medical Electronics: Prosthetics, Drug Delivery, and Health Monitoring*, 2016.
- [150] A. B. Amar, A. B. Kouki, and H. Cao, "Power approaches for implantable medical devices," *Sensors*, vol. 15, pp. 28889-28914, 2015.
- [151] Y. Rajavi, M. Taghivand, K. Aggarwal, A. Ma, and A. S. Y. Poon, "An RF-Powered FDD Radio for Neural Microimplants," *IEEE Journal of Solid-State Circuits*, vol. PP, pp. 1-9, 2017.
- [152] N. Fattah, S. Laha, D. Sokolov, G. Chester, and P. Degenaar, "Wireless data and power transfer of an optogenetic implantable visual cortex stimulator," in *37th Annual International Conference of the IEEE Engineering in Medicine and Biology Society (EMBC)*, Italy, 2015, pp. 8006-8009.
- [153] H. Gensler, R. Sheybani, P.-Y. Li, R. Lo, and E. Meng, "An Implantable MEMS Micropump System for Drug Delivery in Small Animals," *Biomedical Microdevices*, vol. 14, pp. 483-496, 2012.
- [154] J. Lee, H. G. Rhew, D. R. Kipke, and M. P. Flynn, "A 64 Channel Programmable Closed-Loop Neurostimulator With 8 Channel Neural Amplifier and Logarithmic ADC," *IEEE Journal of Solid-State Circuits*, vol. 45, pp. 1935-1945, 2010.
- [155] S. Fedel, M. A. Afromowitz, and R. A. Sigelmann, "Micropower Pulse Frequency Modulator for Use in an Optically Isolated Catheter System," *IEEE Transactions on Biomedical Engineering*, vol. BME-29, pp. 549-551, 1982.
- [156] E. K. C. Tsang and B. E. Shi, "A Neuromorphic Multi-chip Model of a Disparity Selective Complex Cell," 2003, pp. 1051-1058.
- [157] J. I. Loewenstein, S. R. Montezuma, J. F. Rizzo, and Iii, "Outer retinal degeneration: An electronic retinal prosthesis as a treatment strategy," *Archives of Ophthalmology*, vol. 122, pp. 587-596, 2004.
- [158] S. Szczesny, S. Jetzki, and S. Leonhardt, "Review of Current Actuator Suitability for Use in Medical Implants," in *28th IEEE Annual International Conference of the Engineering in Medicine and Biology Society (EMBS)*, 2006, pp. 5956-5959.
- [159] D. C. Sigg, P. A. Iaizzo, Y.-F. Xiao, and B. He, *Cardiac electrophysiology methods and models*: Springer Science & Business Media, 2010.
- [160] D. C. Bock, A. C. Marschilok, K. J. Takeuchi, and E. S. Takeuchi, "Batteries used to power implantable biomedical devices," *Electrochimica Acta*, vol. 84, pp. 155-164, 2012.

- [161] W. Greatbatch, J. H. Lee, W. Mathias, M. Eldridge, J. R. Moser, and A. A. Schneider, "The Solid-State Lithium Battery: A New Improved Chemical Power Source for Implantable Cardiac Pacemakers," *IEEE Transactions on Biomedical Engineering*, vol. BME-18, pp. 317-324, 1971.
- [162] E. S. Takeuchi and R. A. Leising, "Lithium Batteries for Biomedical Applications," *MRS Bulletin*, vol. 27, pp. 624-627, 2002.
- [163] C. F. Holmes, "The role of lithium batteries in modern health care," *Journal of Power Sources*, vol. 97-98, pp. 739-741, 2001.
- [164] A. M. Crespi, S. K. Somdahl, C. L. Schmidt, and P. M. Skarstad, "Evolution of power sources for implantable cardioverter defibrillators," *Journal of Power Sources*, vol. 96, pp. 33-38, 2001.
- [165] E. Lee, E. Matei, J. Gord, P. Hess, P. Nercessian, H. Stover, *et al.*, "A Biomedical Implantable FES Battery-Powered Micro-Stimulator," *IEEE Transactions on Circuits and Systems I: Regular Papers*, vol. 56, pp. 2583-2596, 2009.
- [166] (2013). *Li-Ion Family*. Available: <http://www.eaglepicher.com/li-ion-family>
- [167] M. R. Palacin, "Recent advances in rechargeable battery materials: a chemist's perspective," *Chemical Society Reviews*, vol. 38, pp. 2565-2575, 2009.
- [168] P. Li and R. Bashirullah, "A Wireless Power Interface for Rechargeable Battery Operated Medical Implants," *IEEE Transactions on Circuits and Systems II: Express Briefs*, vol. 54, pp. 912-916, 2007.
- [169] V. S. Mallela, V. Ilankumaran, and S. N. Rao, "Trends in cardiac pacemaker batteries," *Indian pacing and electrophysiology journal*, vol. 4, pp. 201-212, 2004.
- [170] K. Goto, T. Nakagawa, O. Nakamura, and S. Kawata, "An implantable power supply with an optically rechargeable lithium battery," *IEEE Transactions on Biomedical Engineering*, vol. 48, pp. 830-833, 2001.
- [171] L. Shuenn-Yuh, C. Chih-Jen, and L. Ming-Chun, "A Low-Power Bidirectional Telemetry Device With a Near-Field Charging Feature for a Cardiac Microstimulator," *IEEE Transactions on Biomedical Circuits and Systems*, vol. 5, pp. 357-367, 2011.
- [172] Y. Yang and J. Liu, "Evaluation on the Power-Generation Capacity of an Implantable Thermoelectric Generator Driven by Radioisotope Fuel," *Journal of Heat Transfer*, vol. 135, pp. 071004-071004, 2013.
- [173] S. n. Suzuki, T. Katane, H. Saotome, and O. Saito, "A proposal of electric power generating system for implanted medical device's," in *IEEE International Magnetism Conference (INTERMAG)*, 1999, pp. HF03-HF03.
- [174] W. J. Spencer, W. T. Corbett, L. R. Dominguez, and B. D. Shafer, "An electronically controlled piezoelectric insulin pump and valves," *IEEE Transactions on Sonics and Ultrasonics*, vol. 25, pp. 153-156, 1978.
- [175] C. B. Williams and R. B. Yates, "Analysis of a micro-electric generator for microsystems," *Sensors and Actuators A: Physical*, vol. 52, pp. 8-11, 1996.
- [176] C. Hyoun-Kyu, P. Woo-Tae, and J. Minkyu, "A CMOS Rectifier With a Cross-Coupled Latched Comparator for Wireless Power Transfer in Biomedical Applications," *Circuits and Systems II: Express Briefs, IEEE Transactions on*, vol. 59, pp. 409-413, 2012.
- [177] E. G. Kilinc, C. Dehollain, and F. Maloberti, *Remote Powering and Data Communication for Implanted Biomedical Systems*: Springer International Publishing, 2015.

- [178] B.-J. Jang, S. Lee, and H. Yoon, "HF-band wireless power transfer system: Concept, issues, and design," *Progress in electromagnetics research*, vol. 124, pp. 211-231, 2012.
- [179] Y. P. Lin, C. Y. Yeh, P. Y. Huang, Z. Y. Wang, H. H. Cheng, Y. T. Li, *et al.*, "A Battery-Less, Implantable Neuro-Electronic Interface for Studying the Mechanisms of Deep Brain Stimulation in Rat Models," *IEEE Transactions on Biomedical Circuits and Systems*, vol. 10, pp. 98-112, 2016.
- [180] G. Xu, X. Yang, Q. Yang, J. Zhao, and Y. Li, "Design on Magnetic Coupling Resonance Wireless Energy Transmission and Monitoring System for Implanted Devices," *IEEE Transactions on Applied Superconductivity*, vol. 26, pp. 1-4, 2016.
- [181] S. Stoecklin, A. Yousaf, T. Volk, and L. Reindl, "Efficient Wireless Powering of Biomedical Sensor Systems for Multichannel Brain Implants," *IEEE Transactions on Instrumentation and Measurement*, vol. 65, pp. 754-764, 2016.
- [182] T. Volk, A. Yousaf, J. Albesa, S. Stöcklin, S. Hussain, C. A. Gkogkidis, *et al.*, "Wireless power distribution system for brain implants," in *IEEE International Instrumentation and Measurement Technology Conference (I2MTC)*, 2015, pp. 1249-1254.
- [183] B. Swain, K. Kumar, D. P. Kar, P. P. Nayak, S. Bhuyan, and R. Sharma, "Development of miniature wireless energy transfer system for implantable pressure sensor," in *524th IEEE International Conference: Electrical, Electronics, Signals, Communication & Optimization, (IEESCO)*, 2015.
- [184] X. Li, C. Y. Tsui, and W. H. Ki, "A 13.56 MHz Wireless Power Transfer System With Reconfigurable Resonant Regulating Rectifier and Wireless Power Control for Implantable Medical Devices," *IEEE Journal of Solid-State Circuits*, vol. 50, pp. 978-989, 2015.
- [185] R. Carta and R. Puers, "Wireless power and data transmission for robotic capsule endoscopes," in *18th IEEE Symposium on Communications and Vehicular Technology in the Benelux (SCVT)*, 2011, pp. 1-6.
- [186] J. Uei-Ming and M. Ghovanloo, "Design and Optimization of Printed Spiral Coils for Efficient Transcutaneous Inductive Power Transmission," *IEEE Transactions on Biomedical Circuits and Systems*, vol. 1, pp. 193-202, 2007.
- [187] M. Ghovanloo and S. Atluri, "A Wide-Band Power-Efficient Inductive Wireless Link for Implantable Microelectronic Devices Using Multiple Carriers," *IEEE Transactions on Circuits and Systems I: Regular Papers*, vol. 54, pp. 2211-2221, 2007.
- [188] C. Sauer, M. Stanacevic, G. Cauwenberghs, and N. Thakor, "Power harvesting and telemetry in CMOS for implanted devices," *IEEE Transactions on Circuits and Systems I: Regular Papers*, vol. 52, pp. 2605-2613, 2005.
- [189] G. A. Kendir, L. Wentai, W. Guoxing, M. Sivaprakasam, R. Bashirullah, M. S. Humayun, *et al.*, "An optimal design methodology for inductive power link with class-E amplifier," *IEEE Transactions on Circuits and Systems I: Regular Papers*, vol. 52, pp. 857-866, 2005.
- [190] M. A. Stuchly and S. S. Stuchly, "Dielectric properties of biological substances—tabulated," *Journal of Microwave Power*, vol. 15, pp. 19-25, 1980.
- [191] J.-M. Kim, D. H. Oh, J.-H. Park, J.-W. Cho, Y. Kwon, C. Cheon, *et al.*, "Permittivity measurements up to 30 GHz using micromachined probe," *Journal of Micromechanics and Microengineering*, vol. 15, p. 543, 2004.

- [192] S. Gabriel, R. W. Lau, and C. Gabriel, "The dielectric properties of biological tissues: II. Measurements in the frequency range 10 Hz to 20 GHz," *Physics in medicine and biology*, vol. 41, p. 2251, 1996.
- [193] W. R. Adey, "Biological effects of electromagnetic fields," *Journal of cellular biochemistry*, vol. 51, pp. 410-416, 1993.
- [194] N. Ahuja, M. M. Eshaghian-Wilner, Z. Ge, R. Liu, A. S. N. Pati, K. Ravicz, *et al.*, "WIRELESS POWER FOR IMPLANTABLE DEVICES: A TECHNICAL REVIEW," *Wireless Computing in Medicine: From Nano to Cloud with Ethical and Legal Implications*, p. 187, 2016.
- [195] K. Agarwal, R. Jegadeesan, Y. X. Guo, and N. V. Thakor, "Wireless Power Transfer Strategies for Implantable Bioelectronics: Methodological Review," *IEEE Reviews in Biomedical Engineering*, vol. PP, pp. 1-1, 2017.
- [196] N. Shinohara, *Wireless power transfer via radiowaves*: John Wiley & Sons, 2014.
- [197] A. E. Umenei, "Understanding low frequency non-radiative power transfer," *Wireless Power Consortium contribution by Fulton Innovation LLC*, vol. 7575, 2011.
- [198] A. Karalis, J. D. Joannopoulos, and M. Soljačić, "Efficient wireless non-radiative mid-range energy transfer," *Annals of Physics*, vol. 323, pp. 34-48, 2008.
- [199] K. Finkenzeller. (2003). *RFID Handbook: Fundamentals and Applications in Contactless Smart Cards and Identification (2nd ed ed.)*.
- [200] P. D. Youbok Lee. (2003) Antenna Circuit Design for RFID Applications. *Microchip*. 50. Available: <http://www.microchip.com>
- [201] Kirk and Hodgson. (2007). *Topic 12: Electromagnetic Induction* Available: <http://www.patana.ac.th/secondary/science/anrophysics/ntopic12/commentary.htm>
- [202] R. Pethig and D. B. Kell, "The passive electrical properties of biological systems: their significance in physiology, biophysics and biotechnology," *Physics in medicine and biology*, vol. 32, p. 933, 1987.
- [203] F. W. Grover, *Inductance calculations, working formulas and tables* USA, New York: D. Van Nostrand 1946.
- [204] F. R. Spellman. (2000). *Electricity : Electricity*. Available: <http://NCL.ebib.com/patron/FullRecord.aspx?p=263195>
- [205] W. Storr. (2013). *Electronics Tutorial about Mutual Inductance*. Available: <http://www.electronics-tutorials.ws/>
- [206] K. A. Grajski, R. Tseng, and C. Wheatley, "Loosely-coupled wireless power transfer: Physics, circuits, standards," in *IEEE MTT-S International Microwave Workshop Series on Innovative Wireless Power Transmission: Technologies, Systems, and Applications (IMWS)*, 2012, pp. 9-14.
- [207] H. Ali, T. J. Ahmad, and S. A. Khan, "Inductive link design for medical implants," in *IEEE Symposium on Industrial Electronics & Applications (ISIEA)*, 2009, pp. 694-699.
- [208] J. Kim, H.-C. Son, K.-H. Kim, and Y.-J. Park, "Efficiency analysis of magnetic resonance wireless power transfer with intermediate resonant coil," *IEEE Antennas and Wireless Propagation Letters*, vol. 10, pp. 389-392, 2011.
- [209] R. A. De Graaf, *In vivo NMR spectroscopy: principles and techniques*: John Wiley & Sons, 2008.
- [210] W. Ko, S. Liang, and C. F. Fung, "Design of radio-frequency powered coils for implant instruments," *Medical and Biological Engineering and Computing*, vol. 15, pp. 634-640, 1977.

- [211] C. J. Stevens, "Magnetoinductive Waves and Wireless Power Transfer," *IEEE Transactions on Power Electronics*, vol. 30, pp. 6182-6190, 2015.
- [212] B. Teck Chuan, I. Takehiro, K. Masaki, and H. Yoichi, "Basic study of improving efficiency of wireless power transfer via magnetic resonance coupling based on impedance matching," in *IEEE International Symposium on Industrial Electronics*, 2010, pp. 2011-2016.
- [213] J. Hantschel, "A P P L I C A T I O N N O T E: Wireless Energy Transmission Coils as Key Components," 2013.
- [214] T. P. Duong and J.-W. Lee, "Experimental results of high-efficiency resonant coupling wireless power transfer using a variable coupling method," *IEEE Microwave and Wireless Components Letters*, vol. 21, pp. 442-444, 2011.
- [215] S. Mutashar, M. A. Hannan, S. A. Samad, and A. Hussain, "Efficiency Improvement of Wireless Power Transmission for Bio-Implanted Devices," *International Journal of Biomedical Engineering*, vol. 7, 2013.
- [216] T. T. Le, J. Han, A. von Jouanne, K. Mayaram, and T. S. Fiez, "Piezoelectric micro-power generation interface circuits," *IEEE journal of solid-state circuits*, vol. 41, pp. 1411-1420, 2006.
- [217] D. Alghisi, M. Ferrari, and V. Ferrari, "Active rectifier circuits with sequential charging of storage capacitors (SCSC) for energy harvesting in autonomous sensors," *Procedia Engineering*, vol. 25, pp. 211-214, 2011.
- [218] B. L. Dokić and B. Blanuša, *Power Electronics*: Springer, 2015.
- [219] "LT1763 Series 500mA, Low Noise, LDO Micropower Regulators," L. Technology, Ed., ed, 1999.
- [220] W. Huang, "Li-Polymer Battery Technology Specification ", L. SHENZHEN PKCELL BATTERY CO., Ed., ed. China: ENGINEERED IN NYC Adafruit, 2014.
- [221] C. Simpson, "Characteristics of Rechargeable Batteries," Texas Instruments Incorporated 2011.
- [222] Ian. (28 Nov 2008). *PARTS: 133MHZ-16.2KHZ PROGRAMMABLE OSCILLATOR (DS1077)*. Available: <http://hackaday.com/2008/11/28/parts-133mhz-162khz-programmable-oscillator-ds1077/>
- [223] J. H. Han, H. G. Lim, J. M. Kim, M. K. Kim, C. W. Lee, I. Y. Park, *et al.*, "Inductively-Coupled Control Unit for Fully Implantable Middle Ear Hearing Devices," in *27th Annual Conference IEEE Engineering in Medicine and Biology 2005*, pp. 4704-4707.
- [224] M. D. Hanamane, R. R. Mudholkar, B. T. Jadhav, and S. R. Sawant, "Implementation of fuzzy temperature control using microprocessor," 2006.
- [225] P. Heydari and Y. Zhang, "A novel high frequency, high-efficiency, differential class-E power amplifier in 0.18 μm CMOS," in *International symposium on Low power electronics and design*, 2003, pp. 455-458.
- [226] F. H. Raab, "Effects of circuit variations on the class E tuned power amplifier," *IEEE Journal of Solid-State Circuits*, vol. 13, pp. 239-247, 1978.
- [227] E. A. Kimbrel and R. Lanza, "Current status of pluripotent stem cells: moving the first therapies to the clinic," *Nat Rev Drug Discov*, vol. 14, pp. 681-692, 2015.
- [228] D. Purves, G. J. Augustine, D. Fitzpatrick, W. C. Hall, A.-S. LaMantia, and L. E. White, "Neuroscience, Animation 5.3: Ionotropic and Metabolic Receptors," 2012.
- [229] V. R. Gaddam, R. Langseth, S. Ljødal, P. Gurdjos, V. Charvillat, C. Griwodz, *et al.*, "Interactive zoom and panning from live panoramic video," p. 19.

- [230] E. Upton. (2015). *RASPBERRY PI ZERO: THE \$5 COMPUTER*. Available: <https://www.raspberrypi.org/blog/raspberry-pi-zero/>
- [231] M. B. Pawloski, "System and method for producing input/output expansion for single chip microcomputers," ed: Google Patents, 1995.
- [232] VYSAKH. (2011). *Basics of Microcontrollers*. Available: <http://www.circuitstoday.com>
- [233] S. D. P. R. Dawoud, *Digital system design - use of microcontroller*. Aalborg, Denmark: River Publishers, 2010.
- [234] "Kinetis K64F Sub-Family Data Sheet," N. Semiconductors, Ed., ed, 2016.
- [235] "OMAP-L138 C6000™ DSP+ ARM® Processor Datasheet," T. Instruments, Ed., ed, Jan 2017.
- [236] "XS1-L4A-64-TQ48 Datasheet," X. Ltd, Ed., ed, 2015.
- [237] "Atmel-11238D-ATARM-SAMA5D4-Datasheet," A. Corporation, Ed., ed, 2016.
- [238] "BCM2835 ARM Peripherals," B. Corporation, Ed., ed. Broadcom Europe Ltd. 406 Science Park Milton Road Cambridge CB4 0WW, 2012.
- [239] "Cortex™-M0 Technical Reference Manual," A. Limited, Ed., ed. ARM DDI 0432C (ID113009), 2009.
- [240] "Kinetis K64F Sub-Family DataSheet," N. Semiconductors, Ed., ed. Document Number K64P144M120SF5; <http://www.nxp.com/>, 2016.
- [241] "LPC4350/30/20/10," N. Semiconductors, Ed., ed, 2016.
- [242] Plugable. (2016). *PLUGABLE USB 2.0 BLUETOOTH ADAPTER*. Available: <http://plugable.com/products/usb-bt4le/>
- [243] V. Stanković, D. Jovanović, D. Krstić, V. Marković, and N. Cvetković, "Temperature distribution and Specific Absorption Rate inside a child's head," *International Journal of Heat and Mass Transfer*, vol. 104, pp. 559-565, 2017.
- [244] P. Bustamante, "Analysis of experimental licenses of the federal communications commission (FCC)," Master's Thesis, 2017.
- [245] I. ada, "Adafruit Powerboost 1000C," 26 Nov 2016.
- [246] (2017). *PCB Technical Capability*. Available: <http://www.pcbtrain.co.uk/resources/pcb-technical-capability/>
- [247] ISO, "Implants for surgery -- Active implantable medical devices -- Part 1: General requirements for safety, marking and for information to be provided by the manufacturer," 2014.
- [248] sparkfun. (2017). *Coin Cell Battery - 20mm (CR2032)*. Available: <https://www.sparkfun.com/products/338>
- [249] P. Muggler, "Filter-Free™ Class-D Audio Amplifiers," 2010.

Appendix A. Calculating the total impedance RLC

Matlab code for total impedance for parallel RLC circuit

```
clear all;
clc;
% components
R1=0; XL1=179; XC1=182;
R2=0; XL2=0; XC2=110;
R3=50; XL3=0; XC3=0;

% claculating impedance
Z1=R1+(XL1-XC1)*1j;
Z2=R2+(XL2-XC2)*1j;
Z3=R3+(XL3-XC3)*1j;

% Total impedance
ZT=(Z1*Z2*Z3)/((Z2*Z3)+(Z1*Z3)+(Z1*Z2));
MT=abs(ZT); thetaZT=angle(ZT)*180/pi;
disp('Total Impedance ZT='); disp(ZT);
fprintf('in polar form M=%0.4fohms\ttheta=%0.4fdegree\n', MT, thetaZT);
```

Appendix B. Programing DS1085L

Arduino cod script for programing the DS1085 programmable oscillator

```
#include <Wire.h>

const int DS_1085L_address = 0xB0 >> 1;
const byte freq_pin = 1;

void setup() {
  Wire.begin();

  Serial.begin(9600);
  pinMode(freq_pin, INPUT);

  //Initialize the programmer
  i2c_write(DS_1085L_address, 0x08, 0x50, 0xF9); //Access DAC [08h]
  //delay(500);
  i2c_write(DS_1085L_address, 0x0E, 0x08); //Access OFFSET [0Eh]
  // delay(500);
  i2c_write(DS_1085L_address, 0x01, 0x00, 0x32); //Access DIV [01h]
  // delay(500);
  i2c_write(DS_1085L_address, 0x02, 0x00, 0x00); //Access MUX [02h]
  // delay(500);
  i2c_write(DS_1085L_address, 0x0D); //Access ADDR [0Dh]
  // delay(500);
  i2c_write(DS_1085L_address, 0x37, 0x00); //Access RANGE [37h]
  //delay(500);
  i2c_write(DS_1085L_address, 0x3F, 0x00, 0x00); //Write E2 [3Fh]
  //delay(500);
}

void loop() {
  // Read frequency
  Serial.println(getFrequency(freq_pin));
}

void i2c_write(int device, byte address)
{
  Wire.beginTransaction(device);
  Wire.write(address);
  Wire.endTransmission();
}

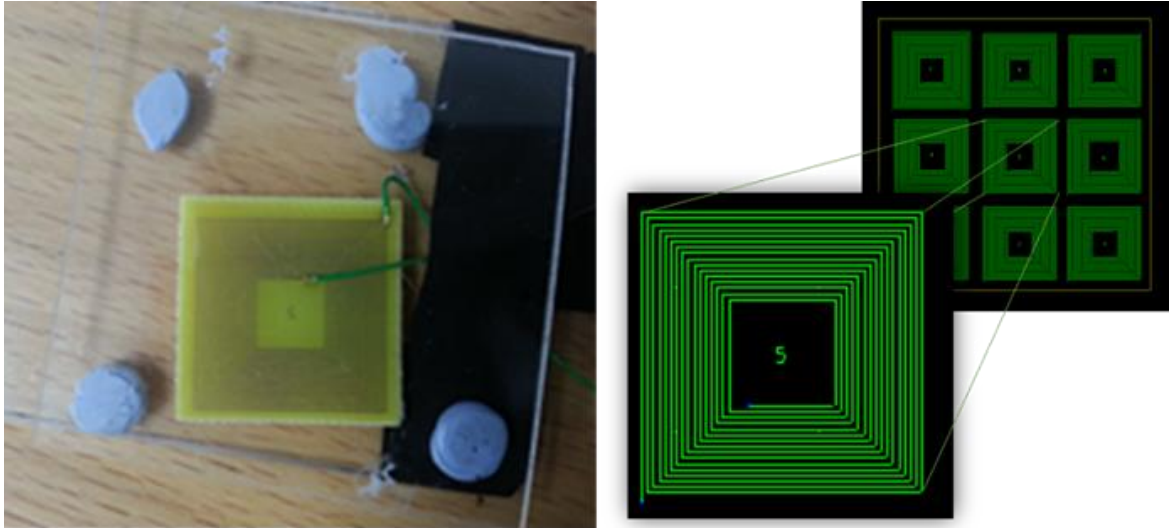
void i2c_write(int device, byte address, byte val1)
{
  Wire.beginTransaction(device);
  Wire.write(address);
  Wire.write(val1);
  Wire.endTransmission();
}
```

```
void i2c_write(int device, byte address, byte val1, byte val2) {  
    Wire.beginTransaction(device);  
    Wire.write(address);  
    Wire.write(val1);  
    Wire.write(val2);  
    Wire.endTransmission();  
}
```

```
long getFrequency(int pin) {  
    #define SAMPLES 4096  
    long freq = 0;  
    for(unsigned int j=0; j<SAMPLES; j++)  
        freq+= 500000/pulseIn(pin, HIGH, 250000);  
    return freq / SAMPLES;  
}
```


Appendix C. PCB coil

(Right) Layout of the printed circuit board coil design using national instrument software package. (Left) The sample of coil after printing in the Newcastle University.

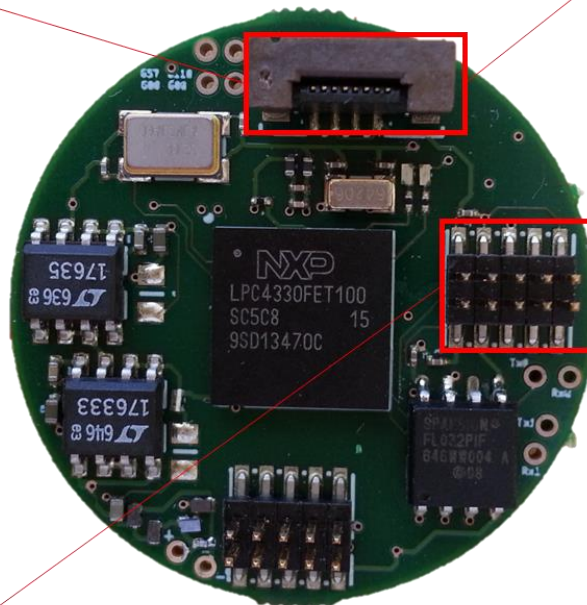


Appendix D. LPC4330 V2.0 pinout

The μ LED header for controlling the optrode and SPI for general serial peripheral interfaces.

μ LED header pinout

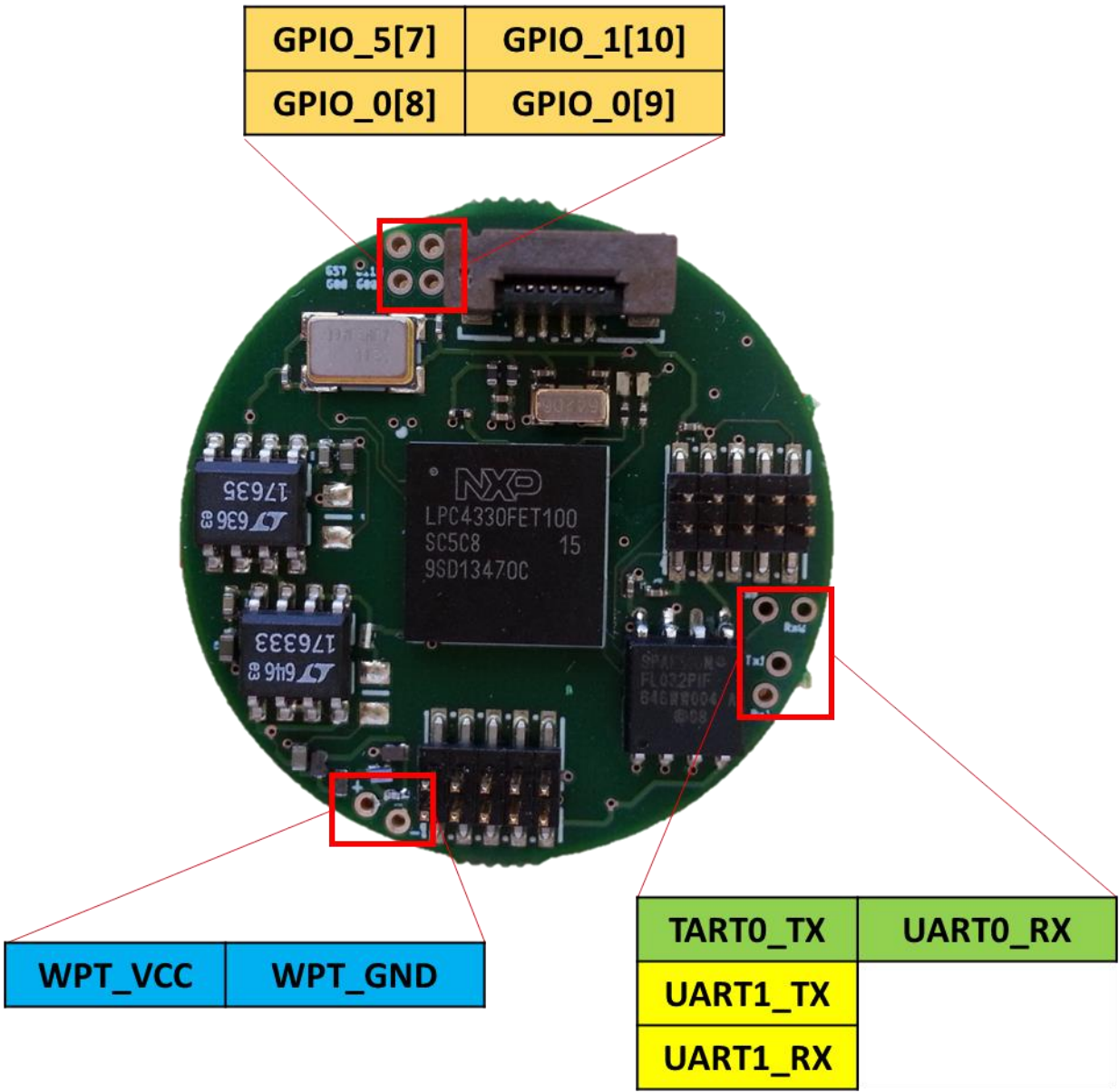
4	3	2	1
gnd	GPIO_02	5V	GPIO_01
GPIO_00	5V	GPIO_03	5V
5	6	7	8



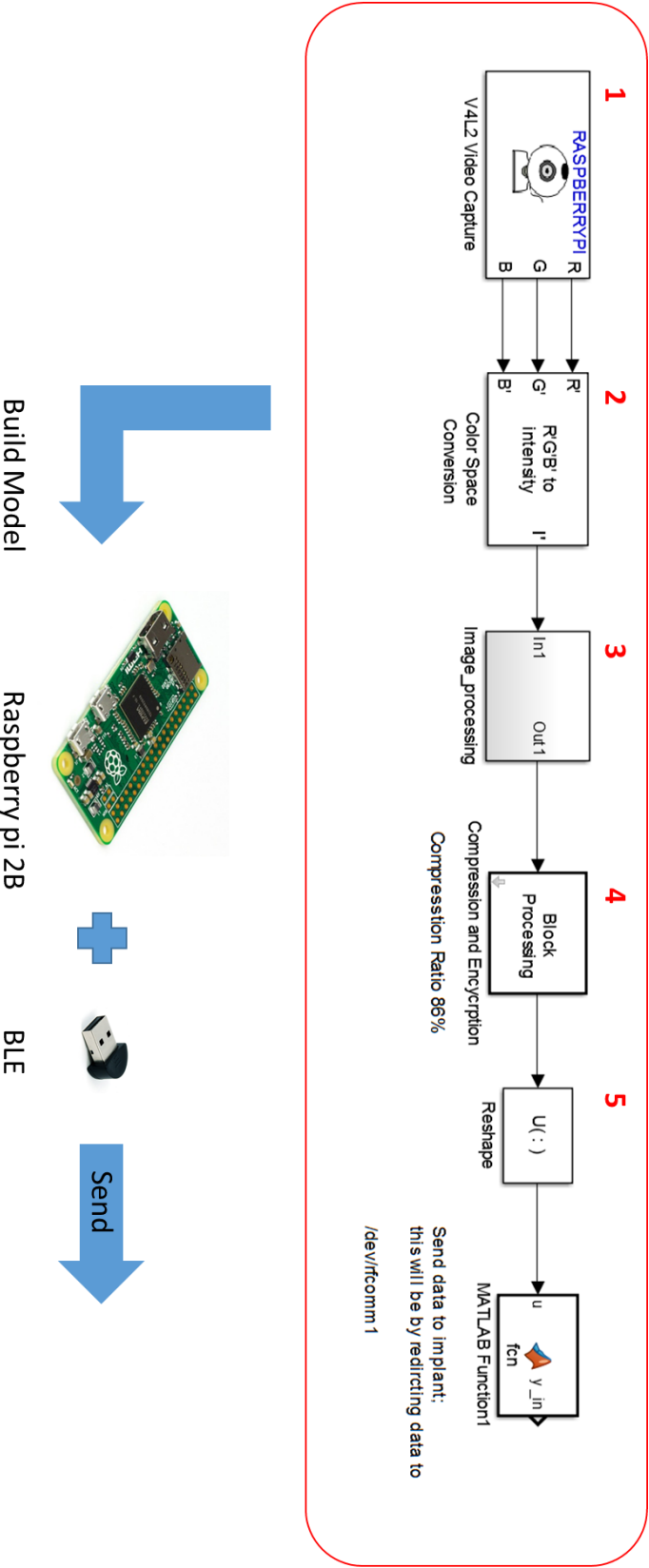
SPI header pinout

2	4	6	8	10
5V	gnd	SPIFI_SCK	SPIFI_CS	gnd
3.3V	SPIFI_MOSI	SPIFI_MISO	SPIFI_SI02	SPIFI_SI03
1	3	5	7	9

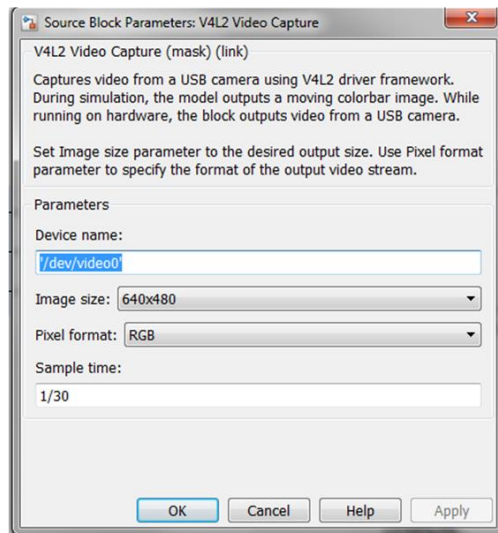
The WPT_VCC and VCC_GND for connecting the receiver coil for the wireless power transfer.



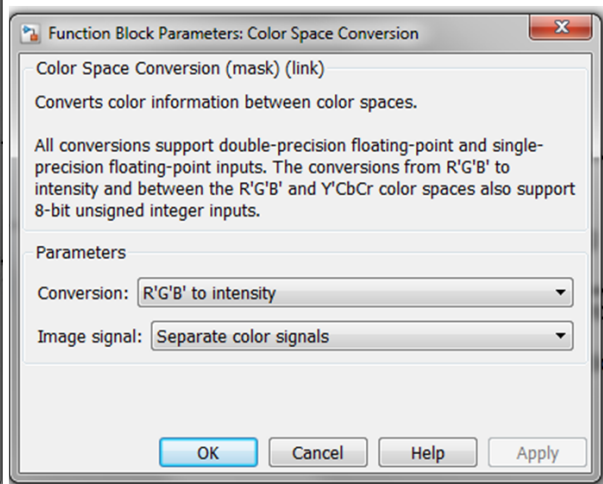
Appendix E. Matlab Simulink for image processing



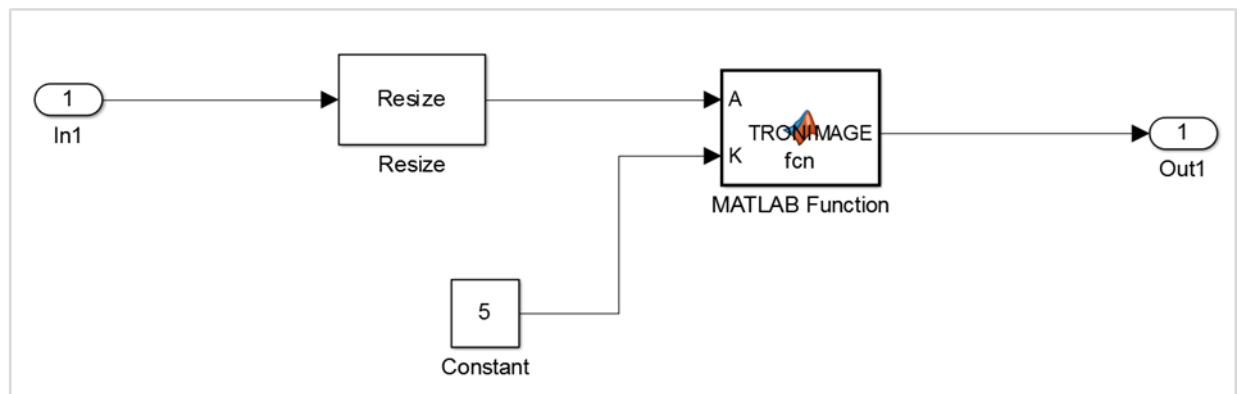
1



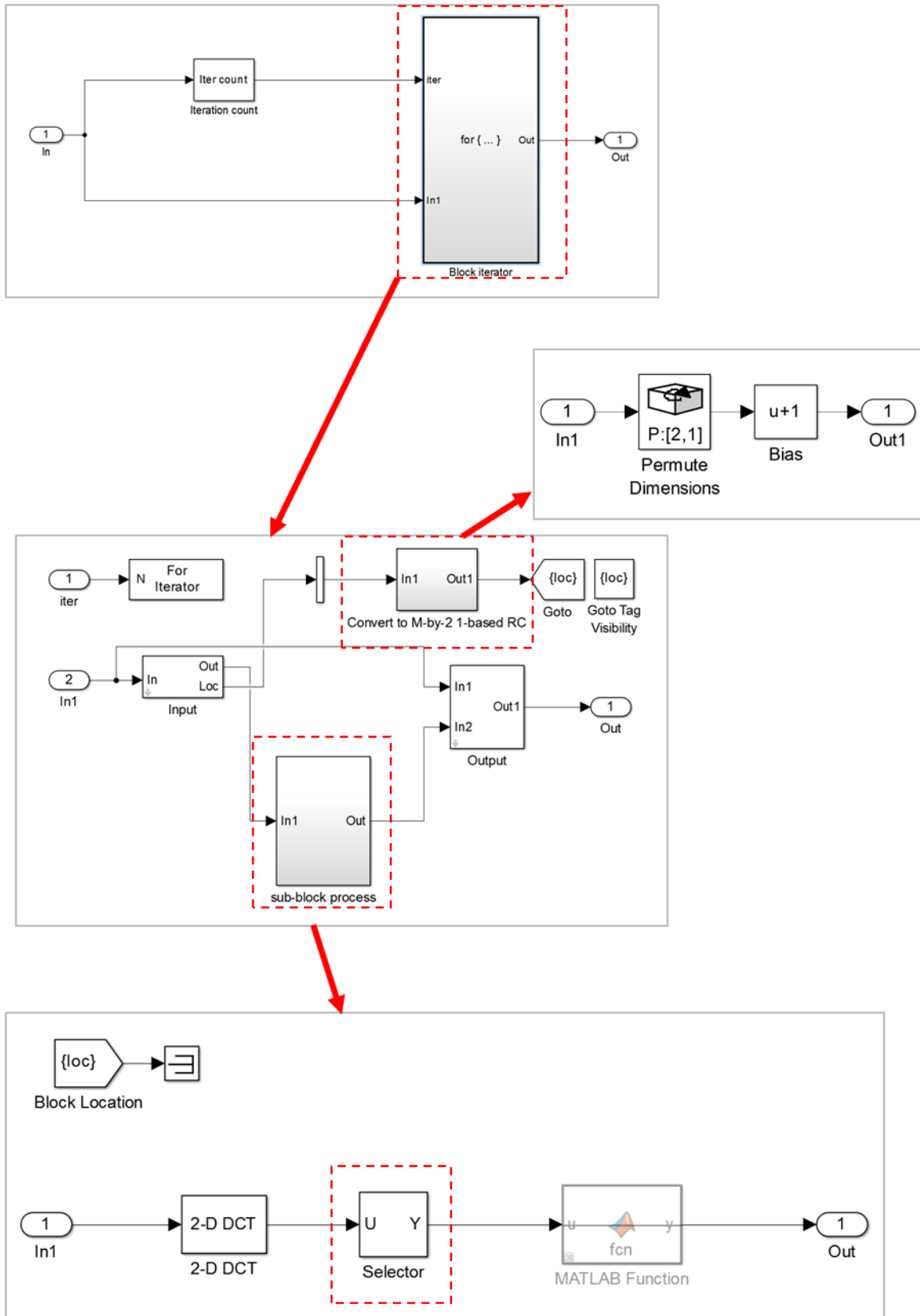
2



3



4



Appendix F. Bit Error Rate (BER) test for Bluetooth

Variables - result100
result100 0 result1000 result5000 result10000 result50000 result100K result500K result1M result2M
1x16 char
1
1 Comparing files D:\BITERROR_BLE\TX_DATA\100.txt and D:\BITERROR_BLE\RX_DATA\100.TXTFC: no differences encountered

Variables - result500
result100 result500 0 result5000 result10000 result50000 result100K result500K result1M result2M
1x16 char
1
1 Comparing files D:\BITERROR_BLE\TX_DATA\500.txt and D:\BITERROR_BLE\RX_DATA\500.TXTFC: no differences encountered

Variables - result1000
result100 result500 result1000 0 result10000 result50000 result100K result500K result1M result2M
1x18 char
1
1 Comparing files D:\BITERROR_BLE\TX_DATA\1000.txt and D:\BITERROR_BLE\RX_DATA\1000.TXTFC: no differences encountered

Variables - result5000
result100 result500 result1000 result5000 0 result50000 result100K result500K result1M result2M
1x18 char
1
1 Comparing files D:\BITERROR_BLE\TX_DATA\5000.txt and D:\BITERROR_BLE\RX_DATA\5000.TXTFC: no differences encountered

Variables - result10000
result100 result500 result1000 result5000 result10000 0 result100K result500K result1M result2M
1x120 char
1
1 Comparing files D:\BITERROR_BLE\TX_DATA\10000.txt and D:\BITERROR_BLE\RX_DATA\10000.TXTFC: no differences encountered

Variables - result50000
result100 result500 result1000 result5000 result10000 result50000 0 result100K result500K result1M result2M
1x120 char
1
1 Comparing files D:\BITERROR_BLE\TX_DATA\50000.txt and D:\BITERROR_BLE\RX_DATA\50000.TXTFC: no differences encountered

Variables - result100K
result100 result500 result1000 result5000 result10000 result50000 result100K 0 result1M result2M
1x118 char
1
1 Comparing files D:\BITERROR_BLE\TX_DATA\100K.txt and D:\BITERROR_BLE\RX_DATA\100K.TXTFC: no differences encountered

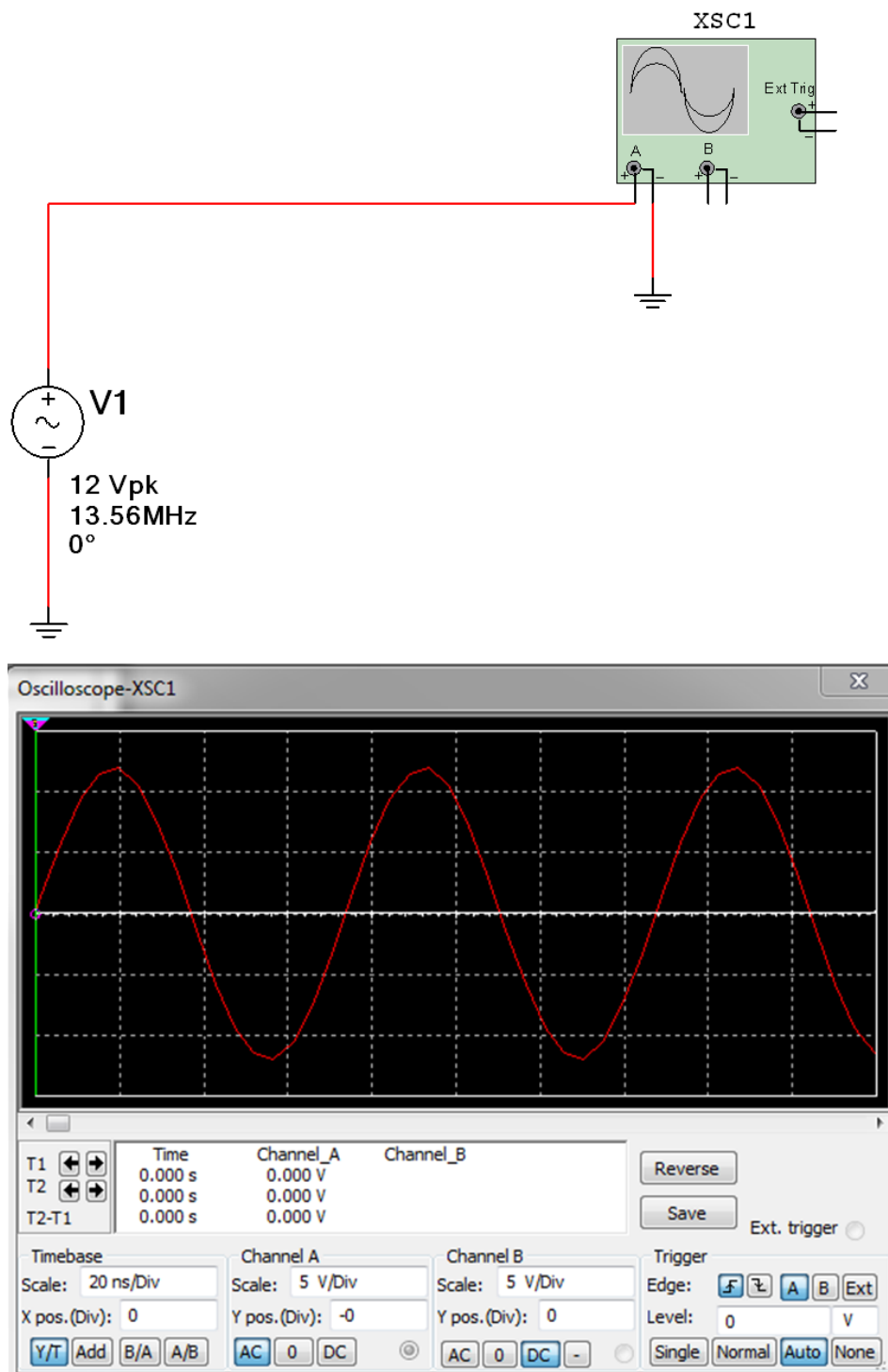
Variables - result500K
result100 result500 result1000 result5000 result10000 result50000 result100K result500K 0 result2M
1x118 char
1
1 Comparing files D:\BITERROR_BLE\TX_DATA\500K.txt and D:\BITERROR_BLE\RX_DATA\500K.TXTFC: no differences encountered

Variables - result1M
result100 result500 result1000 result5000 result10000 result50000 result100K result500K result1M 0 result2M
1x114 char
1
1 Comparing files D:\BITERROR_BLE\TX_DATA\1M.txt and D:\BITERROR_BLE\RX_DATA\1M.TXTFC: no differences encountered

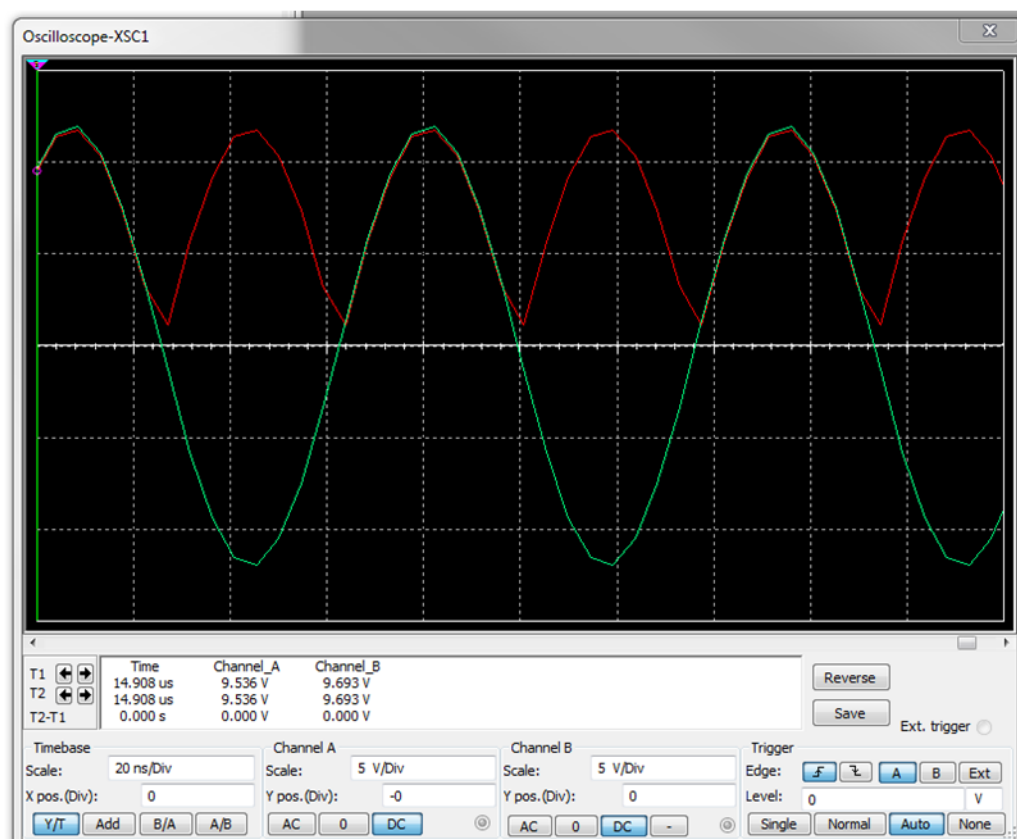
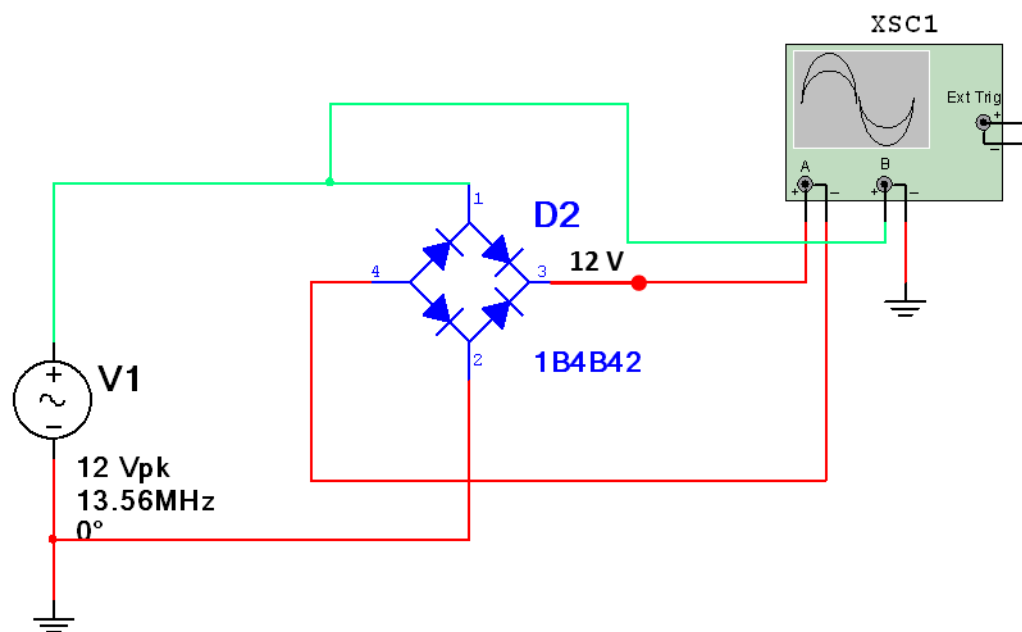
Variables - result2M
result100 result500 result1000 result5000 result10000 result50000 result100K result500K result1M result2M 0
1x114 char
1
1 Comparing files D:\BITERROR_BLE\TX_DATA\2M.txt and D:\BITERROR_BLE\RX_DATA\2M.TXTFC: no differences encountered

Appendix G. Step by step voltage regulator

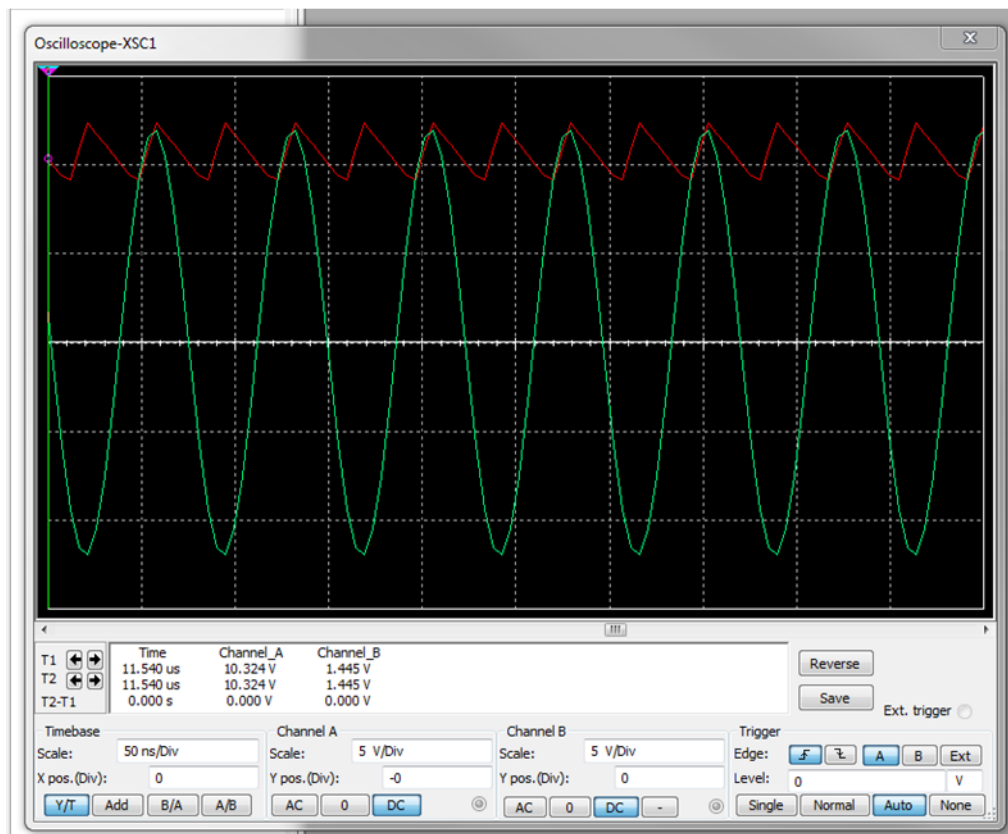
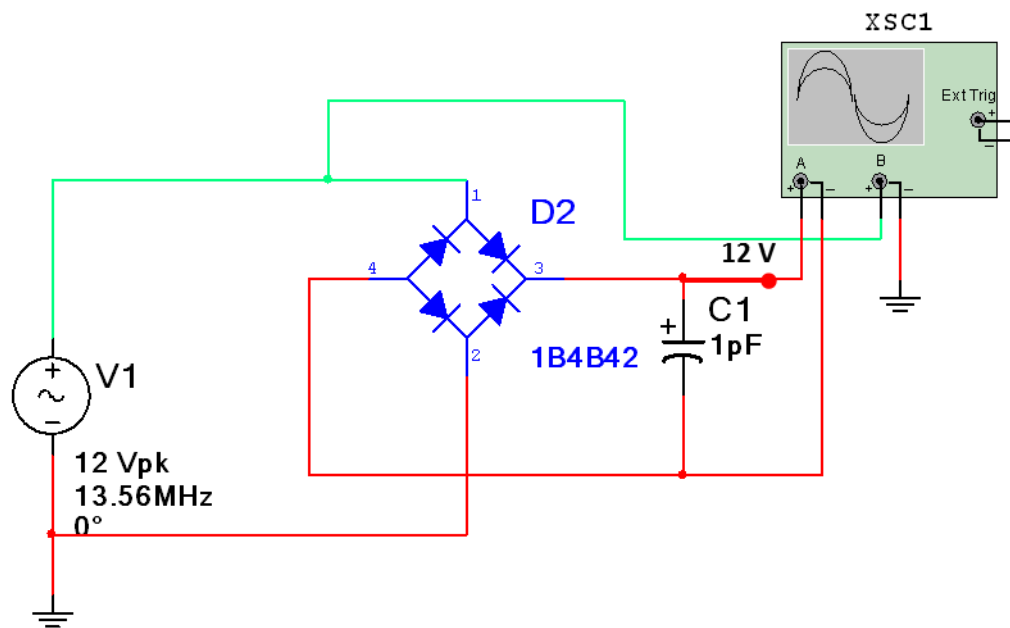
1. Connecting the AC power source to the oscilloscope



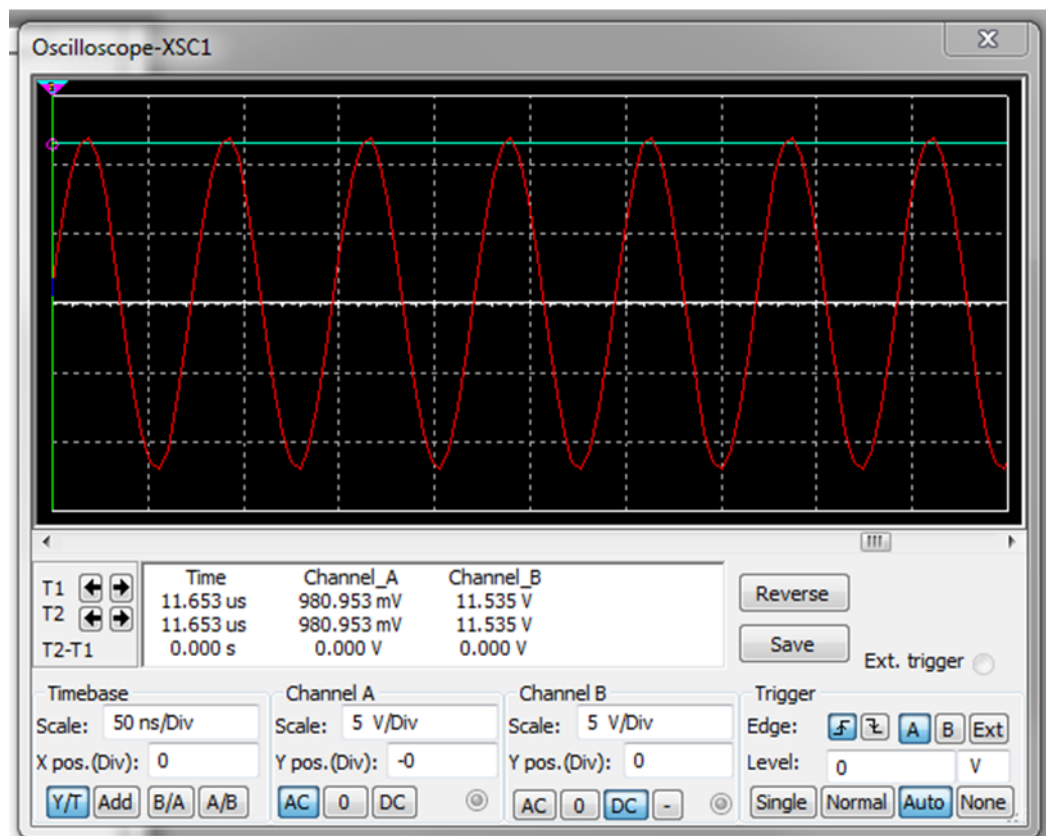
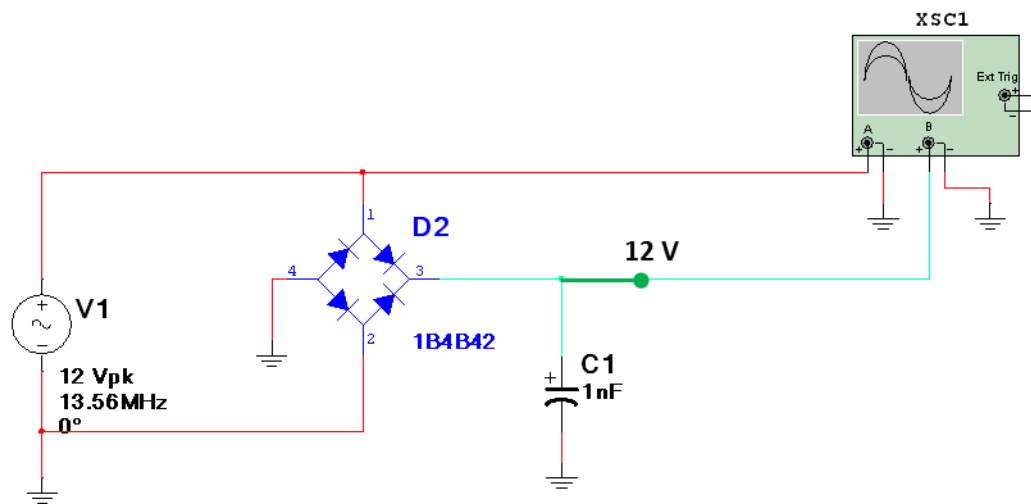
2. Converting AC to DC signal using full bridge rectifier



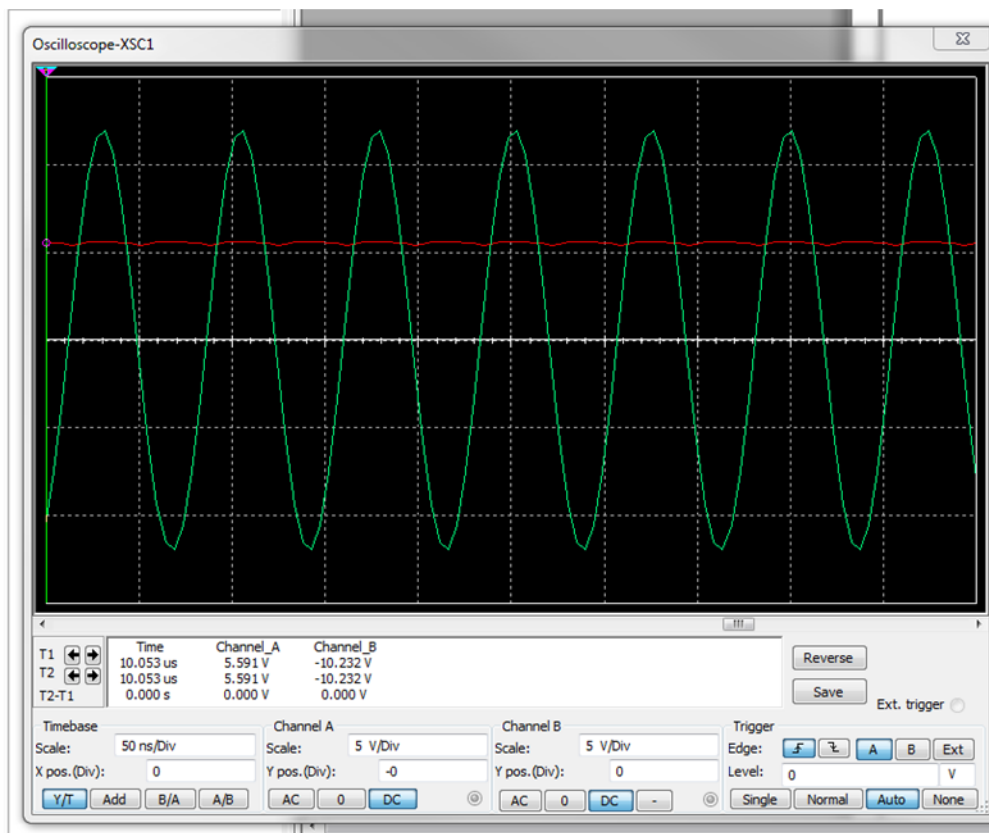
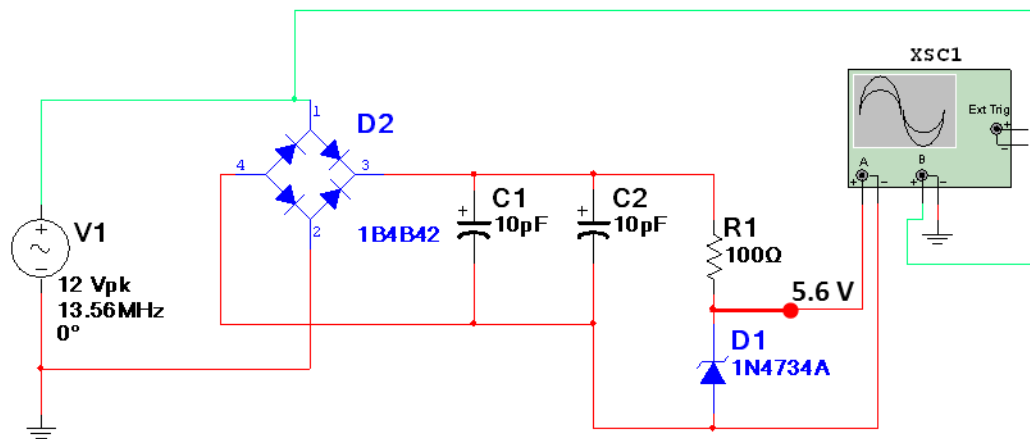
3. Connecting a small capacitor in parallel with the rectifier for reducing ripple voltage



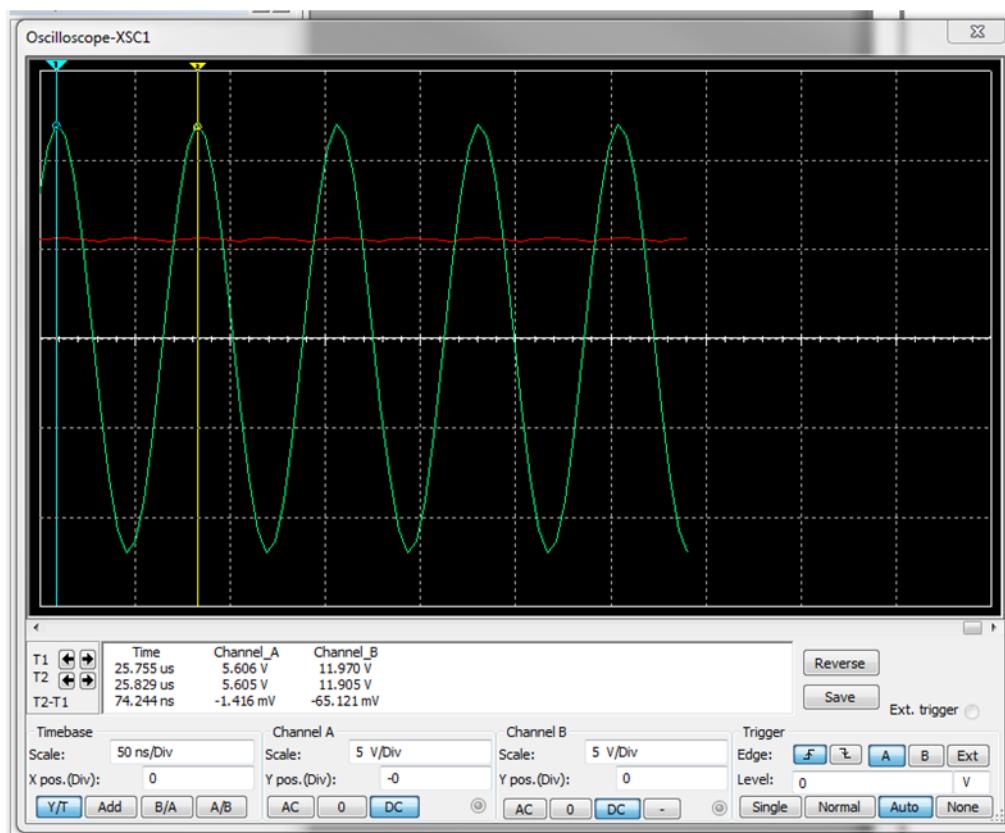
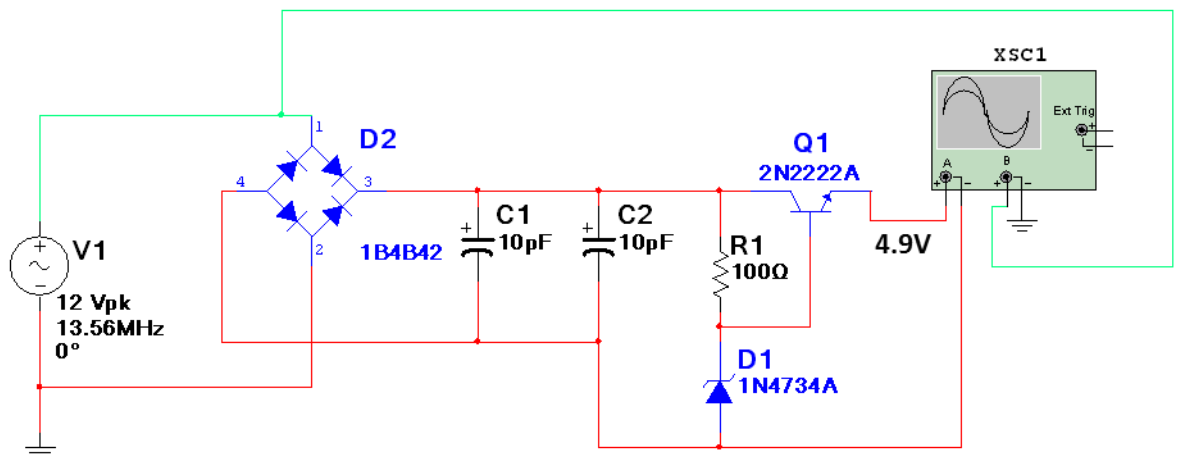
4. Replacing the value of the parallel capacitor from 1 pf to 1 nf.



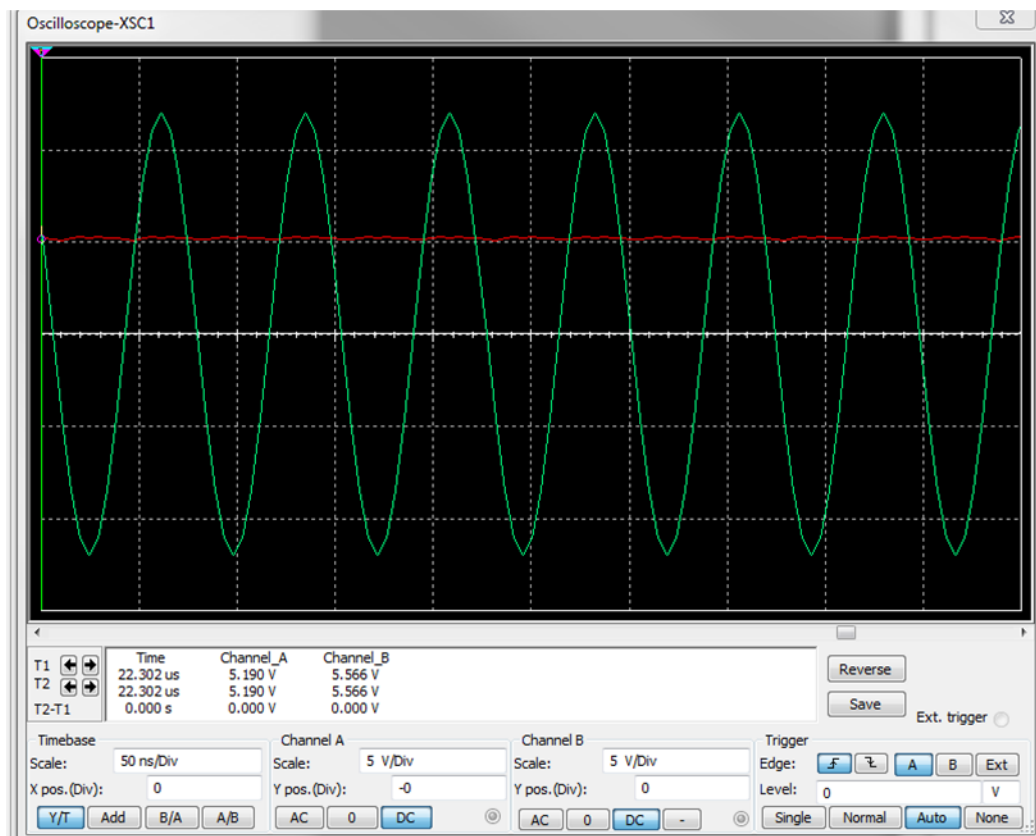
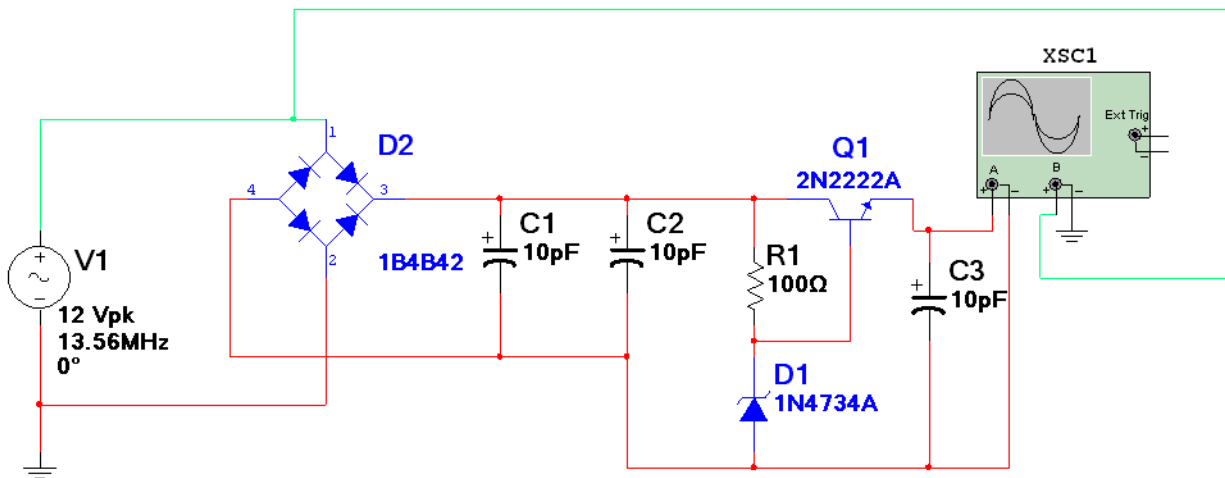
5. Example non stable voltage regulator



6. By connecting the transistor such as 2N2222A the output voltage will be stable



7. The parallel capacitor is required to be connected to the regulator for the output buffer voltage. This is to protect the circuit against the fast voltage drop.



Appendix H. Turn-off Pi automatically

The command line for shutting the Raspberry Pi off after pressing the switch. This script was authored by AndrewH7 (www.instructables.com/member/AndrewH7).

```
#You have permission to modify and use this script only for your own personal usage
#You do not have permission to redistribute this script as your own work
#Use this script at your own risk
```

```
import RPi.GPIO as GPIO
import os

gpio_pin_number= 7

GPIO.setmode(GPIO.BCM)

GPIO.setup(gpio_pin_number, GPIO.IN, pull_up_down=GPIO.PUD_UP)

try:
    GPIO.wait_for_edge(gpio_pin_number, GPIO.FALLING)

    os.system("sudo shutdown -h now")

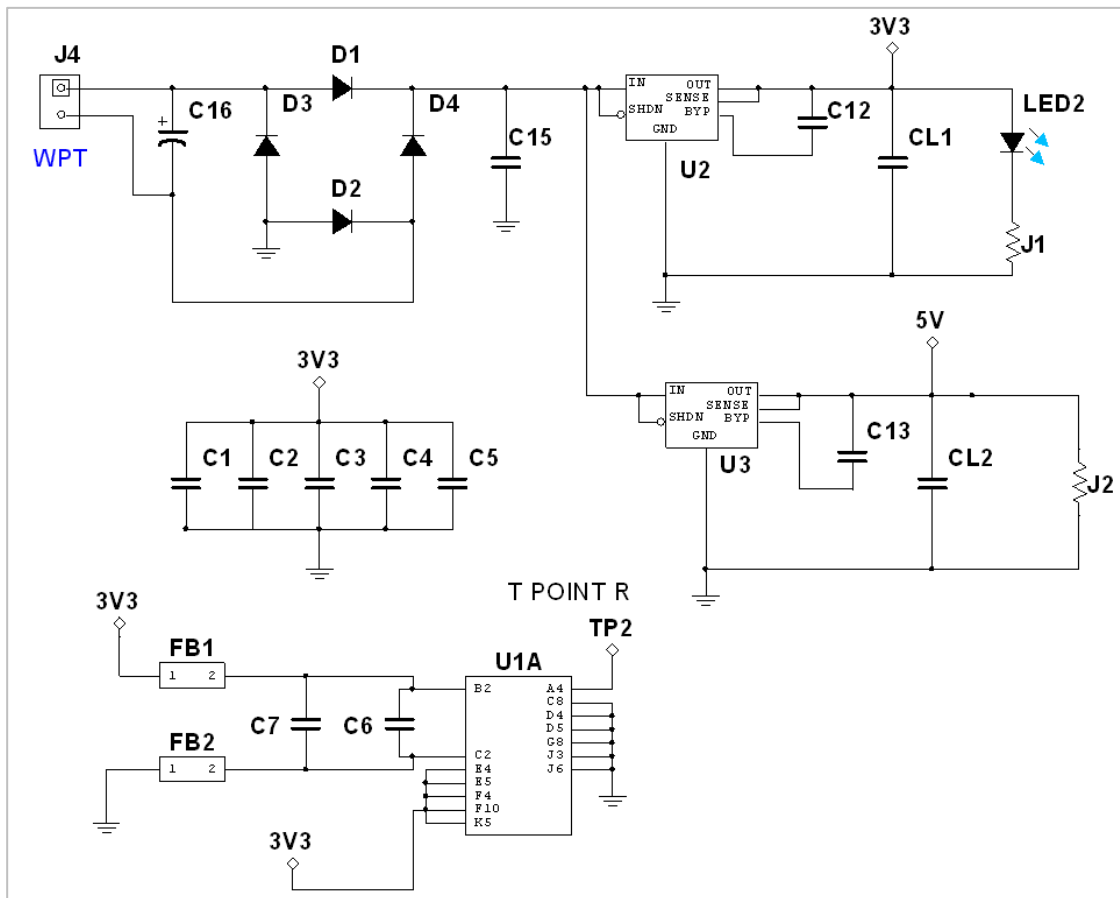
    #Send command to system to shutdown

except:
    pass
GPIO.cleanup()

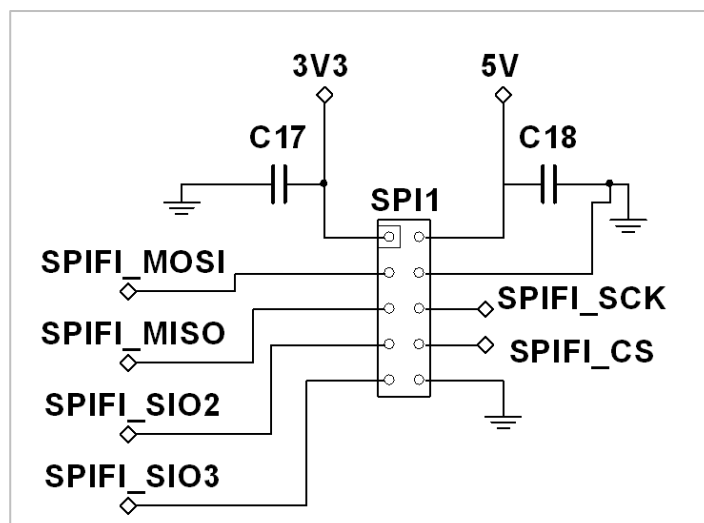
#Revert all GPIO pins to their normal states (i.e. input = safe)
```

Appendix I. Circuit schematic of LPC4330 V2.0

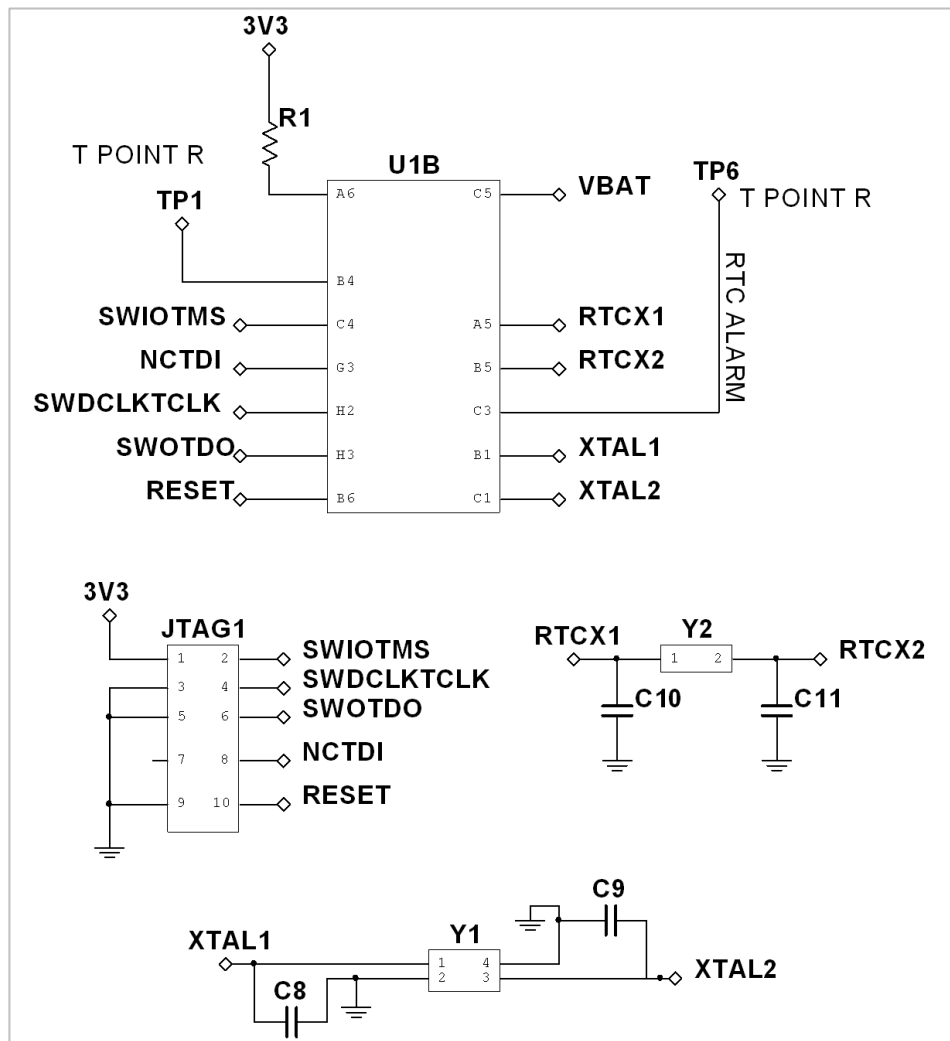
The power management part



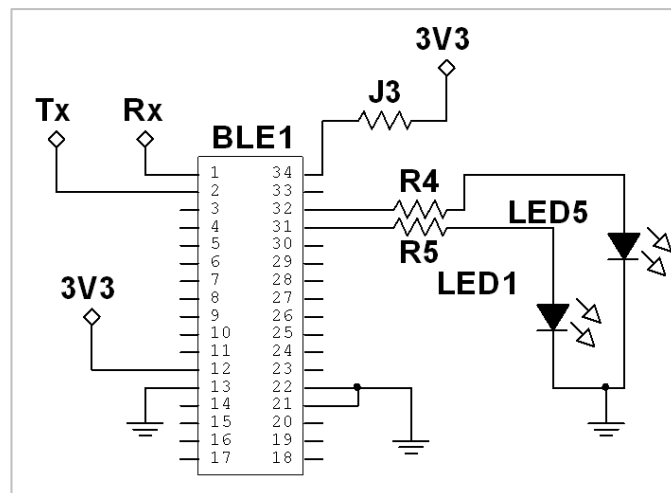
Serial Peripheral Interface bus (SPI)



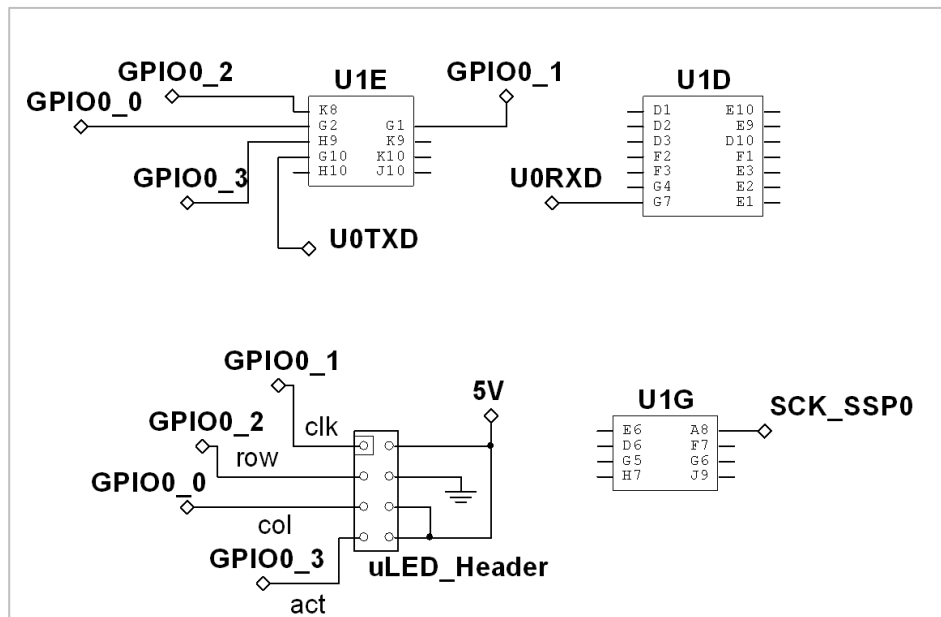
The Joint Test Action Group (JTAG)



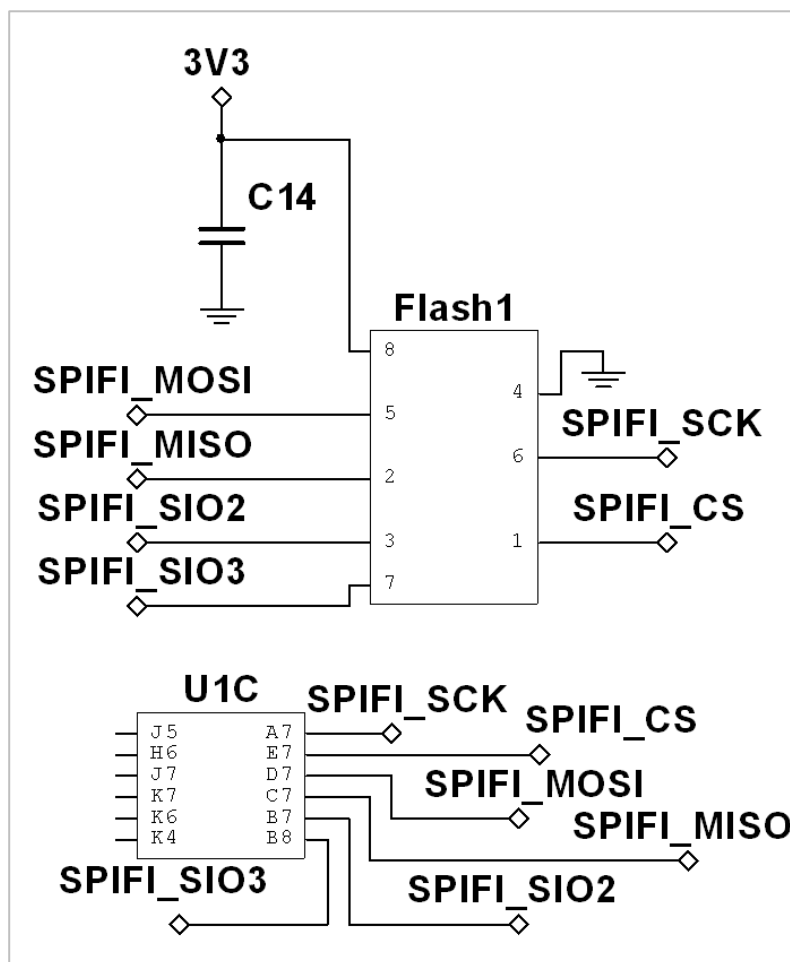
Bluetooth



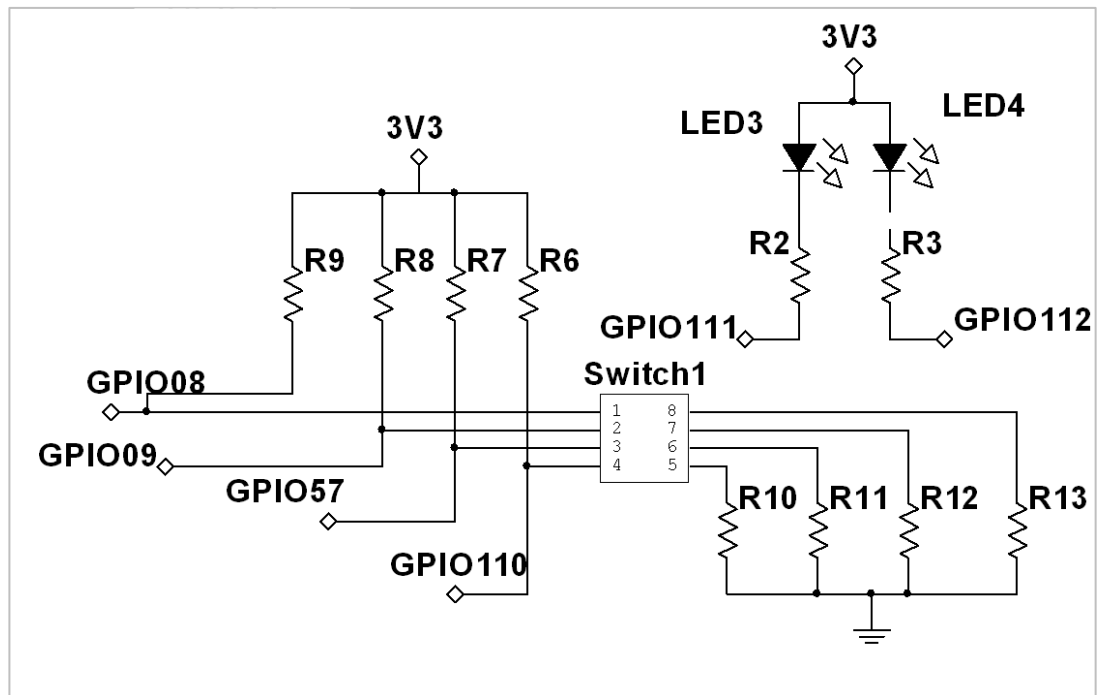
The μ LED header for connecting the μ LED to the board



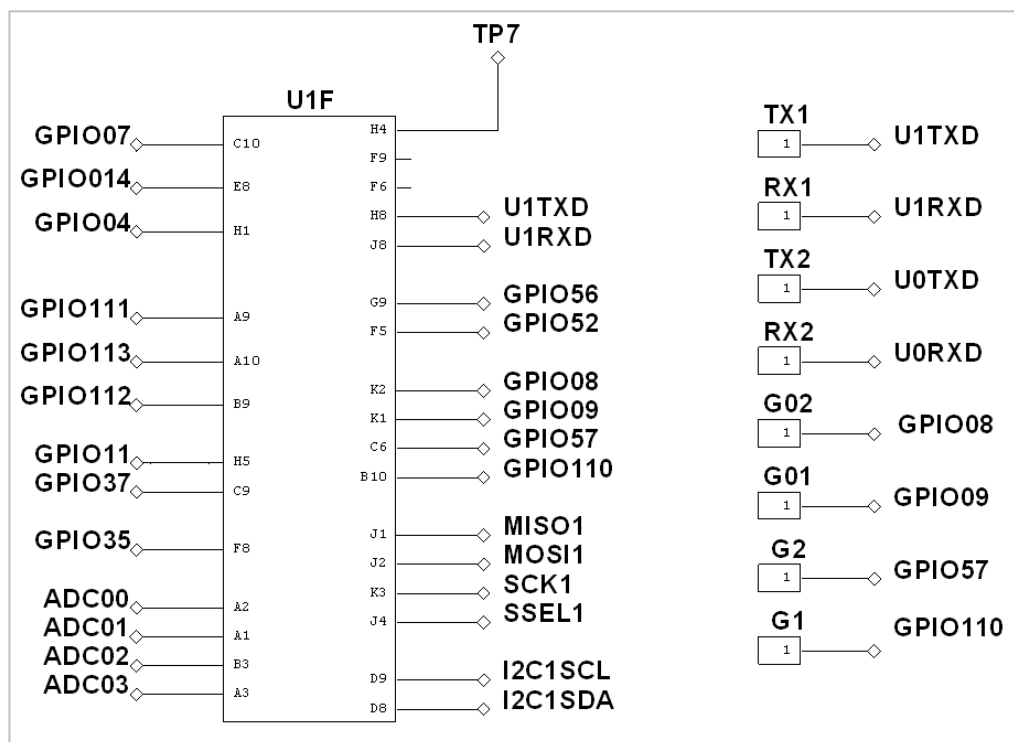
Flash memory



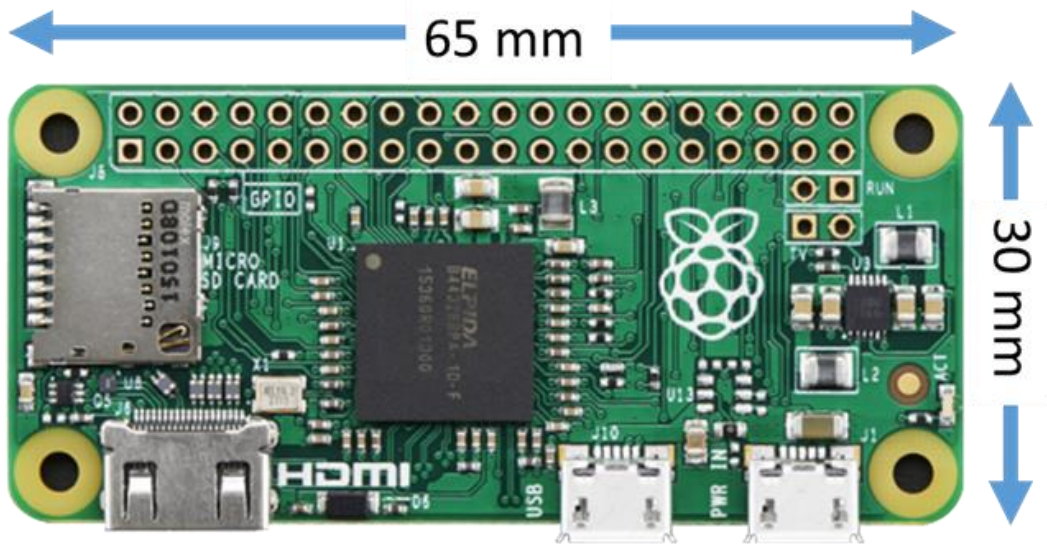
Switch for booting options



The headers for general purpose



Appendix J. Raspberry Pi Zero Version 1.3



The Raspberry Pi Zero version 1.3 is used in transmitter side for real time image processing. The image processing consists of image simplification, image compression and encoding data. Matlab is used for programing Pi.

Appendix K. Packaging

After completing the subsystems, it is time for collecting and assembly all the parts. In general, the assembly parts includes:

- The eyeglass.
- The case.
- The implantable system.

The eyeglass or the headset is collecting the camera and Wireless Power Transfer circuit. Whereas, the case, is to hold the power management, power boost for WPT, Raspberry Pi Zero, Bluetooth and the USB hub. The implantable devices was assembled in a single PCB except the optrodes.

Headset

The basic ideas behind the 3D printing is melting of plastic in a single trace. Then by moving the head of the printer the 2D dimension shape can be created. Moreover, by combining multiple of 2D when the printer is continue in printing, the 3D shape will be made. Using this technology for creating a 3D model is significantly depends on the maximum build volume of the printer.

The headset was designed and printed to hold some parts from the transmitter side. It holds the USB camera, power boost 3.7 V to 12 V and the wireless power transfer circuit. That was designed using Google SketchUp and printed in Newcastle University. It is consists of four separate parts the base, side/arms and the cover. They assembled after printing and they fitted on the base. The example of the design is shown in Figure 1. This is just demo eyeglass are used for this project.

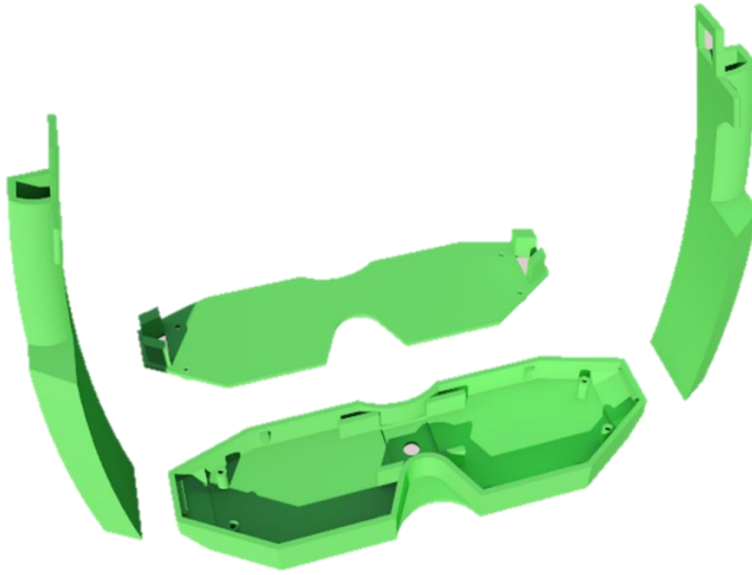


Figure 17: The eyeglass designed by Google SketchUp. It is to hold the USB web cam, the power boost for running the Raspberry Pi Zero and the wireless power transfer circuit.

The case is from the off the shelf devices, which it carries the battery, power management board, power boost, raspberry pi zero, USB hub and switches.

Implantable unit

The implantable unit includes: voltage rectifier, voltage regulator, controlling unit, flash memory, header for programming, SPI out, GPIO out, UART and switch for boot selecting. These components are all collected on a PCB shown in Figure 2.

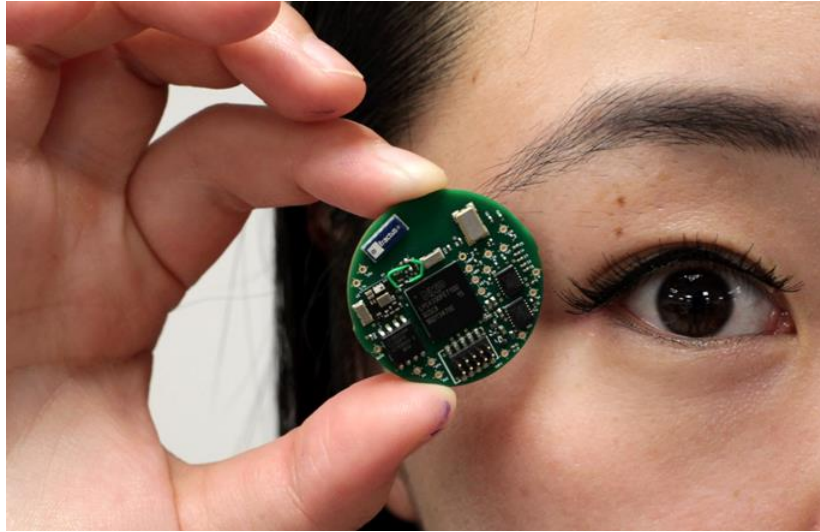


Figure 2: The LPC4330 fabricated board version 1.0. The dimension of the board is 30 mm. The board includes: LPC4330 microcontroller, flash memory, Bluetooth, External crystal oscillator, wireless power receiver circuit, JTAG and GPIOs.